

NASA/TM—2004-212303



# Durability Assessment of Gamma TiAl— Final Report

Susan L. Draper, Bradley A. Lerch, J. Michael Pereira, and Kazuhisa Miyoshi  
Glenn Research Center, Cleveland, Ohio

Vinod K. Arya  
University of Akron, Akron, Ohio

Wyman Zhuang  
Aeronautical and Maritime Research Laboratory, Melbourne, Australia

## The NASA STI Program Office . . . in Profile

Since its founding, NASA has been dedicated to the advancement of aeronautics and space science. The NASA Scientific and Technical Information (STI) Program Office plays a key part in helping NASA maintain this important role.

The NASA STI Program Office is operated by Langley Research Center, the Lead Center for NASA's scientific and technical information. The NASA STI Program Office provides access to the NASA STI Database, the largest collection of aeronautical and space science STI in the world. The Program Office is also NASA's institutional mechanism for disseminating the results of its research and development activities. These results are published by NASA in the NASA STI Report Series, which includes the following report types:

- **TECHNICAL PUBLICATION.** Reports of completed research or a major significant phase of research that present the results of NASA programs and include extensive data or theoretical analysis. Includes compilations of significant scientific and technical data and information deemed to be of continuing reference value. NASA's counterpart of peer-reviewed formal professional papers but has less stringent limitations on manuscript length and extent of graphic presentations.
- **TECHNICAL MEMORANDUM.** Scientific and technical findings that are preliminary or of specialized interest, e.g., quick release reports, working papers, and bibliographies that contain minimal annotation. Does not contain extensive analysis.
- **CONTRACTOR REPORT.** Scientific and technical findings by NASA-sponsored contractors and grantees.

- **CONFERENCE PUBLICATION.** Collected papers from scientific and technical conferences, symposia, seminars, or other meetings sponsored or cosponsored by NASA.
- **SPECIAL PUBLICATION.** Scientific, technical, or historical information from NASA programs, projects, and missions, often concerned with subjects having substantial public interest.
- **TECHNICAL TRANSLATION.** English-language translations of foreign scientific and technical material pertinent to NASA's mission.

Specialized services that complement the STI Program Office's diverse offerings include creating custom thesauri, building customized databases, organizing and publishing research results . . . even providing videos.

For more information about the NASA STI Program Office, see the following:

- Access the NASA STI Program Home Page at <http://www.sti.nasa.gov>
- E-mail your question via the Internet to [help@sti.nasa.gov](mailto:help@sti.nasa.gov)
- Fax your question to the NASA Access Help Desk at 301-621-0134
- Telephone the NASA Access Help Desk at 301-621-0390
- Write to:  
NASA Access Help Desk  
NASA Center for Aerospace Information  
7121 Standard Drive  
Hanover, MD 21076

NASA/TM—2004-212303



# Durability Assessment of Gamma TiAl— Final Report

Susan L. Draper, Bradley A. Lerch, J. Michael Pereira, and Kazuhisa Miyoshi  
Glenn Research Center, Cleveland, Ohio

Vinod K. Arya  
University of Akron, Akron, Ohio

Wyman Zhuang  
Aeronautical and Maritime Research Laboratory, Melbourne, Australia

National Aeronautics and  
Space Administration

Glenn Research Center

---

January 2004

## Acknowledgments

This work was supported by NASA's Aerospace Industry Technology, Ultra Safe, and Higher Operating Temperature Propulsion Components (HOTPC) programs. The authors would like to thank C. Austin, T. Kelly, O. Erdmann, and K. McAllister from GEAE, M.Y. Nazmy and M. Staubli from Alstom Power, D. Clemens from Howmet Research Corp., Y.W. Kim from UES, Inc., and T. Pollock and P. Steif from Carnegie Mellon University for materials and helpful discussions. The authors would also like to thank Mike Nathal for many useful discussions and Bill Karpinski, John Juhas, and Ralph Corner for technical support in conducting the impact and fatigue tests.

The authors are also grateful for the editing support from Laura Becker of InDyne, Inc.

Trade names or manufacturers' names are used in this report for identification only. This usage does not constitute an official endorsement, either expressed or implied, by the National Aeronautics and Space Administration.

This work was sponsored by the Low Emissions Alternative Power Project of the Vehicle Systems Program at the NASA Glenn Research Center.

Available from

NASA Center for Aerospace Information  
7121 Standard Drive  
Hanover, MD 21076

National Technical Information Service  
5285 Port Royal Road  
Springfield, VA 22100

Available electronically at <http://gltrs.grc.nasa.gov>

# Durability Assessment of Gamma TiAl—Final Report

Susan L. Draper, Bradley A. Lerch, J. Michael Pereira, and Kazuhisa Miyoshi  
National Aeronautics and Space Administration  
Glenn Research Center  
Cleveland, Ohio 44135

Vinod K. Arya  
University of Akron  
Akron, Ohio 44325

Wyman Zhuang  
Aeronautical and Maritime Research Laboratory  
Melbourne, Australia

## Executive Summary

### Background

This is the final report for investigations on the durability of gamma TiAl alloys. This work was conducted on cast  $\gamma$ -TiAl alloys under the auspices of the NASA Aerospace Industry Technology Program (AITP) and Ultra Safe project. A small amount of work on one wrought  $\gamma$ -TiAl alloy was also performed under the Higher Operating Temperature Propulsion Components (HOTPC) Project. The thrust of this effort was to assess the impact resistance and residual fatigue life of gamma alloys leading to implementation of this new class of materials into commercial turbine engines.

Because of its low density and good high-temperature properties,  $\gamma$ -TiAl is a candidate for implementation into rotating turbine machinery. To demonstrate the feasibility of using  $\gamma$ -TiAl, General Electric Aircraft Engines (GEAE, Cincinnati, OH) successfully manufactured low-pressure turbine (LPT) blades from their Ti-48Al-2Cr-2Nb (Ti-48-2-2) alloy and engine tested them. These blades were only partially redesigned such that the beneficial properties of  $\gamma$ -TiAl were not fully accommodated. NASA AITP funding was awarded to a GEAE-led team to develop an optimized design and manufacturing capability that would lead to implementation of the Ti-48-2-2 LPT blades into commercial service. One of the goals of the program was to realize a weight reduction of 40 percent from the currently used Ni-base superalloys.

Because of the limited ductility of  $\gamma$ -TiAl there was a concern about its impact resistance. The AITP program identified this as a performance-related risk to the implementation of this alloy system. Impact resistance was therefore studied by NASA for risk abatement purposes. These investigations were conducted in a manner which simulated actual engine conditions as closely as possible. This was accomplished by casting a test sample with similar geometries as an LPT blade and impacting the sample according to expected impact velocities and trajectories that the low pressure turbine would experience from domestic object damage. Residual fatigue strength was subsequently measured.

Additional investigations were conducted under NASA's Ultra Safe project to further define acceptable design limitations associated with impact damage on titanium aluminide. Additional gamma alloys were included in this study to provide a more complete scientific understanding of alloying effects on impact and fatigue in cast alloys. An in-house capability was developed to predict the extent of cracking due to impacting via a computational model. Additionally, a small study on the fretting resistance of  $\gamma$ -TiAl was performed to assess potential wear in the dovetail.

## Impact and Fatigue

Seven cast alloys were used in this study, including Ti-48-2-2 and three low-Al variants of Ti-48-2-2: ABB-2, ABB-23, and NCG359E. A wrought alloy, 95A, was also examined. To capture as many actual engine conditions as possible, flat specimens of Ti-48-2-2 and ABB-2 alloys were cast to size to obtain elliptical leading edges that simulated the leading edges of actual LPT blades. Cast-to-size samples were made from the Ti-48-2-2 and ABB-2 alloys. The remaining alloys were available in plate form (either cast or wrought), and specimens were machined to a geometry similar to that of the cast-to-size samples. Specimens were impacted at a 90° angle to the leading edge in a ballistic impact rig. The projectiles were either 1.6- or 3.2-mm-diameter annealed steel ball bearings. A wide variety of impact conditions were studied, which encompassed conditions expected during engine operations. Variables studied were impact energy, distance of impact from leading edge, specimen thickness, impact temperature, projectile hardness, projectile size, and impact velocity.

Extensive post-impact microscopy was performed to document the size, type, and morphology of the cracks resulting from impacts. Two major types of cracks were observed. On the front side of the sample and near the impacted region, cone-shaped cracks formed at angles to the leading edge. These cracks were classified as Hertzian (HZ) cracks. At higher impact energies, the HZ cracks propagated through the sample thickness and a chunk of material was removed. This condition was termed a “blowout.” On the back side of the sample, cracks formed near the leading edge and were perpendicular to the specimen axis. These were classified as back-side (BS) cracks. The length of both of these crack types were correlated with the impact variables using multiple linear regression. Of the main variables, impact energy had the largest effect on crack length for both crack types. Sample thickness was also important, with thinner samples experiencing larger cracks. Impact location,  $X$ , also played a significant role in the crack size, where intermediate values of  $X$  gave the largest crack lengths, and values of  $X$  either closer to or farther from the leading edge resulted in smaller crack lengths.

The bulk of the crack correlations were performed on the cast-to-size Ti-48-2-2 material since this material had immediate commercial interest. For the other materials fewer samples were available, and the regression analyses were either limited or not performed. All of the materials showed similar impact damage for equivalent impact energies. There were small differences for some of the other impact variables among the alloys.

High-cycle fatigue (HCF) tests were performed on the impacted samples as well as on a few virgin (not impacted) samples. Tests were conducted at 650 °C at a frequency of 100 Hz. Tests were also conducted at 730 °C for a few alloys. Multiple load-ratios,  $R_\sigma$ , were used, but all specimens were cycled in tension to prevent buckling. The step test method was employed in which the specimens were cycled for a given block size ( $10^6$  or  $10^7$  cycles). If the specimen survived, the maximum stress level was increased by an increment of 14 MPa. This process continued until the sample failed.

Residual fatigue strengths were found to be correlated with the size of the defect that led to failure of the sample. This defect size for impacted samples was the crack length as determined by the microscopy measurements. In cases where casting porosity was the critical defect, the defect sizes were measured on the fracture surfaces after the tests. There were a few cases where cracking initiated at large facets—a result of the large  $\gamma$ - $\alpha_2$  lamellar grains. Such grains resulted in low fatigue strengths and large variability. Also, failure at these facets could not be predicted.

The residual fatigue strength was reasonably predicted using a threshold approach based on linear elastic fracture mechanics. Through knowledge of the threshold stress intensity and the crack size and shape, the fatigue strength could be calculated. This is based on the observation that the controlling step in failure is the initiation of the fatigue crack out of the existing defect and that once initiated, it grows to a critical size in a limited number of cycles. While the defect size and shape were well known, the threshold stress intensity was unknown. Therefore, given the fatigue failure stress, the threshold stress intensity was back-calculated and compared with values appearing in the literature. Good agreement was observed between the calculated and published values.

## Fretting

Since  $\gamma$ -TiAl is being considered for LPT blade applications, there is a concern about fretting in the dovetail region of the blade. To study this, a few fretting tests were performed on the cast and machined, low-Al Ti-47-2-2 material against IN718 (a common disc alloy). Ti-6Al-4V was also used against IN718 for comparison. A series of reciprocating pin-on-flat tests were performed in air. Test temperature, load, frequency, and slip amplitudes were varied and related to the amount of wear. The wear patterns were characterized using an optical profiler and microscopy.

Transfer of material to the IN718 flats from the  $\gamma$ -TiAl was observed. Likewise the Ti-6Al-4V also transferred material to the IN718 flats, however in much greater amounts than the  $\gamma$ -TiAl. The wear patterns consisted of wear debris, scratches, plastically deformed asperities, and cracks. In general, the amount of wear increased with decreasing frequency, increasing load and increasing slip amplitude. Wear reached a minimum at a temperature of 200 °C due to the formation of a protective oxide film. At still higher temperatures, wear began to increase as the oxide film broke down.

Fretting-fatigue tests were performed on a few Ti-47-2-2 samples. Fretting was performed using three types of IN718 contact pads: a flat-ended wedge, a knife-edged wedge, and a hemispherical pin. Various fretting conditions were used to create linear wear patterns on the face of the fatigue samples, perpendicular to the specimen axis. The samples were subsequently fatigue tested using the step method. None of the samples failed at the frets, but failed elsewhere in the gage. This suggests that either  $\gamma$ -TiAl is not as sensitive to surface defects as originally expected or more severe defects were elsewhere in the samples.

## Conclusions

This study has shown that  $\gamma$ -TiAl (particularly Ti-48-2-2) has sufficient durability to allow the design of robust LPT blades. The alloys can both survive relatively large impacts without failing catastrophically and can survive the cyclic design loads even with greater than expected impact damage. Gamma alloys can also tolerate relatively large amounts of casting porosity. These defects affect the fatigue strength, which can be predicted using a fracture mechanics approach. This information has helped both GEAE and ALSTOM Power (ABB, Baden, Switzerland) develop damage-tolerant design and lifing approaches to ensure that gamma parts will have the necessary robustness to have long life in engine service.

Both impact and subsequent HCF strengths are only marginally affected by lower Al content in the Ti-48-2-2 alloy system. Similarly, there is minimal variation with alloy composition in the impact resistance and fatigue strength between the majority of the alloys examined. The one possible exception may be the ABB-23 alloy which appears to have slightly superior fatigue properties due to its small lamellar grain size. We conclude that stronger, less ductile alloys do not suffer impact or HCF penalties and that selection of an alloy for a specific application may be based on other properties of interest.

## Introduction

Families of alloys based on  $\gamma$ -TiAl have recently been developed for aerospace applications. Their advantage is their low density (3.8 g/cm<sup>3</sup>) coupled with good high-temperature properties. The density-compensated strengths make the alloys attractive for rotating components in aircraft engines. To demonstrate the feasibility of this application for  $\gamma$ -TiAl, General Electric Aircraft Engines (GEAE, Cincinnati, OH) successfully manufactured low-pressure turbine (LPT) blades from their  $\gamma$ -TiAl alloy, Ti-48Al-2Cr-2Nb (at.%) and engine tested them in 1993 (ref. 1). These blades were cast overstock and only partially redesigned such that the beneficial properties of  $\gamma$ -TiAl were not fully accommodated. Thus, in 1995 a team consisting of GEAE, Precision Castparts Corporation (Portland, OR), Howmet

Castings (Whitehall, MI), Oremet-Wah Chang (Pittsburgh, PA), and Chromalloy Turbine Airfoils Division (Harrisburg, PA) was awarded NASA-sponsored Aerospace Industry Technology Program (AITP) funding to develop an optimized design and manufacturing capability that will lead to the eventual implementation of Ti-48Al-2Cr-2Nb (Ti-48-2-2) LPT blades into commercial service. An LPT blade made of  $\gamma$ -TiAl presents the greatest weight-savings potential for use of this alloy in high-bypass turbofan engines. In the last two LPT stages the temperatures were suitable for this material, and the strength requirements were modest. Also, should a catastrophic failure of blades in these stages occur it would have a relatively minimal impact on engine performance and safety. Thus, confidence in designing LPT blades with this material is achieved as there is minimal risk. One of the goals of the program was to realize a weight savings of 70 kg per stage (a 40 percent weight reduction from currently used Ni-base superalloys), while maintaining the current system cost.

In order to achieve the cost goals of the AITP—the prime emphasis of the program—the TiAl LPT blades had to be cast net shape. Other manufacturing operations, such as ingot making, chemical analysis, and dimensional correction were also addressed. The shape of the low-pressure turbine blade is naturally difficult to cast, having thick ends and a very thin middle. Both PCC and Howmet conducted repeated casting trials, using a wide range of casting configurations and designs. Nonstandard gating schemes led to reasonable success in filling the airfoil sections, but only limited success was achieved in preventing shrinkage-related quality problems. After much iteration, the selected LPT blade design was thickened in several areas to improve both castability and impact resistance. However, this design did not meet the weight savings goals and also incurred a small performance debit due to the thick trailing edge. While considerable progress was achieved in casting net-shape LPT blades (ref. 2), an economical process that met the weight savings goals was not realized and, combined with GE's decision to discontinue work for the next version of GE90 engine that was targeting TiAl LPT blades, the program was discontinued.

The AITP program also studied two performance-related risks to the implementation of TiAl LPT blades into service: impact resistance and tip rub. GEAE examined tip rub, while the impact resistance was primarily examined by NASA. It was noted early in the program that  $\gamma$ -TiAl had poorer impact resistance compared to the currently used nickel-based superalloy, Rene 77. A study of the effect of ballistic impacts on the high-cycle fatigue (HCF) strength of Ti-48-2-2 was therefore initiated to address this risk. Engine test hardware was examined, and service shop personnel surveyed to determine the severity and frequency of damage on these blades so that a typical impact event could be defined. The conclusion was that “impact damage does not occur in LPT blades, absent a significant upstream event” (ref. 3). However, because of the lower capabilities of  $\gamma$ -TiAl with respect to impact damage, the fatigue capability of  $\gamma$ -TiAl with impact damage was nevertheless defined for risk abatement purposes.

The effect of ballistic impacts on the HCF properties of Ti-48-2-2 was studied in great detail (ref. 3) using cast-to-size specimens. The main conclusion of this program was that given the fatigue design stresses expected for a GE90 sixth-stage LPT blade, Ti-48Al-2Cr-2Nb would survive an impact under normal service-oriented conditions. At this location in the engine domestic object, damage is more likely to occur than foreign object damage. These impacts would most likely be from small bits of seals upstream in the engine or pieces of thermal barrier coatings causing only very small dents in the blades. It would take a large impact event, with an energy of 1.5 J or higher, as might result from a catastrophic event, to cause impact damage large enough to result in subsequent fatigue failure of a Ti-48-2-2 LPT blade under normal service-related loads.

As a complement to the initial NASA–GEAE study, additional investigations were conducted under NASA's Ultra Safe project to further define the acceptable design limitations associated with impact damage on Ti-48-2-2. Impact studies were also expanded in the Ultra Safe project to include several different TiAl alloys. Investigating these additional alloys not only resulted in a more complete scientific understanding of alloy effects on impact and fatigue properties, but also benefited other companies associated with the production of TiAl components. The Ultra Safe project also led to the development of a computational model to predict the extent of cracking due to impacting of  $\gamma$ -TiAl, as well as to a small study on  $\gamma$ -TiAl's fretting resistance. While this is the final report for the Ultra Safe TiAl impact

resistance program, it also includes a summary of the work performed under the NASA–GEAE AITP and a small amount of work on impact and fatigue of a wrought TiAl alloy performed under the Higher Operating Temperature Propulsion Components (HOTPC) Project.

## Procedures

The bulk of this report deals with the impact behavior of various gamma alloys. In short, specimens were impacted ballistically under a range of conditions. The damage (i.e., cracks) due to impacts were measured and documented. The specimens were then fatigue tested to determine the amount of degradation due to impacting. Various mean stresses were also employed in fatigue to simulate actual design conditions.

The damage was modeled using finite element modeling (FEM) to permit prediction of cracking severity with minimal future experiments. Finally, since these alloys are new and relatively little is known of their behavior, a small study on fretting was also performed. Fretting was chosen since the LPT blades will experience wear with the mated disk in the dovetail areas. If the wear is severe enough, it could initiate a fatigue crack, leading to eventual failure of the blade. Thus, some of the fretted specimens were fatigue tested as well.

## Impact-Fatigue Tests

The impact behavior and its effect on fatigue were investigated in a number of  $\gamma$ -TiAl alloys. The bulk of the work was performed on cast Ti-48-2-2, and this is referred to in the rest of the report as the baseline alloy. Additional alloys were added as interest in this work grew. While not originally planned, the additional alloys allowed some general comparisons between tensile properties, microstructures, and chemistry and their effects on impact and fatigue resistances.

**Materials.**—Ti-48-2-2 impact specimens were cast to size in a dog-bone configuration by Precision Castparts under the AITP program. The flat specimens had gage sections that were reduced in both the width and thickness dimensions with elliptical cross sections 25 mm wide. The cast-to-size sample edges simulated the leading edges of actual LPT airfoils (fig. 1) by capturing the same leading edge radii and neighboring curvature as would be designed into an LPT blade. The specimens were processed in a sequence typical for an LPT blade: hot isostatic pressing, chem.-milling, heat treating, and media finishing. The specimens were given an exposure of 650 °C for 20 hr to simulate typical embrittlement at service conditions. Two different batches of samples were used. The first batch was used in the microstructural design of experiments (ref. 3) and contained specimens with three different leading-edge thicknesses, each with a different bluntness. The specimen thicknesses in the center of the gage sections were 2.1, 2.6, and 3.7 mm. The thin-specimen geometry simulated the currently used RENE 77 blades, while the thicker geometries were configured in anticipation of the poorer performance of TiAl in ballistic impact resistance compared to superalloys. The second batch of specimens was cast using only the thickest geometry; these specimens were used for the fatigue studies in this report.

Through a cooperative agreement with Howmet Castings, ALSTOM Power, CH, Ltd., Baden, Switzerland, provided cast-to-size specimens of their ABB–2 alloy using the same thicker specimen design as used for the Ti-48-2-2 study with GEAE. The ABB–2 has higher strength and lower ductility than Ti-48-2-2. Although sufficient specimens were obtained to complete the study, the specimens were difficult to cast to size because of the hourglass shape configuration, and thus the casting yield was low. The cast-to-size ABB–2 specimens had large, lamellar grains at the specimen surface in many samples, and significant variation in impact crack lengths was attributed to these large grains (ref. 4).

While the cast-to-size specimens offered the best opportunity to match actual blade manufacturing conditions, the cost and difficulty of casting these specimens inhibited progress in studying the impact

resistance of additional cast-to-size alloys. Therefore, a machined specimen (fig. 2) with a thickness of 2 mm and leading edges resembling those of the cast-to-size specimen was designed. Ti-47Al-2Nb-2Cr cast plates supplied by GEAE were machined into impact specimens. The impact resistance and remnant fatigue strength of the cast and machined Ti-47-2-2 specimens were directly compared to the cast-to-size Ti-48-2-2 specimens.

Additional  $\gamma$ -TiAl alloys studied using cast plates machined into elliptically shaped specimens included alloys with lower Al (nominally Ti-47-2-2), ABB-23, and NCG395E. Since the Al content varies slightly from casting to casting, and the strength and ductility of Ti-48Al-2Cr-2Nb varies with Al content (ref. 5), the effect of low Al on the impact resistance of Ti-48-2-2 was of interest. To this end a plate of a lower Al alloy (Ti-47-2-2) was obtained from Carnegie Mellon University (CMU), and impact specimens were machined from this plate. Additional plates of Ti-47-2-2 were also purchased from Howmet for additional impact characterization and fatigue studies, including a study on coaxing. A small, irregularly shaped piece of ABB-23 was available from ALSTOM Power for limited ballistic impact characterization, as were a few samples for fatigue testing taken from a heat shield made from ABB-23. ABB-23 has boron added to refine the grain size; thus the effect of the refined grain size on the impact resistance was evaluated. Details of the compositions and microstructures in these alloys are discussed in the Chemistry and Microstructure section. NCG395E is a cast TiAl alloy developed by GEAE. This Ta-containing alloy has a higher strength than Ti-48-2-2. Slabs of NCG395E were purchased from Howmet Castings and machined into elliptically shaped impact-fatigue specimens. The ability to study the impact resistance of wrought  $\gamma$ -TiAl alloys was also of interest to study the effect of a more refined, uniform microstructure typical of wrought alloys. Wrought alloys have a potential use as compressor blades. The alloy chosen was alloy 95A, a version of the Air Force's K5 alloy. Y.W. Kim of UES, Inc. (Dayton, OH) supplied a forged pancake of 95A from which samples were machined.

**Experiments.**—An effort was made to capture as much of actual engine conditions as possible in laboratory tests including casting the Ti-48-2-2 and ABB-2 specimens to shape with simulated leading edges of LPT blades. However, due to cost and availability issues, subsequent specimens were machined from cast or wrought plates into impact specimens. The samples were rough cut by electrodischarge machining (EDM) and then low-pressure ground to final shape. Every surface was ground to eliminate EDM damage.

The microstructure of the specimens was studied using polarized light on an optical microscope. Grain size was measured using a line-intercept technique, and lamellar volume fraction was determined by point counting. The Al content of the samples was determined by X-ray fluorescence (XRF), while the remaining elements were analyzed by inductively coupled plasma emission spectrometry (ICP) and gas analysis.

Specimens were impacted in a ballistic impact rig that consists of a precision gun barrel mounted on a load frame and an attached furnace (fig. 3). The gun barrel was at a 90° angle to the width of the specimen, and the end of the gun barrel was placed 4 mm away from the leading edge. The projectiles were either 1.6- or 3.2-mm-diameter ball bearings with a mass  $m$  of 0.0164 or 0.131 g, respectively. The kinetic impact energy  $E$  was calculated based on  $E = \frac{1}{2}mv^2$ , where  $v$  is the velocity of the projectile. The steel ball bearings were annealed for 1 h at 700 °C to reduce their hardness to  $\leq 20$  HRC on the Rockwell C scale, which is more representative of possible debris in an engine. The specimens were impacted at 260 °C in air under a tensile load of 70 MPa, simulating operating conditions for LPT blades. The tensile load represents the in-service centrifugal load on the blade. The cast-to-shape specimens were impacted three times with one impact condition. Two of the impacts were placed on one edge of the sample separated by approximately 20 mm, and one additional impact was placed on the opposite edge, centered between the other two impacts. The locations of these impacts are referred to throughout this report as impacts 1, 2, and 3 as indicated in figure 1. Because of the narrower width, the machined samples were only impacted once, in the center of the gage section on one of the leading edges. The nominal distance  $X$  from the leading edge to the impact center was 0.51 mm for the small projectile and

0.64 mm for the large projectile, but specimen variability and an imprecise fit between the projectile and gun barrel resulted in some deviation in the aimed distance.

Static mechanical properties of the alloys were measured using miniature tensile specimens machined by low-stress grinding from the grip end of impact specimens for cast-to-size samples or from the cast plate if sufficient material was available. The 51-mm-long specimens had a 19-mm gage length and a 4-mm gage diameter. The tensile specimens were tested in air at room temperature and at 650 °C, using a constant strain rate of  $1 \times 10^{-4} \text{ s}^{-1}$ . Strain was measured with a 12.7-mm-gage-length axial extensometer attached to the gage of the specimen.

After impacting, the specimens were examined in a scanning electron microscope (SEM). Five types of crack lengths (fig. 4) were measured: (1) front side (FS) major, (2) FS total, (3) Hertzian (HZ), (4) back side (BS) straight, and (5) BS total. FS major is a summation of the largest, somewhat continuous crack observed on the front (impacted) side of the specimen while FS total is a summation of the length of all cracks observed. A HZ crack was defined as the longest crack on the impacted side of the sample that was at an angle from the impact to the specimen edge. A BS straight crack length is measured from the specimen edge to the end of any cracking on the back side of the impact, whereas BS total is a summation of all the crack lengths on the back side of the sample. In addition,  $X$  (see fig. 4) was measured.

As-received and impacted samples were tested in high-cycle fatigue at 650 °C with a frequency of 100 Hz. The fatigue crack growth rate is the highest for Ti-48Al-2Nb-2Cr at 650 °C (ref. 6), and therefore this temperature was chosen for testing to simulate the worst-case scenario. All the other alloys were tested at 650 °C for comparison. ABB-2 also had a few HCF tests conducted at 730 °C, since this was a possible service temperature. Because of the thin plate form of the samples, all fatigue tests were conducted with tension loads only. Generally, a load ratio  $R_\sigma$  of 0.05 ( $R_\sigma = \sigma_{\min}/\sigma_{\max}$ , the ratio of minimum to maximum applied stress) was used. However, in many of the alloys other values for  $R_\sigma$  were used to investigate the influence of tensile mean stress on fatigue. Because of the flat nature of the S-N (stress versus cycles to failure) curve for  $\gamma$ -TiAl, step tests (refs. 7 and 8) were used to determine the maximum fatigue strength. Step tests were found to be a convenient method to test both as-received and impacted  $\gamma$ -TiAl alloys. These tests resulted in a failure for every sample; that is, no runouts occurred. However, it should be noted that a potential drawback to such testing is the possibility of coxing, which would lead to fatigue strengths that were meaningless for design. Coxing is an artificially high-fatigue-limit strength that results from step testing rather than conventional single stress limit-to-failure procedures (ref. 9). As part of this study, coxing was investigated and shown to not occur. The details of this work can be found in reference 10.

Based on the amount of initial damage and previous experience, a starting fatigue stress level was chosen such that the sample would survive a predetermined cycle number. In most cases, this block size was  $10^6$  cycles, although for the cast-to-size Ti-48-2-2 samples a block size of  $10^7$  was also used. If the sample survived the block, then the maximum stress level was increased by approximately 14 MPa, which was decided upon as an optimum value for the stress increment. Note that early in this study a step size of 7 MPa was used, but the size of the step had no influence on the fatigue strength and the larger step size of 14 MPa resulted in quicker tests. From what we could ascertain, the only importance of the stress increment is in the accuracy of determining the fatigue strengths. If the stress increment is large, then the difference between the failure strength and the stress at the penultimate step is large, leading to a larger uncertainty in estimating the fatigue limit. By using smaller stress increments this uncertainty is reduced. However, the estimation can only be off by a maximum of 14 MPa, which, as will be shown later in the section Effect of Defect Size, is much smaller than the variation in the data.

The starting stress level was also chosen so that the specimen would not fail on the first step. If it failed on the first step, there is the chance that the actual failure stress is lower than the measurement would determine. For this reason, such tests were usually not included in the various data plots. Only when sufficient repeats showed that the failure stress was within scatter of other repeats, or when the cycles to failure on the first step was high and approached the block size, were such data included in the analyses.

If the starting stress level was chosen too low, the test took an inordinate amount of time and was inefficient. Also, until the coaxing study was completed at the end of this program, there was always the concern about coaxing, and we therefore attempted to keep the number of steps to a minimum. As a consequence, the selection of the starting stress level was delicate. Its choice was further exacerbated by the lack of knowledge on the severity of defects, either from the impacts or from any casting defects in the sample.

The process of cycling and increasing the stress level for each step continued until failure (two pieces) occurred. The fatigue stress at failure is defined as the failure stress on the last step where the cycle limit had not been reached due to failure. The fatigue strength or fatigue strength at threshold is defined as the maximum stress at the penultimate step, in other words, the last stress at which the sample successfully survived the block ( $10^6$  or  $10^7$  cycles).

### Fretting Tests

The initial application for  $\gamma$ -TiAl in aeroengines is for use as LPT blades. Since the blades are joined to the turbine disk in a dovetail arrangement (fig. 5), fretting is an obvious concern. Dovetail regions are often areas involving high wear. For example, observations of service-exposed Ti-based alloy fan blade-disk couples revealed the presence of severe fretting fatigue damage on the contacting surfaces of blade dovetails and disk slots (ref. 11).

Fretting fatigue is a complex problem of significant interest to aircraft engine manufacturers (refs. 11 to 14). Fretting failure can occur in a variety of engine components. The components of interest in the present investigation were the LPT blades and disks. A concern for these airfoils is the fretting in fitted interfaces at the dovetail where the blade and disk are connected. Numerous approaches, depending on the component and the operating conditions, have been taken to address the fretting problem. Careful design can reduce fretting in most cases—but not completely eliminate it—because of the skewed (angled) blade-disk dovetail attachment, which leads to a complex stress state due to the alternating centrifugal force and natural high-frequency blade vibration (fig. 5). Further, the local stress state becomes more complex when the influence of the metal-metal contact and the edge of the contact is considered.

The blades in the present investigation were  $\gamma$ -TiAl, and the disk was a nickel-base superalloy. Various titanium alloys have been used with great success as compressor blades in aeroengines. Experience has shown that a compact protective oxide film can develop on the surface of titanium alloys in an oxidative environment. However, when mechanical vibrations result in a minute reciprocating sliding motion (microslip) between the interacting surfaces in dovetail joints, fretting processes locally damage the protective oxide films on the surfaces. These oxide films cannot be healed because continuous fretting will cause fresh metal to be exposed and then increase adhesion between the interacting surfaces. Because titanium and titanium-based alloys in the clean state will exhibit strong adhesive bonds (refs. 15 and 16) when in contact with themselves and other materials, this adhesion leads to heavy surface damage (wear) and high friction in practical cases. The consequences of fretting wear include the loss of dimensional control at critical interfaces, which can lead to dramatic changes in the dynamic loading. Even if the wear produced by fretting is mild, the reduction in fatigue life can be substantial.

Adhesion, a manifestation of mechanical strength over an appreciable area, has many causes, including chemical bonding, deformation, and the fracture processes involved in interface failure. A clean metal in contact with another clean metal will fail either in tension or in shear because some of the interfacial bonds are generally stronger than the cohesive bonds within the cohesively weaker metal (ref. 17). The failed metal subsequently transfers material to the other contacting metal. Adhesion undoubtedly depends on the surface cleanliness; the area of real contact; the chemical, physical, and mechanical properties of the interface; and the modes of junction rupture. The environment influences the adhesion, deformation, and fracture behaviors of the contacting materials in relative motion.

Clean surfaces can be created by repeated sliding in vacuum, making direct contact of the fresh, clean surfaces unavoidable in practical cases (ref. 15). This situation also applies in some degree to sliding contact in air, where fresh surfaces are continuously produced on interacting surfaces in relative motion. Microscopically small, surface-parallel relative motion, which can be vibration (in fretting or false brinelling) or creep (in fretting), produces fresh, clean interacting surfaces and causes junction (contact area) growth in the contact zone (refs. 18 to 20).

Fretting wear produced between contacting elements is adhesive wear taking place during a nominally static contact under normal load and repeated microscopic vibratory motion (refs. 21 to 25). The most damaging effect of fretting is the possible significant reduction in the fatigue capability of the fretted component, even though the wear produced by the fretting appears to be quite mild. For example, Hansson, et al. (ref. 25) reported that the reduction in fatigue strength by fretting of Ti-47Al-2Nb-2Mn containing 0.8 vol% TiB<sub>2</sub> was approximately 20 percent.

The objective of this part of the investigation was to evaluate the fretting resistance of Ti-47Al-2Cr-2Nb ( $\gamma$ -TiAl). As a new structural material, the fretting behavior of  $\gamma$ -TiAl is relatively unknown. Since the LPT blades are usually mated to an IN718 turbine disk, fretting of the TiAl in contact with IN718 was examined at temperatures from 25 to 550 °C. Selected reference experiments were also conducted with Ti-6Al-4V in contact with IN718, as there is a large experience base with Ti-6Al-4V—a compressor blade material. The parameters of microscopic, surface-parallel motion, such as fretting frequency, slip amplitude, and load, were systematically examined in this study. Scanning interference microscopy (noncontact optical profilometry) was used to evaluate surface characteristics such as topography, roughness, material transfer, and loss of wear volume. Scanning electron microscopy (SEM) with energy-dispersive spectroscopy (EDS) was used to determine the morphology and elemental composition of fretted surfaces, transferred material, and wear debris. In addition, fatigue specimens of  $\gamma$ -TiAl were fretted, and the resulting fatigue properties were evaluated. Additional work was planned to develop wear coatings (if necessary) and to perform in situ fretting fatigue experiments. However, the program was terminated before these two studies could be performed.

**Materials.**—The specimens tested were made of the GEAE Ti-47Al-2Cr-2Nb alloy machined from cast plates. The IN718 samples were taken from extruded bar then solutioned and aged according to Aerospace Material Specification AMS 5596G, SAE, Warrendale, PA, 1987, yielding an HRC value of 36. Tensile properties for both materials as well as the Ti-6Al-4V are shown in table I. The ultimate tensile strength of IN718 is greater than that of Ti-47Al-2Cr-2Nb by a factor of ~3.

**Experiments.**—In order to investigate the fretting behavior of this  $\gamma$ -TiAl alloy, a two-pronged approach was used. First, its fretting wear was investigated by using reciprocating pin-on-flat tests. Second, fatigue samples were fretted and subsequently fatigued to examine the influence of wear on the fatigue strength.

Figure 6 presents the fretting wear apparatus used in this investigation. Reciprocating pin-on-flat experiments were conducted with 9.4-mm-diameter, hemispherical IN718 pins in contact with Ti-47-2-2 flats; 6-mm-diameter, hemispherical Ti-47-2-2 pins in contact with IN718 flats; or 9.4-mm-diameter hemispherical Ti-6Al-4V pins in contact with IN718 flats. Tests were conducted in air at temperatures from 25 to 550 °C. All the flat and pin specimens used were polished with 3- $\mu$ m-diameter diamond powder. Both the pin and flat surfaces were relatively smooth, having centerline-average roughness  $R_a$  in the range of 18 to 83 nm (table II). The Vickers hardness  $H_V$  measured with a load of 1 N for the polished flat and pin specimens is also shown in table II.

All pin-on-flat wear experiments were conducted for 1 to 20 million cycles at loads from 1 to 40 N; frequencies of 50, 80, 120, and 160 Hz; and slip amplitudes between ~50 and 200  $\mu$ m. Both pin and flat surfaces were rinsed with ethyl alcohol before installation in the fretting apparatus.

Two to three fretting experiments were conducted with each material couple at each fretting condition. The data were averaged to obtain the loss of wear volume for the materials. The loss of wear volume was determined by using an optical profiler (noncontacting, vertical scanning, white-light interferometer), which characterizes and quantifies surface roughness, height distribution, and critical

dimensions (such as areas and volumes of damage, wear scars, and topographic features). The profiler has three-dimensional profiling capability with excellent precision and accuracy (e.g., profile heights ranging from  $\leq 1$  nm up to 5000  $\mu\text{m}$  with 0.1-nm height resolution). The shape of a surface can be displayed by a computer-generated map developed from digital data derived from a three-dimensional interferogram of the surface. A computer directly processes the quantitative volume and depth of a fretted wear scar.

Fretting-fatigue tests were performed on the machined sample design shown in figure 2(a). Figure 7 presents a three-dimensional optical interferometry image of the gage section of the fatigue specimen. The surface has a relatively homogeneous texture containing machined grooves along the length of the specimen in the direction of the fatigue loading. The mean value of  $R_a$  measured parallel to the length of the specimen is 0.57  $\mu\text{m}$  with a standard deviation of 0.17  $\mu\text{m}$ . The  $R_a$  measured perpendicular to the length of the specimen is 0.75  $\mu\text{m}$  with a standard deviation of 0.10 mm. However, occasional larger variations arising from defects were observed, as shown by the 70- $\mu\text{m}$ -long casting defect in figure 7(b). These specimens generally contained cavities with depths of 2 to 4  $\mu\text{m}$  and cutting grooves with depths of 3  $\mu\text{m}$ . Therefore, the maximum height (peak-to-valley) of the surface was relatively large, having a value of 8.8  $\mu\text{m}$  and a standard deviation of 2.2  $\mu\text{m}$ . Note that the maximum height is the vertical distance between the highest and lowest points as calculated over the entire measured surface. The largest profile peak height is the distance between the highest point of the surface and the mean surface for the entire measured surface. The largest profile valley depth is the distance between the lowest point of the surface and the mean surface.

The fatigue samples were fretted using three types of IN718 contact pads. One pad (fig. 8(a)) had a wedgelike shape (ref. 12) with two rectangular flats (1.00 by 12.70 mm), where one of the rectangular-shaped flats was brought into contact with the Ti-47-2-2 fatigue specimen (fig. 9(a)). The second (fig. 8(b)) was a two-sided wedge with 12.70 mm long knife edges. The contained angle between the two sides was  $35^\circ$  and the average radius of curvature for the knife edge was less than 0.1 mm (fig. 8(b)). One of the knife edges was brought into contact with the Ti-47Al-2Cr-2Nb fatigue specimen, as schematically shown in fig. 9(b). The third type of contact pad was a 9.4-mm-diameter hemispherical pin (fig. 6), as used in the pin-on-disk tests. The spherical surface was brought into contact with the  $\gamma$ -TiAl fatigue specimen. Table II also lists  $R_a$  and  $H_v$  for the IN718 contact pads (including pins) as well as for the fatigue specimens.

Fretting experiments were conducted with aged IN718 pads in contact with the  $\gamma$ -TiAl fatigue specimens (fig. 9). The fatigue specimen was placed on a rectangular parallelepiped strip heater (127 by 16 by 6.4 mm) and was held by four clamps (6.4 by 12.7 by 2.0 mm), as shown in figure 9. All fretting wear experiments were conducted under the conditions shown in table III(a) to (d). Both the IN718 contact pads and  $\gamma$ -TiAl fatigue specimens were rinsed with ethyl alcohol before installation in the fretting apparatus. Fretted fatigue specimens were subsequently tested using the step test method described earlier in the Fatigue Tests section. Fatigue tests were conducted at 650  $^\circ\text{C}$ , a frequency of 80 Hz, and a load ratio  $R_\sigma$  of 0.05. A block size of  $10^6$  cycles and a step size of 14 MPa were used.

## Impact Modeling

It was desired to simulate analytically the cracking patterns in  $\gamma$ -TiAl resulting from the high-velocity impacts. This is particularly desirable since the number of impact variables (e.g., shape, hardness and size of the projectile, angle of incidence, temperature, impact energy, etc.) are numerous. If this was successful, then cracking could be predicted with minimal future experiments. The ability to predict crack size and type of cracking could then be coupled to the subsequent detriment in residual fatigue properties, which would aid engineers in component design. Thus, our aim was to develop and validate an in-house modeling capability. The model was based upon the approach used by CMU (ref. 26).

**Purpose.**—To conduct the simulations of impact damage, finite-element analyses of impact were performed for three specimens of the cast-to-size Ti-48-2-2 alloy. To judge the capability of finite-element analyses to simulate the impact of cast specimens and to develop suitable damage and cracking criteria, three differently tested samples were chosen for modeling. The selected tests involved different energies (impact velocities) and both the 1.6- and 3.2-mm projectile sizes for a given impact location  $X$  of nominally 0.6 mm. These three tests represent widely differing damage states: The first test involved impact at a low energy, which resulted in a small BS crack, with minimal FS cracking. The second test had a larger BS crack and more severe FS cracking due to the intermediate  $E$ . The third test resulted in a near blowout due to the high  $E$ . The cracking patterns on both front and back sides for each test are shown in figure 10. All pertinent details of the experiments selected for the finite-element simulations are listed in table IV.

The principle objective of the modeling part of the investigation was to study the damage produced on the front and rear faces of the elliptical specimens under various impacting conditions of different impact energies and projectile sizes. It was our goal to develop a set of simple but reasonably accurate cracking criteria to predict the range of cracking observed in actual experiments. Earlier investigations by Steif and McKenna (ref. 26) have shown that for the leading edge impact of TiAl specimens, a cracking criterion based only on stress or only on plastic strain does not accurately predict the cracking of the specimens. However, cracking criteria involving both the stress and plastic strain reasonably predicted the observed BS cracking of the specimens. Based upon their observations and experimental results, the following set of cracking criteria was adopted for the present analyses. A crack at a location of the specimen was considered to occur only if the following conditions were concurrently satisfied:

1. The von Mises stress must be equal to or greater than 400 MPa.
2. The von Mises plastic strain must be equal to or greater than 1.0 percent.

Additionally, for the formation of a BS crack, the tensile stress must occur in the  $z$ -direction, (i.e., the stress parallel to the specimen axis, the  $z$ -stress). The stress value of 400 MPa is comparable to the ultimate tensile strength value of  $\gamma$ -TiAl material at a strain rate of  $\approx 10^{-4}$ /sec. The strain value of 1.0 percent is the same as used by Steif and McKenna (ref. 26) in their work. It should be noted that this value of strain is on the lower side of the ductility of TiAl observed here in tensile tests, since the value of the plastic strain at failure was seen to be 1.7 percent or higher at room temperature. The actual specimens were impacted at 260 °C, and the ductilities at 260 °C were similar to those at room temperature. However, the tensile ductility at ballistic strain rates should be smaller than that from a static tensile test based on typical strain-rate sensitivities of metals. Thus the use of 1 percent plastic strain is not unrealistic, and, using this smaller value of the plastic strain maintains conservative predictions.

**Finite element models.**—The finite-element models of the elliptical cast-to-size Ti-48-2-2 specimens and the spherical projectiles for the three experiments were generated by using the preprocessing software of MSC.Patran (ref. 27). The dimensions of the cast specimens and the projectile (spherical ball) are given in table IV. Because of the symmetry in the width direction, only one-half of the specimen was modeled for finite-element simulations. The finite-element model of the elliptical specimen and the spherical projectile is shown in figure 11. As can be seen from this figure, a very fine finite-element mesh was employed at the leading edge of the sample, i.e., in the impact zone. This was necessary for the finite-element simulations to accurately capture the damage and cracking caused by the high-velocity impact of the cast specimens by the projectile.

The finite-element analyses for the selected cases were performed using the ABAQUS/Explicit (ref. 28) finite-element program. The test specimen for each simulation was constructed with solid eight-noded brick elements with reduced integration and hourglass control. This is the type C3D8R element in ABAQUS/Explicit. The total number of elements used to construct the specimen for each simulation is listed in table IV. The spherical projectile was constructed with four-noded linear tetrahedron elements (Type C3D4 in ABAQUS/Explicit). The sizes of the projectile for each test and the number of finite-elements used are shown in table IV. Detailed experimental (ref. 3) and analytical (ref. 29) investigations have previously been performed to study the effect of projectile hardness on the extent and pattern of damage in TiAl specimens. These experimental investigations (ref. 3) showed little effect of projectile hardness on impact damage in specimens and the analytical work (ref. 29) showed that the deformation of the projectile was close to that of a rigid body. Therefore, the projectile was modeled as a rigid body, and the RIGID BODY option in ABAQUS/Explicit was employed for this purpose. The specification of the exact boundary conditions for the problem was not necessary because of the short duration of the analysis (6  $\mu$ sec). The ABAQUS/Explicit program automatically selects the time increments for the duration of the analysis and does not allow the user to exercise any control on picking these time increments. A total of 50 time steps were chosen for the duration of the analysis. The impact was modeled as frictionless. Additionally, a 70-MPa load along the specimen axis was applied to the model. This replicated the experimental procedure and was done to represent the in-service centrifugal load on the blade.

Like most materials  $\gamma$ -TiAl is a strain-rate-sensitive material. For realistic finite-element simulations of the impact, it is, therefore, necessary to include into the model the strain-rate sensitivity of  $\gamma$ -TiAl. High-strain-rate data have been generated on Ti-48-2-2 by performing split Hopkinson pressure bar tests at strain rates ranging from 1000 to 8000  $s^{-1}$  (ref. 30) and fitted to a Zerilli-Armstrong model (ref. 31). These strain-rate-sensitive, true-stress, true-strain responses were included in the current finite-element analyses. The uniaxial behavior described in these responses was generalized to multiaxial states by employing the corresponding von Mises invariants.

The outputs of the finite-element analyses were scanned to find the time instants at which the peak values of von Mises stress, von Mises strain, and other quantities of interest occurred. The postprocessing capability of MSC.Patran was then utilized to plot the results of interest at these time instants.

## Results and Discussion

### Chemistry and Microstructure

The chemistries of the TiAl alloys studied are given in table V. All chemistries except for the 95A and ABB-23 were measured at NASA. The composition of 95A was supplied by UES, Inc., and the chemistry of ABB-23 was given by ALSTOM Power. The Al level of the cast-to-size Ti-48Al-2Cr-2Nb was analyzed to be 47.5 at.% by x-ray fluorescence using powder metallurgy TiAl standards that covered high and low aluminum levels. This technique has been shown to have better accuracy than wet chemical methods in determining the Al level in TiAl (ref. 5). The Al level was intentionally lower, 47.1 at.%, in the subsequent cast and machined Ti-47-2-2 specimens, as a slightly lower Al level was found to result in higher room-temperature yield strengths while maintaining the same plastic elongation as in the 48 at.% Al-containing alloy (ref. 5). The low-Al slab obtained from CMU had an Al level of 46.5 at.%, similar to the Ti-47-2-2 slabs cast at Howmet used for the coaxing fatigue study. The cast-to-size ABB-2 specimens contained 2.28 at.% W for strengthening, and ABB-23 had boron added for grain refinement.

Figure 12 and table VI present the microstructures of the studied alloys. The cast-to-size Ti-48Al-2Cr-2Nb samples and the cast Ti-47-2-2 plates had duplex microstructures. The cast-to-size samples had approximately 61 percent gamma grains with an average grain size of 64  $\mu$ m (fig. 12(a)). The GEAE Ti-47Al-2Cr-2Nb plates (fig. 12(b)) and the lower Al CMU plates (fig. 12(c)) had similar microstructures

with 65 percent  $\gamma$ - $\alpha_2$  lamellar grains and gamma grains with average diameters between 58 and 60  $\mu\text{m}$ . However, the Ti-47-2-2 plates purchased from Howmet for the fatigue coxing experiment had a nonuniform microstructure (fig. 12(d)). The edges of the plates had a nearly fully lamellar microstructure with columnar colony grains but the center of the plates had a more duplex microstructure with a bimodal distribution of gamma grains. The NCG359E plates also had a duplex microstructure with 32 percent gamma grains having an average grain size of 69  $\mu\text{m}$  (fig. 12(h)).

The cast-to-size ABB-2 samples had a nonuniform microstructure with columnar lamellar colonies at the edge (fig. 12(e)) and a more duplex microstructure at the center of the samples (fig. 12(f)). The addition of boron in the ABB-23 resulted in a refined lamellar microstructure with lamellar grain sizes averaging 59  $\mu\text{m}$  (fig. 12(g)). The only wrought alloy investigated, 95A, had a thermomechanically treated lamellar microstructure with a lamellar colony size averaging 288  $\mu\text{m}$  (fig. 12(i)). Note that the expectation of the wrought alloy having a more refined microstructure was not realized.

### Tensile Properties

The tensile properties of the various alloys are given in table VII. The cast and machined Ti-48-2-2 tensile data (room-temperature data only) were supplied by GEAE, and ALSTOM Power supplied the ABB-23 data due to a lack of excess material to make tensile specimens. The cast-to-size Ti-48-2-2 had the lowest tensile strength but the highest ductility with an average 0.2 percent offset yield strength (0.2%YS) of 326 MPa, an average ultimate tensile strength (UTS) of 422 MPa, and a plastic elongation of 1.7 percent, all at room temperature. The cast plates supplied by GEAE and CMU and those purchased from Howmet had higher strengths but lower ductility. Their average YS ranged from 433 to 458 MPa, the UTS values ranged from 499 to 536 MPa, and the plastic elongations ranged from 0.99 to 1.42 percent at room temperature. The NCG359E plate had very similar tensile properties to the Ti-47-2-2 plates. While the ABB-2 and ABB-23 had significantly different microstructures (figs. 12(e) to (g)), their tensile properties were similar, and both had higher strengths and lower ductilities than the other alloys (table VII).

### Crack Morphology

Cracks resulting from the impact experiments are described and discussed in this section.

**Cast-to-size Ti-48-2-2.**—A detailed report of results from the cast-to-size Ti-48-2-2 study in reference 3 is summarized here. The crack measurement results are given in table VIII(a). The type of impact damage produced depended mainly on the thickness of the sample and the energy level of the projectile. Low-energy impacts resulted in dents but very little cracking on the front side of the specimens. At higher energies, FS circumferential—Hertzian (HZ)—cracks initiated at the impact crater and grew towards the specimen edge. These HZ cracks extended through the thickness of the specimen, producing an expanding half-cone-shaped crack that resembles the HZ cracks commonly observed in glass (ref. 32). For extreme conditions, this crack propagated completely through the specimen and resulted in a blowout; that is, a cone-shaped chunk of material was completely removed. An example of a nearly blown-out thin specimen is shown in figure 13. The HZ cracks had nearly penetrated through the thickness and were visible from the back side of the sample. Simultaneous with this FS cracking, a straight crack was produced on the back side of the specimen, opposite the impact. This cracking usually proceeded from the specimen edge to roughly the location opposite the impact crater. These back-side (BS) cracks were perpendicular to the loading axis of the fatigue specimen and occasionally branched out in several directions as shown in figure 13. The BS crack lengths increased with increasing  $E$ . For blowouts, the BS crack length was measured from the edge of the sample to the back side of the HZ crack (fig. 13(c)).

For low-energy impacts, the BS straight crack length was plotted as a function of  $E$  in figure 14(a). The BS straight crack length was strongly dependent on  $E$ . The influence of specimen thickness was more pronounced at low  $E$ , below 0.35 J (fig. 14(a)). The thin- and medium-thickness specimens ( $t_1$  and  $t_2$ , respectively, see fig. 1) exhibited similar crack resistance for  $E$  between 0.04 to 0.25 J, while the BS straight crack length increased substantially for the thin specimens impacted at  $E$  between 0.28 and 0.35 J, as these specimens were either blowouts or near blowouts. The thin and medium-thickness specimens also exhibited cracking at very low  $E$ , whereas the thick specimens could withstand some level of impact without cracking. In general, the thick specimens exhibited improved impact resistance for  $E$  below 0.40 J, and this led to the selection of the thicker specimens for the follow-on fatigue studies, as well as thicker leading edges for the LPT blades.

The HZ and BS straight crack lengths are plotted over a wider range of  $E$  in figures 14(b) and (c). The level of impact damage was similar for both 1.6- and 3.2-mm projectiles when impacted at similar energies. However, there was more of a tendency for the thin specimens to be blown out when impacted with the small projectiles. The smaller projectiles resulted in smaller diameter indents on the sample surface. Therefore, the smaller projectiles caused a larger stress under the impact than did the large projectiles when impacted with the same energy. Unlike BS straight cracks, HZ crack lengths were not influenced by whether or not the impact was blown out. The HZ crack length data had a larger amount of scatter when compared to the BS straight crack length data, particularly at the 1.55 J energy level. The large variability in HZ crack length may have to do with the influence of local microstructure and orientation of lamellar grains.

Multiple linear regression was used to model the cracking response as a function of impact variables. Included in the multiple regression models was  $X$ , the distance of the center of the impact crater from the specimen edge, as variations in  $X$  could potentially result in large variations in cracking degree and ultimately fatigue life. Subtracting the midpoint from the variable and dividing by half of the variable range normalized the variables. In this way, each term's coefficient indicates the relative importance of that term to the model. The models are only valid over the range studied for each variable. Interactive terms, i.e.,  $E*X$ , indicate that the effect of a variable is dependent on the level of another variable. Terms were included in the models at a significance level of 0.05 or lower. The first impact experiments discussed in reference 3 were performed at low impact energies and were designed experiments, where models describing the effects of  $E$ , specimen thickness,  $X$ , projectile hardness, and presence of a blowout ( $BO$ ) on HZ and BS crack length were obtained. Of the main variables,  $E$  was the most important for all crack types. Although thickness was more important for the BS crack types, it also had some significance for the FS cracks. Projectile hardness did appear in two models, but with small coefficients. The variable  $X$  appeared in the models as a small main effect for two of the FS cracks, but was also included as an interactive term in several of the models and as a quadratic term for BS straight cracks. As a result of the method of measurement,  $BO$  was a major influence on the BS straight cracks and was included in two of the models. The BS straight cracks were measured from the leading edge to the end of the blowout on the back side, figure 13(c), which is actually the back side of the HZ crack. In actuality, the BS crack would have been contained in the blown-out portion only and thus smaller in length than was measured. All of the various crack measurements were accurately described as functions of the impact parameters. Values for  $R^2$  ( $R$  is the sample correlation coefficient) in the 85 to 90 percent range indicate that these models can account for most of the variability in crack lengths.

The earlier impact experiments in reference 3 were pooled with the impact experiments in this study to obtain cracking models over a wider range of  $E$ . However, these follow-on experiments were performed to satisfy a variety of objectives, and the pooled data do not constitute a statistically balanced set of experiments. For example, the thickness of the specimen (and subsequently the leading edge) was only varied in the early experiments, and therefore, the majority of the data is from the thick samples. Therefore, it is perhaps not surprising that the present attempts to model the combined data resulted in models that suffered from lack of fit. Subsequently, a small experiment was undertaken to systematically vary  $E$  and  $X$  over a wide range. Impact energy  $E$  was varied from 0.2 to 2.0 J, and the distance from the leading edge to the center of the impact  $X$  was varied from 0.15 to 1.9 mm. The data were pooled with the

earlier thick-specimen data to model HZ and BS straight crack length over a larger range of  $E$  and  $X$ . The resulting models are given as equations (1) and (2) and plotted in figure 15. The follow-on fatigue studies determined that the HZ and BS straight cracks were the most directly linked to fatigue failure; therefore, these two crack measurements are emphasized in the plots and discussion. The HZ ( $\text{mm}^{1/2}$ ) and BS straight (mm) crack lengths are described as follows:

$$\begin{aligned}
 (\text{HZ})^{1/2} = & -0.727 \left[ \frac{(X - 1.031)}{0.939} \right]^2 \\
 & + 0.670 \frac{(E - 1.125)}{0.946} - 0.247 \frac{(X - 1.031)}{0.939} \\
 & - 0.304 \frac{(E - 1.125)}{0.946} * \frac{(X - 1.031)}{0.939} \\
 & + 1.384
 \end{aligned} \tag{1}$$

$$\begin{aligned}
 \text{BS straight} = & -0.519 \left[ \frac{(X - 1.031)}{0.939} \right]^2 \\
 & - 0.238 \left[ \frac{(E - 1.125)}{0.946} \right]^2 \\
 & + 0.906 \frac{(E - 1.125)}{-0.946} + 0.724 \frac{(X - 1.031)}{0.939} \\
 & + 1.160 [(BO = 1) \text{ or } (\text{no } BO = -1)] \\
 & + 0.515 \frac{(E - 1.125)}{0.946} * \frac{(X - 1.031)}{0.939} \\
 & + 3.033
 \end{aligned} \tag{2}$$

with  $R^2 = 78$  percent for equation (1), and  $R^2 = 91$  percent for equation (2).

These models are only valid for the thick specimens at  $E = 0.2$  to  $2.0$  J, and variables modeled were  $E$ ,  $X$ , and  $BO$ . Again, the major factor for both HZ and BS straight crack lengths was  $E$ . For HZ crack lengths, the effect of  $X$  was small at lower energies but significant at higher energies. The lengths reached a maximum at an  $X$  value of approximately  $1.0$  mm (fig. 15(a)). Also,  $E$  had the largest influence on BS straight crack length coming into the model as a main, interactive, and quadratic effect (fig. 15(b)), but  $BO$  and  $X$  were also significant factors. At low  $E$  ( $0.2$  J), the BS crack lengths increased as  $X$  was increased from  $0.2$  to  $1.0$  mm and then decreased as  $X$  went from  $1.0$  to  $2.0$  mm. At an  $X$  of  $2.0$  mm, the low-energy impacts did not create BS cracks. BS cracks continued to increase in length with increasing  $X$  at the high energies ( $2.0$  J). The largest  $X$  value studied was  $1.9$  mm. Here the leading edge still had some curvature, and the specimen thickness had not reached its maximum. As stated earlier, the models are only valid over the range of variables studied. At a large enough  $X$ , the impacts should start to look like thick-plate impacts, which have a star-shaped pattern on the back side (ref. 30) instead of a BS crack coming into the width from the leading edge.

**GEAE Ti-47-2-2.**—This alloy is similar to the cast-to-size Ti-48-2-2, and the two will be directly compared throughout the report; the major difference is that the GEAE specimens were machined from

cast plates. Crack measurements for the GEAE Ti-47-2-2 specimen are given in table VIII(b). The type and level of impact damage was comparable for the cast-to-size and machined samples at similar impact conditions. The type of impact damage produced depended on both  $E$  and  $X$ . Low-energy impacts of 0.06 J resulted in dents but very little cracking (fig. 16) on the front, impact side of the specimens for both machined and cast-to-size samples. Whereas the low-energy impacts did not produce BS cracks on the cast-to-size specimens, the machined specimens had a range of BS crack lengths resulting from the low-energy impacts (figs. 16(b) and (d)). BS cracks typically proceed from the specimen edge to roughly the location opposite the impact crater (perpendicular to the loading axis of the fatigue specimens). The BS crack shape, direction, and length for the low-energy impacts on the machined samples depended on  $X$ . Some variation in  $X$  occurred during the impact testing because of specimen variability and an imprecise fit between the projectile and gun barrel. The BS cracks originated at the specimen edge and proceeded into the thickness of the sample for two low-energy impacts with  $X$  values between 0.5 and 0.6 mm (fig. 16(d)). However, for the two low-energy impacts with  $X$  around 0.65 mm, the BS cracks were star shaped and located opposite the edge of the impact closest to the leading edge (fig. 16(b)), while no BS crack was visible from the specimen surface for the impact with the largest  $X$  (0.79 mm). As  $X$  increased, the thickness of the sample slightly increased at the point of impact (fig. 2(b)). At the  $X$  values of 0.55 and 0.79 mm, the machined samples were approximately 1.06 and 1.22 mm thick, respectively. The BS crack morphology for low-energy impacts changed significantly from a straight BS crack to a star-shaped crack to no cracking at all from a relatively small variation in  $X$ .

At higher  $E$ , HZ cracks initiated at the impact crater and grew towards the specimen edge (fig. 17 (a) and (c)). These HZ cracks extended through the thickness of the specimen, producing an expanding half-cone-shaped crack. For high  $E$ , the HZ cracks propagate completely through the specimen and result in a blowout. The 1.6-mm projectiles blew out the machined samples at an  $E$  of 0.8 J, significantly lower than the 1.5 J or higher required to blow out the thick cast-to-size samples. However, the thin cast-to-size specimens from the first set of experiments would blow out at  $E$  values as low as 0.3 J with the small, 1.6-mm-diameter projectiles (ref. 3). Machined samples occasionally experienced partial blowouts (fig. 17(a)). On the front side of a partial blowout, the top portion of the impact dent was visible after impacting, but the HZ cracks closer to the leading edge would connect and blow out the leading edge of the sample. Partial blowouts were not observed in cast-to-size samples. In the range 0.9 to 1.1 J of energy, the machined GEAE Ti-47-2-2 samples were impacted with both 1.6- and 3.2-mm projectiles. The 1.6-mm impacts resulted in blowouts with larger HZ crack lengths. The intended  $X$  value for the 3.2-mm projectiles was 0.64 mm; however,  $X$  actually ranged from 0.86 to 1.27 mm. The smaller HZ crack lengths for the 3.2-mm projectiles are most likely a result of the unintentionally large  $X$  (fig. 17(c)).

The HZ crack length increased with increasing  $E$  (fig. 18(a)). At the lowest  $E$ , 0.06 J, the cast-to-size samples had dents but no cracks on the impact side of the sample, whereas a couple of the machined samples did have some minor cracks as a result of the low-energy impacts. For the cast-to-size samples, HZ crack lengths were modeled to reach a maximum at an  $X$  of around 1.0 mm (ref. 3). However, the HZ crack length for machined samples did not show the same trend with the present models. The machined samples impacted with 3.2-mm projectiles had  $X$  values close to 1.0 mm but had shorter than average HZ crack lengths (fig. 18(a)). A fairly large variation in HZ crack lengths has been observed in previous studies (ref. 4), and the wide range has partially been attributed to lamellar grain orientation at the sample edge. The microstructure of the machined samples had more lamellar content than the cast-to-size samples. While there were some differences in HZ crack length, in general, the cast-to-size and machined samples had reasonably similar HZ crack lengths for similar impact conditions.

As expected, BS crack length increased with  $E$  for both cast-to-size and machined impact specimens (fig. 18(b)). As a result of the method of measurement and the cast-to-size specimen shape, a significant increase in BS crack length was obtained for the cast-to-size samples that blew out. The BS crack lengths were measured from the leading edge to the end of the blowout on the back side of the specimen which is actually the back side of the HZ crack. The BS crack would have been smaller in length and contained in the blown-out portion. The cast-to-size samples are thicker than the machined samples (fig. 2(b)), and the cone shape of the HZ crack leads to a larger chunk of material missing for thicker samples. Thus, the

thinner, machined samples tended to have smaller BS cracks for blowouts in comparison to cast-to-size specimens. Despite these slight differences, the cast-to-size and machined samples generally had comparable BS crack lengths.

**CMU and Howmet Ti-47-2-2.**—The CMU plate was obtained to assess the effect of variations of Al content on impact resistance. The Howmet plates were used primarily in the virgin, nonimpacted condition, to study the effect of coxing on fatigue strength, but a few of the samples were impacted at low energies. Both batches of material had similar chemistry and tensile properties, and therefore their crack morphology is plotted together in figure 19. The crack length measurements are given in tables VIII(c) (CMU) and (d) (Howmet). The HZ crack lengths for the CMU material were generally longer than those for the cast-to-size samples at  $E$  less than 1.0 J, but within the scatter of the cast-to-size samples at  $E$  greater than 1.0 J. The Howmet Ti-47-2-2 HZ crack lengths are within the scatter of the cast-to-size data. At the lower  $E$  values, the CMU Ti-47-2-2 samples had slightly larger HZ cracks than the machined GEAE Ti-47-2-2 (fig. 18(a)). The CMU impacts were generally impacted closer to the leading edge than the machined Ti-47-2-2. In these cases,  $X$  averaged  $0.47 \pm 0.04$  and  $0.59 \pm 0.10$  mm for the CMU and GEAE Ti-47-2-2 materials, respectively. While the HZ crack length for machined samples couldn't be modeled with the available data, the effect of  $X$  on HZ crack length appears to be different for the machined than for the cast-to-size samples. This is not surprising given the different leading edge profile (fig. 2(b)). Small  $X$  values result in impacting a narrower area of the leading edge and appears to result in larger HZ crack lengths for the machined sample design compared to the cast-to-size samples. The BS crack length for both the CMU and Howmet Ti-47-2-2 samples fell within the scatter band of both the cast-to-size and the GEAE machined impact data. Given the variation in  $X$  and similar BS crack lengths, the effect of slightly lower Al from the cast-to-size and GEAE machined alloys appears to be insignificant.

**ABB-2 and ABB-23.**—The TiAl alloy ABB-2 has considerably different chemistry, microstructure, and mechanical properties compared to Ti-48-2-2. Of particular concern, ABB-2 has only half the ductility of Ti-48-2-2. Therefore, the ballistic impact resistance of ABB-2 was expected to be different from Ti-48-2-2. The ABB-2 samples were also cast to size in the same configuration as the Ti-48-2-2 cast-to-size samples. Based on the results of the ABB-2 as discussed below, a more refined and homogeneous microstructure was desired, and a cast irregularly shaped piece of ABB-23 was machined into impact samples according to the drawing in figure 2(a).

The HZ and BS straight crack lengths are plotted as a function of  $E$  in figure 20 for both ABB-2 and Ti-48-2-2. The crack length measurements are given in table VIII(e) for ABB-2. The level of impact damage was similar for ABB-2 and Ti-48-2-2 at similar  $E$  values. However, at the lowest impact energy, 0.22 J, half of the impacts on ABB-2 did not produce any apparent HZ or BS cracks, whereas all of the 0.22 J impacts on Ti-48-2-2 resulted in both FS and BS cracks. This could be a consequence of the higher UTS for ABB-2. Both HZ and BS crack lengths increased with increasing  $E$  up to 1.5 J. As with the cast-to-size Ti-48-2-2 and machined GEAE specimens, the significant increase in BS crack lengths obtained for ABB-2 was a result of the method of crack length measurement. Unlike the BS crack lengths, the HZ crack lengths were not influenced by whether or not the impact was blown out. For non-blown-out samples, the HZ crack length data had a larger amount of scatter than the BS straight crack length data, particularly at the 1.5 J energy level where the HZ crack lengths ranged from 0.48 to 4.2 mm (fig. 21). Four of the twenty-four impacts were blown out from the 1.5 J impacts. When the samples were not blown out, the BS crack lengths were within the normal scatter and ranged from 1.4 to 2.7 mm. Several ABB-2 samples were impacted with a particularly severe impact condition, an  $E$  of 6.09 J at 730 °C. This impact condition resulted in all blowouts and the HZ and BS cracks that resulted from these impacts were approximately the same length as the impacts which blew out from the 1.5 J energy impacts (fig. 20). This is not unreasonable since once blowouts start occurring, higher energy levels will not create a larger blowout. For larger blowouts to occur, a larger value of  $X$  or a larger projectile would be required. A small reduction in impact damage has been observed in Ti-48-2-2 at elevated temperatures (ref. 3); however, the extremely high  $E$  utilized overshadowed any benefit of the increased impact temperature.

The impact sites were polished from several angles to determine the effect of grain orientation on impact damage. Large lamellar grains were fairly common along the specimen surfaces (fig. 12e), but were not present in all of the samples. The large variability in HZ crack length may be attributed to the presence of these large grains at the specimen surface. The HZ cracks appeared to propagate readily when running parallel to the lamellae, as the crack path is straight and long in length (fig. 22). HZ cracks that run perpendicular to lamellae have a more tortuous and shorter crack path. For the impact shown in figure 22, the longest HZ crack is on the right where the lamellae are oriented parallel to a typical crack path. On the left side of the impact, the lamellae are oriented at an angle to the typical crack path, and very little cracking occurred. BS crack length was not influenced by the grain size or orientation. For similar impact conditions, the BS crack length was very reproducible for non-blown-out samples.

The effect of impact parameters on HZ and BS crack lengths was fit for Ti-48-2-2 using multiple regression techniques, and three-dimensional representations of the equations for non-blown-out impacts are shown in figure 15. These predictions are only valid for impacts with  $E$  from 0.22 to 2.0 J and  $X$  of up to 2.0 mm. Insufficient data exists to formulate predictions for the ABB-2 alloy. However, since both the Ti-48-2-2 and ABB-2 were cast-to-size specimens, the Ti-48-2-2 equations were used to predict crack lengths for ABB-2, and the predicted crack lengths were compared to actual crack lengths. For HZ cracks, the large amount of scatter in actual crack lengths resulted in little correlation between predicted and actual crack lengths. However, a plot of measured BS versus predicted BS crack lengths resulted in a slope of 0.98 with a correlation coefficient of 81 percent. Therefore, the effect of  $E$ ,  $X$ , and  $BO$  on BS crack length for the ABB-2 alloy can be adequately predicted using the Ti-48-2-2 model. For ABB-2, resistance to ballistic impacts was comparable to Ti-48-2-2 despite its lower ductility and is most likely related to its higher tensile strength. For high-speed impacts near the leading edge, a stress criterion has been shown to limit cracking more than a plastic strain criterion (ref. 26).

A small study on the impact resistance of ABB-23 was undertaken to eliminate the effect of large lamellar grains on the sample edges of ABB-2. The ABB-23 has a refined microstructure (fig. 12(g)) due to the addition of boron. The HZ and BS crack lengths as a function of  $E$  for ABB-2, ABB-23, and cast-to-size Ti-48-2-2 are shown in figure 23. The ABB-23 crack lengths (table VIII(f)) were within the scatter for the 0.2 and 1.5 J energy impacts for Ti-48-2-2. However, the 0.75 J energy impacts on the ABB-23 samples had a tendency to blow out and have higher HZ crack lengths. The ABB-23 samples were machined samples that have a high tendency to blow out using the 1.6-mm projectiles at 0.75 J of energy. Only one  $X$  value was measurable on the blown-out samples, and it was 0.5 mm. This  $X$  value is similar to that of the CMU low-Al samples and resulted in similar HZ crack lengths, between 2 and 4 mm. The refined microstructure of the ABB-23 samples did not improve the impact resistance of this alloy. Possibly, a decrease in the variation in HZ crack length occurred with the ABB-23 alloy, but a larger data set of ABB-23 impacts would be necessary to demonstrate statistical significance.

**NCG359E.**—NCG359E is a cast TiAl alloy which contains Ta as a strengthening element. A few ballistic impacts were performed on machined specimens to check the impact resistance of this alloy, and the results are plotted in figure 24. The impact resistance of the NCG359E alloy was comparable to the other alloys tested. The crack length measurements are given in table VIII(g).

**95A.**—95A was the only wrought alloy tested in this study. The crack length measurements are given in table VIII(h). The HZ and BS crack lengths as a function of  $E$  are also shown in figure 24. The uniform, thermomechanically treated lamellar microstructure of the 95A alloy did not improve the impact resistance of TiAl; it was similar to all the other alloys. Note also that the room-temperature tensile properties were also similar to those of the Ti-48-2-2.

### Analytical Simulations of Impact Cracking

For the cast-to-size Ti-48-2-2, three impact conditions (samples) were modeled analytically, and the conditions are given in table IV. Intuitively, an impact near the leading edge of the  $\gamma$ -TiAl specimen will result in the bending of the leading edge in its own plane and in a plane normal to it, as depicted in

figure 25. Although this figure shows the results only for sample 005-08-3, similar bending results were also obtained for the other two samples.

Results were obtained for the von Mises stress, von Mises plastic strain, and z-stress distributions on both the front and back sides. The von Mises stress and von Mises plastic strain on the front side and the z-stress distributions on the back side will only be presented here, since they were found to be correlated with cracking. Hereafter, the von Mises stress will be referred to simply as stress, and the von Mises plastic strain simply as plastic strain.

Figures 26 to 28 display the stress and plastic strain on the front face and the z-stress distributions on the rear face of specimen 008-10-3 tested at low  $E$ . Combining results for stress (fig. 26) and plastic strain (fig. 27), one can find a zone on the front face of the specimen where the stress-strain cracking criteria are satisfied, and a potential cracking of the specimen can occur. This area is outlined in figure 26. Additionally, an examination of the z-stress distribution on the back side of the specimen (fig. 28) reveals the z stress to be in tension and larger than 400 MPa at a small area near the leading edge. The dashed line highlights the location of the predicted BS crack. Although not shown, both the stress and the plastic strain criteria were also met on the back side in the area of cracking. These predictions can be compared to the actual cracking conditions in figure 10(a).

The stress and plastic strain on the front face and z-stress distributions on the rear face of specimen 005-08-3 tested at intermediate  $E$  are displayed in figures 29 through 31, respectively. A potential cracking zone can be identified by combining the stress-strain cracking criteria with results for stress and plastic strain from figures 29 and 30 and is depicted by the dashed line in figure 29. The results for the back side are similar to those of the specimen impacted at low  $E$  with the exception that the length of the crack is larger as predicted by the z stress. This similarity is in agreement with the actual results on the sample (fig. 10(b)) and is due to the higher impact energies used on specimen 005-08-3.

Results for stress and plastic strain, shown in figures 32 and 33, respectively, can be combined as a stress and strain cracking criterion to identify a potential cracking zone on the front face of specimen 009-08-2 tested at high  $E$  (dashed line, fig. 32). It is noteworthy that both the critical stress and plastic strain fields penetrate the thickness of the sample for this test. This is in contrast to the two previous tests, where at least the critical plastic strain field terminated somewhere at midthickness. The fact that these fields at high-energy impact penetrate the thickness correlates with the near-blowout situation observed in the actual sample (fig. 10(c)).

The back side shows that the criteria for cracking are satisfied for the formation of a BS crack. Figure 34 shows the tensile z stress in this zone. The predicted length of the BS crack is significantly longer than for the other two tests because of the higher  $E$  and larger projectile used. The dashed line depicts the BS crack in figure 34.

The BS straight crack lengths for the three tests were calculated on the basis of the cracking criteria proposed earlier in this paper. The prediction capability of the model for BS crack lengths is shown in figure 35. The model reasonably predicts the BS crack length observed in the experiments. While the crack length on the front side was not determined from the FE model, there is good agreement between the prediction and experiment as far as crack severity and its relationship to impact energy. These results indicate that the proposed cracking criteria do a reasonably good job of capturing and predicting the general cracking patterns and accurate BS crack lengths.

## Fatigue Strength

This section addresses the fatigue properties of the various  $\gamma$ -TiAl alloys. Both virgin and impacted samples were cycled under HCF conditions at elevated temperatures. The main goal of this section is to assess the contribution of defects to the fatigue strength. These defects are from impacting as well as from other inherent defects in the samples, such as casting defects and anomalous microstructural features. These effects are modeled using a conventional LFM (linear elastic fracture mechanics) approach. The fatigue properties are related to various alloy-specific properties.

**Fatigue worksheets.**—Tables IX(a) to (h) give the resulting fatigue properties for the different alloy specimens after impact. In these tables the samples in the first column can be directly related to the samples listed in the corresponding tables VIII(a) to (h). Only data from the indent which initiated the critical fatigue crack is given in table IX. The load ratio  $R_\sigma$  ( $\sigma_{\min}/\sigma_{\max}$ ) is presented with the  $A$ -ratio in parentheses, where  $A$  is the ratio of the amplitude of the load range to the mean load,  $\sigma_{\text{amp}}/\sigma_{\text{mean}}$ , or  $A = (1-R_\sigma)/(1+R_\sigma)$ . The net section stress at failure is provided, as well as the life of the sample—the cycles to failure—in the last step. “Failure type” describes the type of defect causing initiation of the critical fatigue crack, and the area of these defects as measured on the fracture surfaces is in the next column. The main failure types are

- Porosity—initiation at microshrinkage or gas pore
- Face—crack or defect on face of sample (not result of impacting)
- BS—back-side crack from impact
- FS—crack on front side from impact, which is perpendicular to specimen axis (resembles BS crack but exists on front side)
- HZ—HZ crack from impact

There are various combinations of these flaws, and occasionally modifiers are used with these failure types in an attempt to better describe the initiation site. For the BS or HZ crack that caused the failure, the crack size as measured on the sample surface before fatigue testing is highlighted on the corresponding tables VIII(a) through (h). The net section stress at threshold identifies the maximum fatigue stress in the last complete cycle block, and the minimum stress is also given. The number of steps to the last complete cycle block inclusive is shown as the number of steps to threshold. If an entry of zero is given here, then the sample failed during the first block. The fatigue strength in the last complete block is an estimate of the fatigue endurance limit for the corresponding block size. This may also be called the fatigue strength at threshold since this value is the highest stress achievable before the existing crack begins to propagate.

**S–N curve.**—Figure 36 presents S–N data for the various  $\gamma$ -TiAl alloys studied. The data were taken from virgin samples either free of defects or containing defects having an area less than  $0.1 \text{ mm}^2$ —a size which was deemed by inspection to have no influence on fatigue strength. Note that of the data points representing the 50 samples in figure 36, only 12 of the points represent samples with observable defects. In general, the data fall into one grouping with fatigue stresses at a life of 10 000 cycles ranging from approximately 290 to 390 MPa. Endurance limits (at  $10^6$  cycles) from conventional, single-stress fatigue tests are given by Wright et al. (ref. 33) as 335 MPa for cast Ti-48-2-2 at 650 °C and by Recina and Karlsson (ref. 34) as 325 MPa for ABB–2, and these values are consistent with our data. Two alloys seem to have superior fatigue properties: CMU Ti-47-2-2 and the ABB–23. At a life of 10 000 cycles, ABB–23 has the highest fatigue strength of approximately 470 MPa, and the CMU Ti-47-2-2 alloy has a fatigue strength of 400 MPa. Note that the enhancement in fatigue strength of these two alloys is not necessarily a consequence of their respective tensile properties (table VII), since the other alloys have similar or better properties. Nor is there any obvious correlation with either chemistry or microstructure. These variables interact and may have conflicting influences on the fatigue strength. Figure 36 does not address the effects of these variables on fatigue strength in a controlled fashion; it merely provides a more conventional look at the data.

Another observation can be made in figure 36. Of the 50 data points in this figure, only 7 represent samples that lasted longer than 25 000 cycles in the final step. It can be implied that during the step tests the crack grows rapidly once the threshold stress value is reached. This is consistent with observations on impacted samples both in this study and in others (refs. 35 and 36) where the specimen fails in the last step in a limited number of cycles. Nicholas (ref. 36) has shown for Ti-6Al-4V that precracked samples failed during step testing early in the last step and attributed this to a well-defined threshold and the lack of importance of an initiation phase. He continued to show that uncracked samples failed at a more random cycle number, indicating that the initiation phase for these samples was both random and dominant to the life. By applying the conclusions of Nicholas (ref. 36) to figure 36, we believe that the

majority of the cast  $\gamma$ -TiAl alloys have sufficient, available initiation mechanisms—whether it is some small casting or machining defect, lamellae oriented for easy crack initiation, or some unknown microstructural anomaly—such that initiation has already happened or can easily occur, and the bulk of the life in the last step is therefore propagation controlled and relatively constant.

**Mean stress effects.**—The effect of tensile mean stress on the fatigue strength of cast-to-size Ti-48-2-2 specimens impacted at two energies, 0.7 and 1.5 J, was evaluated. Four impacted samples were tested at each of three load ratios, 0.05, 0.2, and 0.5, such that a total of twelve specimens were tested for each energy level. The results show a classical mean stress dependence of the fatigue strength as implied with a Goodman diagram (fig. 37). Additional data with  $E$  ranging between 0.2 and 1.5 J are also included in figure 37, along with a line representing cylindrical-shaped, smooth-bar specimens tested by GEAE. The data for the defect-free, as-received samples from the current study lie near, but somewhat lower, than the smooth-bar line despite the somewhat sharp edges and rough, as-cast and chem-milled surfaces of the samples used in the current study. The data in figure 37 fall into two groups represented by the two different  $E$  levels. It appears as if both mean stress curves and the curve from the smooth-bar data extrapolate to points between the 0.2% YS and the UTS of the material.

The effect of tensile mean stress on fatigue strength was also evaluated for alloy ABB-2. The specimens were impacted at a number of energies, 0.2, 0.7, 1.5, and 6 J. Several impacted samples were tested at each of two load ratios, 0.05 and 0.5. Similar to the results on the baseline Ti-48-2-2 material (fig. 37), the results show a classical mean stress dependence of the fatigue strength as displayed with a Goodman diagram in figure 38. Data for samples tested at both 650 and 730 °C are shown, and there was no observable difference between the two temperatures. A dashed line is also shown in figure 38 to represent data supplied by ABB for smooth-bar results at 650 °C. Note that the two virgin samples, one at each temperature, fall just short of the smooth-bar data. However, since there are only two points, and the data for the smooth bars were scarce and from a different material batch, the similarity is remarkably good. The data from impacted samples, in general, group into three energy classes, with the two highest  $E$  values (1.5 and 6 J) being grouped into one class of data. The division amongst the energy levels is not as clear as it was for the baseline data. For convenience, the lines showing the energy levels were visually approximated and extrapolated to the point where the smooth-bar data intersects the abscissa. This point lies approximately halfway between the 0.2%YS and the UTS, a similar position to that observed for the baseline data.

Figure 39 shows the affects of mean stress at two different load ratios,  $R_\sigma = 0.05$  and 0.5, and three different  $E$  levels for alloy 95A. While the data can be ranked according to  $E$  for the fatigue tests at an  $R_\sigma$  value of 0.05, at 0.5 the data fall into one group. However, there are only two energy levels used at the higher  $R_\sigma$  value. Both of these energy levels (0.7 and 1.5 J) are fairly high and, based on this, could justify the grouping of the data. Four samples failed at small EDM pits, yet approximate virgin strengths. They fall just short of datum from Larsen (ref. 6) for a smooth-bar sample tested at room temperature. A second point is plotted for a smooth-bar sample tested at 600 °C (ref. 37). Both of these points are for the original K5 material, so a direct comparison may not be that useful.

**Porosity.**—Several as-received cast-to-size Ti-48-2-2 specimens contained casting defects and were rejected by the vendor as being acceptable specimens (ref. 38). However, it was thought that by testing these samples we would gain an understanding of the effects of these defects on the fatigue strength, which would help guide approaches in damage tolerance for this class of materials. The results of these fatigue tests (table X) could also help establish selection and/or rejection limits for some component castings and to help establish reparability limits for parts developing in-service damage. Therefore, these samples were examined by various nondestructive evaluation (NDE) methods both at the NASA Glenn Research Center and Precision Castparts to document the size and location of the defects (table XI). These numbers can be compared with the actual size of the critical defect measured on the fracture surface after the fatigue test (column 3). Microfocus x-ray (fig. 40(a)) was successful in identifying 9 out of the 10 casting defects that caused failure and was an improvement in the detection capabilities over conventional radiography. Computed tomography (CT), a time-consuming method, was only performed

on two samples. This method gave cross-sectional information about the defects (fig. 40 (b)) similar to what would be measured on the fracture surface. Ultrasonic evaluation detected the general area of the defects, but could not provide specific information regarding the exact defect location and size.

In spite of correctly identifying the critical defect, the size of the defect was always overestimated by NDE and hence would have predicted a conservative fatigue strength. The primary reason for this is that the defects are often microshrinkage, which is a complicated three-dimensional network of voids (fig. 40). In addition, radiographs often show a halo around the defect, probably due to some chemical inhomogeneities. It is unclear from any NDE process which portions of the indication should be assumed as the flaw size. We tended to take the entire size of the largest NDE indication as being the critical defect, but based on the resulting fatigue strengths, only a portion of the assumed defect actually seemed to contribute to the severity of the defect. Since we did not want the specimen to fail in the first block, we chose a starting fatigue stress that was conservatively small. Because of the influence of these defects on the fatigue strength and the inability to determine their effective size, the fatigue tests were usually begun at much lower stresses than necessary, which led to long test times.

**Crack lengths and areas.**—The sizes of the defects leading to fatigue failure were evaluated for each alloy to establish a relationship between defect size and fatigue strength.

*Cast-to-size Ti-48-2-2:* The crack lengths highlighted in table VIII(a), which initiated the critical fatigue cracks, are plotted versus the fatigue strength at threshold in figure 41. Only data for  $R_\sigma = 0.05$  are plotted. The data for the BS and HZ cracks were measurements made from the surface of the sample prior to fatigue testing. The virgin samples often failed at microshrinkage, gas pores, lamellar facets, or some other defects. The crack length measurement from these specimens was taken parallel to the specimen width on the fracture surface after the specimen had failed. The different crack types can generally be categorized as follows: The samples initiating at surface pores generally represented the smallest defect sizes, the BS crack lengths were intermediate, and the HZ cracks were the largest. However, many of the samples had large areas containing internal shrinkage, and so these data spanned a large range of defect sizes. We tested these samples to gain insight on how specimens with these defects would compare to samples with impact cracks. As can be seen in figure 41, data from all types of defects fall on the same curve and can be well represented by a quadratic equation. The fitting parameters are given in figure 41, and this baseline curve will be used for comparison to other alloys in future similar plots.

Two additional points need to be made concerning figure 41. First, there are two points on the ordinate, which are specimens containing no defects and thus represent the fatigue strengths (i.e., endurance limit) of virgin samples. Second, the approximate range of data scatter in this figure is approximately 100 MPa ( $\pm 50$  MPa).

It should be noted that as  $X$  increased, the BS crack area became much larger, encompassing most of the sample thickness (fig. 42). It is therefore reasonable that crack depths might also play a role in determining the fatigue strengths. The fatigue stress may not be well represented by the surface crack length alone and through-thickness dimensions may also be important. Therefore figure 43 is a plot of the dependence of fatigue strength on the defect area and is plotted similarly to the crack length in figure 41. The crack area was measured on the fracture surface and is listed under "Defect area" in table IX(a). The crack area is a good predictor of fatigue strength, but not any better than the crack length.

*GEAE Ti-47-2-2:* Figures 44 and 45 document the affect of defect length and area, respectively, on the fatigue strength at threshold for the machined Ti-47-2-2 alloy. The data fit reasonably well with the baseline data (curve), but points fall below the curve, particularly for those samples with small defect lengths and areas. Note that most of the crack areas for the machined Ti-47-2-2 samples cover a smaller range (0 to 1.2 mm<sup>2</sup>) than for the baseline data (0 to 6 mm<sup>2</sup>). For the same size crack this represents a higher percentage of the cross sectional area for the machined samples. Thus this could be why many of the specimens failed at lower fatigue strengths than the cast-to-size Ti-48-2-2.

There is a group of points at small (approximately zero) crack lengths and areas that represent virgin samples. Many of these samples failed at porosity or other inherent defects, and their crack dimensions were taken from the fracture surfaces after the test. Also, the data point for specimen 4-1-3 which has a crack length of 0.79 mm in table VIII(b) was adjusted after examining the fracture surface. The actual

length of this crack was smaller than originally listed because it did not start at the leading edge of the sample. The virgin samples have a mean fatigue strength of 332 MPa with a standard deviation of 45 MPa. This average fits within the values of mean strength for the two virgin samples of the baseline material.

There is also a virgin sample that failed at very low stresses (118 MPa) and is the rightmost point in figures 44 and 45. This sample actually failed on the first step but was included in the data to illustrate a point: This sample failed at a very large interlamellar facet on the face of the sample (fig. 46). Thus while not actually a prior defect, the large lamellar grain was weak enough to crack at a lower stress than would be needed to propagate the existing impact crack.

*CMU Ti-47-2-2*: Figure 47 shows the influence of defect length on fatigue strength at threshold of the CMU alloy. The data are predicted reasonably well by the baseline data with the exception of the three samples that failed at porosity. These three samples had strengths higher than the baseline predictions. Likewise, the effect of defect area on fatigue strength (fig. 48) is predicted reasonably well by the baseline data. Note that out of the 20 impacted samples, 14 of them had leading edges that were bent from impacting (fig. 49). This occurred at  $E \approx > 0.4$  J, or at the lower energies if the location of impact  $X$  was  $< 0.4$  mm. Only 2 of the 18 GEAE Ti-47-2-2 samples had bent leading edges.

*Howmet Ti-47-2-2*: Figures 50 and 51 document the affects of defect length and area, respectively, on fatigue strength on Howmet Ti-47-2-2. The data are plotted along with the data from CMU. The data from both materials fall in the same scatter band and can be predicted by the baseline data. The majority of the Howmet samples were used for a coaxing study and are mostly virgin samples containing no defects. Their fatigue strengths range between 219 and 348 MPa, and this is shown by the two points on the ordinate with the double-sided arrow. Note that this range of virgin fatigue strengths is in the same range as the cast-to-size 48-2-2 data.

*ABB-2 and ABB-23*: The fatigue strengths of ABB-2 and ABB-23 are plotted as a function of defect lengths and areas in figures 52 and 53, respectively. In both figures, the baseline data fit the data of these alloys fairly well. The ABB alloy data do fall slightly lower than the baseline data at small defect lengths and areas. There is no apparent difference in these plots between samples tested at 650 or 730 °C. Data for defect-free ABB-2 samples at both 650 and 730 °C fall in the same range as the baseline data. However, the defect-free ABB-23 material has significantly higher fatigue strengths (approximately 460 MPa) compared with a strength of 300 MPa for the baseline material and may be a result of its higher UTS and more refined microstructure.

*NCG359E*: Figures 54 and 55 show the affects of defect lengths and areas, respectively, on fatigue strength at threshold for machined NCG359E. Again, the data are well represented by the baseline curve for the few data points available. Unfortunately, there were no defect-free samples for comparing with the other alloys.

*95A*: The affects of defect lengths and areas on fatigue strength at threshold for the wrought and machined 95A alloy are shown in figures 56 and 57, respectively. The data are very well represented by the baseline curve. The few defect-free, or nearly defect-free, samples have an average strength of 300 MPa, which is consistent with the baseline material.

**Threshold analysis.**—Many researchers (refs. 6 and 39 to 41) have shown that a threshold-based approach reasonably predicts the fatigue strengths of impacted gamma alloys. By plotting the fatigue strength versus the crack size in a Kitagawa diagram (ref. 42), the data are correlated with the calculations for stress intensity from LEFM. For very small cracks LEFM breaks down, and the fatigue strength is given by the fatigue endurance limit of the material. A similar approach will be taken here with the exception that instead of using the Kitagawa diagram, the fatigue strength calculated from LEFM will be plotted against the measured fatigue strength at threshold. This was done for two reasons. First, the Kitagawa diagram is a log-log plot and this gives a distorted image of the scatter in the data. Second, since we have several different types of defects, the quality of the LEFM predictions can be shown with one line rather than many neighboring lines as in the Kitagawa diagram.

To calculate the fatigue strength, the following equation was used:

$$\Delta\sigma = \frac{\Delta K_{th}}{F(a/w)\sqrt{\pi a}} \quad (3)$$

where  $\Delta\sigma$  is the predicted fatigue strength range for the block size,  $\Delta K_{th}$  is the stress intensity range at the threshold,  $F(a/w)$  is a geometry correction factor, and  $a$  is the defect length. Since the load ratio for these tests was approximately zero (i.e.,  $R_\sigma = 0.05$ ), the deltas on  $\sigma$  and  $K$  will henceforth be dropped. Also, no attempt was made to predict tests conducted with other mean stresses (i.e., other than  $R_\sigma = 0.05$ ), although an identical process would be used. Note that  $K_{th}$  was unavailable for these alloys. It would have been ideal to have this information on the exact lots of material used in this study. However, this was beyond the scope of the current study. There are some values for  $K_{th}$  for similar alloys in the literature. These will be used for comparison and discussed later in this report. Given the lack of threshold values, we chose to back-calculate them from an iterative process, trying various values for  $K_{th}$  until a visual good fit with the data was obtained. This method was adequate since we had various defect types that covered a wide range of flaw sizes.

The correct form of equation (3) depends on both the defect type and the geometries of the defect and sample. Various stress intensity solutions were assumed for the defects observed in this work. Note that these are simplifications of the actual situation in the  $\gamma$ -TiAl samples and assume, among other things, that the specimen is rectangular rather than the elliptical shape used in the experiments. Thus some small inaccuracies are inherent in the predictions due to these assumptions.

For BS cracks, a corner crack solution was often used as given by Newman and Raju (ref. 43). However, as the crack depth increased or the BS crack approached the edge of the sample (and this happened for the CMU Ti-47-2-2, ABB-2, and 95A materials), the crack was better represented by a single-edge notch (SEN) solution (ref. 44).

HZ cracks looked most like edge cracks that have a different crack length at the front and the back surfaces (ref. 45). It was found that using the smaller crack length (i.e., the length on the impacted side) gave the best fit of the data. The smaller crack length could also be used in an SEN solution to give identical results. The inclination of the HZ crack out of the plane, which would introduce mixed-mode loading, was not taken into account in the modeling.

Defect configurations in the porosity-containing samples were approximated using an embedded crack solution (ref. 43). Occasionally, cracks initiated at surface defects (face defects) due to either machining or casting. These configurations were approximated using a surface crack solution (ref. 43).

Fatigue strength predictions are shown for the cast-to-size Ti-48-2-2 in figure 58. A  $K_{th}$  value of  $8.8 \text{ MPa}\sqrt{\text{m}}$  ( $8.0 \text{ ksi}\sqrt{\text{in}}$ ) was found to best fit the data for all of the defect types. There were a number of the porosity-containing samples whose data are overpredicted. This is a result of an inaccuracy in measuring the defect size. For example, figure 59 is a micrograph of specimen 007-02 containing a large area of microshrinkage in the middle of the sample. The solid line outlines the defect size as was used to calculate the point in figure 58. If however, the dashed outline is used, the predicted fatigue strength drops from 386 to 217 MPa and falls very near the prediction line (the arrow tip represents the position of the adjusted point). While this is a large difference in predicted fatigue strength, the difference in defect size (fig. 59) is marginal. Without knowledge of figure 58, either crack outline in figure 59 would seem acceptable.

As the measured fatigue strength increases in figure 58, the prediction line crosses a band of values representing the range of virgin material strengths displayed by the undamaged samples. This band represents the fatigue endurance limit for the corresponding block size and was determined based only on two defect-free samples. The band has a range of approximately 58 MPa. Note that for future graphs, the virgin strengths may include strengths from undamaged samples as well as strengths from samples with defects of areas less than  $0.1 \text{ mm}^2$ , as these small, defect-containing samples were noticed by inspection to have similar strengths as the undamaged specimens.

The threshold approach is shown in figure 60 for the GEAE Ti-47-2-2 alloy. Good predictive capabilities are observed when using a  $K_{th}$  of  $8.2 \text{ MPa}\sqrt{\text{m}}$ . The range of virgin strengths (141 MPa) was based on nine samples, two of which were defect free. Note that there are two data points, one from a small BS crack and one from a crack on the sample face (i.e., surface crack) that fall in the measured range of the undamaged samples. The face crack, while largely over-predicted, contained anomalous microstructural features, which, if taken into account in the defect size, could have greatly reduced its predicted value to the prediction line. The sample containing the BS crack was well predicted by LEFM.

Predictions for the CMU Ti-47-2-2 are presented in figure 61. For this material, the BS cracks looked more like through-cracks and were therefore treated as SEN. A  $K_{th}$  value of  $12.1 \text{ MPa}\sqrt{\text{m}}$  predicted the data best. This value is higher than the assumed  $K_{th}$  value for both previous sets of data and may be due to the excess plasticity as shown by both the leading edge deformations (fig. 49) and the large tensile ductilities at 650 °C (table VII). The range of virgin strengths (36 MPa) was taken from only three samples, of which only one sample was defect free. Interestingly enough, this defect-free sample had the lowest fatigue strength of the three samples.

The fatigue strengths for the cast-to-size ABB-2 samples are given in figure 62. For both crack types (BS and HZ) a  $K_{th}$  of  $9.9 \text{ MPa}\sqrt{\text{m}}$  best fit the data. Contrary to the cast-to-size Ti-48-2-2 samples, the BS cracks for ABB-2 were nearly through-cracks and were therefore modeled as SEN instead of corner cracks. Two undamaged samples were tested: one at 650 °C and the other at 730 °C, yielding strengths of 301 and 325 MPa, respectively. Since both have strengths above 300 MPa, they do not appear in figure 62.

There were only six samples available for analysis from the machined ABB-23 material. The predictions of their fatigue strengths are given in figure 63 for a  $K_{th}$  of  $11 \text{ MPa}\sqrt{\text{m}}$  ( $10 \text{ ksi}\sqrt{\text{in}}$ ). The range of virgin strengths is from the results of two specimens.

The prediction capability for the NCG359E alloy is given in figure 64. Similar to the ABB-23 material,  $K_{th}$  was calculated to be  $11 \text{ MPa}\sqrt{\text{m}}$ . Unfortunately, no virgin strengths were available. While there are only a few data points, they fall over a wide range of strengths (and therefore defect sizes) and show good correlation over this range for the  $K_{th}$  value utilized.

Predictions for the wrought alloy 95A are shown in figure 65 for a  $K_{th}$  of  $11 \text{ MPa}\sqrt{\text{m}}$ . In this figure there is a sample, F-11, which failed from a FS crack. It was modeled as a HZ crack. The range of virgin strengths was taken from samples with small defects. Defects for three of these samples were very small pits from the EDM process. Note that for these four samples, the range of virgin strengths (25 MPa) is much smaller than for the cast alloys.

Back-calculated  $K_{th}$  values indicated that four of the  $\gamma$ -alloys (CMU, ABB-23, NCG359E, and 95A) have superior resistance to crack propagation. Of these alloys ABB-23 has the most refined microstructure. However, its tensile elongation and its UTS is the same as the other three above-mentioned alloys. Any correlation between  $K_{th}$  and microstructural and tensile properties is vague. It is possible that a refined microstructure is responsible for a larger  $K_{th}$ , thus giving ABB-23 an advantage. The seemingly high  $K_{th}$  from the other three alloys may be a result of their high elongation at the fatigue test temperature of 650 °C.

**Crack initiation and fatigue strength.**—The influence of defect length on fatigue strength can be easily plotted as shown in figures 41, 44, 47, 50, 52, 54, and 56 for the alloys studied. It should be pointed out that these curves are nothing more than a linearized Kitagawa diagram. The data in these plots represent various defect geometries. Therefore, it is not expected that all of the points would fall on one continuous curve, since the stress intensity should play a role in the severity of the crack. In actuality the threshold approach should give a better representation of the data. However, the above-mentioned figures show that the threshold approach is not necessary. The reason for this is that the geometric factor,  $F(a/w)$ , in equation (3) is similar for the defect types and sizes studied here. For example, for a crack length of 2 mm and a crack depth of 1 mm, the following geometry correction factors were calculated:

1.17	Corner crack (BS)
1.16	Through crack (HZ)
0.96	Embedded defect (pores)

Hence, the three defects can be simply plotted versus crack size with minimal error. This is fortuitous since surface crack length is the only available information prior to failure on either a sample or an actual component. The use of LEFM would require either knowledge of the crack shape and depth—like what would be gained from a CT scan—or an assumption of these crack characteristics. Using the surface crack is much simpler and gives reliable results.

One area of concern in this study is the scatter in the fatigue strength data. An attempt at describing the scatter is given in table XII. In this table the range of scatter as estimated from various figures is shown, along with the sample size,  $n$ , used for this estimation. Viewing the spread of data for virgin  $\gamma$ -TiAl samples in table XII suggests that a sample size of approximately 10 is required to confidently estimate the scatter. Smaller sample sizes give much smaller scatter. For the Ti-47-2-2 alloys, the scatter is approximately 135 MPa as estimated from virgin specimens. The scatter as visually estimated from the surface crack plots (e.g., fig. 41) is close to 100 MPa, and this number decreases for smaller samples sizes. Since the points are spread along the x-axis for these plots, a minimum of 15 points is probably required to give reliable estimates of the scatter in these plots. The range of scatter for flawed samples as perceived from the threshold analysis is approximately 90 MPa for reasonable sample sizes. A number of conclusions can be drawn from table XII. First, given sufficient data, the typical scatter for this class of materials is 90 MPa for defect-containing samples and possibly as large as 150 MPa for virgin samples (figs. 44 and 45). This is not unusually large as many cast aluminum alloys (ref. 46) and cast steels (ref. 47) have a spread in their fatigue data of 70 to 100 MPa. The scatter in the fatigue endurance limit from conventional fatigue tests on extruded Ti-6Al-4V is 140 MPa (ref. 48). Also, this size of scatter can be ascertained from the data of various researchers on cast gamma alloys (refs. 34 and 49). Second, regardless of the method used to view the data, the scatter remains similar suggesting that the scatter is truly a material issue and not one of manipulating the data. Third, while the alloys other than Ti-47-2-2 show lower scatter in their virgin state, they have similar scatter to the Ti-47-2-2 in the defect-containing state. It is therefore suspected that their virgin scatter is only a manifestation of the limited sample size. In fact, fatigue studies (refs. 34 and 49) on virgin samples of other cast gamma alloys show scatter that is at least as large as that measured here. Finally, since 95A is a wrought alloy, it was anticipated that it would exhibit less scatter. There is a limited amount of data on the virgin samples suggesting that they may exhibit less scatter. However, for at least the defect-containing samples the scatter remains as large for the wrought alloy as for the cast alloys.

The  $\gamma$ -TiAl in the lamellar form is susceptible to cleavage fractures. Many researchers (refs. 34, 37, 39, and 50 to 57) have shown that cracked lamellae occur during cyclic loading and that this susceptibility leads to early crack initiation (refs. 34, 39, and 50 to 57). Recina and Karlsson (ref. 34) suggest that the scatter in fatigue life is partially due to the ease of interlamellar cleavage. Furthermore, Wu et al. (ref. 50) postulate that the scatter in low-cycle fatigue (LCF) data is a direct consequence of the initial size of the cleavage crack (i.e., the lamellae colony size). Given the large colony sizes of most of the alloys used in this study, the observed large scatter is to be expected. The ABB-23 alloy has the smallest lamellae colony size (fig. 12) and appears to have the smallest scatter across table XII. This alloy also had the highest tensile and fatigue strengths as well as one of the highest  $K_{th}$  values.

Many researchers (refs. 50, 51, and 56) have shown that lamellar colonies oriented at 45° to 90° to the loading axis are favored for easy crack initiation. This can be observed by examining specimens 5-1-3 and 6-3-4 from the machined GEAE Ti-47-2-2 data. Both of these samples failed on the first step because of fracture at large lamellae oriented at favorable angles. Specimen 6-3-4 is the point with the largest crack length and area in figures 44 and 45 and the low fatigue strength of this specimen is a direct result of the large interlamellar crack (facet). Per the suggestions of Bowen (ref. 55) and Recina (ref. 34), and consistent with the results shown here, reducing the lamellar colony size should reduce fatigue scatter and improve the mean strength of these alloys. Recina (ref. 34) has gone as far as saying that colonies should

be kept to sizes  $<100\ \mu\text{m}$ . The colony sizes for the  $\gamma$ -alloys used in this report are generally larger, sometimes an order of magnitude larger than  $100\ \mu\text{m}$ . Even if the colony size is smaller than  $100\ \mu\text{m}$ , there can be an occasional lamella of large size or neighboring lamellae of similar orientations that—when combined—can act as a large colony. Therefore, for minimal scatter the lamellar colony size should be uniform and probably on the order of  $60\ \mu\text{m}$  (similar to the ABB-23).

The fatigue strengths can be accurately predicted using an LEFM approach. Typically a Kitagawa (ref. 42) diagram is used, where the log of the fatigue stress is plotted versus the log of the flaw size. This yields a series of parallel lines, dependent on the specific stress intensity solution, with slopes of  $-1/2$ . At small flaw sizes the curves level off to a horizontal line, which represents the fatigue endurance limit. This approach delineates fail-safe regions under cyclic loads (ref. 58). Because of the myriad of flaw types in this study, we chose instead to plot predicted versus measured fatigue strengths. While both methods use equation (3), the plotting method used in this report forces all the data onto one line and made it easier estimate  $K_{th}$ . Also, since these are linear plots, it is easier to visualize the amount of scatter present. As shown in figures 58 and 60 to 65, this approach gave good results. The predicted values were taken only from the threshold  $K$  solutions (eq. (3)). Neither short crack corrections nor residual stress effects were considered. Many researchers have also used the El Haddad et al. (ref. 59) correction in the Kitagawa plot to create a smooth transition between the long crack threshold and the endurance limit. However, given the scatter in the data this approach was not deemed worthwhile. Additionally, this correction involves defect sizes, which are normally smaller than most of the defect sizes observed in this study.

The back-calculated  $K_{th}$  values are given in table XIII along with values taken from the literature. In general  $K_{th}$  for this class of alloys is approximately  $9\ \text{MPa}\sqrt{\text{m}}$ , and our results compare favorably with these values. There is some variation in the literature values presented in table XIII. Most of these points were taken at temperatures other than  $650\ ^\circ\text{C}$ . Also, test frequencies and actual microstructures were different and may affect these values. It has been well documented (refs. 6, 55, and 60 to 63) that the fatigue crack growth rates are fastest and the  $K_{th}$  is the lowest at or around  $650\ ^\circ\text{C}$ , the temperature used in this study. It has also been shown that alloys with duplex microstructures have poorer crack growth resistance and lower  $K_{th}$  than alloys with lamellar microstructures (refs. 6, 52, 55, 56, 60, 62, and 63). Hence, as the volume percent of lamellar colonies increases  $K_{th}$  should increase. The effects of test frequency are not well defined for fatigue crack growth in  $\gamma$ -TiAl, but it would be likely that frequency has an effect. The tests run in this study were performed at  $100\ \text{Hz}$ . Tests for the literature values in table XIII were conducted at frequencies less than or equal to  $20\ \text{Hz}$ . Hence, only a general comparison of  $K_{th}$  values can be done. It would have been ideal to have  $K_{th}$  values (and smooth-bar LCF values as well) on the actual materials studied here, but it was beyond the scope of this project. Also, this would have been impractical for the cast-to-size samples, where each sample is essentially its own lot.

## Fretting

**Reciprocating pin-on-flat tests.**—Surface and subsurface damage always occurred on the interacting surfaces of GEAE Ti-47-2-2 fretted in air. The surface damage consisted of material transfer, pits, oxides and debris, scratches, fretting craters and/or wear scars, plastic deformation, and cracks.

**Adhesion and material transfer:** Figure 66 presents a backscattered electron image and an EDS spectrum taken from the fretted surface of the IN718 pin after contact with the  $\gamma$ -TiAl flat. Clearly,  $\gamma$ -TiAl transferred to the IN718 pin. The  $\gamma$ -TiAl failed either in tension or in shear because some of the interfacial adhesive bonds (solid state or cold welding) were stronger than the cohesive bonds within the cohesively weaker  $\gamma$ -TiAl. The failed  $\gamma$ -TiAl subsequently covered the IN718 surface in amounts ranging from 10 to 60 percent of the IN718 contact area at all fretting conditions in this study. The thickness of the transferred  $\gamma$ -TiAl was as much as  $\sim 20\ \mu\text{m}$ .

As with the materials pair of  $\gamma$ -TiAl and IN718, material transfer was also observed on the IN718 flat surface after fretting against the Ti-6Al-4V pin at 423 and 550 °C in air. However, the degree of material transfer was much greater for the Ti-6Al-4V, covering between 30 and 100 percent of the IN718 contact area for identical fretting conditions. The thickness of transferred Ti-6Al-4V material was as much as 50  $\mu\text{m}$ .

*Fretting wear:* Figure 67 shows typical wear scars produced on the  $\gamma$ -TiAl pin and the IN718 flat. Because of the specimen geometry a large amount of wear debris was deposited just outside the circular contact area. Pieces of the metals (both  $\gamma$ -TiAl and IN718) and their oxides were torn out during fretting, suggesting that the cohesive bonds in some of the contact areas of both metals fractured. SEM and EDS studies of wear debris produced under fretting verified the presence of metallic particles of both  $\gamma$ -TiAl and IN718. In the central region of the wear scars produced on the  $\gamma$ -TiAl there was generally a large, shallow pit, where  $\gamma$ -TiAl had torn out or sheared off and subsequently transferred to the IN718. The central regions of wear scars produced on the  $\gamma$ -TiAl and on the IN718 were morphologically similar (fig. 67), generally having wear debris, scratches, plastically deformed asperities, and cracks.

Figure 68 shows examples of surface damage: metallic wear debris of  $\gamma$ -TiAl and IN718, oxides and their debris, scratches (grooves), small craters, plastically deformed asperities, and cracks. The scratches (fig. 68(a)) can be caused by hard protuberances (asperities) on the IN718 surface (two-body conditions) or by wear particles between the surfaces (three-body conditions). The hard asperities and trapped wear particles plow or cut the  $\gamma$ -TiAl surface resulting in a severe form of wear (abrasion). The trapped wear particles have a scratching effect on both surfaces; and because they carry part of the load, they cause concentrated pressure peaks on both surfaces. The pressure peaks may well be the origin of crack nucleation in the oxide layers and the bulk alloys, both of which were observed on the wear surface of  $\gamma$ -TiAl.

Oxide layers readily formed on the  $\gamma$ -TiAl surface at 550 °C and reduced the wear problems. This is due to the additional lubricating properties of the oxides and the fact that the strong metal-to-metal adherence is avoided. However, the bulk  $\gamma$ -TiAl will deform elastically or plastically under fretting contact if the oxide is not hard enough to carry the load, and because of the deformation of the  $\gamma$ -substrate, cracks occurred in the oxide layer both within and around the contact area (fig. 68(b)). Fractures in the protective oxide layer produced cracks in the bulk  $\gamma$ -TiAl (fig. 68(c)) and also produced wear debris; chemically active, fresh surfaces; plastic deformation; and craters or fracture pits (fig. 68(d)). The wear debris caused third-body abrasive wear (fig. 68(a)). Local, direct contact between the fresh surfaces of the  $\gamma$ -TiAl and IN718 resulted in increased adhesion and local stresses, which may have caused plastic deformation, flakelike wear debris, and craters (e.g., the fracture pits in the  $\gamma$ -TiAl shown in fig. 68(d)).

Cross sections of a wear scar on the  $\gamma$ -TiAl revealed subsurface cracking and craters. For example, figure 69 shows propagation of subsurface cracks, nucleation of small cracks, formation of a large crater, and generation of debris. Cracks are transgranular and have no preferential alignment with microstructural features.

*Parameters influencing wear loss of Ti-47-2-2:* Figure 70 shows the wear volume loss measured by the optical interferometer as a function of the fretting frequency for the Ti-47-2-2 in contact with the IN718. Although there were some exceptions, the loss of wear volume generally decreased with increasing fretting frequency. A reasonable amount of material transfer from the  $\gamma$ -TiAl specimen to the IN718 specimen was observed at all frequencies. At the lowest frequency of 50 Hz a remarkable amount of plastic deformation (grooving) and surface roughening in the  $\gamma$ -TiAl wear scar were observed. At high frequencies wear scars were noticeably smooth with cracks in the  $\gamma$ -TiAl surface.

Temperature influences the adhesion, deformation, and fracture behaviors of contacting materials in relative motion. It is known that temperature interacts with the fretting process in two ways: first, the rate of oxidation or corrosion increases with temperature; and second, the mechanical properties of the materials, such as hardness, are also temperature dependent (ref. 24). Figure 71 presents the loss of wear volume measured by optical interferometry as a function of temperature for  $\gamma$ -TiAl in contact with the

IN718. The wear volume loss dropped to a minimum at 200 °C. The worn surface at 200 °C was predominantly oxidized and relatively smooth. A protective oxide film prevented direct metal-to-metal contact and ensured, in effect, that a mild oxidative wear regime prevailed. However, fretting wear increased as the temperature was increased from 200 to 550 °C. The highest temperatures of 450 and 550 °C resulted in a disruption of the oxide film, forming a crack and loose wear debris and causing pitting of the  $\gamma$ -TiAl wear surface.

Figure 72 shows the loss of wear volume measured by optical interferometry as a function of slip amplitude for the  $\gamma$ -TiAl in contact with IN718. The fretting wear volume loss was directly proportional to the slip amplitude, increasing as the slip amplitude increased. Increases in amplitude tended to produce more metallic wear debris, causing severe abrasive wear in the contacting metals. Figure 73 presents a three-dimensional optical interferometry image of the  $\gamma$ -TiAl wear scar at a slip amplitude of 200  $\mu\text{m}$  and a temperature of 25 °C. In the wear scar are grooves where the wear debris particles have scratched the  $\gamma$ -TiAl surface in the slip direction.

Figure 74 shows the measured loss of wear volume as a function of load for the  $\gamma$ -TiAl flats in contact with an IN718 pin at a temperature of 550 °C, a fretting frequency of 80 Hz, and a slip amplitude of 50  $\mu\text{m}$  for 1 million cycles. The fretting wear volume loss generally increased as the load increased; this generated more metallic wear debris in the contact area, the primary cause of abrasive wear in both the  $\gamma$ -TiAl and the IN718.

**Fretting fatigue.**—Fretted GEAE Ti-47-2-2 samples were subsequently fatigue tested to assess the effect of fretting on the fatigue strength.

*Fretting of fatigue samples:* Surface and subsurface damage always occurred on the interacting surfaces of the Ti-47-2-2 and IN718 during fretting in air. The surface damage of the  $\gamma$ -TiAl and IN718 consisted of material transfer and back transfer, pits, oxides and debris, scratches, fretting craters and wear scars, plastic deformation, and cracks. In general the damage of  $\gamma$ -TiAl is analogous to that of the IN718. Since the observation of surface and subsurface damage of  $\gamma$ -TiAl was already reported in the previous section, the damage of the IN718 contact pads will be primarily discussed below.

Figures 75(a) to (d) show examples of the surface damage produced on IN718: metallic wear debris of  $\gamma$ -TiAl and IN718, oxides, scratches (grooves), small craters, plastically deformed asperities, and cracks, all of which are similar to those observed on  $\gamma$ -TiAl. The scratches (fig. 75(a)) can be caused by hard, oxidized wear particles of the IN718 and  $\gamma$ -TiAl, which are trapped between the interacting surfaces or are adhered to or embedded in the counterpart  $\gamma$ -TiAl surface. In figure 75(a) scratches and fracture pits (craters) were produced by abrasion, a severe form of wear. The trapped wear particles and the adhered (or embedded) wear particles plow or cut the IN718 surface. The trapped wear particles have a scratching effect on both surfaces, and because they carry part of the load, they cause concentrated pressure peaks on both surfaces. The pressure peaks may well be the origin of crack nucleation in the oxide layers and the IN718. Oxide layers readily form on the IN718 surfaces at 550 °C and are often a favorable solution to wear problems. However, cracks occurred in the oxide layers both within and around the contact areas (fig. 75(b)), which may initiate subsequent fatigue cracks.

Fractures in the protective oxide layers produced cracks in the bulk IN718 (fig. 75(c)) and also produced wear debris, chemically active fresh surfaces, plastic deformation, craters, and fracture pits (fig. 75(d)). The wear debris can cause third-body abrasive wear. Local, direct contacts between the fresh surfaces of  $\gamma$ -TiAl and IN718 resulted in increased adhesion and local stresses, which may cause plastic deformation, flakelike wear debris, and craters.

All of the  $\gamma$ -TiAl fatigue specimens and the IN718 contact pads showed fretting damage. Typical damage observed on a  $\gamma$ -TiAl fatigue specimen at a low magnification is shown in figure 76. Because of the contact geometry, a long wear scar was produced perpendicular to the length of the fatigue specimen in the center of the gage section. In figure 76 the wear debris has been removed from the fatigue specimen surface to show the overall geometry of the wear scar. Figure 77 shows a typical example of a wear scar with wear debris from fretting produced on the  $\gamma$ -TiAl fatigue specimen in contact with an IN718 contact pad. Because of the specimen geometry, a large amount of wear debris is deposited just outside the line

contact area. Pieces of the  $\gamma$ -TiAl and its oxides are generally torn out or sheared off during fretting. Protective oxide layers readily form on both the  $\gamma$ -TiAl and IN718 at 550 °C in air. Cracks did occur in the oxide layers formed on the  $\gamma$ -TiAl and IN718 (figs. 78(a) and (b), respectively), and this limited the protection by these oxide layers. Figures 79(a) and (b) show examples of the  $\gamma$ -TiAl and IN718 surfaces that are torn out or sheared off during fretting. There are fractured pits, flakelike wear debris, and oxide wear particles in the contact areas of both the  $\gamma$ -TiAl and IN718 surfaces.

*Fatigue tests:* The results from the tests on prefretted fatigue samples are listed in table XIV and plotted versus the virgin samples in figure 80. The lives of the fretted samples are equivalent to those of the virgin samples. This was expected, since none of the fatigue samples failed at the fret, but failed elsewhere in the gage. Metallographic samples were taken to view the thickness of the sample and hence the depth and type of damage from the frets. An example of the fretted area is shown in figure 81. A slight depression approximately 3  $\mu\text{m}$  deep was observed on the gage surface from the fretting process. No cracks were observed as a result of the fret in the metallographic samples. Thus, the fretting conditions used were too mild to produce cracks and influence the residual fatigue strength. Noting that even some of the impacted samples did not fail at the impact site and that these had cracks several hundred microns in length, it is not to be expected that a mere 3- $\mu\text{m}$ -deep depression would influence the fatigue strength of the  $\gamma$ -TiAl. This suggests that either  $\gamma$ -TiAl is not as sensitive to surface defects as originally expected, and/or that more severe defects were elsewhere in the samples. Simultaneous fretting and fatigue may have produced more severe damage and degraded the fatigue life had the in situ method been pursued. The results presented here are encouraging as they suggest good wear resistance in  $\gamma$ -TiAl. Also, the pin-on-flat results show superior wear resistance of  $\gamma$ -TiAl over Ti-6Al-4V.

## Summary of Results

This is the programmatic final report addressing durability of  $\gamma$ -TiAl alloys. The purpose of this research was to support the application of  $\gamma$ -TiAl alloys as LPT blades in aircraft engines. Seven cast alloys and one wrought alloy were evaluated to assess their ballistic impact resistance—a key barrier to their application. Cracking severity was documented and related to a number of specimen and impact variables. The crack type and length were predicted analytically using FEM. Impacted fatigue specimens were subjected to HCF using the step test method. The amount of degradation in the fatigue strength was measured. The fatigue strength was predicted using a threshold-based fracture mechanics approach. Fretting resistance of one  $\gamma$ -TiAl alloy was also evaluated and a small number of fatigue tests were conducted on fretted samples. This study showed that

1. TiAl can survive a relatively large impact and is tolerant of relatively large amounts of casting porosity.
2. There is a minimum specimen (blade) thickness at which some impact can be tolerated without cracking.
3. Crack type and severity correlated primarily with impact energy  $E$ . The location of impact  $X$  also played a significant role. Alloy chemistry was not an important variable in determining the severity of impact damage.
4. The machined sample geometry is a suitable replacement for the more expensive cast-to-size specimen. Cracking morphologies in each sample design were similar for similar impact conditions.
5. The slight variation in Al content for a nominal Ti-48Al-2Cr-2Nb alloy is insignificant with respect to impact properties.
6. All seven alloys had comparable postimpact fatigue resistance, in spite of their varying tensile properties and microstructures. However, the fatigue strengths of virgin samples from the CMU Ti-47-2-2 and ABB-23 materials appeared superior. The remaining five alloys had comparable virgin fatigue strengths, in spite of their varying tensile properties and microstructures.

7. Analytical models were successful in predicting the impact crack severity by utilizing a set of cracking criteria involving the von Mises stress, the von Mises plastic strain, and a tensile stress parallel to the specimen axis.
8. The alloys exhibited a classic mean stress dependence of the fatigue strength. The fatigue strength for specimens impacted at similar energies were affected similarly by a tensile mean stress. This allowed data to be grouped by impact energy level in a Goodman Diagram and lines extrapolated across mean stresses to a point on the abscissa between the YS and UTS.
9. NDE methods were effective at identifying critical casting flaws in Ti-48-2-2, but often led to a prediction of conservative fatigue strengths based on an overestimated flaw size. Accurate representation of the flaw size, particularly casting defects, was necessary to accurately predict the fatigue strength.
10. Fatigue strength was correlated with defect length and area as expected from fracture mechanics.
11. A threshold-based fracture mechanics approach successfully predicted residual fatigue strengths based on the flaw size. Back-calculated fatigue crack thresholds were found to be in the  $9 \text{ MPa}\sqrt{\text{m}}$  regime. These thresholds agreed with values from the literature for related alloys.
12. Fretting was unable to produce sufficient damage to degrade the residual fatigue strength.
13. The  $\gamma$ -TiAl has superior wear resistance compared to Ti-6Al-4V.

## Concluding Remarks

This study has shown that despite having limited ductility,  $\gamma$ -TiAl alloys are able to withstand a relatively large impact without failing catastrophically. All of the alloys examined, regardless of their tensile strength or ductility, exhibited similar damage resulting from ballistic impacts. Over the range of impact energies expected in standard engine operations, the resulting damage in  $\gamma$ -TiAl is such that the defect would remain noncritical for the expected design service loads. Thus impact resistance is removed as a potential barrier for introducing these early generation TiAl alloys as LPT blades. However, it should be stated that the higher strength of future  $\gamma$ -TiAl alloys will result in a smaller critical defect size, and damage tolerance could become an issue. Gamma TiAl was also shown to have good wear resistance in contact against IN718 reducing the likelihood of fretting damage in dovetail applications with these alloys.

The use of fracture mechanics was shown to be a useful tool for damage tolerant design: the fatigue strength can be easily predicted, having accurate knowledge of the flaw size and assuming that the fatigue crack threshold  $K_{th}$  is well known for the alloy, an assumption that was not realized in this study. Obviously, improvement of the damage tolerance of these alloys would necessitate a larger  $K_{th}$ . It is not clear from this study how this improvement would be accomplished. These results suggest that a more refined and uniform grain size may be beneficial, as evidenced by both the high  $K_{th}$  and the highest virgin fatigue strength in the ABB-23 alloy. Higher tensile ductilities also seem to lead to apparent high  $K_{th}$  values, perhaps through the additional plastic deformation at the impact site and the influence of the incurred plasticity on the crack tip. Further investigations are required in this area, as the current study was not able to distinguish the relationship between microstructural, tensile, and fatigue properties. These relationships were often obscured by conflicting variables. The most significant nuisance variable was the large lamellar colonies in most of the alloys, including the one wrought material. It is therefore recommended that this line of research be pursued further once more refined microstructures are available.

## References

1. Austin, C.M.; and Kelly, T.J.: Progress in Implementation of Cast Gamma Titanium Aluminide. Gamma Titanium Aluminides, Y.W. Kim, R. Wanger, and M. Yamaguchi, eds., TMS, Warrendale, PA, 1995, pp. 21–32.
2. Erdmann, O., et al.: Affordable Processes for Manufacturing Gamma Titanium Aluminide Engine Components. NASA Contract NCC3–416—Final Report for period 10 July 1995 through 31 Dec. 1998, 2000. Available from the NASA Center for Aerospace Information.
3. Draper, S.L., et al.: The Effect of Ballistic Impacts on the High-Cycle Fatigue Properties of Ti-48Al-2Nb-2Cr (Atomic Percent). Metall. Mater. Trans. A—Phys. Metall. Mater. Sci., vol. 32, no. 11, 2001, pp. 2743–2758.
4. Draper, S.L., et al.: Effect of Impact Damage on the Fatigue Response of TiAl Alloy-ABB-2. Structural Intermetallics 2001, K.J. Hemker et al., eds., TMS, Warrendale, PA, 2001, pp. 295–304.
5. Austin, C.M., et al.: Aircraft Engine Applications for Gamma Titanium Aluminide. Structural Intermetallics 1997, M.V. Nathal et al., eds., TMS, Warrendale, PA, 1996, pp. 413–425.
6. Larsen, J.M., et al.: An Overview of the Structural Capability of Available Gamma Titanium Aluminide Alloys. Gamma Titanium Aluminides, Y.W. Kim, R. Wagner, and M. Yamaguchi, eds., TMS, Warrendale, PA, 1995, pp. 821–834.
7. Collins, J.A.: Failure of Materials in Mechanical Design: Analysis, Prediction, Prevention. Second ed., John Wiley & Sons, New York, NY, 1993.
8. Denk, J.; and Amhof, S.: Determination of the High Cycle Fatigue Strength With a Load-Increasing Single-Specimen Technique. Fatigue '96: Proceedings of the Sixth International Fatigue Congress. Elsevier Science, Inc., New York, NY, 1996, pp. 1967–1972.
9. Sinclair, G.M.: An Investigation of the Coaxing Effect in Fatigue of Metals. Proc. ASTM, vol. 52, 1952, pp. 743–758.
10. Lerch, B.A.; Draper, S.L.; and Pereira, J.M.: Conducting High-Cycle Fatigue Strength Step Tests on Gamma TiAl. Metall. Mater. Trans. A—Phys. Metall. Mater. Sci., vol. 33, no.12, 2002, pp. 3871–3874.
11. Chakravarty, S., et al.: The Effect of Surface Modification on Fretting Fatigue in Ti Alloy Turbine-Components. JOM J. Min. Met. Mater. Soc., vol. 47, no. 4, 1995, pp. 31–35.
12. VanStone, R.H.; Lawless, B.H.; and Hartle, M.: Fretting in Ti-6Al-4V at Room Temperature. Paper presented at the 5th National Turbine Engine High Cycle Fatigue (HCF) Conference, Chandler, AZ, Mar. 2000.
13. Hoepfner, David; Adibnazari, Saeed; and Moesser, Mark W.: Literature Review and Preliminary Studies of Fretting and Fretting Fatigue Including Special Applications to Aircraft Joint (Final Report). DOT/FAA/CT–93/2, 1994.
14. Hutson, A.L.; and Nicholas, T.: Fretting Fatigue Behavior of Ti-6Al-4V Under Flat-on-Flat Contact With Blending Radii. ASTM STP 1367, 2000, pp. 308–321.
15. Miyoshi, K.: Aerospace Mechanisms and Tribology Technology—Case Study. Tribol. Int., vol. 32, no. 11, 1999, pp. 673–685.
16. Miyoshi, K., et al.: Sliding Wear and Fretting Wear of Diamondlike Carbon-Based, Functionally Graded Nanocomposite Coatings. Wear, pt. 1, vol. 229, 1999, pp. 65–73.
17. Miyoshi, K.: Considerations in Vacuum Tribology (Adhesion, Friction, Wear, and Solid Lubrication in Vacuum). Tribol. Int., vol. 32, no. 11, 1999, pp. 605–616.
18. Tallian, T.E.: Fretting Wear. Failure Atlas for Hertz Contact Machine Elements, ASME Press, New York, NY, 1992, pp. 141–143.
19. Waterhouse, R.B.: Plastic Deformation in Fretting Processes—A Review. ASTM STP 1367, 2000, pp. 3–18.

20. Waterhouse, R.B.: Occurrence of Fretting in Practice and Its Simulation in the Laboratory. Proceedings of the Materials Evaluation Under Fretting Conditions Symposium, ASTM STP 780, 1982, pp. 3–16.
21. Kusner, D.; Poon, C.; and Hoepfner, D.W.: A New Machine for Studying Surface Damage Due to Wear and Fretting. Proceedings of the Materials Evaluation Under Fretting Conditions Symposium, ASTM STP 780, 1982, pp. 17–29.
22. Satoh, T.: Influence of Microstructure on Fretting Fatigue Behavior of a Near-Alpha Titanium Alloy. ASTM STP 1367, 2000, pp. 295–307.
23. Lutynski, C.; McEvily, A.J.; and Simansky, G.: Fretting Fatigue of Ti-6Al-4V Alloy. Proceedings of the Materials Evaluation Under Fretting Conditions Symposium, ASTM, Philadelphia, PA, 1982, pp. 150–164.
24. Bill, R.C.: Review of Factors That Influence Fretting Wear. Proceedings of the Materials Evaluation Under Fretting Conditions Symposium, ASTM, Philadelphia, PA, 1982, pp. 165–182.
25. Hansson, T., et al.: High Temperature Fretting Fatigue Behavior in an XD  $\gamma$ -Base TiAl. ASTM STP 1367, 2000, pp. 65–79.
26. Steif, Paul S.; and McKenna, Volus T.: Surface and Foreign Object Damage. PRET: A University-Industry Partnership Research and Transition of Gamma Titanium Aluminides (Final Report), Tresa M. Pollock and Paul S. Steif, eds., Carnegie Institute of Technology, Pittsburgh, PA, 1999, pp. 7–1 to 7–13.
27. MSC.Patran 2001. MSC.Software Corp., Santa Ana, CA, 2001.
28. ABAQUS/Explicit. Version 5.8, Hibbit, Karlsson and Sorensen, Inc., Pawtucket, RI, 1998.
29. McKenna, V.T., et al.: Cracking in  $\gamma$ -TiAl Due to High Speed Particle Impact. Metall. Mater. Trans. A—Phys. Metall. Mater. Sci., vol. 33, no. 3, 2002, pp. 581–589.
30. Steif, P.S., et al.: Damage in Gamma Titanium Aluminides Due to Small Particle Impact. J. Mech. Phys. Solids, vol. 46, no. 10, 1998, pp. 2069–2086.
31. Zerilli, F.J.; and Armstrong, R.W.: Dislocation-Mechanics-Based Constitutive Relations for Material Dynamics Calculations. J. Appl. Phys., vol. 61, no. 5, 1987, pp. 1816–1825.
32. Hertz, Heinrich: Hertz's Miscellaneous Papers, chs. 5 and 6, Macmillan, London, 1896.
33. Wright, P.K., et al.: Defect Behavior in Gamma Titanium Aluminides. Structural Intermetallics 2001, K.J. Hemker et al., 2001, pp. 315–322.
34. Recina, V.; and Karlsson, B.: High Temperature Low Cycle Fatigue Properties of Ti-48Al-2W-0.5Si Gamma Titanium Aluminide. Mater. Sci. Eng., vol. 262, nos. 1–2, 1999, pp. 70–81.
35. Harding, Trevor S., et al.: Fatigue Behavior of Gamma TiAl. PRET: A University-Industry Partnership Research and Transition of Gamma Titanium Aluminides (Final Report). Tresa M. Pollock and Paul S. Steif, eds., Carnegie Institute of Technology, Pittsburgh, PA, 1999, pp. 8–1 to 8–23.
36. Nicholas, T.: Step Loading, Coaxing and Small Crack Thresholds in Ti-6Al-4V Under High Cycle Fatigue. Fatigue: David L. Davidson Symposium, TMS, Warrendale, PA, 2002, pp. 91–106.
37. Kumpfert, J.; Kim, Y.W.; and Dimiduk, D.M.: Effect of Microstructure on Fatigue and Tensile Properties of the Gamma-TiAl Alloy Ti-46.5Al-3.0Nb-2.1Cr-0.2W. Mater. Sci. Eng., vol. 193, 1995, pp. 465–473.
38. Lerch, Bradley A., et al.: Effect of Defects on the Fatigue Life of Gamma-TiAl. HITEMP Review 1999: NASA/CP—1999-208915, 1999, paper no. 30. Available from the NASA Center for Aerospace Information.
39. Nazmy, M., et al.: Effect of Surface Defects on the Fatigue Behavior of a Cast TiAl Alloy. High-Temperature Ordered Intermetallic Alloys IX, MRS, Warrendale, PA, 2001, pp. N5.44.1–N5.44.6.
40. Harding, T.S.; and Jones, J.W.: The Effect of Impact Damage on the Room-Temperature Fatigue Behavior of Gamma-TiAl. Metall. Mater. Trans. A—Phys. Metall. Mater. Sci., vol. 31, no. 7, 2000, pp. 1741–1752.

41. Smith, R., et al.: The Role of Impact Damage and Fatigue Strength Reduction in Gamma Titanium Aluminide Alloys. *Structural Intermetallics 2001*, K.J. Hemker et al., TMS, Warrendale, PA, 2001, pp. 259–268.
42. Kitagawa, H.; and Takahashi, S.: Applicability of Fracture Mechanics to Very Small Cracks or the Cracks in the Early Stage. *Proceedings of the Second International Conference on Mechanical Behavior of Materials*, ASM, Metals Park, OH, 1976, pp. 627–631.
43. Newman, J.C., Jr.; and Raju, I.S.: Stress-Intensity Factor Equations for Cracks in Three-Dimensional Finite Bodies. *ASTM STP 791*, 1983, pp. 238–265.
44. Tada, Hiroshi; Paris, Paul C.; and Irwin, George R.: The Single Edge Notch Test Specimen. *The Stress Analysis of Cracks Handbook*. Second ed., Paris Productions, Inc., St. Louis, MO, 1985, pp. R.1–R.25.
45. Murakami, Y., et al., eds.: An Edge Crack Having Different Length at Front and Back Surface. *Stress Intensity Factors Handbook*, Pergamon, Oxford, 1987, p. 837.
46. Brown, William F., Jr.; Mindlin, Harold; and Ho, C.Y., eds.: Aluminum Alloys; Cast (AIC–3100). *Aerospace Structural Metals Handbook*, Purdue University, West Lafayette, IN, 1997.
47. Properties and Selection of Metals. *Metals Handbook*, ASM, Metals Park, OH, 1961, pp. 130 and 385.
48. *Metallic Materials and Elements for Aerospace Vehicle Structures*. MIL–HDBK–5G, vols. 1 and 2, 1994.
49. Trail, S.J.; and Bowen, P.: Effects of Stress Concentrations on the Fatigue Life of a Gamma-Based Titanium Aluminide. *Mater. Sci. Eng. A*, vol. 192, nos. 1–2, 1995, pp. 427–434.
50. Wu, X.H., et al.: Micro-Yield and the Fatigue Limit of TiAl Alloys. *Structural Intermetallics 2001*, K.J. Hemker et al., eds., TMS, Warrendale, PA, 2001, pp. 289–294.
51. Hamada, S., et al.: Microstructure and Environment-Dependent Fatigue Crack Propagation Properties of Ti-48Al Intermetallics. *J. Mater. Sci.*, vol. 37, no. 6, 2002, pp. 1107–1113.
52. Lupinc, V., et al.: Creep, Fatigue and Crack Propagation Behavior of a New Industrially Developed Gamma-TiAl Alloy. *Structural Intermetallics 2001*, K.J. Hemker et al., eds., TMS, Warrendale, PA, 2001, pp. 709–716.
53. Wang, P., et al.: An In-Situ Study of Crack Propagation in Binary Lamellar TiAl. *High-Temperature Ordered Intermetallic Alloys IX*, MRS, Warrendale, PA, 2001, pp. N1.9.1–N1.9.6.
54. Chan, K.S.; and Shih, D.S.: Fundamental Aspects of Fatigue and Fracture in a TiAl Sheet Alloy. *Metall. Mater. Trans. A—Phys. Metall. Mater. Sci.*, vol. 29A, no. 1, 1998, pp. 73–87.
55. Bowen, P.; Chave, R.A.; and James, A.W.: Cyclic Crack Growth in Titanium Aluminides. *Mater. Sci. Eng. A*, vol. 192, nos. 1–2, 1995, pp. 443–456.
56. Ritchie, R.O.; Kruzic, J.J.; and Campbell, J.P.: On the Fatigue Behavior of Gamma-Based Titanium Aluminides: Role of Small Cracks. *Acta Materialia*, vol. 47, no. 3, 1999, pp. 801–816.
57. Evangelista, E., et al.: Toughening Mechanism in the Lamellar and Duplex TiAl-Based Alloys at Ambient Temperature: Microcrack Analysis. *Scrip. Metal.*, vol. 33, no. 3, 1995, pp. 467–472.
58. Lipsitt, H.A.; Blackburn, M.J.; and Dimiduk, D.M.: Commercializing Intermetallic Alloys: Seeking a Complete Technology. TMS, Warrendale, PA, 2001, pp. 73–82.
59. El Haddad, M.H.; Smith, K.N.; and Topper, T.H.: Fatigue Crack Propagation of Short Cracks. *ASME Paper 78–MAT–7*, vol. 101, 1979, pp. 42–46.
60. Rosenberger, A.H.; Worth, B.D.; and Balsone, S.J.: Environmental Effects on the Fatigue Crack Growth of Gamma Titanium Aluminides. *Fatigue '96: Proceedings of the Sixth International Fatigue Congress*. Elsevier Science, Inc., New York, NY, 1996, pp. 1785–1790.
61. Rao, K.T.V.; Kim, Y-W.; and Ritchie, R.O.: High-Temperature Fatigue-Crack Growth Behavior in a Two-Phase ( $\gamma + \alpha_2$ ) TiAl Intermetallic Alloy. *Scrip. Metal.*, vol. 33, no. 3, 1995, pp. 459–465.

62. Venkateswara Rao, K.T., et al.: Fatigue-Crack Growth and Fracture Resistance of a Two-Phase ( $\gamma + \alpha_2$ ) TiAl Alloy in Duplex and Lamellar Microstructures. *Mater. Sci. Eng. A*, vol. 192, nos. 1–2, 1995, pp. 474–482.
63. Balsone, S.J., et al.: Effects of Microstructure and Temperature on Fatigue Crack Growth in the TiAl Alloy Ti-46.5Al-3Nb-2Cr-0.2W. *Mater. Sci. Eng. A*, vol. 192, nos. 1–2, 1995, pp. 457–464.
64. Harding, T.S.; and Jones, J.W.: Fatigue Thresholds of Cracks Resulting From Impact Damage to  $\gamma$ -TiAl. *Scrip. Mater.*, vol. 43, no. 7, 2000, pp. 623–629.
65. Harding, T.S.; and Jones, J.W.: Effect of Foreign Object Damage on the Fatigue Strength of an XD  $\gamma$ -TiAl Alloy. *Scrip. Mater.*, vol. 43, no. 7, 2000, pp. 631–636.

TABLE I.—AVERAGE TENSILE PROPERTIES OF FRETTING MATERIALS

Alloy	Temperature, °C	Modulus, GPa	Ultimate tensile strength, MPa
GEAE Ti-47Al-2Cr-2Nb	25	170	536
	650	140	---
Ti-6Al-4V <sup>a</sup>	25	112	900
	650	90	630
IN718 <sup>a</sup>	25	206	1434
	650	169	1160

<sup>a</sup>Ref. 49

TABLE II.—SURFACE ROUGHNESS AND VICKERS HARDNESS OF FRETTING SPECIMENS

Specimen	Centerline-average roughness, $R_a$ nm		Vickers hardness, <sup>a</sup> $H_v$ GPa	
	Mean	Standard deviation	Mean	Standard deviation
<b>Pins (hemispherical)</b>				
IN718, 9.4-mm diameter	40	8.9	5.52	0.44
GEAE Ti-47Al-2Cr-2Nb, 6-mm diameter	42	7.1	4.12	0.42
Ti-6Al-4V, 9.4-mm diameter	83	2.0	3.85	0.092
<b>Flats</b>				
GEAE Ti-47Al-2Cr-2Nb	35	3.3	3.78	0.57
IN718	18	7.2	4.78	0.21
<b>Low-cycle fatigue sample</b>				
GEAE Ti-47Al-2Cr-2Nb	370	49	3.78	0.57
<b>Wedges</b>				
IN718, two-sided with 12-mm-long knife edge	2750	65	4.85	0.28
IN718, wedgelike shape with rectangular flat	419	42	4.78	0.21

<sup>a</sup>Load, 1 N.

TABLE III.—GEAE Ti-47-2-2 FRETTING TEST CONDITIONS

(a) Fatigue specimen 063-03-3

9.4-mm-diameter spherical pin .....	IN718
Environment .....	air at 25 °C
Load, N .....	1.5 for first 600 000 cycles, then 3.0 for 6.4 million cycles
Frequency, Hz .....	81
Slip amplitude, $\mu\text{m}$ .....	50
Total number of cycles .....	7 million
Fretting direction .....	in the direction of fatigue loading

(b) Fatigue specimen 6-3-3

Fretting on front side	
Knife-edge-shaped contact pad .....	IN718
Environment .....	air at 550 °C
Load, N .....	1.5 to 3.0
Frequency, Hz .....	80 for first 20 million cycles, then 160 for 80 million cycles
Slip amplitude (mean value), $\mu\text{m}$ .....	50
Total number of cycles .....	100 million
Fretting direction .....	perpendicular to the direction of fatigue loading
Fretting on back side	
Knife-edge-shaped contact pad .....	IN718
Environment .....	air at 550 °C
Load, N .....	1.5 to 3.0
Frequency, Hz .....	80
Slip amplitude (mean value), $\mu\text{m}$ .....	50
Total number of cycles .....	40 million
Fretting direction .....	perpendicular to the direction of fatigue loading

(c) Fatigue specimen 5-1-3

Fretting on front side	
Knife-edge-shaped contact pad .....	IN718
Environment .....	air at 550 °C for 36 million cycles, then 25 °C for 73 million cycles
Load, N .....	1.5 to 3.0
Frequency, Hz .....	160
Slip amplitude (mean value), $\mu\text{m}$ .....	50
Total number of cycles .....	109 million
Fretting direction .....	in the direction of fatigue loading
Fretting on back side	
Knife-edge-shaped contact pad .....	IN718
Environment .....	air at 550 °C for 109 million cycles, then 25 °C for 42 million cycles
Load, N .....	1.5 to 3.0
Frequency, Hz .....	160
Slip amplitude (mean value), $\mu\text{m}$ .....	50
Total number of cycles .....	151 million
Fretting direction .....	in the direction of fatigue loading

(d) Fatigue specimen 5-1-6

Fretting on front side	
Wedgelike contact pad with rectangular flat .....	IN718
Environment .....	air at 550 °C
Load, N .....	450
Frequency, Hz .....	80
Slip amplitude (mean value), $\mu\text{m}$ .....	90
Total number of cycles .....	16 million
Fretting direction .....	in the direction of fatigue loading
Fretting on back side	
Wedgelike contact pad with rectangular flat .....	IN718
Environment .....	air at 25 °C
Load, N .....	450
Frequency, Hz .....	80
Slip amplitude (mean value), $\mu\text{m}$ .....	90
Total number of cycles .....	16 million
Fretting direction .....	in the direction of fatigue loading

TABLE IV.—TEST DETAILS USED IN FINITE-ELEMENT MODELING AND ANALYSIS

Sample number	Impact location, <sup>a</sup> X, mm	Impact energy, E, J	Velocity, m/sec	Specimen			Projectile	
				Width, mm	Thickness, mm	Number of finite elements	Diameter, mm	Number of finite elements
008-10-3	0.64	0.20	155	25.4	3.7	30 000	1.6	7248
005-08-3	0.60	0.68	287	25.4	3.7	30 000	1.6	7248
009-08-2	0.70	1.50	151	25.4	3.7	30 000	3.2	7488

<sup>a</sup>Distance from leading edge.

TABLE V.— $\gamma$ -TiAl ALLOY CHEMISTRIES

Alloy	Composition, at. %									
	Ti	Al	Cr	Nb	W	Ta	Si	C	O	B
Cast-to-size Ti-48-2-2	48.4	47.5	1.87	1.97				0.019	0.212	
GEAE Ti-47-2-2	48.7	47.1	1.91	2.02				0.045	0.167	
CMU Ti-47-2-2	49.4	46.5	2.00	1.90					0.192	
Howmet Ti-47-2-2	49.7	46.4	1.82	1.82					0.176	
Cast-to-size ABB-2	50.6	46.5			2.28		0.48		0.085	
ABB-23	50.6	46.0			1.99		0.48	0.017	0.122	0.65
NCG359E	48.7	46.8	1.64	0.68		1.73		0.030	0.211	
95A	48.0	47.0	2.00	2.50	0.2				0.170	0.12

TABLE VI.— $\gamma$ -TiAl ALLOY MICROSTRUCTURE

Alloy	Lamellar volume fraction	Gamma grain size, $\mu\text{m}$	Lamellar colony size, $\mu\text{m}$
Cast-to-size Ti-48-2-2	0.39 $\pm$ 0.06	64.0 $\pm$ 2.3	
GEAE Ti-47-2-2	0.65 $\pm$ 0.04	60.3 $\pm$ 3.3	
CMU Ti-47-2-2	0.65 $\pm$ 0.04	58.2 $\pm$ 4.4	
Howmet Ti-47-2-2	Non-uniform, but nearly lamellar	Irregular, bimodal	Large, columnar colonies near edge
Cast-to-size ABB-2	Variable. Nearly fully lamellar near edge, duplex in center	Irregular	Large, columnar colonies near edge
ABB-23	~1		58.5 $\pm$ 3.2
NCG359E	0.68 $\pm$ 0.11	69.4 $\pm$ 7.1	
95A	~1		288 $\pm$ 21.4

TABLE VII.—AVERAGE TENSILE PROPERTIES FOR  $\gamma$ -TiAl ALLOYS

Alloy	Temperature, $^{\circ}\text{C}$	Yield strength, MPa	Tensile strength, MPa	Elongation, percent	Elastic modulus, GPa
Cast-to-size Ti-48-2-2	23	326	422	1.70	168
	650	284	474	5.10	141
GEAE Ti-47-2-2	23	458	536	1.42	172
	650	----	----	----	----
CMU Ti-47-2-2	23	433	499	1.00	187
	650	359	552	4.10	166
Howmet Ti-47-2-2	23	449	516	0.99	151
	650	353	526	2.76	128
Cast-to-size ABB-2	23	504	599	0.89	173
	650	413	571	1.97	147
ABB-23	23	528	589	0.58	189
	650	440	532	1.07	156
NCG359E	23	422	482	1.01	161
	650	359	524	3.65	171
95A	23	417	547	1.12	149
	650	331	587	3.93	146

TABLE VIII.—IMPACT CONDITIONS

(a) Cast-to-size Ti-48-2-2

[Three impacts per specimen at 70 MPa stress and 260 °C.]

Sample <sup>a</sup>	Projectile size, mm	Velocity, m/sec	Impact energy, $E_i$ , J	Impact location, $X_i$ , mm	Crack length, <sup>c</sup> mm				
					FS major	FS total	HZ <sup>d</sup>	BS straight <sup>d</sup>	BS total
006-10-1	1.6	173	0.25	0.70	0.68	4.03	0.54	0.78	1.13
006-10-2		170	.24	.77	.48	4.61	.34	<b>1.09</b>	1.88
006-10-3		158	.21	.59	1.20	5.16	.79	.49	.83
008-10-1	1.6	148	0.18	0.60	0	3.88	0.20	0.79	1.11
008-10-2		163	.22	.64	1.46	4.05	.41	<b>.78</b>	1.08
008-10-3		155	.20	.64	.48	3.88	.30	.40	.39
007-12-1	1.6	200	0.33	1.45	0	2.92	0.20	<b>1.46</b>	1.80
007-12-2		210	.36	1.53	0	1.27	.34	1.10	1.08
007-12-3		215	.38	.71	1.06	5.89	.60	1.09	1.49
005-01-1	1.6	215	0.38	0.48	1.50	8.70	0.74	0.69	1.47
005-01-2		217	.39	.55	1.77	4.37	.39	.62	1.53
005-01-3		217	.39	.68	1.49	4.69	.88	<b>.72</b>	.96
005-08-1	1.6	282	0.65	0.57	3.46	7.90	0.66	1.01	1.96
005-08-2		294	.71	.66	3.74	7.77	.60	1.13	3.65
005-08-3		287	.68	.60	3.43	6.92	.88	<b>1.10</b>	2.63
011-03-1	1.6	300	0.74	0.57	5.86	8.23	<b>1.59</b>	1.25	3.02
011-03-2		301	.74	.58	4.21	9.03	.89	1.29	4.44
011-03-3		301	.74	.75	3.44	6.72	1.00	1.26	2.59
009-03-1	1.6	378	1.17	0.49	5.95	7.89	1.45	0.98	1.48
009-03-2		392	1.26	.46	6.03	9.52	<b>1.73</b>	.87	2.69
009-03-3		380	1.19	.69	6.26	11.33	1.46	1.40	3.56
010-09-1	3.2	124	1.00	0.73	4.18	7.43	1.19	1.59	3.07
010-09-2		124	1.00	.80	4.64	11.36	<b>2.47</b>	1.69	3.56
010-09-3		124	1.01	.80	4.32	8.87	1.96	1.80	3.07
006-06-1	3.2	126	1.04	0.58	6.50	10.03	<b>1.89</b>	1.45	4.11
006-06-2		128	1.07	.62	7.53	11.31	1.29	1.22	4.94
006-06-3		126	1.05	.59	5.18	7.58	1.14	1.55	2.82

<sup>a</sup>The "1," "2," and "3" designate site of impact as shown on figure 1.

<sup>b</sup>Distance from leading edge.

<sup>c</sup>FS is front-side, HZ is Hertzian, and BS is back-side.

<sup>d</sup>Bold entries denote location of critical fatigue crack.

TABLE VIII.—CONTINUED. IMPACT CONDITIONS

(a) Continued. Cast-to-size Ti-48-2-2

[Three impacts per specimen at 70 MPa stress and 260 °C.]

Sample <sup>a</sup>	Projectile size, mm	Velocity, m/sec	Impact energy, E, J	Impact location, X, mm	Crack length, ° mm				
					FS major	FS total	HZ <sup>d</sup>	BS straight <sup>d</sup>	BS total
009-08-1	3.2	151	1.50	0.64	7.32	12.63	3.66	1.94	4.36
009-08-2	3.2	151	1.50	.70	7.61	9.83	4.17	2.03	3.97
009-08-3	3.2	154	1.55	.60			<b>3.79</b>	4.59	
011-09-1	3.2	153	1.54	0.53	9.28	13.16	3.67	1.55	5.69
011-09-2	3.2	154	1.55	.57	7.55	9.54	<b>3.33</b>	1.62	6.54
011-09-3	3.2	152	1.52	.44			2.70	3.35	
010-02-1	1.6	291	0.70	0.55	4.02	7.71	0.73	1.05	2.39
010-02-2	1.6	297	.72	.63	3.49	6.77	1.20	1.18	2.79
010-02-3	1.6	281	.65	.74	1.28	4.45	.72	<b>1.00</b>	3.42
008-05-1	1.6	294	0.71	0.65	2.49	7.44	0.67	<b>1.14</b>	1.76
008-05-2	1.6	294	.71	.62	1.99	8.26	.48	1.08	2.79
008-05-3	1.6	294	.71	.50	4.17	7.88	.86	1.08	2.74
010-05-1	1.6	297	0.72	0.43	4.24	7.71	0.37	.64	2.37
010-05-2	1.6	290	.69	.62	2.21	6.91	.47	0.95	2.81
010-05-3	1.6	294	.71	.51	4.09	7.68	.74	<b>1.02</b>	2.27
011-10-1	1.6	295	0.72	0.53	3.38	7.13	0.81	.98	1.61
011-10-2	1.6	295	.72	.62	3.35	6.52	.89	<b>1.10</b>	2.39
011-10-3	1.6	298	.73	.42	3.70	6.11	.89	.92	2.25
008-01-01	1.6	271	0.60	0.60	2.83	5.62	0.52	<b>0.94</b>	1.97
008-01-02	1.6	282	.65	.63	4.82	7.37	.36	1.13	2.15
008-01-03	1.6	291	.70	.47	3.84	6.99	.28	.96	2.16
009-12-1	1.6	297	0.72	0.48	2.91	6.48	0.48	.83	2.67
009-12-2	1.6	294	.71	.53	3.20	6.98	.70	0.98	2.22
009-12-3	1.6	295	.71	.55	1.89	5.50	.65	<b>1.08</b>	1.94
007-01-1	1.6	304	0.76	0.51	5.30	6.91	1.33	.88	2.59
007-01-2	1.6	289	.68	.52	3.03	6.29	.30	<b>1.12</b>	1.36
007-01-3	1.6	293	.70	.44	3.78	8.39	.63	.84	2.43

<sup>a</sup>The "1," "2," and "3" designate site of impact as shown on figure 1.

<sup>b</sup>Distance from leading edge.

<sup>c</sup>FS is front-side, HZ is Hertzian, and BS is back-side.

<sup>d</sup>Bold entries denote location of critical fatigue crack.

TABLE VIII.—CONTINUED. IMPACT CONDITIONS

(a) Continued. Cast-to-size Ti-48-2-2

Sample <sup>a</sup>	Projectile size, mm	Velocity, m/sec	Impact energy, E <sub>i</sub> , J	Impact location, <sup>b</sup> X, mm	Crack length, <sup>c</sup> mm				
					FS major	FS total	HZ <sup>d</sup>	BS straight <sup>d</sup>	BS total
011-02-1	1.6	300	0.74	0.50	3.26	6.57	0.44	<b>0.87</b>	2.60
011-02-2		293	.70	.50	4.62	6.01	2.29	.80	2.11
011-02-3		302	.75	.50	2.35	5.90	1.63	.80	1.98
007-06-1	1.6	302	0.75	0.54	3.06	6.93	0.99	1.18	1.28
007-06-2		287	.68	.52	3.33	6.39	.71	1.11	2.37
007-06-3		293	.70	1.88	0	1.52	.29	<b>2.69</b>	4.42
005-02-1	1.6	297	0.72	0.59	2.83	6.65	0.70	0.32	0.86
005-02-2		297	.72	.51	3.09	7.39	.51	.39	1.16
005-02-3		300	.74	.84	2.82	7.06	1.05	<b>1.02</b>	2.86
006-09-1	1.6	294	0.71	0.45	3.85	5.94	0.91	0.78	2.71
006-09-2		295	.72	.57	4.76	7.26	1.26	1.00	2.62
006-09-3		294	.71	.50	1.97	5.92	.46	.77	1.65
009-07-1	1.6	291	0.70	0.61	3.04	7.11	0.76	1.15	2.58
009-07-2		290	.69	.61	3.09	7.24	.82	<b>1.07</b>	1.41
009-07-3		289	.68	.25	1.74	4.42	1.02	.85	1.73
009-05-1	3.2	150	1.48	0.59	6.88	11.12	2.45	1.58	7.17
009-05-2		152	1.52	.57	-----	-----	<b>3.82</b>	4.10	-----
009-05-3		152	1.52	.58	11.66	12.21	4.13	1.64	7.48
005-10-1	3.2	154	1.55	0.54	-----	-----	<b>3.97</b>	3.99	-----
005-10-2		115	0.86	.72	5.05	9.48	1.18	1.46	2.64
005-10-3		151	1.50	.54	9.06	9.89	4.04	1.44	7.02
011-07-1	3.2	155	1.58	0.52	7.71	8.57	2.64	1.59	17.55
011-07-2		155	1.58	.49	-----	-----	<b>2.79</b>	4.24	-----
011-07-3		153	1.54	.48	8.95	12.55	3.68	1.51	10.92
005-11-1	3.2	153	1.54	0.57	7.02	10.20	2.15	1.22	6.09
005-11-2		154	1.56	.62	8.78	9.57	<b>3.11</b>	1.58	9.56
005-11-3		155	1.58	.56	8.60	11.58	3.47	1.38	9.82

<sup>a</sup>The "1," "2," and "3" designate site of impact as shown on figure 1.

<sup>b</sup>Distance from leading edge.

<sup>c</sup>FS is front-side, HZ is Hertzian, and BS is back-side.

<sup>d</sup>Bold entries denote location of critical fatigue crack.

TABLE VIII.—CONTINUED. IMPACT CONDITIONS

(a) Continued. Cast-to-size Ti-48-2-2

Sample <sup>a</sup>	Projectile size, mm	Velocity, m/sec	Impact energy, $E_i$ , J	Impact location, $X_i$ , mm	Crack length, <sup>c</sup> mm				
					FS major	FS total	HZ <sup>d</sup>	BS straight	BS total
006-08-1	3.2	154	1.56	0.54	8.04	10.86	3.61	1.46	5.15
006-08-2	3.2	154	1.56	.50	8.17	10.82	<b>3.30</b>	1.74	13.87
006-08-3	3.2	154	1.56	.58	7.68	2.40	3.25	1.86	4.66
008-08-1	3.2	151	1.51	0.58	4.98	7.73	0.72	1.33	3.96
008-08-2	3.2	153	1.54	.63	7.69	10.43	<b>2.23</b>	1.79	4.31
008-08-3	3.2	153	1.54	.52	7.64	10.08	2.47	2.34	-----
008-09-1	3.2	152	1.52	0.57	3.71	10.15	1.04	1.51	4.60
008-09-2	3.2	154	1.56	.55	8.81	9.53	<b>3.83</b>	1.75	8.27
008-09-3	3.2	151	1.51	.53	9.19	10.04	1.20	1.79	7.96
009-13-1	3.2	152	1.52	0.58	8.82	11.19	5.27	1.44	10.89
009-13-2	3.2	154	1.56	.72	8.40	13.39	5.76	1.92	7.50
009-13-3	3.2	154	1.56	.52	5.80	6.94	<b>2.90</b>	4.56	-----
006-01-1	3.2	153	1.54	0.51	7.86	11.52	<b>2.74</b>	1.85	12.55
006-01-2	3.2	153	1.54	.56	10.97	16.32	4.46	1.60	9.08
006-01-3	3.2	153	1.54	.57	7.98	11.63	2.42	1.87	10.45
010-11-1	3.2	151	1.50	0.57	9.16	14.60	1.98	1.71	-----
010-11-2	3.2	154	1.55	.59	7.14	7.14	<b>3.57</b>	4.00	-----
010-11-3	3.2	154	1.55	.40	9.07	12.62	2.97	3.32	-----
011-05-1	3.2	154	1.55	0.57	8.03	13.64	3.72	1.72	9.62
011-05-2	3.2	150	1.48	.56	4.50	4.50	<b>2.25</b>	4.12	-----
011-05-3	3.2	153	1.54	.56	11.15	14.42	4.02	1.49	4.77
006-05-1	3.2	152	1.52	0.48	7.65	13.07	3.83	1.77	9.45
006-05-2	3.2	153	1.54	.66	8.49	13.53	4.02	1.61	8.75
006-05-3	3.2	153	1.54	.68	7.78	7.79	<b>3.89</b>	4.05	-----

<sup>a</sup>The "1," "2," and "3" designate site of impact as shown on figure 1.

<sup>b</sup>Distance from leading edge.

<sup>c</sup>FS is front-side, HZ is Hertzian, and BS is back-side.

<sup>d</sup>Bold entries denote location of critical fatigue crack.

TABLE VIII.—CONTINUED. IMPACT CONDITIONS

(a) Concluded. Cast-to-size Ti-48-2-2

[Three impacts per specimen at 70 MPa stress and 260 °C.]

Sample <sup>a</sup>	Projectile size, mm	Velocity, m/sec	Impact energy, E, J	Impact location, X, mm	Crack length, <sup>c</sup> mm				Comments	
					FS major	FS total	HZ <sup>d</sup>	BS straight <sup>d</sup>		BS total
008-13-1	3.2	575	2.01	0.10	4.52	5.94	1.94	0.90	4.38	No fatigue test
007-05-1	3.2	571	1.99	0.13	-----	5.22	2.18	3.09	-----	Blowout, X estimated
007-05-2	3.2	579	2.04	.13	-----	4.33	1.98	3.55	-----	Blowout, X estimated
007-05-3	3.2	579	2.04	.13	-----	4.95	<b>2.48</b>	1.16	9.90	BS crack length = 2.99 if use blowout
008-04-1	3.2	559	1.90	1.00	12.38	17.65	6.22	2.28	13.30	BS crack length = 3.94 to back of HZ
008-04-2	3.2	556	1.88	.88	9.01	11.30	2.25	2.20	12.00	BS crack length = 4.51 to back of HZ
008-04-3	3.2	571	1.99	.80	7.93	12.10	<b>3.63</b>	1.85	12.80	
011-11-1	3.2	583	2.07	1.93	0	8.90	0.62	3.24	9.86	
011-11-2	3.2	571	1.99	1.89	0	12.00	.76	<b>2.84</b>	10.10	
011-11-3	3.2	580	2.05	1.76	0	8.50	.42	3.32	10.80	Velocity estimated
006-02-1	3.2	415	1.05	0.21	2.43	12.12	0.48	0.98	2.85	
006-02-2	3.2	397	.96	.32	4.03	8.76	<b>.89</b>	1.13	2.75	
006-02-3	3.2	411	1.03	.20	3.00	6.15	.53	1.01	3.43	
010-12-1	3.2	417	1.06	0.96	4.32	11.02	1.27	1.75	6.63	
010-12-2	3.2	413	1.04	1.09	2.94	13.86	1.25	2.25	5.25	
010-12-3	3.2	413	1.04	.84	4.41	10.54	<b>1.56</b>	1.88	5.75	
011-01-1	1.6	484	0.18	1.95	0	1.69	0.14	0	0	
011-01-2	1.6	524	.21	1.97	0	1.79	.11	0	0	
011-01-3	1.6	524	.21	1.75	0	1.18	<b>.19</b>	0	0	Failed at FS crack
005-14-1	1.6	484	0.18	0.22	0	1.70	0.24	0.26	0.53	
005-14-2	1.6	524	.21	.22	0	2.34	.21	.17	.65	Failed above #2 at center porosity
005-14-3	1.6	524	.21	.09	0	1.39	.18	.11	.41	
009-06-1	1.6	534	0.22	1.08	0	4.28	0.31	<b>1.16</b>	2.05	
009-06-2	1.6	534	.22	1.09	0	1.88	.25	.86	1.11	Velocity estimated
009-06-3	1.6	534	.22	.86	0	5.26	.35	.68	.73	Velocity estimated
011-04-1	3.2	579	2.04	3.03	0	1.59	0.49	<b>4.60</b>	10.18	Estimated crack lengths from SEM
011-04-2	3.2	579	2.04	2.94	0	2.53	.29	4.55	9.94	Estimated crack lengths from SEM
011-04-3	3.2	579	2.04	2.98	0	0.72	.17	4.54	10.34	Estimated crack lengths from SEM
007-13-1	3.2	700	2.99	3.03	0	5.98	0.35	5.00	12.93	
007-13-2	3.2	700	2.99	3.00	0	6.89	.46	<b>4.77</b>	12.69	
007-13-3	3.2	700	2.99	2.87	0	1.35	.28	5.03	13.74	

<sup>a</sup>The "1," "2," and "3" designate site of impact as shown on figure 1.

<sup>b</sup>Distance from leading edge.

<sup>c</sup>FS is front-side, HZ is Hertzian, and BS is back-side.

<sup>d</sup>Bold entries denote location of critical fatigue crack.

TABLE VIII.—CONTINUED. IMPACT CONDITIONS  
 (b) GEAE Ti-47Al-2Cr-2Nb  
 [One impact per specimen at 70 MPa stress and 260 °C.]

Sample	Velocity, m/s	Impact energy, <i>E</i> , J	Impact location, <sup>a</sup> <i>X</i> , mm	Crack length, <sup>b</sup> mm				Comments	
				FS major	FS total	HZ <sup>c</sup>	BS straight <sup>c</sup>		BS total
Projectile size, 1.6 mm									
4-1-2	83	0.06	0.79	0	0	0	0	0	
5-1-5	90	.07	.57	0	0	0	0.67	0.64	
6-3-5	86	.06	.52	0	0	0	<b>.58</b>	1.11	
4-1-3	85	.06	.65	0	0.63	0.24	<b>.79</b>	1.09	Star-shaped crack on back side
5-1-4	86	.06	.65	0	.24	.07	.51	.87	
4-1-8	155	.20	.55	1.59	3.25	.77	<b>.82</b>	2.63	
6-3-4	152	.19	.60	.40	1.40	.40	.89	2.00	Velocity estimated; didn't break at indent. Facet
4-1-9	154	.19	.68	1.27	4.41	.65	<b>1.03</b>	5.98	
4-1-4	203	.34	.76	1.01	2.80	.56	<b>1.17</b>	4.11	
5-1-1	205	.34	.53	2.07	4.79	.63	<b>.93</b>	3.38	
5-1-10	310	.79	.44	4.58	8.04	2.07	<b>1.07</b>	----	Partial blowout, actual cracks measured, didn't include blowout
4-1-10	310	.79	.55	7.88	7.88	<b>2.81</b>	2.12	10.37	Near blowout
6-3-7	365	1.09	.46	----	----	<b>2.96</b>	1.74	----	Blowout, <i>X</i> estimated
5-1-7	367	1.11	.52	----	----	<b>2.08</b>	1.29	----	Mostly blown out, <i>X</i> estimated
Projectile size, 3.2 mm									
5-1-11	120	0.94	1.15	0	0	0	<b>1.95</b>	6.36	
6-3-8	125	1.03	0.97	2.38	6.44	1.22	<b>1.72</b>	6.61	
4-1-6	155	1.57	1.27	0	3.83	.96	<b>2.09</b>	8.13	
5-1-13	148	1.45	.86	4.25	7.42	2.39	<b>1.95</b>	7.81	
63-03-05	----	----	----	----	----	----	----	----	

<sup>a</sup>Distance from leading edge.

<sup>b</sup>FS is front-side, HZ is Hertzian, and BS is back-side.

<sup>c</sup>Bold entries denote location of critical fatigue crack.

TABLE VIII.—CONTINUED. IMPACT CONDITIONS  
(c) CMU Ti-47-2-2  
[One impact per specimen at 70 MPa stress and 260 °C.]

Sample	Velocity, m/s	Impact energy, $E_p$ , J	Impact location, <sup>a</sup> $X_c$ , mm	Crack length, <sup>b</sup> mm				Comments	
				FS major	FS total	HZ <sup>c</sup>	BS straight <sup>c</sup>		BS total
Projectile size, 1.6 mm									
4-7-12	84	0.06	0.53	0	1.19	0.15	<b>0.75</b>	1.48	BS crack length doesn't include small cracks
4-7-22-1	83	.06	2.28	0	0	0	1.25	1.16	
4-7-22-2	83	.06	.56	0	.48	0	.74	.68	
4-7-16	163	.22	.54	1.05	7.87	1.05	<b>1.23</b>	5.93	
4-7-6	164	.22	.49	2.28	5.84	.94	<b>.88</b>	6.51	
4-7-8	210	.36	.47	5.09	8.02	1.87	<b>1.18</b>	15.81	
4-7-19	210	.36	.49	6.11	10.30	<b>1.66</b>	1.02	7.03	
4-7-2	321	.85	----	----	10.46	<b>2.52</b>	1.64	----	
4-7-17	321	.85	.41	7.12	13.52	3.63	<b>1.73</b>	9.97	
4-7-15	305	.76	.37	8.57	12.75	<b>2.20</b>	1.68	----	
4-7-10	305	.76	----	4.76	4.76	<b>2.38</b>	1.79	----	
4-7-4	310	.79	.43	6.43	9.28	<b>3.22</b>	1.25	13.73	
4-7-13	316	.82	.45	8.59	11.92	<b>3.60</b>	1.50	----	
Projectile size, 3.2 mm									
4-7-14	153	1.54	0.69	7.84	13.21	<b>3.24</b>	2.13	13.60	$X$ incorrect—reimpacted, broke at indent with largest $X$
4-7-11	154	1.56	.79	3.98	15.12	<b>1.84</b>	1.92	13.20	
4-7-7-1	152	1.52	1.50	0	2.06	.21	<b>2.62</b>	9.64	
4-7-7-2	152	1.52	.76	5.85	13.56	2.66	1.90	15.23	
4-7-20	125	1.03	.73	1.68	8.88	.81	<b>1.56</b>	8.93	
4-7-3	124	1.01	.72	3.10	9.01	2.60	<b>1.62</b>	14.60	
4-7-18	156	1.60	.65	5.25	11.13	2.00	<b>1.53</b>	13.54	
4-7-9	154	1.56	.67	6.02	11.73	2.87	<b>1.78</b>	12.08	
4-7-5	155	1.58	.74	8.82	14.02	2.95	<b>2.09</b>	10.82	
Partial blowout, HZ to top of impact									
Blowout									
Bottom of BS crack, not all small cracks counted for back total									
Velocity approximate, Partial blowout, but can estimate $X$									
Distance to top of blowout on front = 1.042									
Leading edge bent due to impact									

<sup>a</sup>Distance from leading edge.

<sup>b</sup>FS is front-side, HZ is Hertzian, and BS is back-side.

<sup>c</sup>Bold entries denote location of critical fatigue crack.

TABLE VIII.—CONTINUED. IMPACT CONDITIONS

(d) Howmet Ti-47Al-2Cr-2Nb

[One impact per specimen with 1.6 mm projectiles at 260 °C and 70 MPa stress.]

Sample	Velocity, m/s	Impact energy, $E$ , J	Impact location, <sup>a</sup> $X$ , mm	Crack length, <sup>b</sup> mm				Comments	
				FS major	FS total	HZ	BS straight <sup>c</sup>		BS total
2-3-9	121	0.12	0.62	----	----	0.43	<b>1.09</b>	----	Back-side crack does not go all the way to edge
2-3-17	120	.12	.62	----	----	.09	.58	----	Back-side crack does not go all the way to edge
2-3-18	125	.13	.56	----	----	.83	.88	----	
2-3-31	122	.12	.57	----	----	.18	<b>.84</b>	----	
2-3-11	120	.12	.52	----	----	.19	.56	----	Back-side crack does not go all the way to edge
2-3-8	121	.12	.55	----	----	.10	.70	----	

<sup>a</sup>Distance from leading edge.

<sup>b</sup>FS is front-side, HZ is Hertzian, and BS is back-side.

<sup>c</sup>Bold entries denote location of critical fatigue crack.

TABLE VIII.—CONTINUED. IMPACT CONDITIONS  
(e) ABB-2

Sample <sup>a</sup>	Impact temperature, °C	Velocity, m/s	Impact energy, E, J	Impact location, X, mm	[Three impacts per specimen at 70 MPa stress.]				Comments	
					Crack length, c, mm					
					FS major	FS total	HZ <sup>d</sup>	BS straight <sup>d</sup>	BS total	
Projectile size, 1.6 mm										
2-20-1	260	162	0.21	0.49	0	0.33	0.07	0.74	0.85	X hard to measure
2-20-2		162	.21	.44	0	.12	.05	<b>.34</b>	.30	X hard to measure
2-20-3		162	.21	.10	0	.27	.08	0	0	
1-12-1	260	165	0.22	0.58	0	0.38	0.06	0	0	Rough edge
1-12-2		166	.23	.51	0	0	.00	0	0	X hard to measure
1-12-3		162	.21	.68	0	.50	.11	<b>0.31</b>	0.31	X hard to measure
2-22-1	260	163	0.22	0.61	0	0	0	<b>0.49</b>	0.46	X hard to measure
2-22-2		164	.22	.59	0	0	0	0	0	X hard to measure
2-22-3		162	.21	.39	0.16	2.29	0.16	.14	.16	X hard to measure
2-17-1	260	165	0.22	0.13	0	0	0	0	0	Rough edge
2-17-2		162	.21	.55	0	0	0	0.42	0.61	X hard to measure
2-17-3		164	.22	.59	0	0	0	<b>0</b>	0	Rough edge
1-9-1	260	164	0.22	0.60	0	0	0	<b>0</b>	0	X hard to measure
1-9-2		164	.22	.58	0	0	0	0	0	
1-9-3		164	.22	.35	0.82	2.88	0.51	0.58	0.75	
1-16-1	260	167	0.23	0.44	0	0	0	0.67	0.54	X hard to measure
1-16-2		165	.22	.53	0	0	0	0	0	
1-16-3		167	.23	.48	0	1.10	0.13	<b>.45</b>	.65	
2-13-1	260	298	0.73	0.53	2.34	4.24	1.05	0.88	1.90	
2-13-2		301	.74	.41	2.96	4.97	<b>1.60</b>	.99	1.16	
2-13-3		302	.75	.36	0	2.11	.17	.73	1.00	
2-12-1	260	299	0.73	0.55	2.00	6.88	0.69	0.72	1.27	
2-12-2		301	.74	.55	4.24	5.62	<b>.84</b>	<b>1.05</b>	2.53	
2-12-3		302	.75	.47	.96	1.84	.29	.81	1.44	
1-6-1	260	302	0.75	0.53	0	0.53	0.12	1.05	3.49	
1-6-2		301	.74	.59	0	.72	.17	<b>.88</b>	1.06	
1-6-3		302	.75	.40	0.83	3.46	.72	.58	1.37	

<sup>a</sup>The "1," "2," and "3" designate site of impact as shown on figure 1.

<sup>b</sup>Distance from leading edge.

<sup>c</sup>FS is front-side, HZ is Hertzian, and BS is back-side.

<sup>d</sup>Bold entries denote location of critical fatigue crack.

TABLE VIII.—CONTINUED. IMPACT CONDITIONS  
(e) Continued. ABB-2

Sample <sup>a</sup>	Impact temperature, °C	Velocity, m/s	Impact energy, E <sub>i</sub> , J	Impact location, X, mm	Crack length, <sup>c</sup> mm				Comments	
					FS major	FS total	HZ <sup>d</sup>	BS straight <sup>d</sup>		BS total
Projectile size, 1.6 mm										
2-15-1	260	302	.75	0.54	3.61	5.14	1.09	0.57	1.21	
2-15-2		300	.74	.47	2.55	5.96	.51	.35	1.10	
2-15-3		300	.74	.34	.60	3.24	.19	<b>.36</b>	.83	
1-8-1	260	297	0.72	0.42	0	0.89	0.12	0.73	1.25	
1-8-2		300	.74	.58	2.15	5.63	.62	<b>.67</b>	2.87	
1-8-3		301	.74	.52	0	.26	.16	0	0	
2-24-1	260	300	0.74	0.54	0.76	3.49	0.59	0.67	3.27	
2-24-2		300	.74	.54	2.14	5.98	.63	.83	1.37	
2-24-3		301	.74	.38	.68	1.63	.27	<b>.70</b>	1.59	
Projectile size, 3.2 mm										
2-8-1	260	156	1.59	0.60	----	8.69	3.91	4.57	----	X estimated, close to 2-10-1
2-8-2		152	1.52	.60	----	7.71	<b>3.86</b>	4.78	----	X estimated
2-8-3		154	1.55	.60	----	9.01	2.92	3.48	----	X estimated
2-14-1	260	154	1.55	0.64	7.41	12.10	<b>4.24</b>	1.47	5.11	
2-14-2		154	1.55	.77	4.81	7.70	2.82	1.44	5.04	
2-14-3		152	1.52	1.69	0	.49	0	2.67	3.56	
1-1-1	260	154	1.55	0.69	6.88	8.79	2.45	1.95	2.42	X hard to measure, BS crack at an angle
1-1-2		154	1.55	.79	5.21	8.47	2.49	2.23	8.98	
1-1-3		150	1.48	.75	0	.67	.48	<b>1.73</b>	3.45	
1-3-1	260	148	1.44	0.91	1.19	3.15	<b>1.19</b>	1.39	3.65	
1-3-2		151	1.50	.82	2.55	5.42	.90	1.59	2.42	
1-3-3		151	1.50	.85	1.19	5.63	2.18	2.35	4.45	High HZ crack
1-5-1	260	150	1.48	0.68	7.67	9.78	2.84	1.64	6.34	
1-5-2		149	1.46	.67	7.41	10.19	3.14	1.42	10.16	
1-5-3		150	1.48	.59	7.27	11.36	<b>2.02</b>	<b>2.16</b>	9.74	

<sup>a</sup>The "1," "2," and "3" designate site of impact as shown on figure 1.

<sup>b</sup>Distance from leading edge.

<sup>c</sup>FS is front-side, HZ is Hertzian, and BS is back-side.

<sup>d</sup>Bold entries denote location of critical fatigue crack.

TABLE VIII.—CONTINUED. IMPACT CONDITIONS  
(e) Concluded. ABB-2

[Three impacts per specimen at 70 MPa stress.]

Sample <sup>a</sup>	Impact temperature, °C	Velocity, m/s	Impact energy, E <sub>i</sub> , J	Impact location, X, mm	Crack length, c, mm				Comments
					FS major	FS total	HZ <sup>d</sup>	BS straight	
Projectile size, 3.2 mm									
2-10-1	260	151	1.50	0.61	8.40	10.16	2.37	2.36	
2-10-2		155	1.57	.73	10.76	11.45	<b>3.71</b>	1.55	5.67
2-10-3		153	1.54	.68	4.06	7.35	1.51	1.67	6.09
2-6-1	730	298	5.83	----	----	11.57	3.32	4.32	----
2-6-2		297	5.79	----	----	12.70	3.22	3.80	----
2-6-3		297	5.77	----	----	7.21	<b>2.46</b>	3.06	----
2-28-1	730	300	5.89	----	----	6.44	2.74	3.77	----
2-28-2		297	5.77	----	----	7.68	<b>2.61</b>	2.85	----
2-28-3		300	5.89	----	----	13.93	2.48	3.75	----
2-5-1	730	302	6.00	----	----	11.10	2.84	3.15	----
2-5-2		301	5.94	----	----	13.89	<b>3.20</b>	3.18	----
2-5-3		298	5.83	----	----	5.12	2.28	2.48	----
2-19-1	730	302	6.00	----	----	7.32	2.68	3.77	----
2-19-2		302	6.00	----	----	10.29	3.64	4.23	----
2-19-3		298	5.83	----	----	10.85	<b>3.00</b>	3.48	----
1-2-1	730	301	5.94	----	----	7.53	2.84	3.97	----
1-2-2		297	5.77	----	----	8.69	<b>2.63</b>	3.18	----
1-2-3		298	5.83	----	----	6.13	2.29	3.72	----
2-2-1	730	301	5.94	----	----	10.77	2.47	3.40	----
2-2-2		302	6.00	----	----	13.14	<b>3.18</b>	3.85	----
2-2-3		297	5.77	----	----	5.88	2.11	2.56	----

<sup>a</sup>The "1," "2," and "3" designate site of impact as shown on figure 1.

<sup>b</sup>Distance from leading edge.

<sup>c</sup>FS is front-side, HZ is Hertzian, and BS is back-side.

<sup>d</sup>Bold entries denote location of critical fatigue crack.

Partial blowout

Velocity estimated

TABLE VIII.—CONTINUED. IMPACT CONDITIONS  
(f) ABB-23

[One impact per specimen at 70 MPa stress and 260 °C.]

Sample	Projectile size, mm	Velocity, m/s	Impact energy, E, J	Impact location, <sup>a</sup> X, mm	Crack length, <sup>b</sup> mm					Comments
					FS major	FS total	HZ <sup>c</sup>	BS straight <sup>c</sup>	BS total	
2	1.6	165	0.22	0.62	0	2.63	0.71	<b>0.98</b>	1.79	Spalling or debris on surface
7	1.6	172	.24	.58	0	2.16	.27	<b>.92</b>	1.95	
5B	1.6	302	.75	----	----	----	<b>3.21</b>	2.54	----	Partial blowout
8B	1.6	299	.73	.50	7.50	7.95	<b>2.96</b>	1.08	----	
1	3.2	149	1.46	----	----	----	<b>2.37</b>	2.37	----	Large, round blowout
4	3.2	151	1.50	0	----	----	<b>2.34</b>	3.39	----	

<sup>a</sup>Distance from leading edge.

<sup>b</sup>FS is front-side, HZ is Hertzian, and BS is back-side.

<sup>c</sup>Bold entries denote location of critical fatigue crack.

TABLE VIII.—CONTINUED. IMPACT CONDITIONS  
(g) NCG359E

Sample	Projectile size, mm	Velocity, m/s	Impact energy, $E$ , J	Impact location, <sup>a</sup> $X$ , mm	Crack length, <sup>b</sup> mm					Comments
					FS major	FS total	HZ <sup>c</sup>	BS straight <sup>c</sup>	BS total	
1-4-5	1.6	161	0.21	0.66	0	1.56	0.27	<b>0.80</b>	1.77	Mostly blown out; $X$ is approximate Small blown out portion  Blowouts Blowouts
1-4-8	1.6	160	.21	.58	0	2.51	.54	<b>1.13</b>	5.04	
1-4-1	1.6	299	.73	.58	5.85	10.29	<b>2.24</b>	1.45	-----	
1-4-3	1.6	302	.75	.49	7.50	8.94	<b>1.61</b>	1.62	8.47	
1-4-6	3.2	152	1.52	-----	-----	-----	<b>3.16</b>	3.49	-----	
1-4-7	3.2	150	1.48	-----	-----	-----	<b>3.72</b>	2.64	-----	

<sup>a</sup>Distance from leading edge.

<sup>b</sup>FS is front-side, HZ is Hertzian, and BS is back-side.

<sup>c</sup>Bold entries denote location of critical fatigue crack.

TABLE VIII.—CONTINUED. IMPACT CONDITIONS  
(h) 95A

Sample	Velocity, m/s	Impact energy, $E_i$ , J	Impact location, <sup>a</sup> $X$ , mm	Crack length, <sup>b</sup> mm				Comments	
				FS major	FS total	HZ <sup>c</sup>	BS straight <sup>c</sup>		BS total
Projectile size, 1.6 mm									
F-2	86	0.06	0.69	0	0	0	0	0	2 leading edge BS cracks
F-2-2 <sup>d</sup>	83	.06	.54	0	0.11	0.06	<b>0.80</b>	0.62	BS crack length not continuous and not to edge
F-23	84	.06	.67	0	.19	.06	.83	.86	BS crack length does not begin at edge
F-23-2 <sup>d</sup>	84	.06	.57	0	.10	.10	.65	.36	BS crack length measured from edge but did not start at edge.
F-17	89	.07	.77	0	1.05	.20	.83	1.19	BS crack length measured from edge but did not start at edge
F-10	88	.06	.80	0	1.02	.20	.83	.19	2 BS and 1 FS crack
F-18	159	.21	.48	0.30	1.76	.30	<b>.83</b>	2.27	2 BS cracks
F-3	151	.19	.52	0	1.85	.18	<b>.83</b>	2.70	
F-11	194	.31	.31	4.17	6.02	<b>.83</b>	.74	4.27	
F-21	197	.32	.52	.84	3.68	.34	<b>.90</b>	4.54	Through-the-thickness crack
F-8	297	.72	.34	4.59	7.37	<b>2.09</b>	1.37	-----	Mostly blown out but can see crater
F-14	297	.72	.50	-----	9.21	1.74	1.07	-----	Mostly blown out but can see some of crater; $X$ not very accurate
F-6	297	.72	.47	3.92	10.60	<b>1.33</b>	1.25	5.22	
F-1	295	.72	-----	-----	6.17	<b>2.50</b>	1.84	-----	Distance to top of blowout is 1.283
F-20	298	.73	.48	7.09	9.86	<b>2.57</b>	1.17	4.44	
F-12	301	.74	-----	-----	6.65	<b>1.69</b>	1.50	-----	

<sup>a</sup>Distance from leading edge.

<sup>b</sup>FS is front-side, HZ is Hertzian, and BS is back-side.

<sup>c</sup>Bold entries denote location of critical fatigue crack.

<sup>d</sup>Second impact on this specimen.

TABLE VIII.—CONCLUDED. IMPACT CONDITIONS

(h) Concluded. 95A

[One impact per specimen at 70 MPa stress and 260 °C.]

Sample	Velocity, m/s	Impact energy, $E_i$ , J	Impact location, <sup>a</sup> $X_i$ , mm	Crack length, <sup>b</sup> mm				Comments	
				FS major	FS total	HZ <sup>c</sup>	BS Straight <sup>c</sup>		BS total
Projectile size, 1.6 mm									
F-5	124	1.01	0.60	2.12	8.64	0.43	<b>1.43</b>	8.16	Through-the-thickness crack Distance to top of blowout is 1.283 Distance to top of blowout is 1.37
F-19	123	.99	.80	.52	4.86	.39	<b>1.58</b>	6.16	
F-4	155	1.57	.57	7.81	13.10	<b>3.11</b>	1.68	7.49	
F-24	151	1.50	-----	-----	8.33	<b>2.85</b>	2.46	-----	
F-22	155	1.57	-----	-----	11.02	<b>3.08</b>	1.90	-----	
F-13	156	1.59	.59	5.72	11.14	<b>2.55</b>	1.40	6.05	
F-9	155	1.57	.62	1.03	6.00	.64	<b>1.65</b>	7.56	
F-16	152	1.52	.57	2.83	10.98	1.05	<b>1.39</b>	8.67	

<sup>a</sup>Distance from leading edge.

<sup>b</sup>FS is front-side, HZ is Hertzian, and BS is back-side.

<sup>c</sup>Bold entries denote location of critical fatigue crack.

TABLE IX.—FATIGUE PROPERTIES

(a) Cast-to-size Ti-48-2-2

[Temperature is 650 °C, frequency is 100 Hz.]

Sample	$R_o(A)$ -ratio	Net section stress at failure, MPa	Cycles to failure	Failure type <sup>a</sup>	Defect area, mm	Net section stress at threshold, MPa	Number of steps to threshold	Minimum stress at threshold, MPa
Block size = 10 <sup>6</sup>								
006-10-2	0.05 (1)	201	33 600	BS	0.37	----	0	---
008-10-2	→	221	25 300	BS	.24	215	10	11
007-12-1		177	30 700	BS	.12	----	0	---
005-01-3		242	19 000	BS	.42	236	10	12
005-08-3	→	209	20 900	BS	.39	196	6	10
011-03-1		212	23 900	HZ	.68	206	10	10
009-03-2	.05 (1)	206	19 900	HZ	1.44	199	9	10
010-09-2	→	150	43 000	HZ	3.70	137	1	7
006-06-1		192	17 700	HZ	1.90	180	7	9
009-08-3	→	124	517 400	HZ	6.00	118	3	6
011-09-2		139	23 200	HZ	5.12	127	4	6
008-13-1	.05 (1)	----	----	----	----	----	----	----
007-05-3	→	121	Missing data	HZ	7.2	110	2	5.5
008-04-3		123	17 300	HZ	8.0	112	2	5.6
011-11-2	→	126	28 200	BS	4.6	115	2	5.8
006-02-2		208	25 600	HZ	.6	197	5	9.9
010-12-3	.05 (1)	171	67 500	HZ	3.1	159	6	8
011-01-3	→	216	16 200	FS	.7	----	0	----
005-14-2		219	31 500	Porosity	.5	207	3	10.4
009-06-1		149	100 900	BS	2.8	----	0	----
011-04-1	→	107	54 800	BS-through	11.5	95	2	4.8
007-13-2		91	51 500	BS+FS	11.3	80	2	4

<sup>a</sup>Indicates where fatigue failure originated. FS is front-side, HZ is Hertzian, and BS is back-side cracking. "Through" indicates a through-the-thickness crack.

TABLE IX.—CONTINUED. FATIGUE PROPERTIES

(a) Concluded. Cast-to-size T1-48-2-2

[Temperature is 650 °C, frequency is 100 Hz.]

Sample	$R_0(A)$ -ratio	Net section stress at failure, MPa	Cycles to failure	Failure type <sup>a</sup>	Defect area, mm	Net section stress at threshold, MPa	Number of steps to threshold	Minimum stress at threshold, MPa
Block size 10 <sup>7</sup>								
010-02-3	.05 (1)	235	16 400	BS	.56	222	5	11
008-05-1	.05 (1)	192	28 900	BS	.45	----	0	---
010-05-3	.05 (1)	242	12 100	BS	1.36	229	5	11
011-10-2	.05 (1)	248	21 100	BS	1.28	235	5	12
008-01-1	.2 (0.67)	246	13 100	BS	.26	233	4	47
009-12-3	.2 (0.67)	242	10 000	BS	.55	229	4	46
007-01-2	.2 (0.67)	246	11 800	BS	.63	233	4	47
011-02-1	.2 (0.67)	257	9 200	BS	.40	244	4	49
007-06-3	.5 (0.33)	236	29 200	BS	.52	----	0	---
005-02-3	.5 (0.33)	290	11 200	BS	.28	278	5	139
006-09-3	.5 (0.33)	293	14 000	BS	.08	280	4	140
009-07-2	.5 (0.33)	254	9 400	BS	.53	242	3	121
009-05-2	.05 (1)	149	20 100	HZ	5.78	140	6	7
005-10-1	.05 (1)	130	20 700	HZ	4.17	----	0	---
011-07-2	.05 (1)	154	8 400	HZ	5.74	148	5	7
005-11-2	.05 (1)	126	25 500	HZ	6.29	----	0	---
006-08-2	.2 (0.67)	140	6 398 700	HZ	6.26	127	1	25
008-08-2	.2 (0.67)	178	17 200	HZ	6.19	165	5	33
008-09-2	.2 (0.67)	140	23 700	HZ	7.06	----	0	---
009-13-3	.2 (0.67)	151	14 700	HZ	4.33	139	2	29
006-01-1	.5 (0.33)	203	20 500	HZ	5.16	191	7	95
010-11-2	.5 (0.33)	195	14 900	HZ	4.67	183	4	92
011-05-2	.5 (0.33)	174	23 500	HZ	4.32	----	0	---
006-05-3	.5 (0.33)	191	18 000	HZ	4.67	178	2	89

<sup>a</sup>Indicates where fatigue failure originated. BS is back-side and HZ is Hertzian cracking.

TABLE IX.—CONTINUED. FATIGUE PROPERTIES

(b) GEAE Ti-47-2-2<sup>a</sup>

[Block size is 10<sup>6</sup>; temperature, 650 °C; and frequency, 100 Hz.]

Sample	$R_c(A)$ -ratio	Net section stress at failure, MPa	Cycles to failure	Failure type <sup>b</sup>	Defect area, mm	Net section stress at threshold, MPa	Number of steps to threshold	Minimum stress at threshold, MPa	Comments
063-03-02 <sup>c</sup>	0.05 (1)	292	13 000	Face	0.008	279	3	14	Surface pore near leading edge
063-03-4 <sup>c</sup>	.05 (1)	288	5 100	Face	.070	---	0	---	2 EDM pores+facets
4-1-7 <sup>c</sup>	.05 (1)	266	681 400	Face	.167	253	6	13	Defect on face
6-3-6 <sup>c</sup>	.05 (1)	314	7 100	Face	.003	299	9	15	Pore on face+facet
5-1-2 <sup>c</sup>	<b>.5 (0.33)</b>	401	13 700	Face	.004	388	14	194	Pore on face
5-1-9 <sup>c</sup>	.05 (1)	346	132 000	Face	0	332	10	17	Multiple face initiation+facet; no defects
4-1-1 <sup>c</sup>	.05 (1)	245	947 040	Leading edge	.006	---	0	---	Very small surface defects
6-3-1 <sup>c</sup>	.05	359	21 680	Leading edge	.009	345	11	17	Pit on surface
4-1-2	.05 (1)	0		Grips	0	0	0	0	
5-1-5	.05 (1)	192	463 500	Face	2.245	178	4	9	Did not break at indent. Facet
6-3-5	.05 (1)	177	1 000 000	BS	.105	163	1	8	
4-1-3	.05 (1)	402	10 560	BS	.021	388	16	19	
5-1-4	0.05 (1)	402	5 840	Face	.010	388	20	19	Did not break at indent. Pit and facet
4-1-8	→	185	240 700	BS	.304	172	4	9	
6-3-4	→	132	127 700	Face	5.613	---	0	---	Broke at facet on face
4-1-9	→	248	28 560	BS	.312	234	6	12	
4-1-4	→	172	403 200	BS	.486	159	3	8	
5-1-1	0.05 (1)	200	238 500	BS	.206	186	5	9	
5-1-10	→	212	32 960	BS	.497	198	10	10	
4-1-10	→	186	17 440	HZ	1.123	172	6	9	
6-3-7	→	159	40 720	HZ	1.239	146	4	7	
5-1-7	→	161	29 600	HZ	1.290	148	2	7	
5-1-11	0.05 (1)	154	53 440	BS	.429	140	1	7	
6-3-8	→	163	25 840	BS	1.000	150	3	7	
4-1-6	→	138	28 800	BS+Facet	1.110	124	2	6	
5-1-13	→	159	25 920	BS+FS	1.232	146	4	7	
063-03-05	→	225	17 900	BS	.312	212	9	11	

<sup>a</sup>Corresponding fatigue properties for prefretted samples can be found in table XIV.

<sup>b</sup>Indicates where fatigue failure originated. FS is front-side, HZ is Hertzian, and BS is back-side cracking. "Grips" indicates sample broke in grips.

<sup>c</sup>Virgin sample.

TABLE IX.—CONTINUED. FATIGUE PROPERTIES

(c) CMU Ti-47-2-2

[Block size is 10<sup>6</sup>; temperature, 650 °C; and frequency, 100 Hz.]

Sample	$R_e(A)$ -ratio	Net section stress at failure, MPa	Cycles to failure	Failure type <sup>a</sup>	Defect area, mm	Net section stress at threshold, MPa	Number of steps to threshold	Minimum stress at threshold, MPa	
4-7-1 <sup>b</sup>	0.05 (1)	368	168 320	Leading edge pit	0	355	9	18	
4-7-23 <sup>b</sup>	→	389	8 320	Leading edge pits	0.02	374	5	19	
4-7-12		344	15 040	BS	.04	330	15	17	
4-7-22-1		404	14 240	Leading edge pit	0	389	16	19	
4-7-16		248	17 920	BS-through	.49	234	8	12	
4-7-6		234	382 320	BS-through	.19	219	3	11	
4-7-8		216	30 320	BS-through	1.56	202	7	10	
4-7-19		248	19 520	HZ	1.59	235	10	12	
4-7-2		148	62 640	HZ	.96	135	5	7	
4-7-17		220	14 400	BS-through	2.16	206	8	10	
4-7-15		187	16 800	BS+HZ	2.65	173	5	9	
4-7-10		0.5 (0.333)	146	1 000 000	HZ	1.08	133	3	67
4-7-4		→	276	17 120	BS+HZ	2.71	261	11	131
4-7-13			255	22 480	HZ	3.25	241	10	121
4-7-14			190	26 640	BS+HZ	3.53	176	6	88
4-7-11			225	21 840	BS-through	3.04	211	8	106
4-7-7-1	142		45 920	BS-through	3.14	128	2	64	
4-7-20	.05 (1)		187	17 600	BS-through	1.58	173	5	9
4-7-3	→		201	28 720	BS-through	1.29	187	6	9
4-7-18			144	68 240	BS+HZ	1.46	130	2	7
4-7-9		205	14 960	BS-through	1.92	192	7	10	
4-7-5	197	15 440	BS-through	1.77	183	5	9		

<sup>a</sup>Indicates where fatigue failure originated. FS is front-side, HZ is Hertzian, and BS is back-side cracking. "Through" indicates through-the-thickness crack.

<sup>b</sup>Virgin sample.

TABLE IX.—CONTINUED. FATIGUE PROPERTIES

(d) Howmet Ti-47Al-2Cr-2Nb

[Block size is  $10^6$ ;  $R_o(A)$ -ratio, 0.05 (1); temperature, 650 °C; and frequency, 100 Hz.]

Sample	Net section stress at failure, MPa	Cycles to failure	Failure type <sup>a</sup>	Defect area, mm	Net section stress at threshold, MPa	Number of steps to threshold	Minimum stress at threshold, MPa
2-3-9	304	11 840	BS	0.22	290	6	15
2-3-17	324	6 720	No defects	0	311	11	16
2-3-18	318	3 920	No defects	0	304	10	15
2-3-31	282	18 320	BS	.16	268	13	13
2-3-11	328	17 280	No defects	0	315	17	16
2-3-8 <sup>b</sup>	232	13 840	Large facet	→	219	9	11
2-3-12 <sup>b</sup>	321	14 000	No defects	→	308	3	15
2-3-30 <sup>b</sup>	334	5 760	→	→	321	4	16
2-3-23 <sup>b</sup>	344	2 080	→	→	331	10	17
2-3-14 <sup>b</sup>	321	9 840	→	→	307	8	15
2-3-13 <sup>b</sup>	280	11 280	→	→	---	---	---
2-3-22 <sup>b</sup>	353	11 040	Porosity	1.11	338	5	17
2-3-7 <sup>b</sup>	280	42 480	→	→	---	---	---
2-3-19 <sup>b</sup>	335	7 360	No defects	0	321	4	16
2-3-15 <sup>b</sup>	346	9 280	→	→	333	5	17
2-3-26 <sup>b</sup>	333	7 600	→	→	320	9	16
2-3-29 <sup>b</sup>	348	6 880	→	→	335	10	17
2-3-27 <sup>b</sup>	354	6 720	→	→	340	5	18
2-3-21 <sup>b</sup>	280	10 720	→	→	---	---	---
2-3-35 <sup>b</sup>	347	13 280	→	→	333	5	17
2-3-24 <sup>b</sup>	333	11 520	→	→	333	4	17
2-3-16 <sup>b</sup>	321	12 800	→	→	321	8	16
2-3-28 <sup>b</sup>	322	18 480	Defect	→	309	---	---
2-3-25 <sup>b</sup>	90	74 480	Defect	3.27	---	---	---

<sup>a</sup>Indicates where fatigue failure originated. BS is back-side cracking.

<sup>b</sup>Virgin sample.

TABLE IX.—CONTINUED. FATIGUE PROPERTIES

(d) Concluded. Howmet Ti-47Al-2Cr-2Nb

Sample	Net section stress at failure, MPa	Cycles to failure	Failure type <sup>a</sup>	Crack area, mm	Net section stress at threshold, MPa	Number of steps to threshold	Minimum stress at threshold, MPa
2-3-33	214	353 360	No defects	0	---	---	---
2-3-32	241	542 640	No defects	↓	228	2	11
2-3-10	214	238 560	No defects	↓	---	---	---
2-3-2	329	10 000	No defects	↓	315	3	16
2-3-4	313	14 800	No defects	↓	299	4	15
2-3-6	307	41 760	Porosity	0.66	293	4	15
2-3-5	295	12 640	No defects	0	281	6	14
2-3-3	362	21 760	No defects	0	348	10	17
2-3-1	319	22 080	Pit	.27	304	7	15
2-5-3	347	6 960	No defects	0	334	8	17
2-5-2	361	24 080	No defects	0	347	9	17

<sup>a</sup>Indicates where failure originated.

TABLE IX.—CONTINUED. FATIGUE PROPERTIES

(e) ABB-2

[Block size is  $10^6$ , frequency is 100 Hz.]

Sample	Test temperature, °C	$R_o(A)$ -ratio	Net section stress at failure, MPa	Cycles to failure	Failure type <sup>a</sup>	Defect area, mm	Net section stress at threshold, MPa	Number of steps to threshold	Minimum stress at threshold, MPa
2-9 <sup>b</sup>	650	.05(1)	312	6 200	Leading edge facet	0	301	6	15
2-23 <sup>b</sup>	730	.05(1)	349	2 800	Leading edge facet	0	325	14	16
2-20-2	650	.05(1)	211	44 400	BS	0.24	200	6	10
1-12-3	650	.05(1)	258	59 500	BS	.18	247	10	12
2-22-1	650	.05(1)	217	20 000	BS	.23	205	6	10
2-17-3	650	.5 (0.33)	245	32 400	BS	.41	234	8	117
1-9-1	650	.5 (0.33)	291	14 600	BS+facet	.09	280	11	140
1-16-3	650	.5 (0.33)	291	24 900	BS	.39	279	10	140
2-13-2	650	.05(1)	210	17 000	HZ	2.10	199	7	10
2-12-2	650	.05(1)	161	25 900	BS+30%HZ	1.56	150	3	8
1-6-2	650	.05(1)	157	18 600	BS irregular + facet	1.54	145	2	7
2-15-3	730	.5 (0.33)	272	4 700	BS+facet	.88	261	13	131
1-8-2	730	.5 (0.33)	265	6 000	BS+facet	.24	254	8	127
2-24-3	650	.5 (0.33)	227	21 400	BS	.94	216	6	108
2-8-2	650	.05(1)	145	11 500	HZ	4.82	140	11	7
2-14-1	650	.05(1)	145	13 300	HZ	6.98	134	3	7
1-1-3	650	.05(1)	133	34 400	BS+FS	2.37	123	2	6
1-3-1	650	.5 (0.33)	183	40 200	HZ+facet	1.55	172	5	86
1-5-3	650	.5 (0.33)	162	40 000	BS+HZ+facet	4.71	150	4	75
2-10-2	650	.5 (0.33)	175	28 400	HZ	2.07	165	7	83
2-6-3	730	.05(1)	136	22 000	HZ	2.64	125	5	6
2-28-2	730	.05(1)	143	28 600	HZ	3.42	131	2	7
2-5-2	730	.05(1)	177	12 100	HZ	2.77	165	7	8
2-19-3	730	.5 (0.33)	201	14 500	HZ	2.52	190	8	95
1-2-2	730	.5 (0.33)	185	14 600	HZ	4.58	174	6	87
2-2-2	730	.5 (0.33)	165	22 600	HZ	3.42	154	4	77

<sup>a</sup>Indicates where fatigue failure originated. FS is front-side, HZ is Hertzian, and BS is back-side cracking.

<sup>b</sup>Virgin sample.

TABLE IX.—CONTINUED. FATIGUE PROPERTIES

(f) ABB-23

Sample	Net section stress at failure, MPa	Cycles to failure	Failure type <sup>a</sup>	Defect area, mm	Net section stress at threshold, MPa	Number of steps to threshold	Minimum stress at threshold, MPa
3 <sup>b</sup>	456	5 760	Facet	0	443	19	22.1
6 <sup>b</sup>	486	7 680	Facet	0	473	18	23.6
2	237	17 200	BS	0.49	224	7	11.2
7	241	16 880	BS	.36	228	7	11.4
5B	134	12 800	HZ	2.38	121	2	6.1
8B	145	15 920	HZ	1.88	132	3	6.6
1	132	22 720	HZ	1.11	119	2	6.0
4	112	12 560	HZ	1.87	0	0	0
5A <sup>b,c</sup>	246	1920	Face defect	2.01	0	0	0
8A <sup>b,c</sup>	299	2960	Face defects	.63	0	0	0
11 <sup>b,c</sup>	310	16 160	Face pore	.06	296	12	14.8

<sup>a</sup>Indicates where fatigue failure originated. BS is back-side and HZ is Hertzian cracking.

<sup>b</sup>Virgin sample.

<sup>c</sup>Sample taken from heat shield.

TABLE IX.—CONTINUED. FATIGUE PROPERTIES

(g) NCG359E

[Block size is 10<sup>6</sup>; R<sub>g</sub>(A)-ratio, 0.05 (1); temperature, 650 °C; and frequency, 100 Hz.]

Sample	Net section stress at failure, MPa	Cycles to failure	Failure type <sup>a</sup>	Crack area, mm	Net section stress at threshold, MPa	Number of steps to threshold	Minimum stress at threshold, MPa
1-4-2 <sup>b</sup>	316	10 240	Leading edge pores	0.11	303	6	15.1
1-4-4 <sup>b,c</sup>	----	-----	----	----	----	----	----
1-4-5	258	5 680	BS	.95	245	9	12.2
1-4-8	268	?	BS	.50	255	10	12.8
1-4-1	188	12 160	HZ	1.65	175	6	8.7
1-4-3	199	19 600	HZ	1.80	186	7	9.3
1-4-6	106	27 280	HZ	2.75	0	0	0
1-4-7	108	19 040	HZ	4.64	94	1	4.7

<sup>a</sup>Indicates where fatigue failure originated. BS is back-side and HZ is Hertzian cracking.

<sup>b</sup>Virgin sample.

<sup>c</sup>Broke during hydraulics shutdown.

TABLE IX.—CONCLUDED, FATIGUE PROPERTIES  
(h) 95A

[Block size is 10<sup>6</sup>; temperature is 650 °C; and frequency is 100 Hz.]

Sample	$R_{\sigma}(A)$ -ratio	Net section stress at failure, MPa	Cycles to failure	Failure type <sup>a</sup>	Defect area, mm	Net section stress at threshold, MPa	Number of steps to threshold	Minimum stress at threshold, MPa
F-2	.05 (1)	317	6 880	BS	0.07	303	7	15
F-23	.05 (1)	312	9 360	Face pore	.03	299	8	15
F-17	.05 (1)	336	11 200	Leading edge defect	0	322	14	16
F-10	.05 (1)	328	9 680	Leading edge defect	0	315	7	16
F-18	.05 (1)	257	10 320	BS+FS	.17	243	9	12
F-3	.05 (1)	291	12 240	BS	.08	277	6	14
F-11	.05 (1)	223	9 920	FS	.78	210	5	11
F-21	.05 (1)	220	17 520	BS	.30	206	2	10
F-8	.05 (1)	195	13 840	HZ	.85	181	6	9
F-14 <sup>b</sup>	.05 (1)	----	----	----	----	----	--	--
F-6	.05 (1)	197	126 240	HZ+BS	1.07	184	7	9
F-1	.5 (.33)	203	13 840	HZ	1.02	189	5	95
F-20	.5 (.33)	223	22 080	HZ	1.80	209	6	105
F-12	.5 (.33)	214	18 640	HZ	.86	199	5	100
F-5	.05 (1)	201	14 960	BS	.78	187	4	9
F-19	.05 (1)	167	20 160	BS	.80	154	3	8
F-4	.05 (1)	132	23 360	HZ	2.29	117	3	6
F-24	.05 (1)	108	25 520	HZ	1.64	0	0	0
F-22	.05 (1)	131	16 800	HZ	1.30	0	0	0
F-13	.5 (.33)	200	15 040	BS+HZ	1.53	186	5	93
F-9	.5 (.33)	208	27 440	BS+FS	.68	194	5	97
F-16	.5 (.33)	202	13 280	BS	1.66	189	5	95

<sup>a</sup>Indicates where fatigue failure originated. FS is front-side, HZ is Hertzian, and BS is back-side cracking.

<sup>b</sup>Specimen broke in compression possibly due to hydraulics shutdown.

TABLE X.—FATIGUE PROPERTIES OF CAST-TO-SIZE Ti-48-2-2  
SAMPLES CONTAINING POROSITY

[All samples were virgin samples.]

[Temperature is 650 °C; frequency, 100 Hz; and  $R_{\sigma}(A)$ -ratio, 0.05(1).]

Sample	Net section stress at failure, MPa	Cycles to failure	Failure type <sup>a</sup>	Defect area, mm <sup>2</sup>	Net section stress at threshold, MPa	Number of steps to threshold	Minimum stress at threshold, MPa
Block size = 10 <sup>6</sup>							
006-11	281	10 400	Porosity	2.08	268	7	13
009-10	280	17 000	Porosity	.12	268	7	13
005-07	228	33 100	Porosity	.86	215	3	11
46-31	208	8 100	Porosity	5.23	183	2	9
47-15	247	18 900	Porosity	.67	235	6	12
Block size = 10 <sup>7</sup>							
005-13	246	184 200	Porosity	1.10	234	5	12
005-04	310	141 200	Porosity	.33	298	9	15
005-05	282	163 300	Porosity	.17	270	7	13
006-12	259	8 034 100	Porosity	.26	247	4	12
007-02	249	172 400	Porosity	1.84	236	7	12
006-07	263	947 600	Porosity	1.88	250	8	13
005-09	338	8 100	Face	0	325	14	16
008-14	280	1 118 200	Face	0	268	14	13
009-02	268	999 100	Porosity	.66	255	13	13
006-14	221	6 877 700	Porosity	3.14	209	3	10
005-03	239	532 600	Porosity	0.95	226	6	11

<sup>a</sup>Indicates where fatigue failure originated.

TABLE XI.—NONDESTRUCTIVE EVALUATION RESULTS FOR CAST-TO-SIZE Ti-48-2-2  
AFTER HIGH-CYCLE FATIGUE

Specimen	Stress at failure, MPa	Defect size, mm			FPI class <sup>c</sup>	Rejected by GEAE for	Computer tomography <sup>a</sup>	Ultrasonic evaluation <sup>a</sup>
		Fracture surface	microfocus X-ray <sup>a,b</sup>	X-ray <sup>c</sup>				
00614	221	1.06	0.127 <sup>d</sup> ×1.27	None	10	FPI	N/A	General area
00503	239	1.1	0.99×1.98	1.91	N/A	Microshrink	Check	General area
00513	246	1.06×0.61	1.27×1.27	1.27	10	Microshrink	Check	General area
00702	249	2.39×0.91 <sup>e</sup>	3.56×5.08	7.62	N/A	Microshrink	N/A	General area
00612	259	0.91×0.69	0.76×0.91 <sup>f</sup>	0.51	N/A	Gas porosity	N/A	General area
00607	263	1.04	2.03×1.02	None	Pass	Pass	N/A	General area
00902	268	0.76	1.27×1.52	3.18	N/A	Microshrink	N/A	General area
00505	282	0.48×0.79	1.14×1.14	None	30	FPI	N/A	General area
00504	310	0.79×0.48	Missed <sup>g</sup>	None	20	FPI	N/A	General area
00509	338	Face initiated	Pass	None	Pass	Pass	N/A	Pass

<sup>a</sup>Performed at NASA Glenn Research Center.

<sup>b</sup>Dimensions perpendicular and parallel to load axis.

<sup>c</sup>Performed at Precision Castparts Corporation.

<sup>d</sup>Within the neighborhood of several 0.01-in. shrinkage-type porosity.

<sup>e</sup>Multiple, spreadout shrinkage.

<sup>f</sup>Broke at microshrink, not gas porosity.

<sup>g</sup>Detected bigger defect nearby.

TABLE XII.—RANGE OF SCATTER IN FATIGUE STRENGTH DATA  
FOR  $\gamma$ -TiAl ALLOYS

Alloy	Virgin samples		Surface cracks		Threshold analysis	
	Range, MPa	Sample size, <i>n</i>	Range, MPa	Sample size, <i>n</i>	Range, MPa	Sample size, <i>n</i>
Cast-to-size 48-2-2	58	2	100	29	74	28
GEAE 47-2-2	141	9	100	23	96	16
Howmet 47-2-2	129	25	---	--	---	--
CMU 47-2-2	36	3	100	16	89	12
Cast-to-size ABB-2	24	2	80	12	63	12
ABB-23	30	2	60	6	40	6
NCG359E	---	--	60	7	61	7
95A	25	4	60	13	101	10

<sup>a</sup>Range is two times the standard error of the regression.

TABLE XIII.—FATIGUE THRESHOLDS FOR VARIOUS  $\gamma$ -TiAl ALLOYS

Alloy	Fatigue threshold, $K_{th}$ MPa $\sqrt{m}$	
	This report <sup>a</sup>	Literature values
Cast-to-size 48-2-2	8.8	---
GEAE 47-2-2	8.2	4.5 (ref. 33) 6 (ref. 64) 6.8 (ref. 40)
CMU 47-2-2	12.1	7 (ref. 6) 8 (ref. 54) 9 (ref. 56) 12 (ref. 6)
Cast-to-size ABB-2	9.9	8 (ref. 52) 8.5 (ref. 39)
ABB-23	11.0	9 (ref. 52)
NCG359E	11.0	---
95A	11.0	7 (ref. 60) 9 (ref. 6)
47XD	---	6.3 (ref. 65)
WMS	---	7 (ref. 40)

<sup>a</sup>Values were back-calculated using equation (3).

TABLE XIV.—FATIGUE RESULTS OF PREFRETTED GEAE 47-2-2 SAMPLES

Sample	Net section stress at failure, MPa	Cycles to failure	Failure type <sup>a</sup>	Defect area, mm	Net section stress at threshold, MPa	Number of steps to threshold	Minimum stress at threshold, MPa	Comments	Table showing fretting conditions
5-1-3	248	6 560	Face	0.163	0	0	0	Not at fret; surface defect on face	IV (c)
6-3-3	331	9 040	Leading edge	.001	317	12	16	Not at fret; very small surface defects	IV (b)
5-1-6	386	12 400	Face	.012	372	9	19	At pore near fret	IV (d)
063-03-3	282	11 200	Leading edge	0	268	10	13	Not at fret; very lamellar leading edge	IV (a)

<sup>a</sup>Indicates where fatigue failure originated.

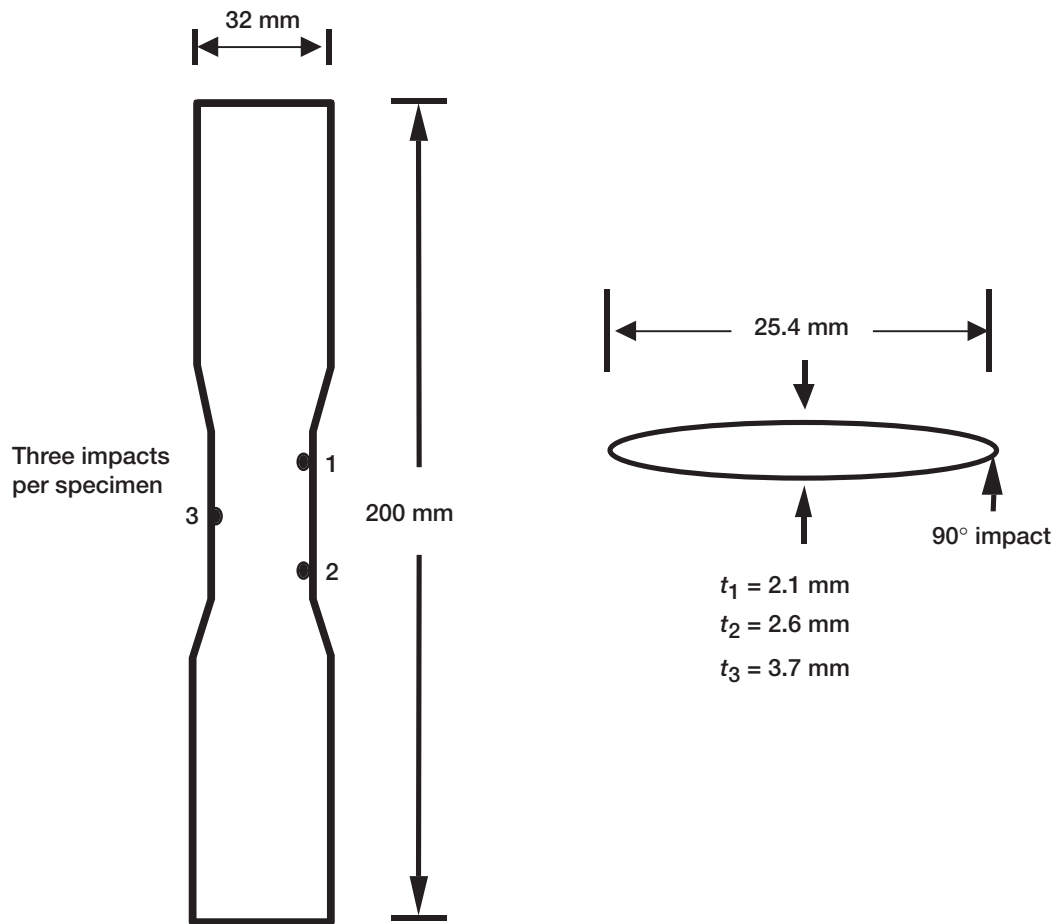


Figure 1.—Cast-to-shape impact specimen design. Center thickness of specimens is represented by  $t$ . Points 1, 2, and 3 represent the impact locations.

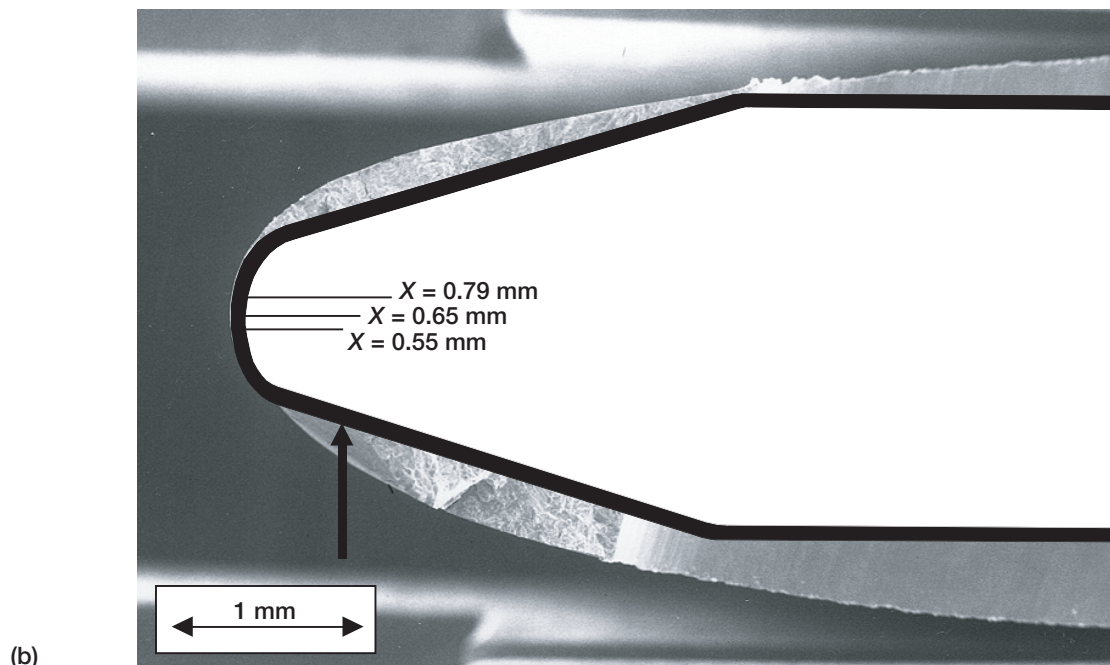
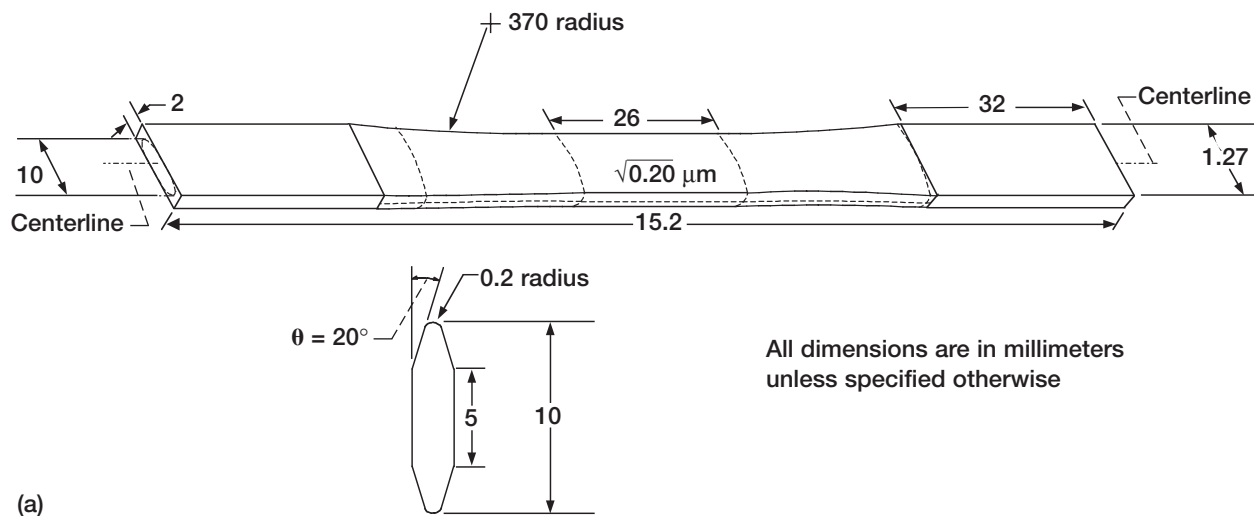


Figure 2.—Specimen configurations. (a) Machined impact specimens. (b) Overlay of leading edge for machined and cast-to-size samples. X illustrates various impact locations relative to the leading edge.

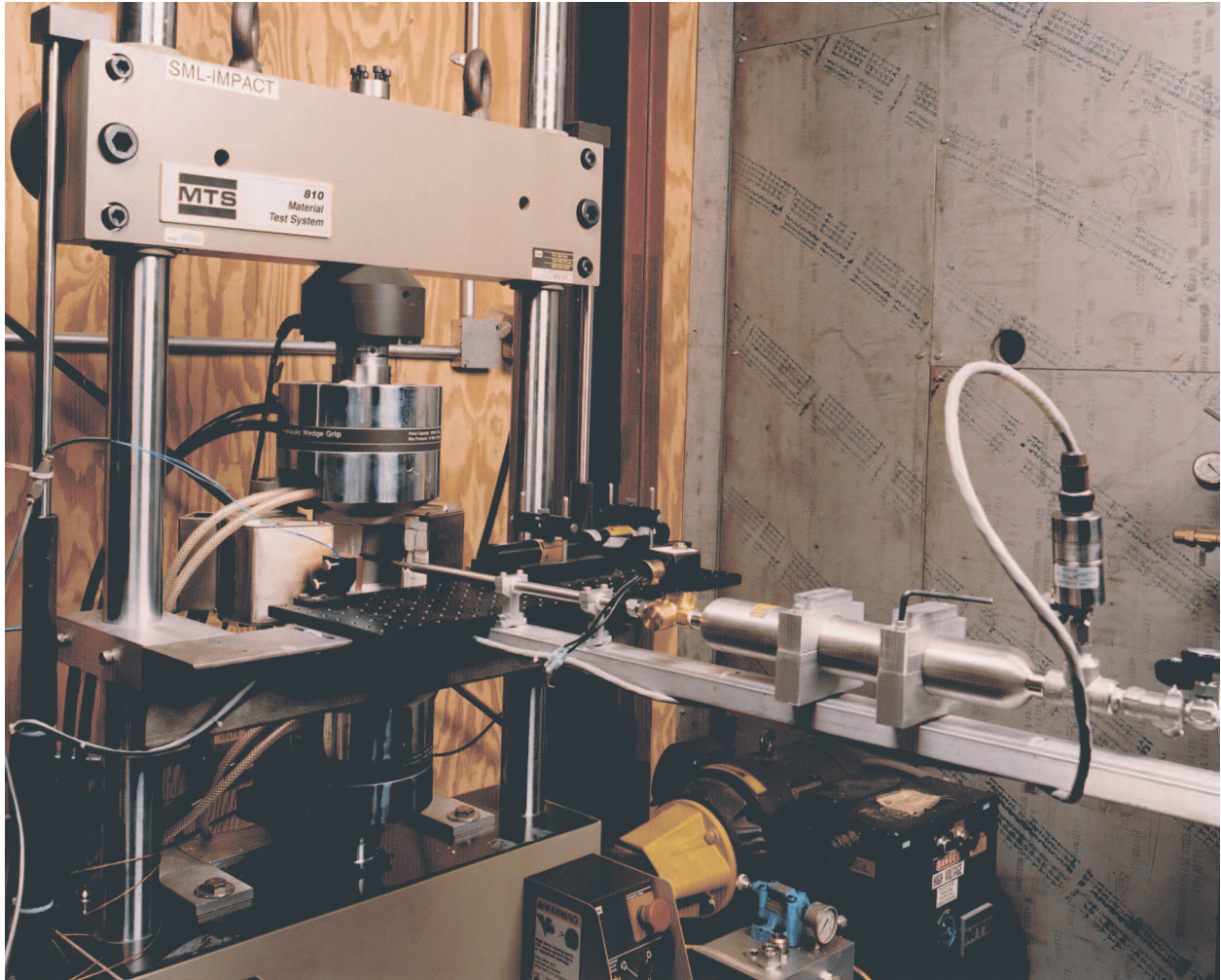


Figure 3.—Ballistic impact rig.

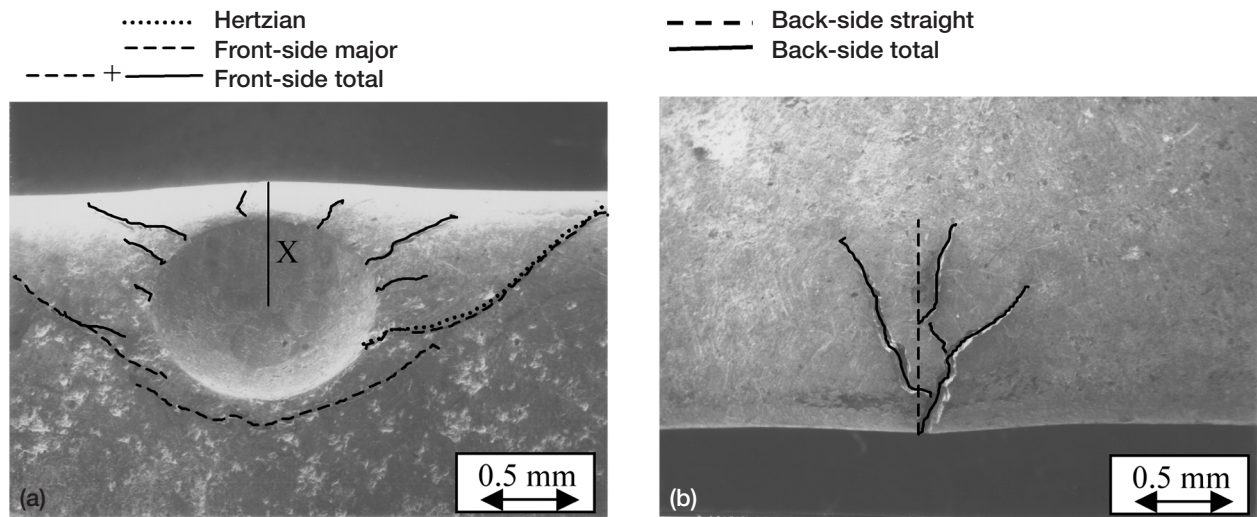


Figure 4.—Crack measurements for  $\gamma$ -TiAl. (a) Front side showing impact location, X. (b) Back side.

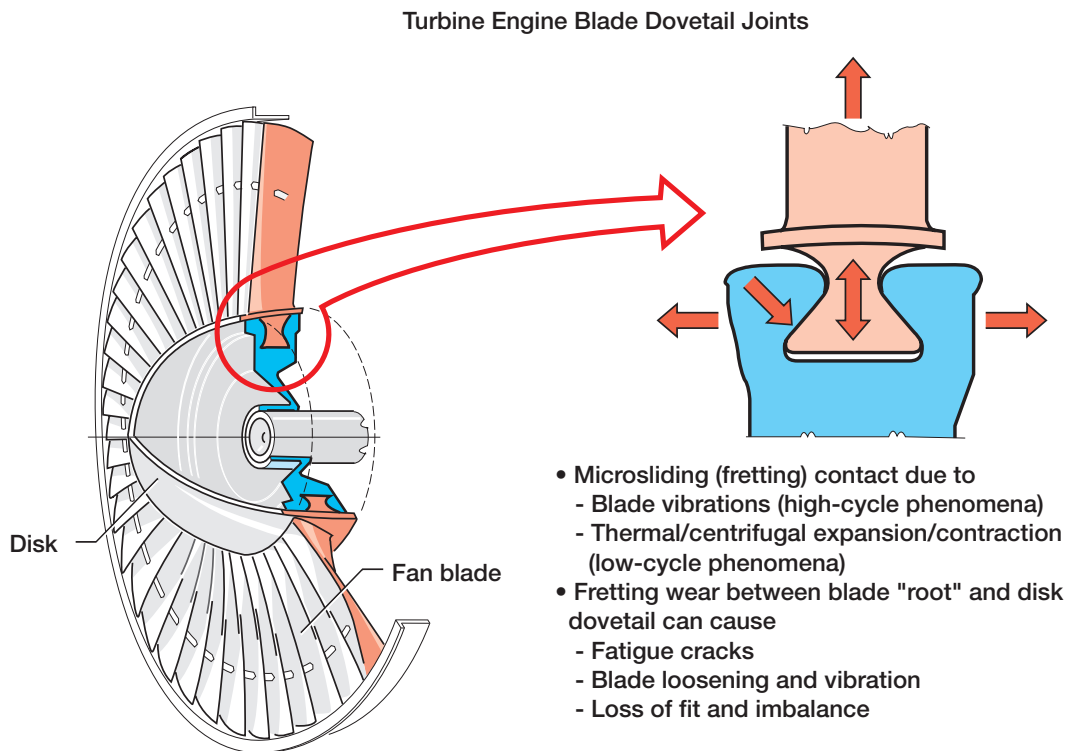


Figure 5.—Blade and disk dovetail configurations.

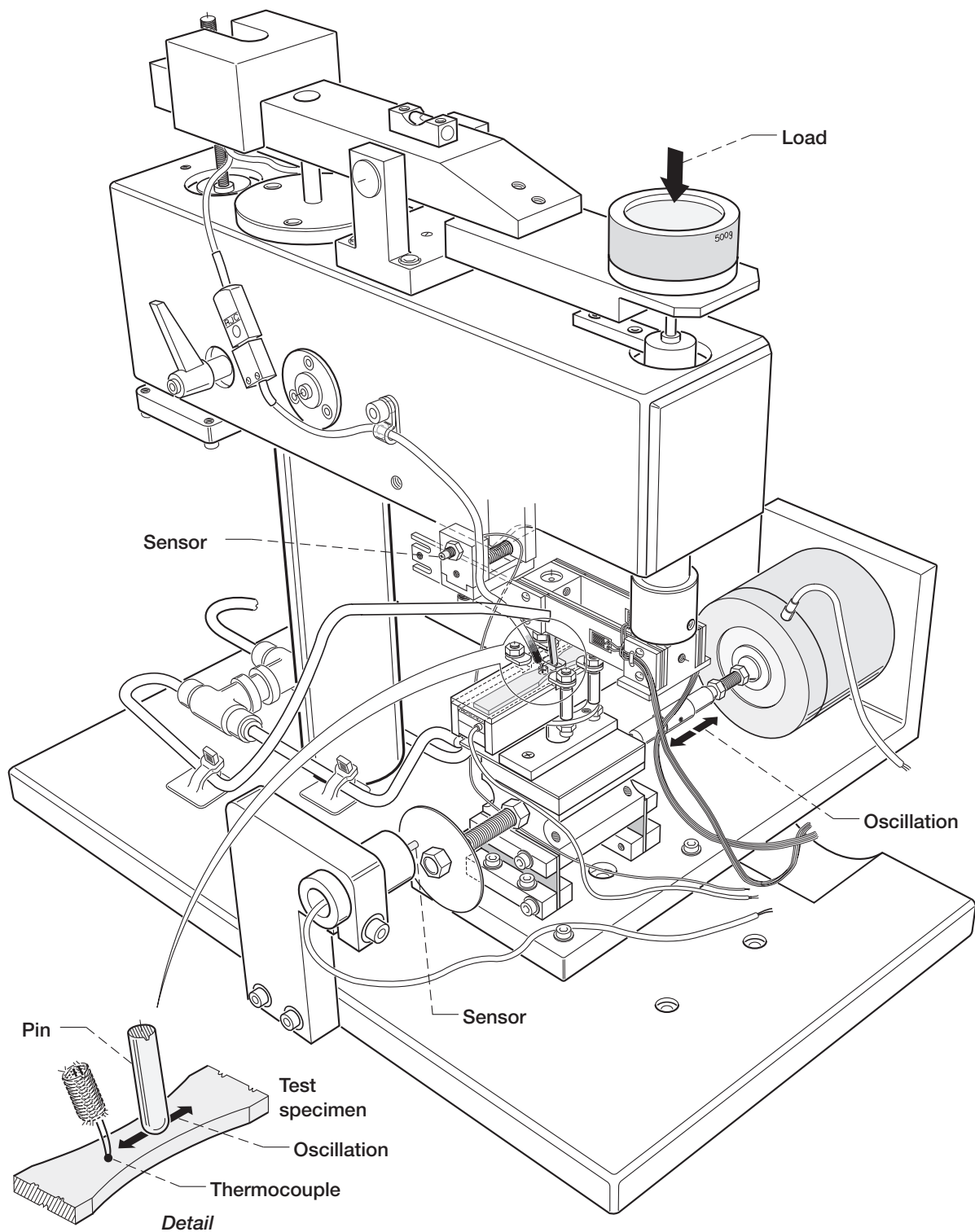


Figure 6.—Fretting apparatus.

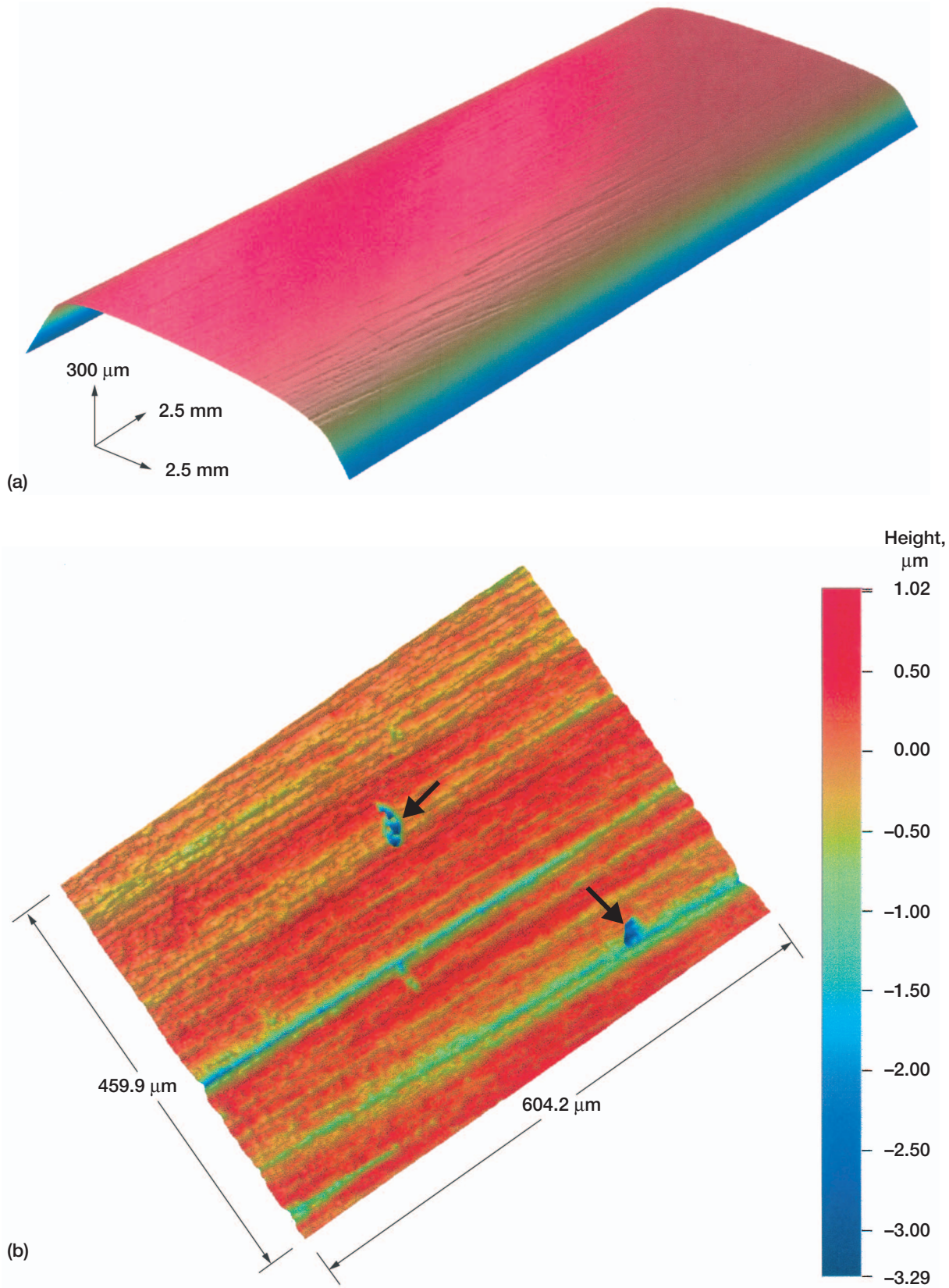


Figure 7.—Three-dimensional, optical interferometry image of gage section of machined Ti-47-2-2 fatigue specimen. (a) Homogeneous surface texture with grooves. (b) Surface texture with casting porosity (arrows).

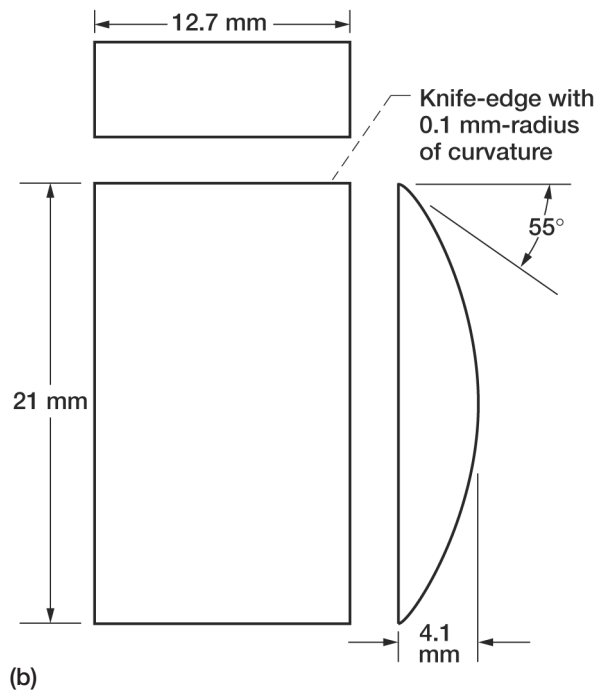
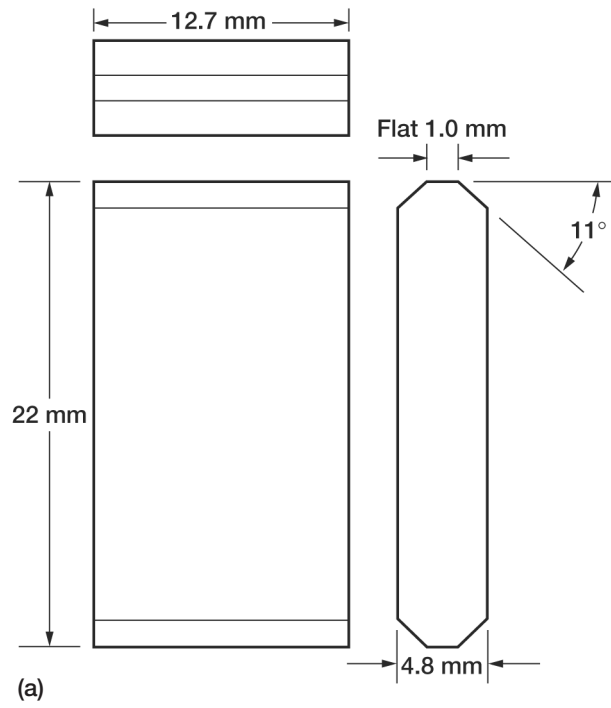
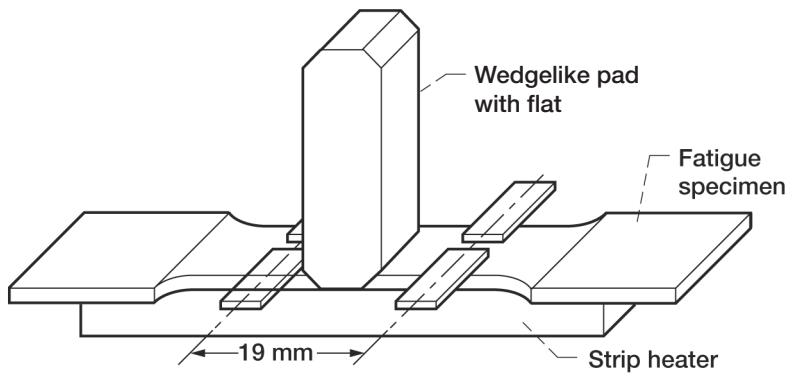
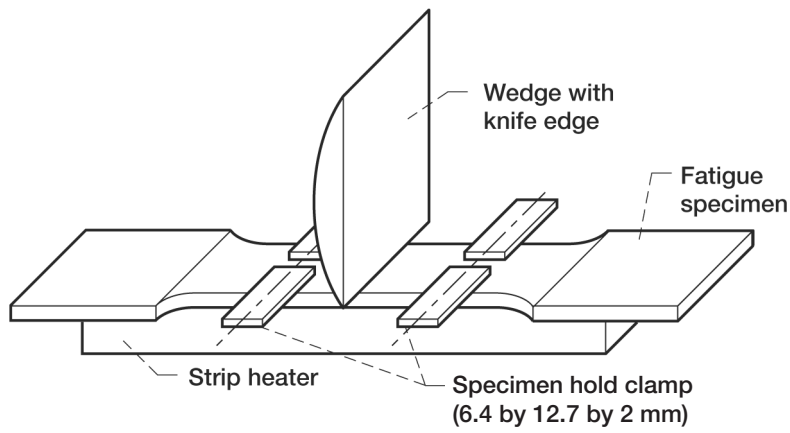


Figure 8.—IN718 contact pads in fretting tests. (a) Wedgelike pad with flats. (b) Wedge with knife edges.



(a)



(b)

Figure 9.—Fatigue specimen and contact configuration. (a) Wedgelike pad with flat on fatigue specimen. (b) Wedge with knife edge on fatigue specimen.

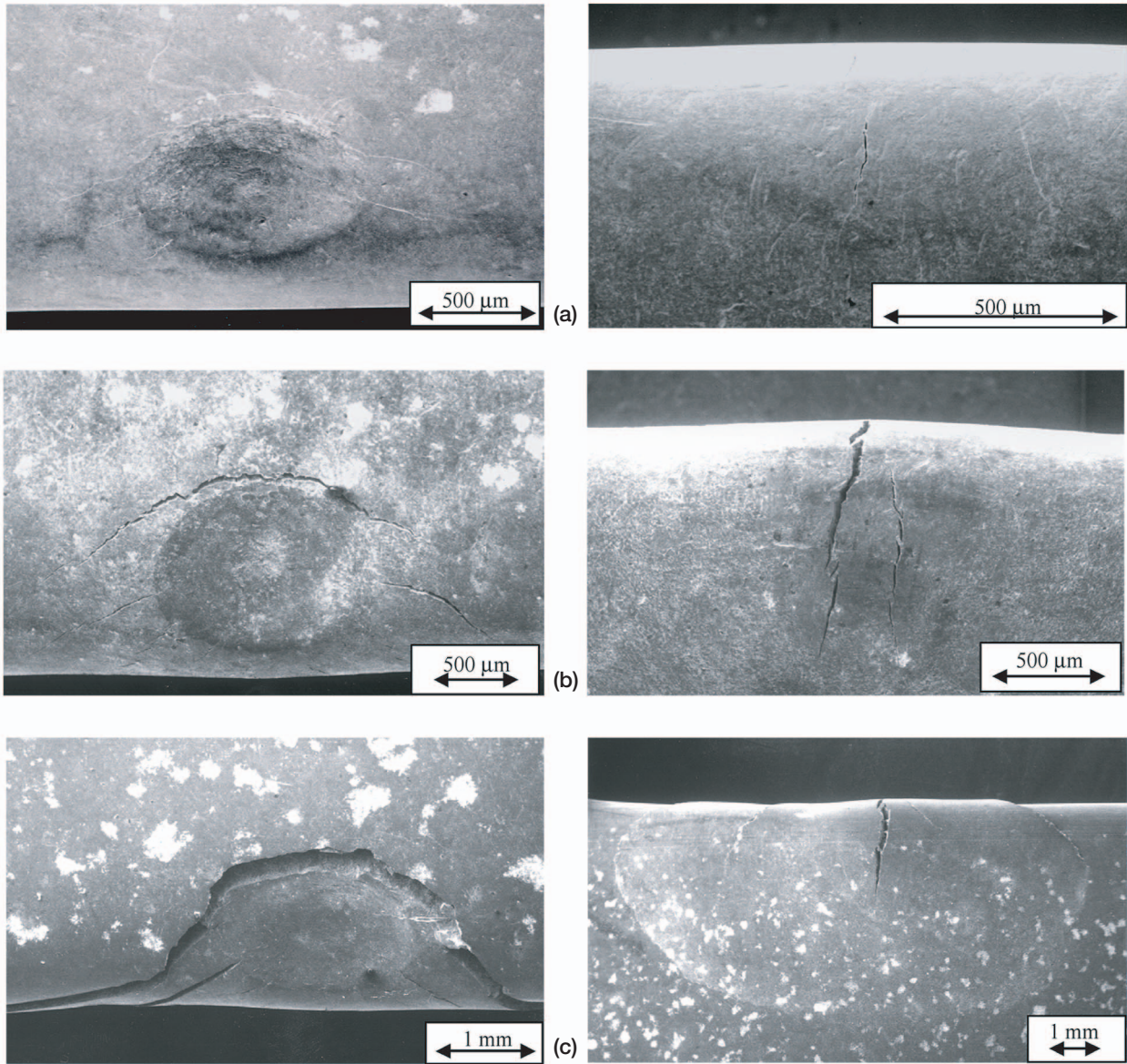


Figure 10.—Front-side (left) and back-side (right) cracking patterns on Ti-48-2-2 samples modeled in study. (a) Low-energy impact, 008-10-3. (b) Medium-energy impact, 005-08-3. (c) High-energy impact, 009-08-2.

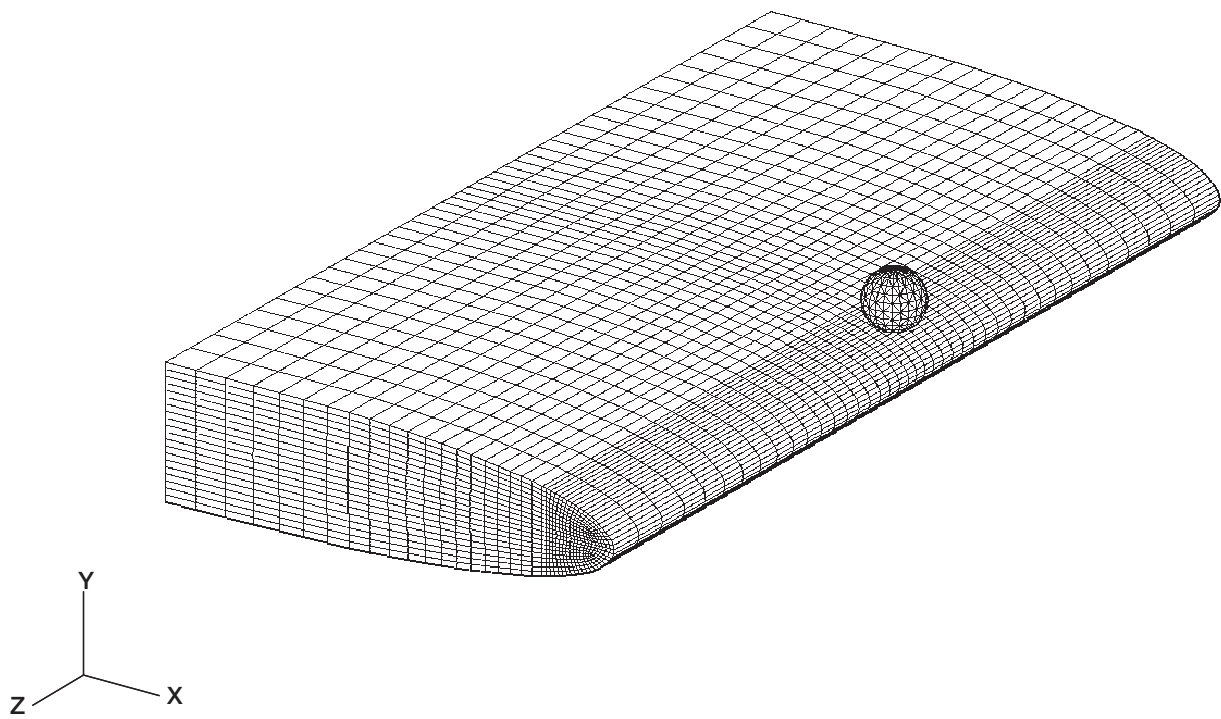


Figure 11.—Finite-element model of specimen 008-10-3 and 1.6-mm spherical projectile.

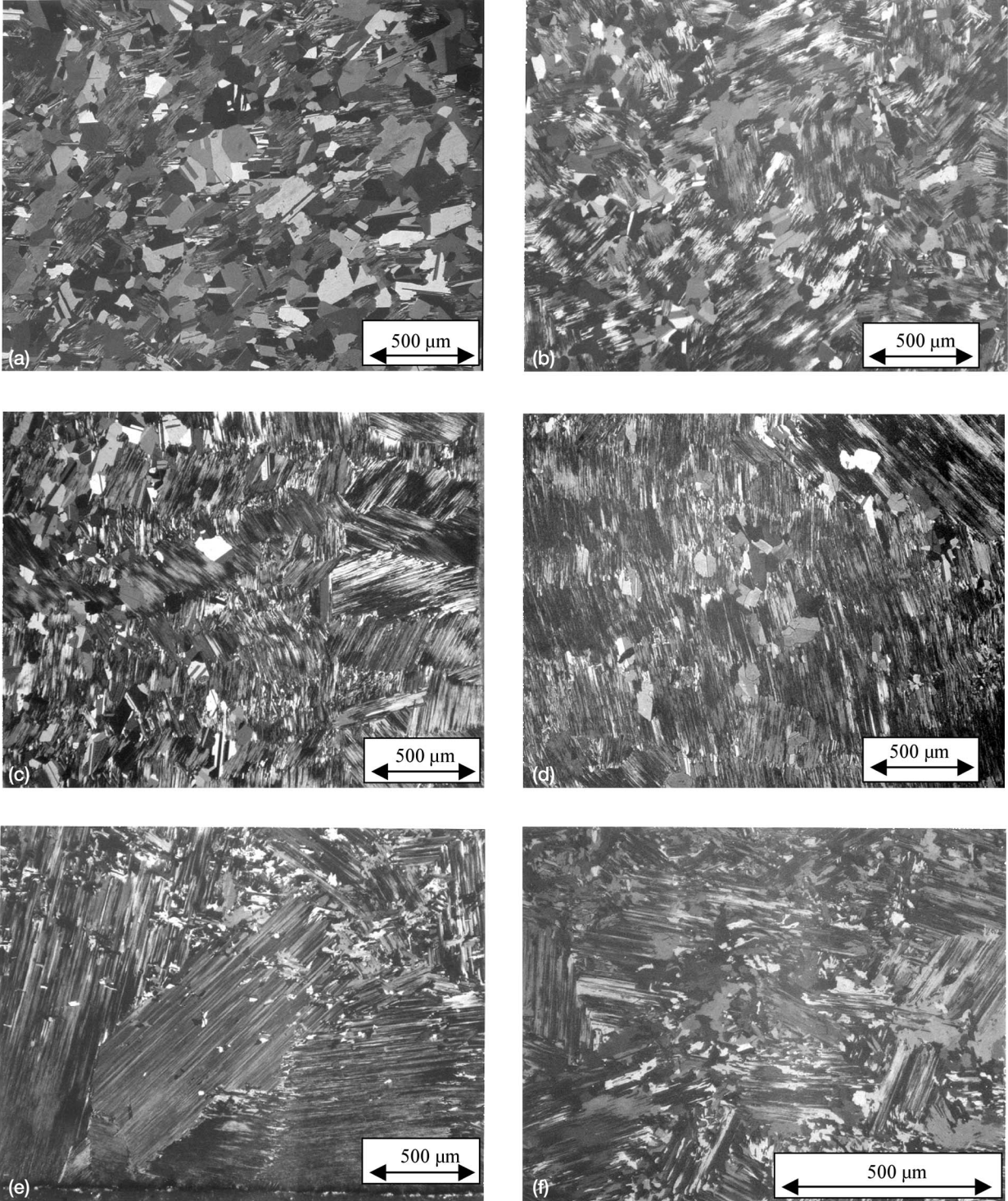


Figure 12.—As-received microstructure. (a) Cast-to-size Ti-48-2-2. (b) GEAE Ti-47-2-2, cast and machined. (c) CMU Ti-47-2-2 low aluminum, cast and machined. (d) Howmet Ti-47-2-2, cast and machined. (e) Cast-to-size ABB-2, near edge. (f) Cast-to-size ABB-2, center. (g) ABB-23, cast and machined. (h) NCG359E, cast and machined. (i) 95A, forged and machined.

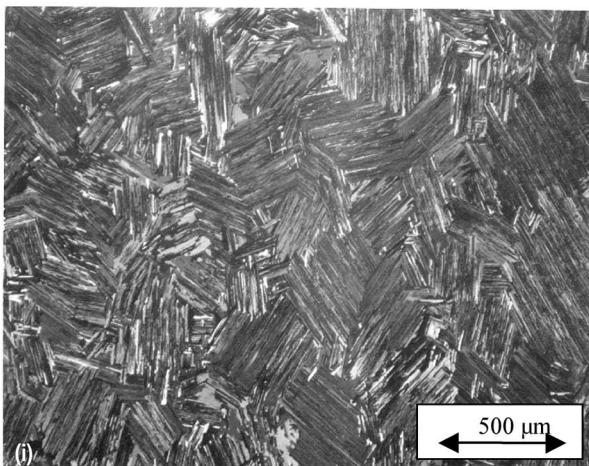
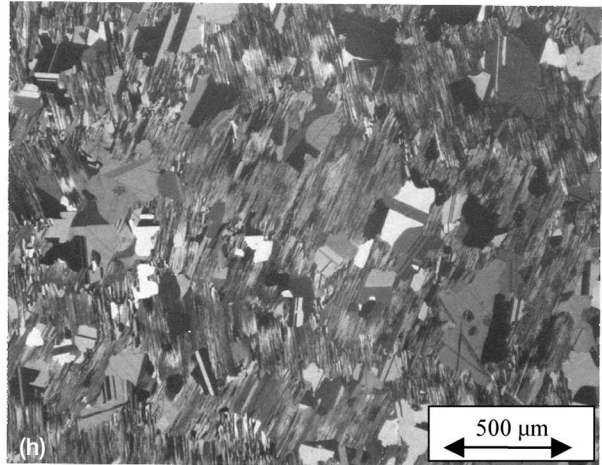
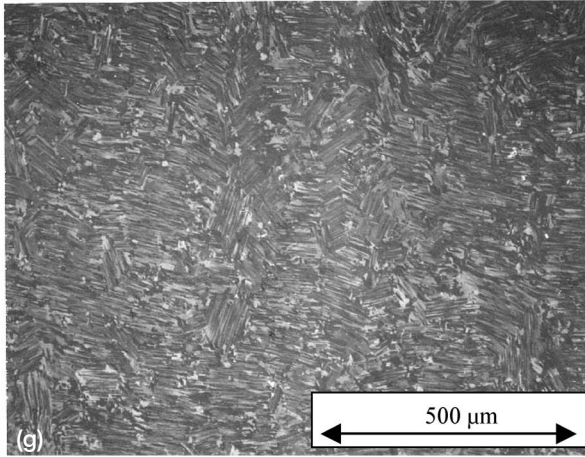


Figure 12.—Concluded. (g) ABB-23, cast and machined. (h) NCG359E, cast and machined. (i) 95A, forged and machined.

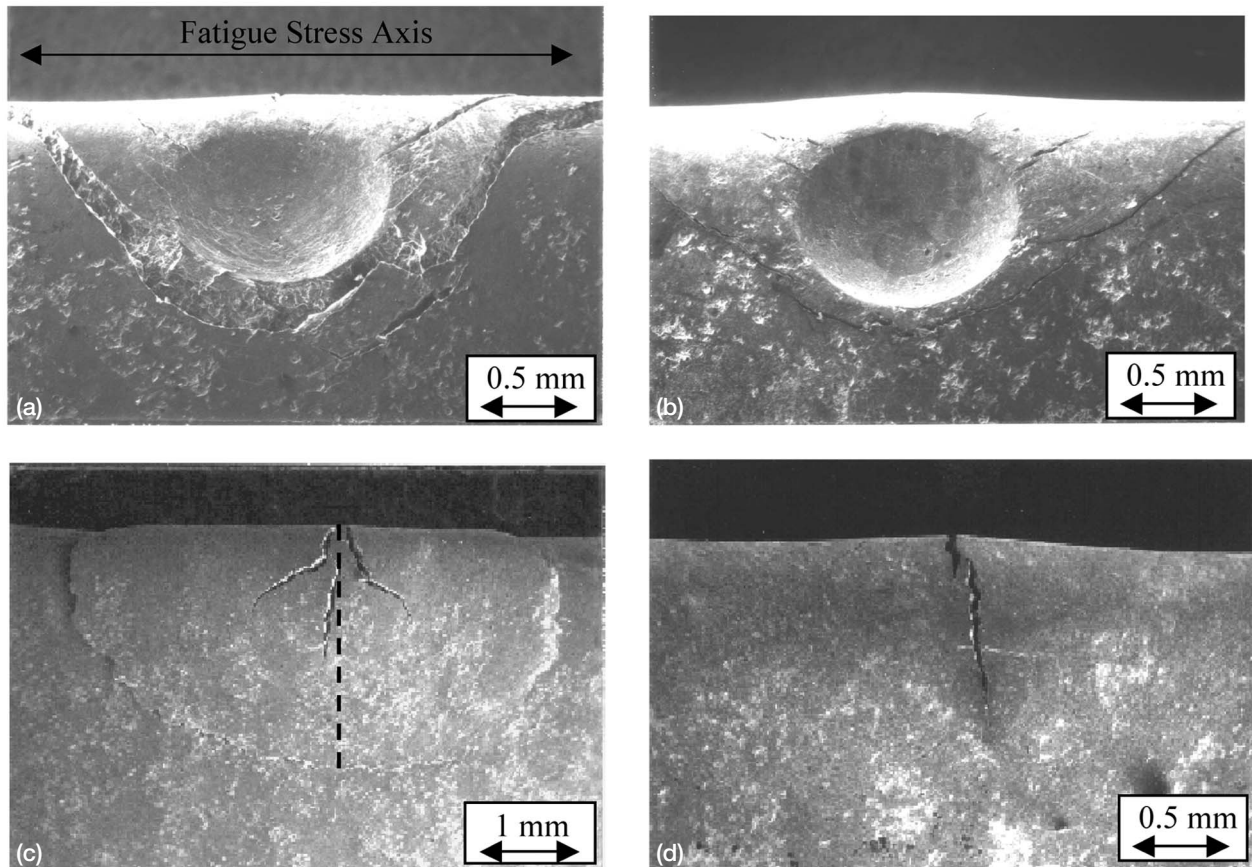


Figure 13.—Front and corresponding back-side damage after impacting cast-to-size Ti-48-2-2 with 0.33 J of energy. Fatigue stress axis is parallel to specimen edge and perpendicular to back-side cracks. (a) Front of thin sample. (b) Front of thick sample. (c) Back side of thin sample. (d) Back side of thick sample. All impacts used 1.6-mm projectiles. Thin samples, (a) and (c), were nearly blown out, and back-side straight crack length measurement for blowout or near blowout is demonstrated.

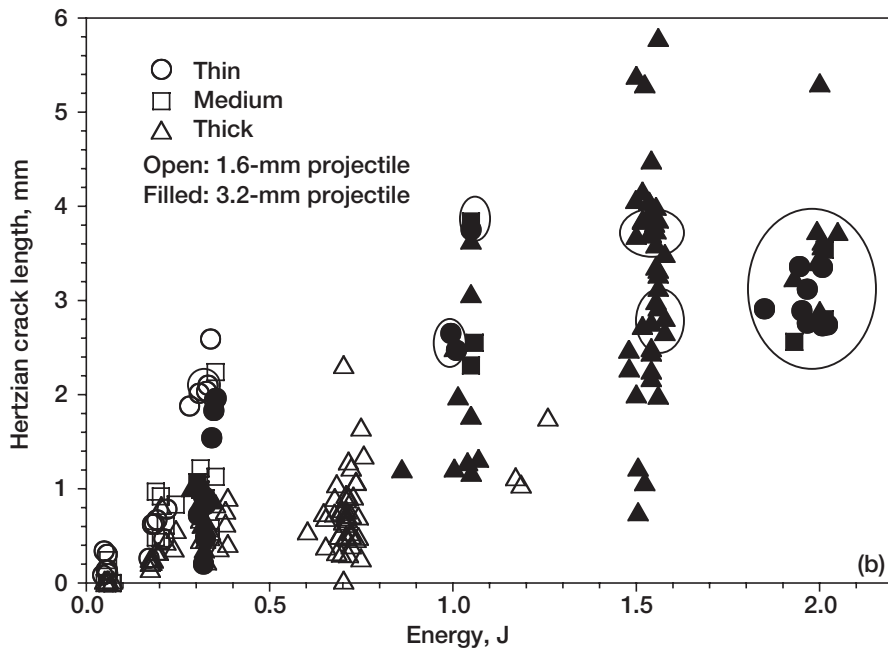
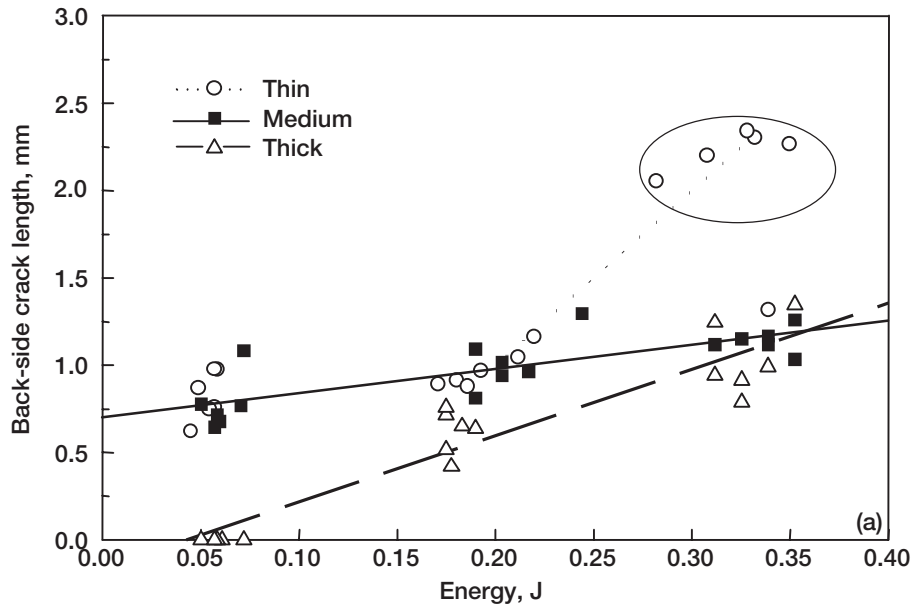


Figure 14.—Crack lengths for cast-to-size Ti-48-2-2 as function of impact energy. All samples impacted at 260 °C. Majority of data within circles are for blown-out specimens. (a) Back-side crack lengths for low-energy impacts. (b) Hertzian crack lengths over a wider impact energy range. (c) Back-side crack lengths over wider impact energy range.

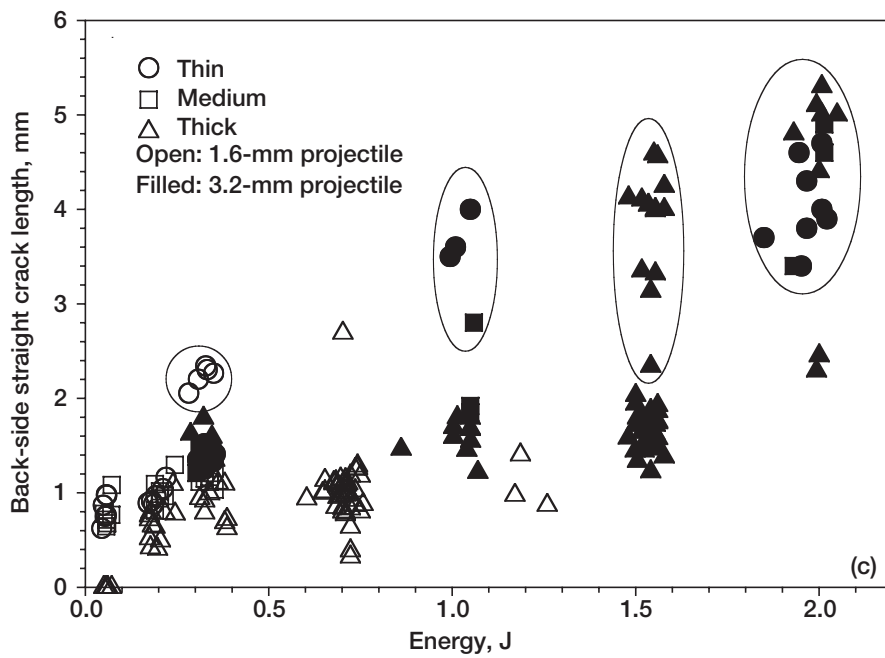
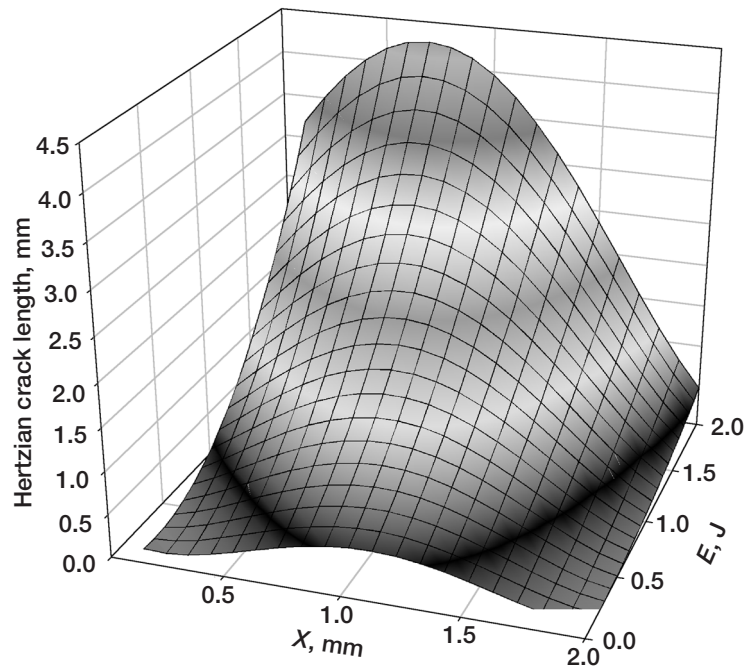
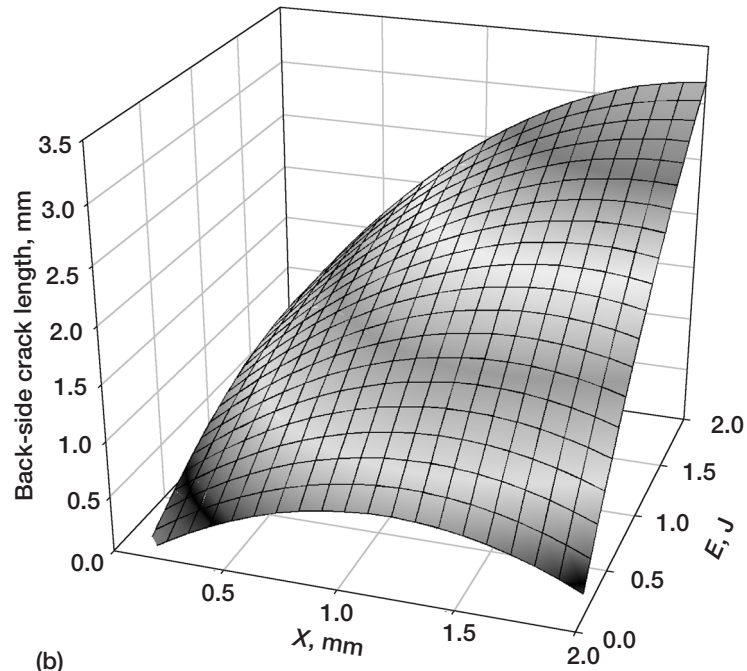


Figure 14.—Concluded. (c) Back-side crack lengths over wider impact energy range.



(a)



(b)

Figure 15.—Three-dimensional models depicting crack length as function of impact energy  $E$  and distance between impact and specimen edge  $X$ . (a) Hertzian. (b) Back-side. Models only valid for thick specimens impacted at 260 °C with no blowouts.

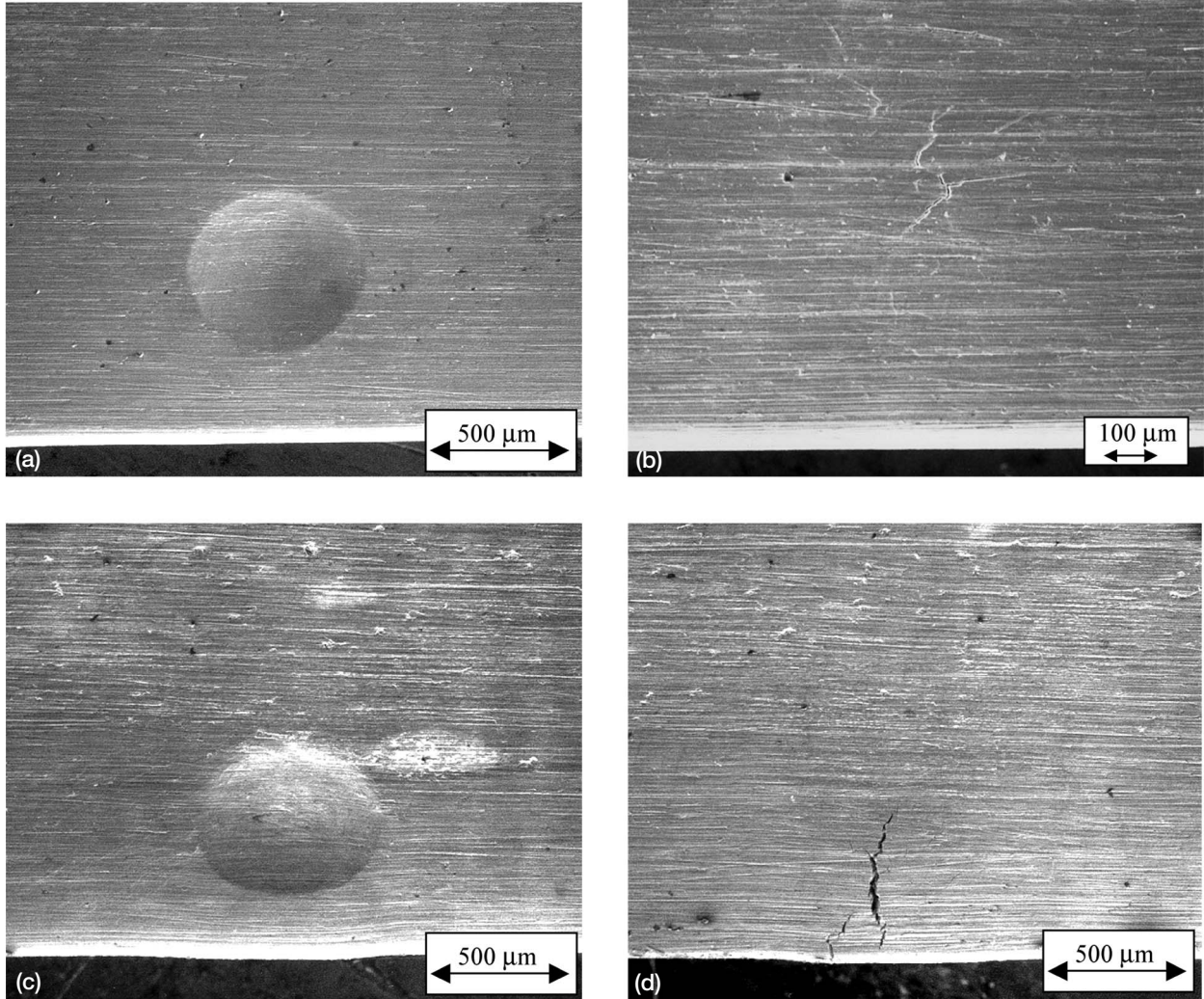


Figure 16.—Low-energy (0.06-J) impacts of machined GEAE Ti-47-2-2 samples. Little damage is on front side but variable damage on back side that was dependent on distance between impact and specimen edge. (a) Front-side damage. (b) Back-side damage. (c) Front-side damage. (d) Back-side damage.

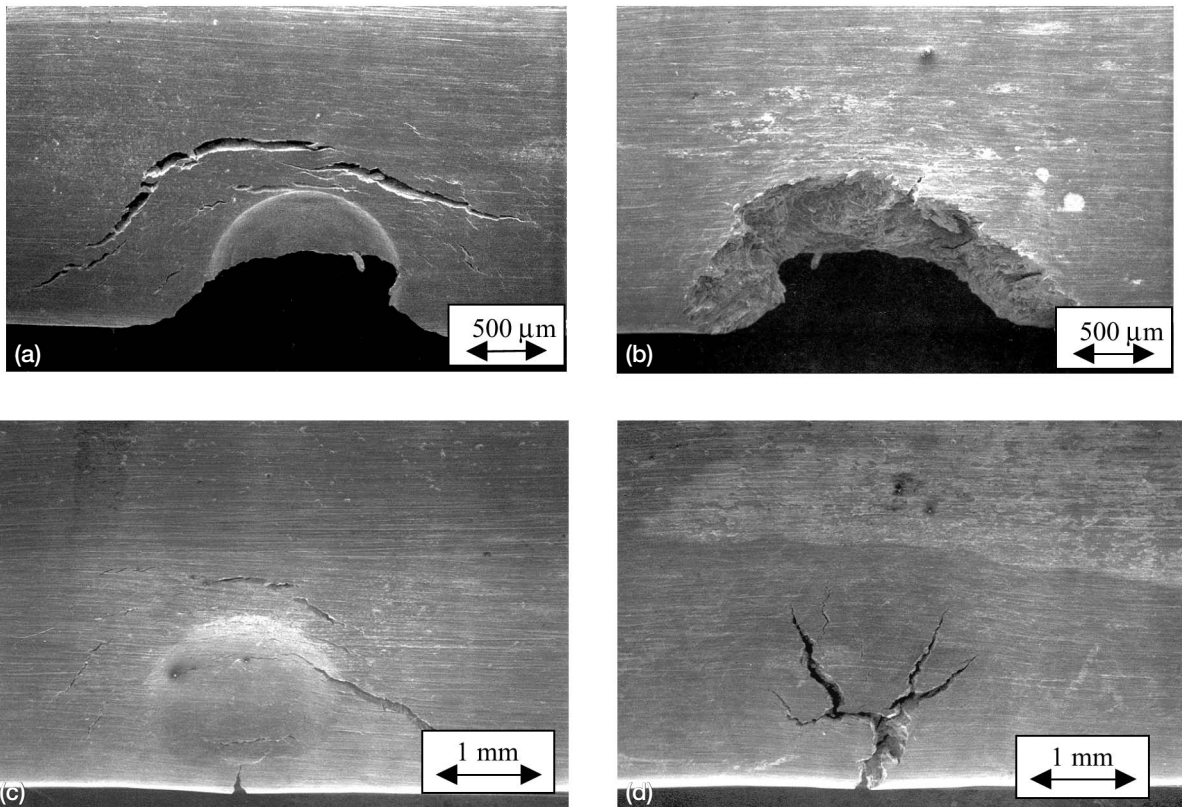


Figure 17.—Impact of machined GEAE Ti-47-2-2 sample. (a) Front side of intermediate-energy impact (0.79 J) with 1.6-mm projectile, showing partial blowout. (b) Back side of partial blowout. (c) Front side of high-energy impact (1.46 J) with 3.2-mm projectile. (d) Back side of high-energy impact.

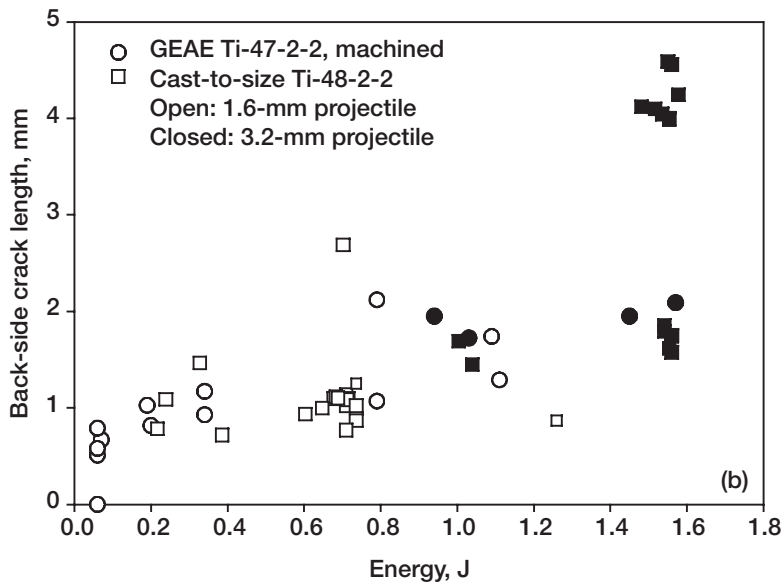
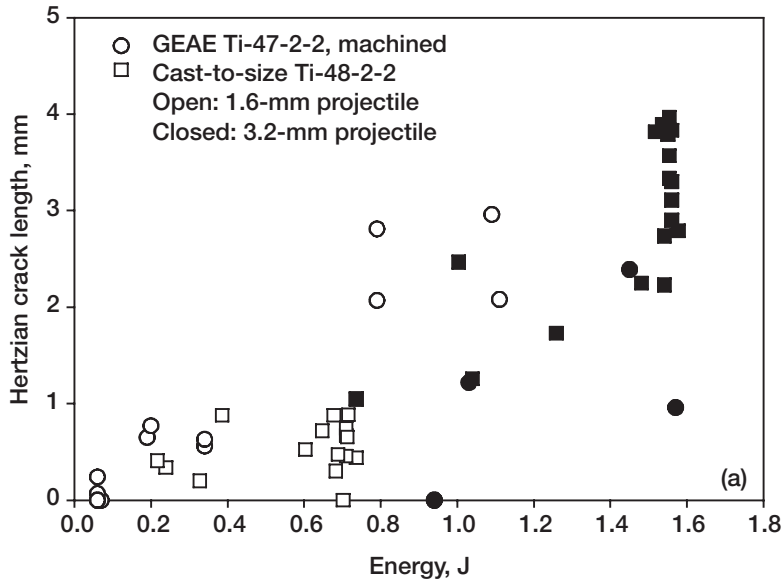


Figure 18.—Comparison of crack lengths as function of impact energy for machined GEAE Ti-47-2-2 and cast-to-size Ti-48-2-2 for different projectile sizes. (a) Hertzian crack lengths. (b) Back-side crack lengths.

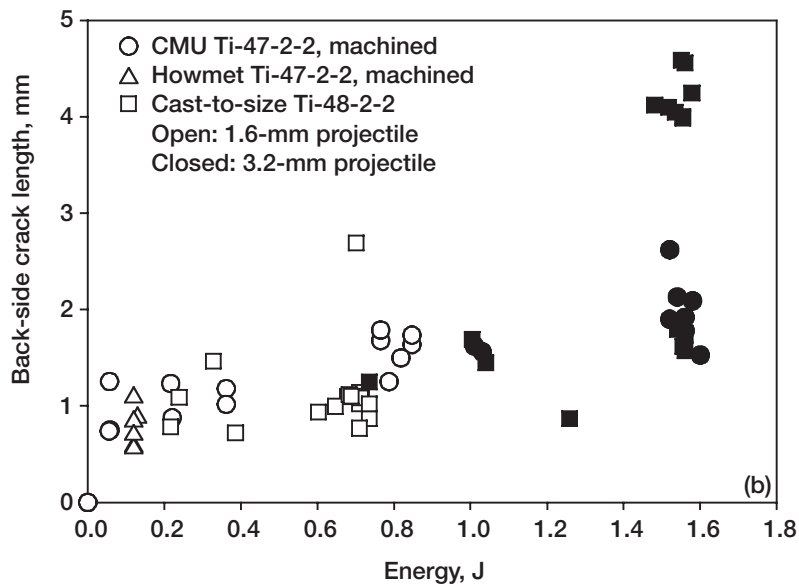
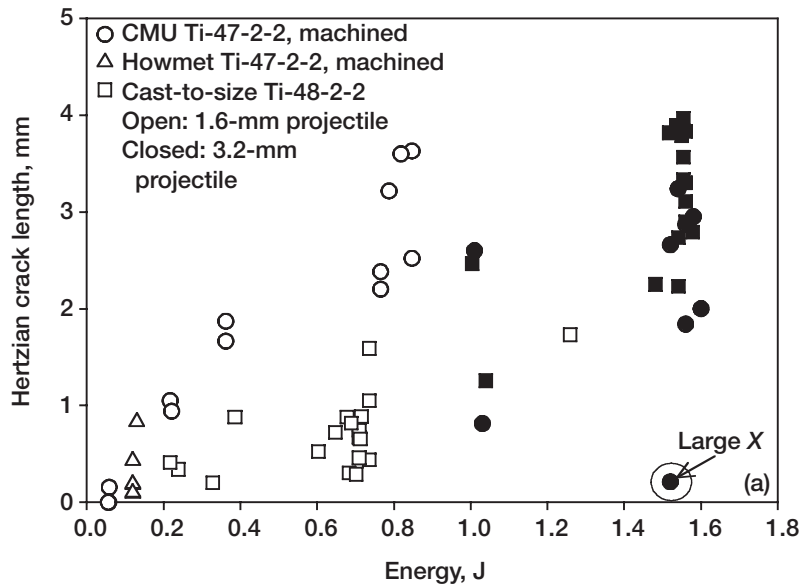


Figure 19.—Crack lengths of CMU Ti-47-2-2 and Howmet Ti-47-2-2 as function of impact energy compared with cast-to-size Ti-48-2-2 crack lengths for different projectile sizes. (a) Hertzian crack lengths. (b) Back-side crack lengths.

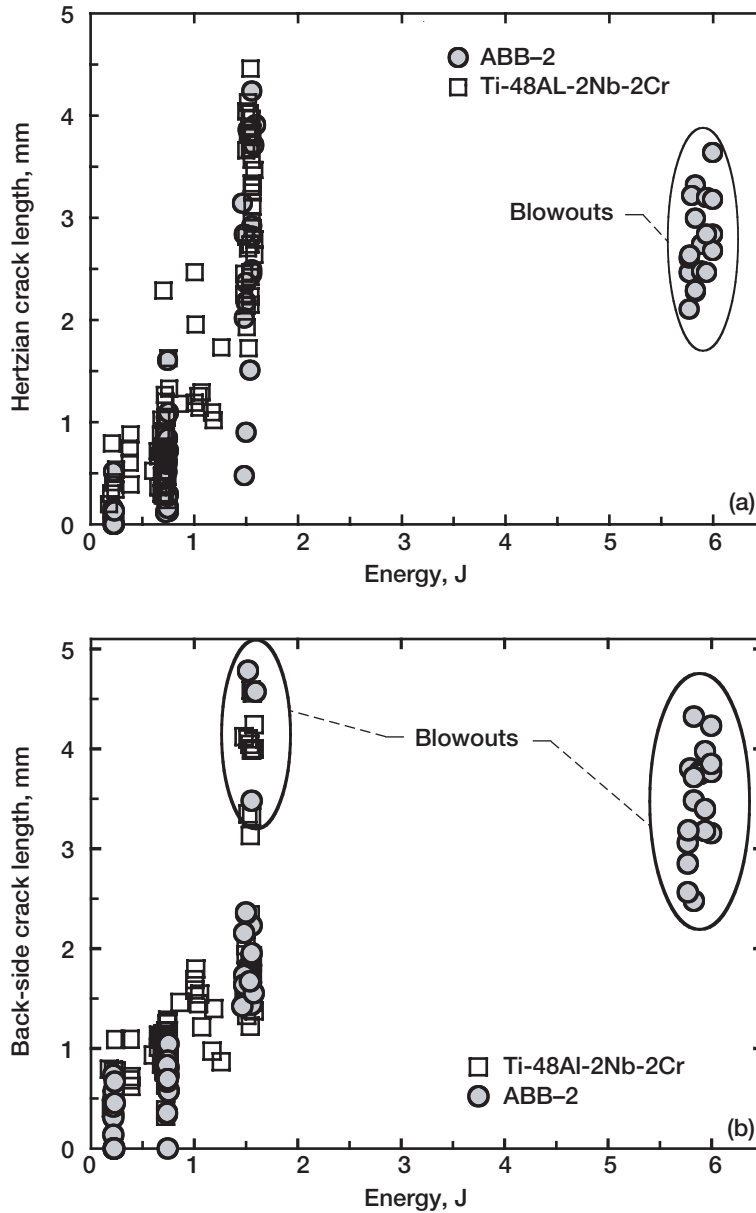


Figure 20.—Comparison of crack lengths of ABB-2 and cast-to-size Ti-48-2-2 as function of impact energy. (a) Hertzian crack lengths. (b) Back-side crack lengths. Some impacts were blown out at 1.5 J of energy, as indicated in (b), but could not be circled in (a) as the blowouts were scattered within the data, and the Hertzian cracks ranged in length from 2.3 to 4.0 mm.

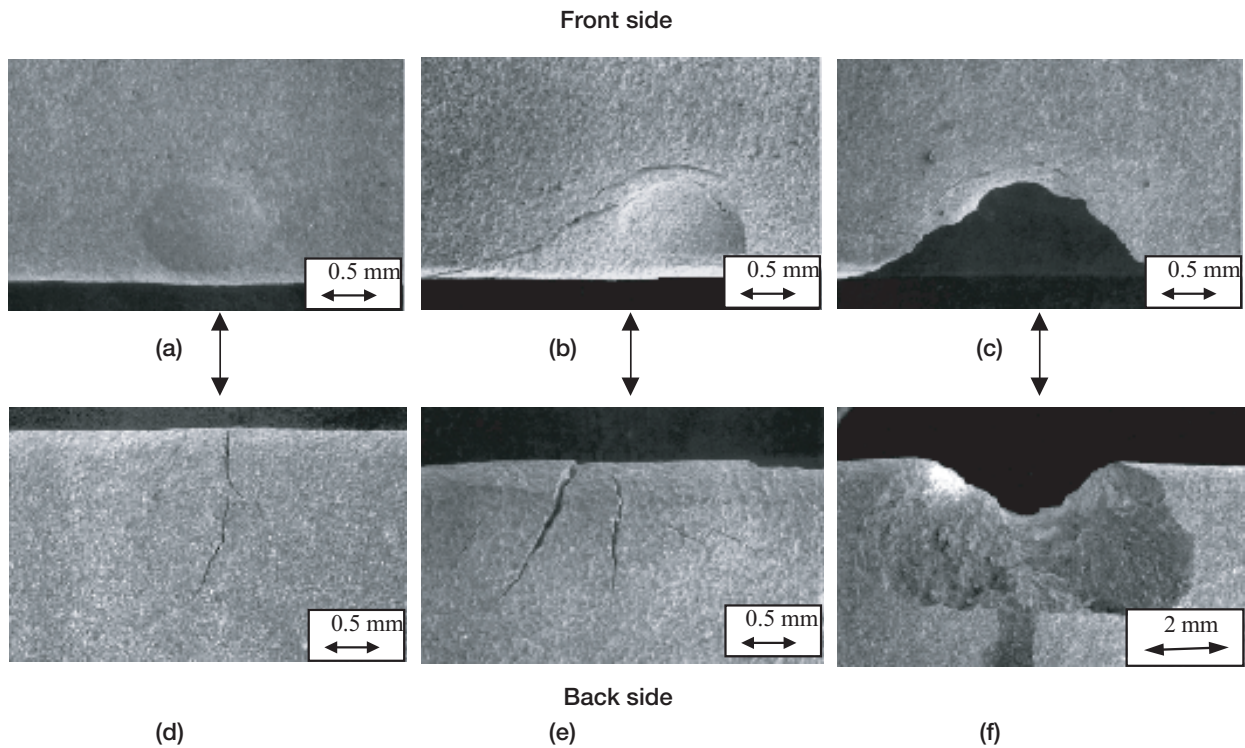


Figure 21.—High-energy (1.5-J) impacts for ABB-2 alloy. (a), (b), and (c) Wide range of front-side Hertzian crack lengths (0.48 to 3.1 mm). (d), (e), and (f) Corresponding back-side crack lengths, which are more consistent. Front and back side of blowout are shown in (c) and (f), illustrating half-cone shape of Hertzian crack.

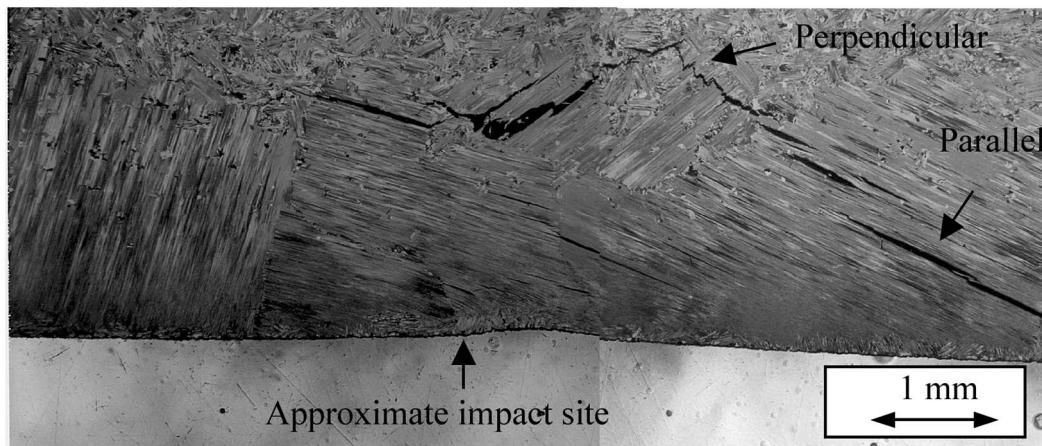


Figure 22.—Hertzian crack morphology in ABB-2 influenced by large lamellar grains near the sample edge. Hertzian cracks propagated easily parallel to lamellar grains but exhibited more torturous crack path when perpendicular to lamellar grains.

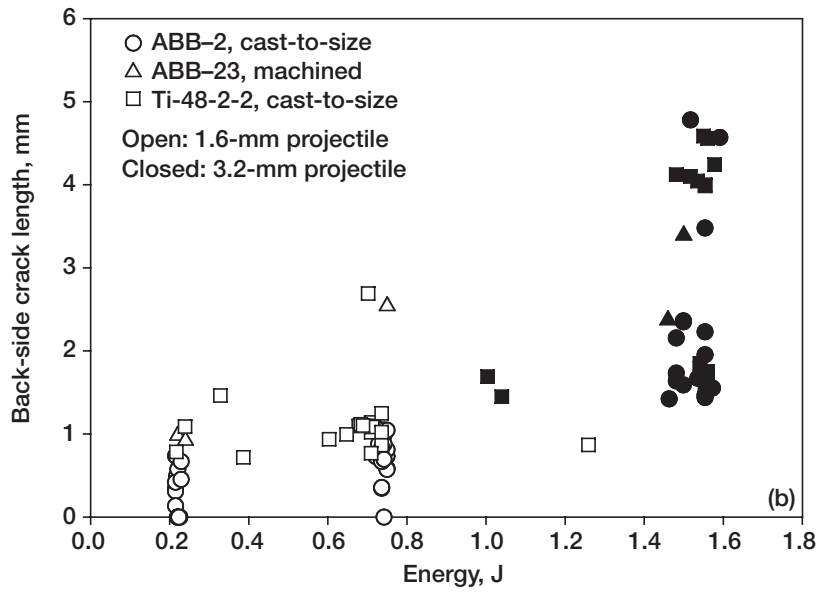
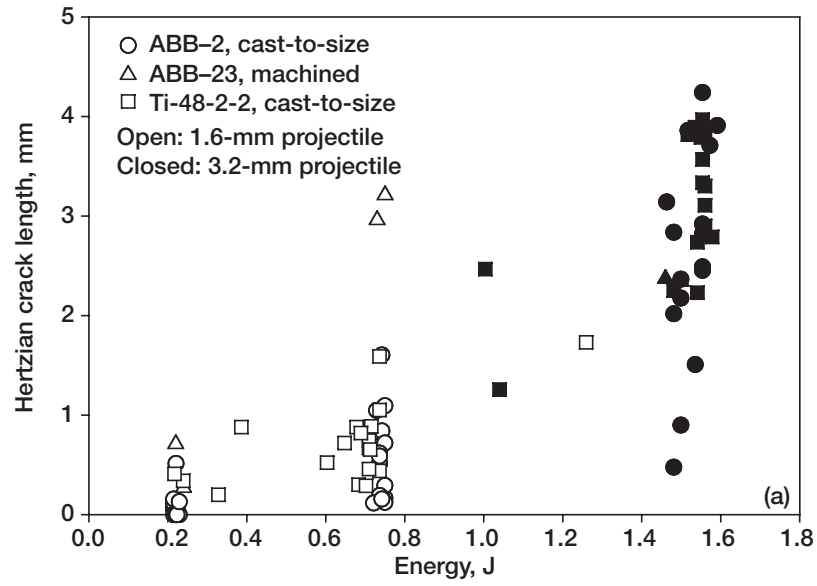


Figure 23.—Crack lengths of cast-to-size ABB-2, cast-to-size Ti-48-2-2, and machined ABB-23 as function of impact energy. (a) Hertzian. (b) Back side.

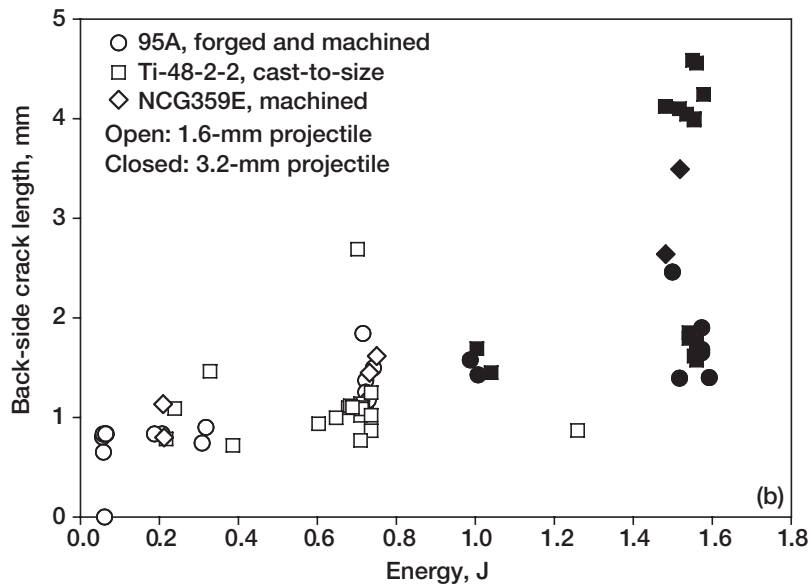
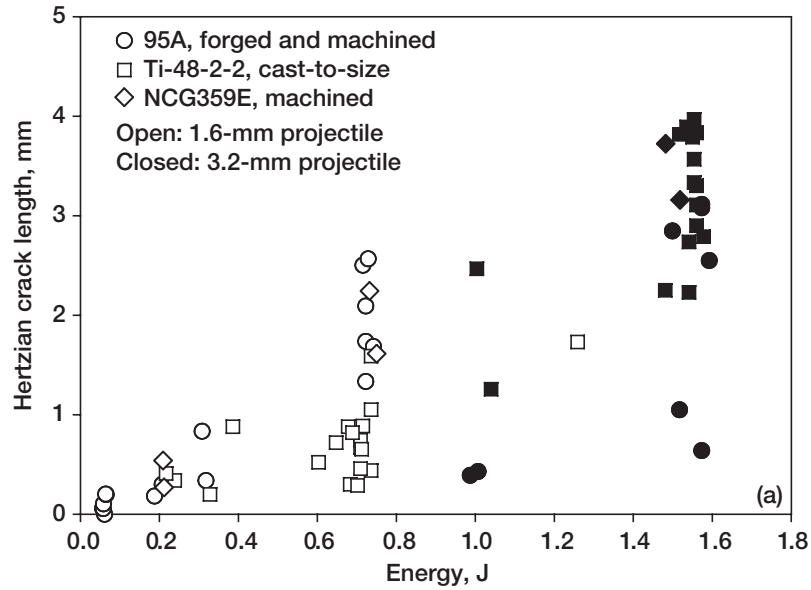


Figure 24.—Crack lengths as function of impact energy for machined 95A and NCG359E compared with cast-to-size Ti-48-2-2. (a) Hertzian. (b) Back side.

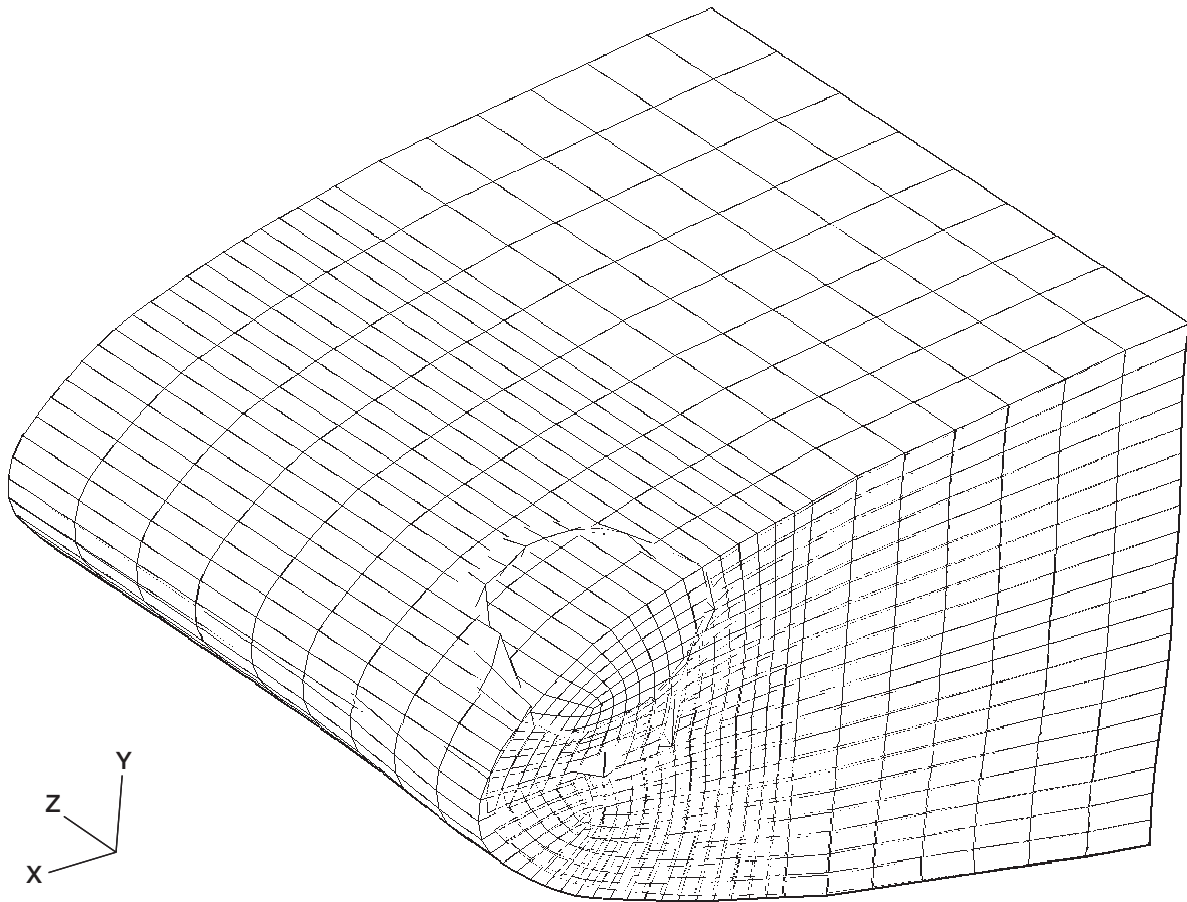


Figure 25.—Deformed shape of Ti-48-2-2 specimen 005-08-3. Bending in plane of specimen and in plane normal to it.

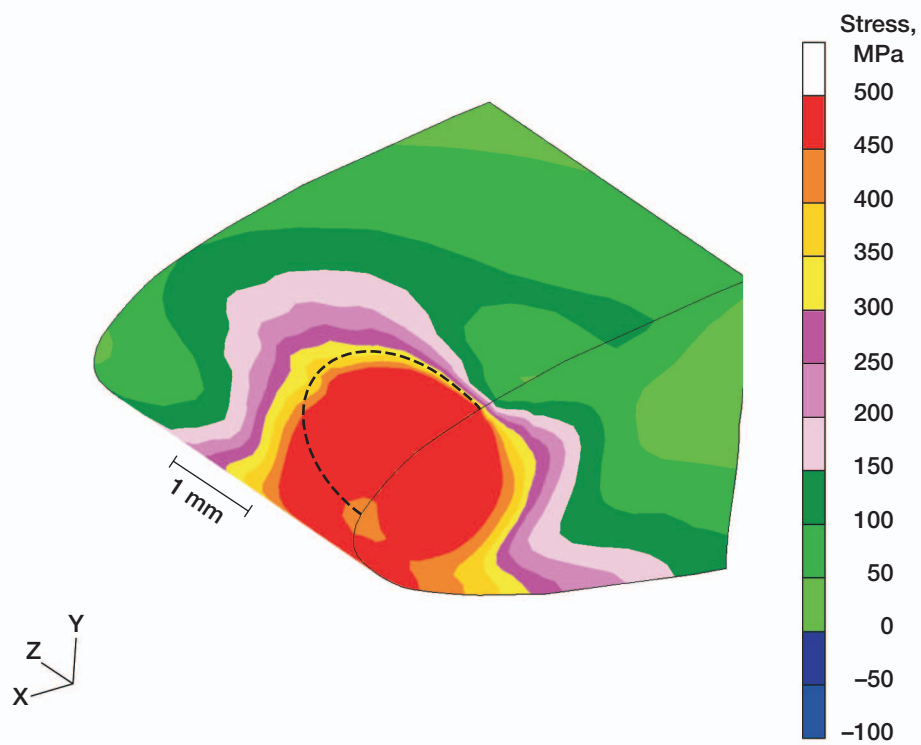


Figure 26.—Prediction of von Mises stress on front side of Ti-48-2-2 after low-energy impact (specimen 008-10-3). Dashed line is cracking zone.

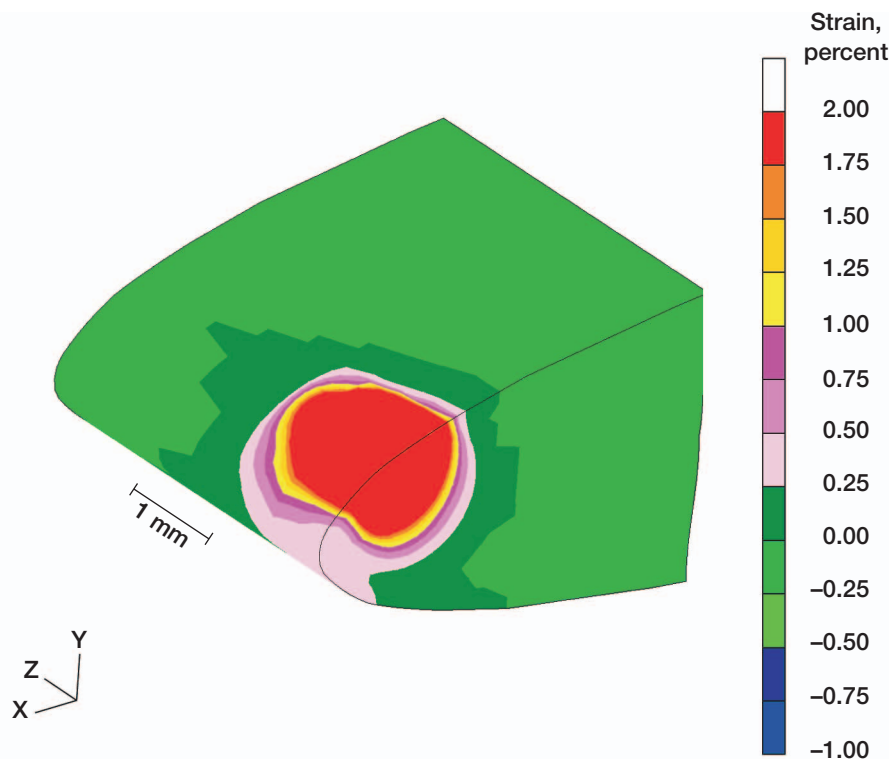


Figure 27.—Prediction of von Mises plastic strain on front side of Ti-48-2-2 after low-energy impact (specimen 008-10-3).

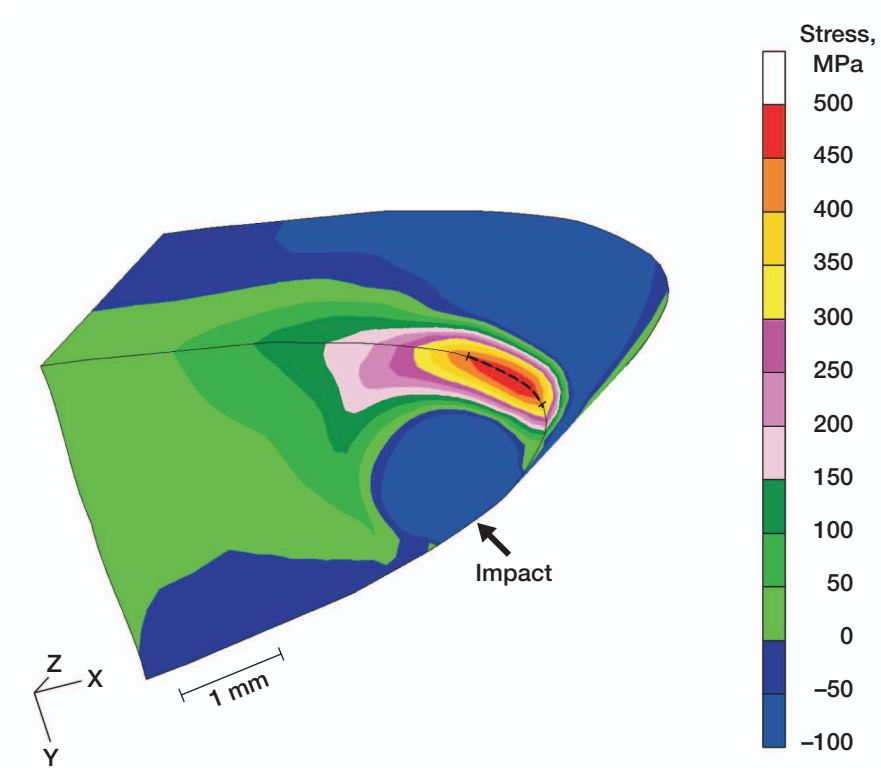


Figure 28.—Prediction of z stress on back side of Ti-48-2-2 after low-energy impact (specimen 008-10-3). Dashed line is cracking zone.

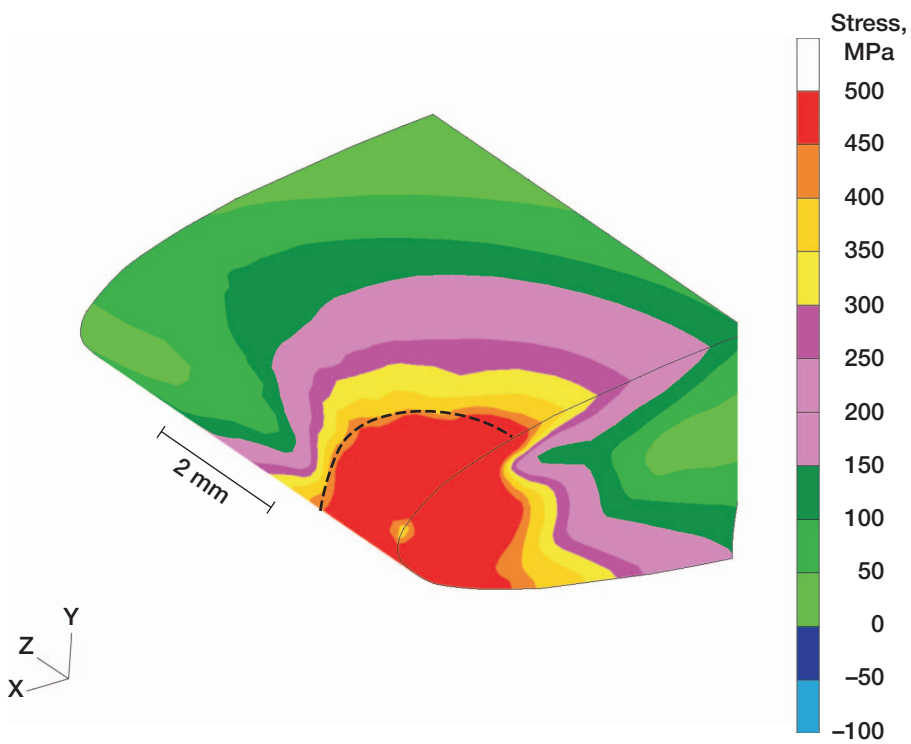


Figure 29.—Prediction of von Mises stress on front side of Ti-48-2-2 after intermediate-energy impact (specimen 005-08-3). Dashed line is cracking zone.

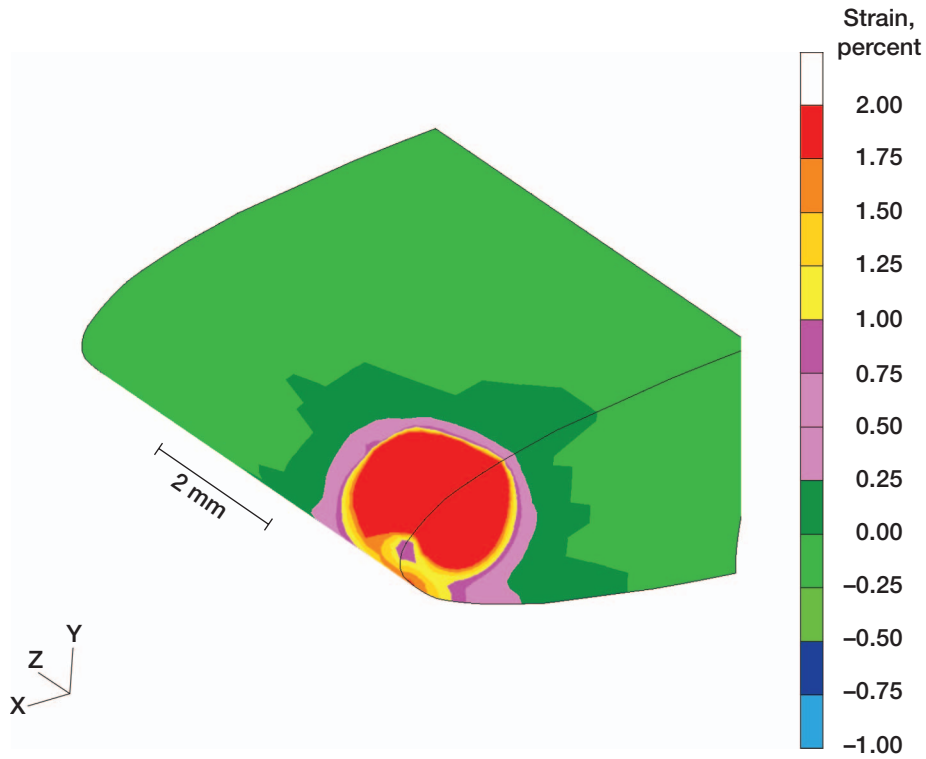


Figure 30.—Prediction of von Mises plastic strain on front side of Ti-48-2-2 after intermediate-energy impact (specimen 005-08-3).

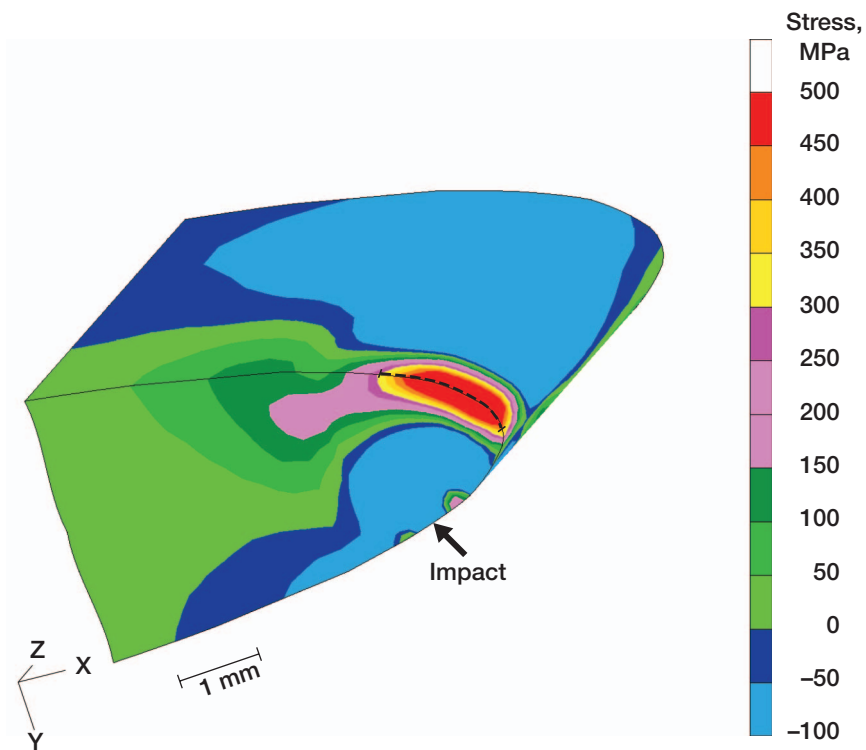


Figure 31.—Prediction of z stress on back side of Ti-48-2-2 after intermediate-energy impact (specimen 005-08-3). Dashed line is cracking zone.

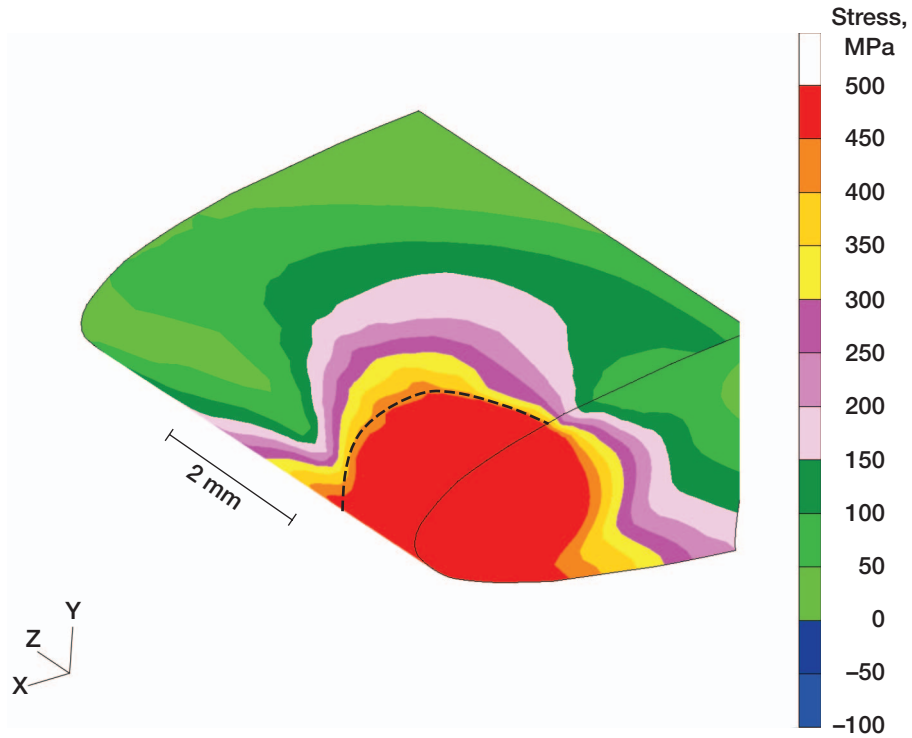


Figure 32.—Prediction of von Mises stress on front side of Ti-48-2-2 after high-energy impact (specimen 009-08-2). Dashed line is cracking zone.

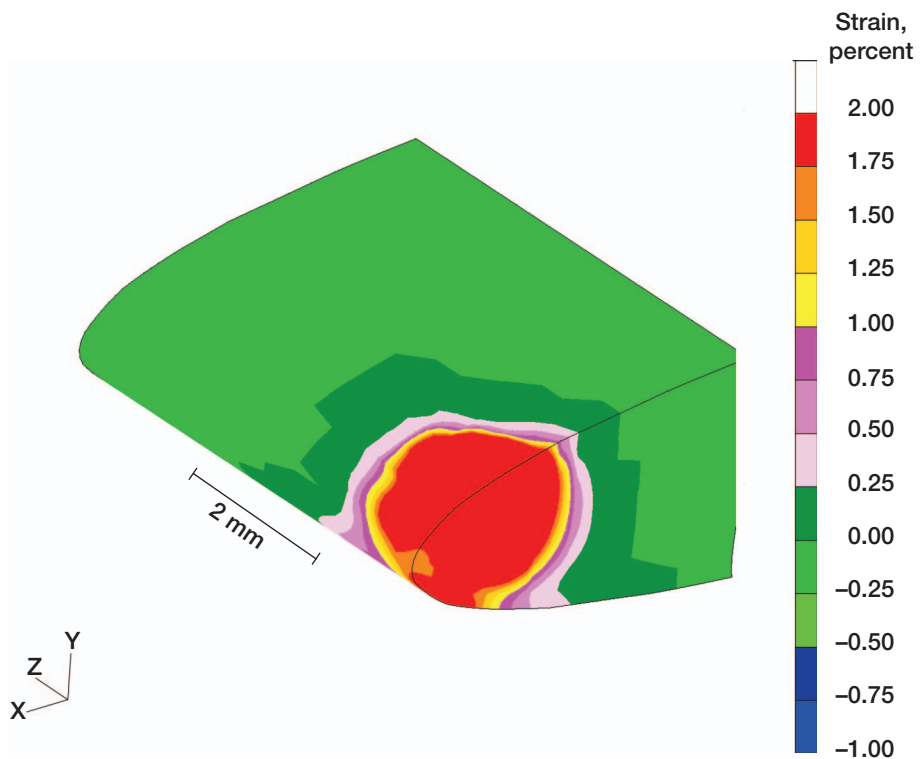


Figure 33.—Prediction of von Mises plastic strain on front side of Ti-48-2-2 after high-energy impact (specimen 009-08-2).

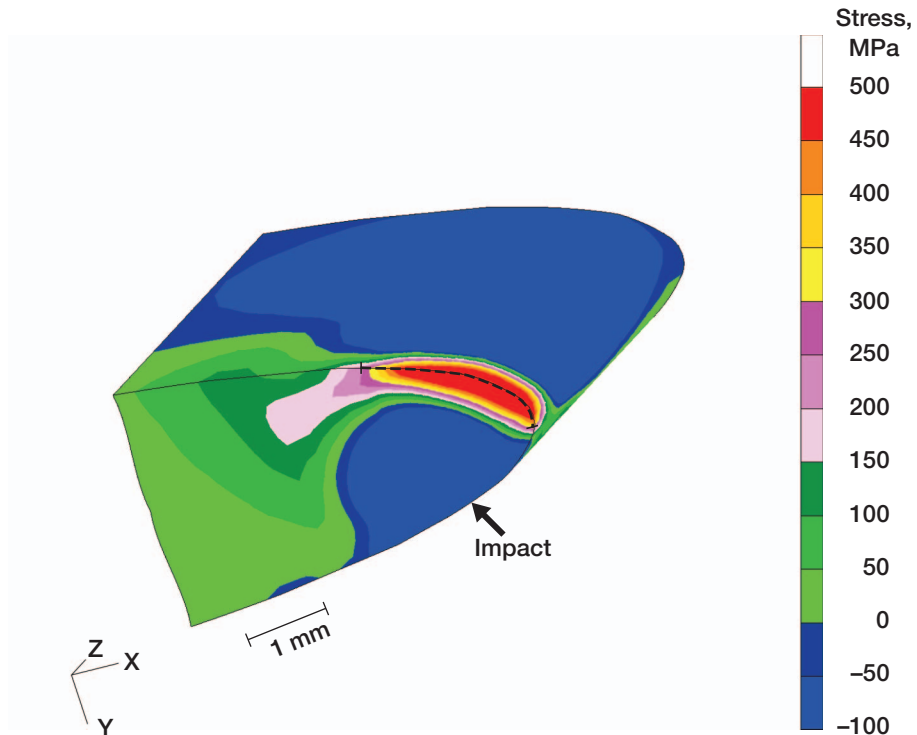


Figure 34.—Prediction of z stress on back side of Ti-48-2-2 after high-energy impact (specimen 009-08-2). Dashed line is cracking zone.

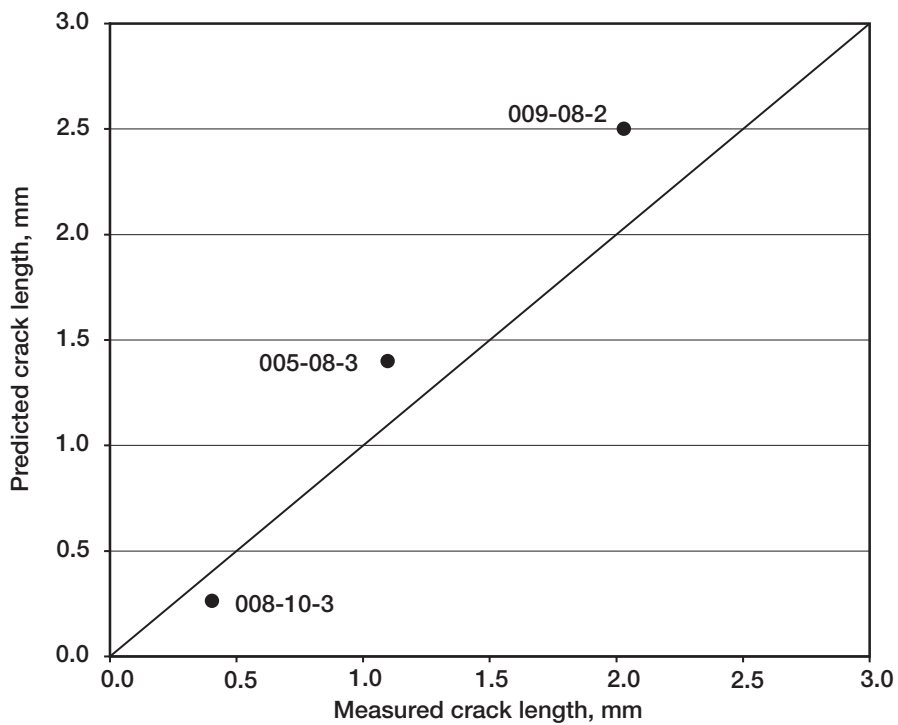


Figure 35.—Prediction capabilities of model for back-side crack lengths of Ti-48-2-2 specimens.

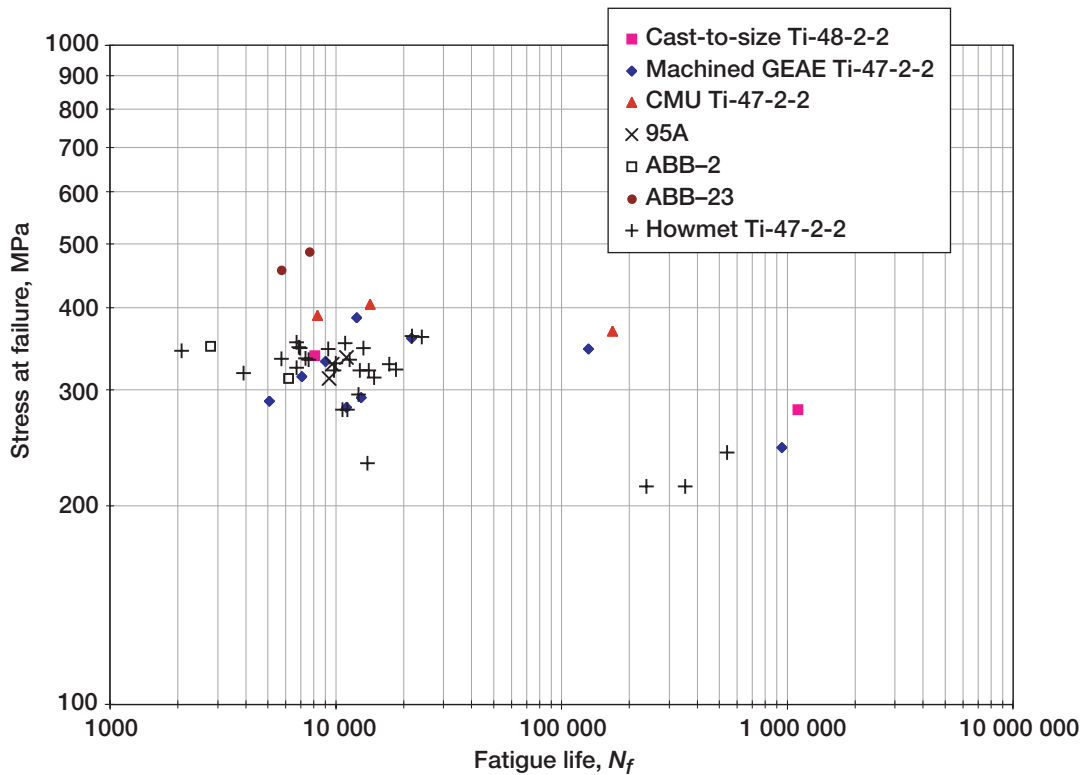


Figure 36.—S–N data for various  $\gamma$ -TiAl alloys. Virgin samples, 650 °C, load ratio  $R_\sigma = 0.05$ , defect area  $< 0.1 \text{ mm}^2$ .

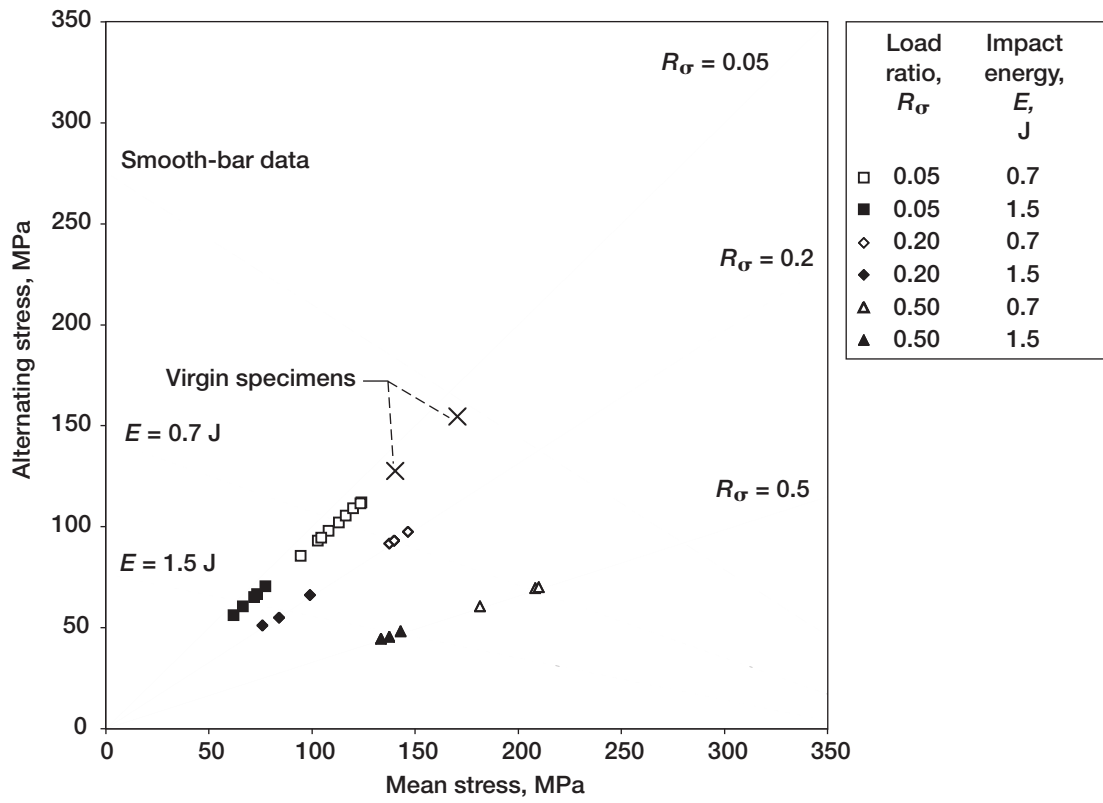


Figure 37.—Tensile mean stress relationships of cast-to-size Ti-48-2-2 with 0.2 percent offset yield strength of 284 MPa and ultimate tensile strength of 474 MPa. Smooth-bar data are from Ti-48-2-2 specimens tested at GEAE.

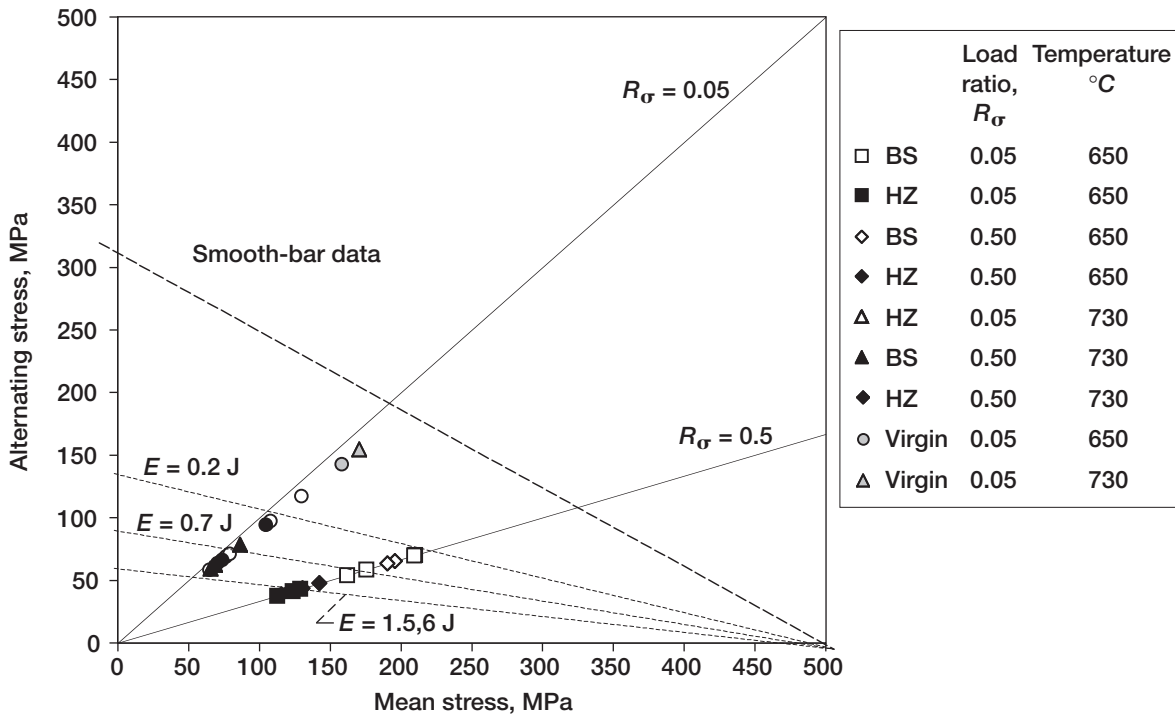


Figure 38.—Tensile mean stress relationships of cast-to-size ABB-2 with 0.2 percent offset yield strength of 400 MPa and ultimate tensile strength of 575 MPa. Smooth-bar data are from ABB-2 specimens tested at GEAE.

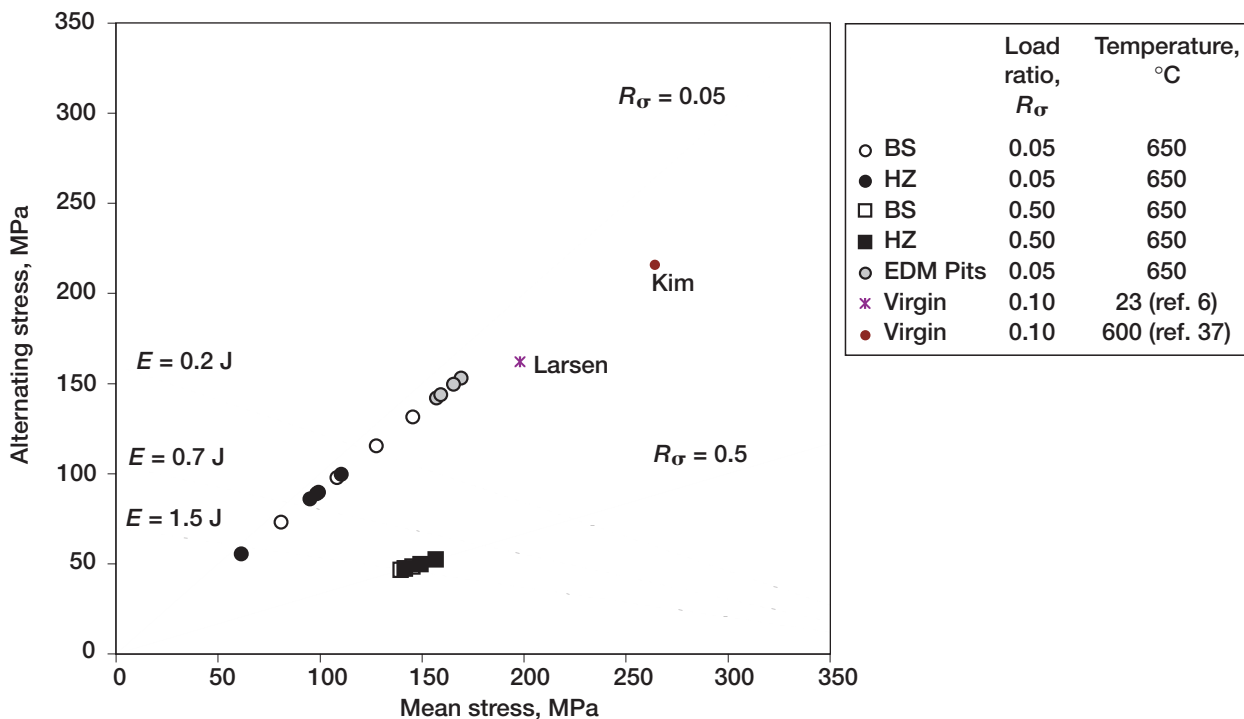


Figure 39.—Tensile mean stress relationships of forged 95A with 0.2 percent offset yield strength of 375 MPa and ultimate tensile strength of 460 MPa.

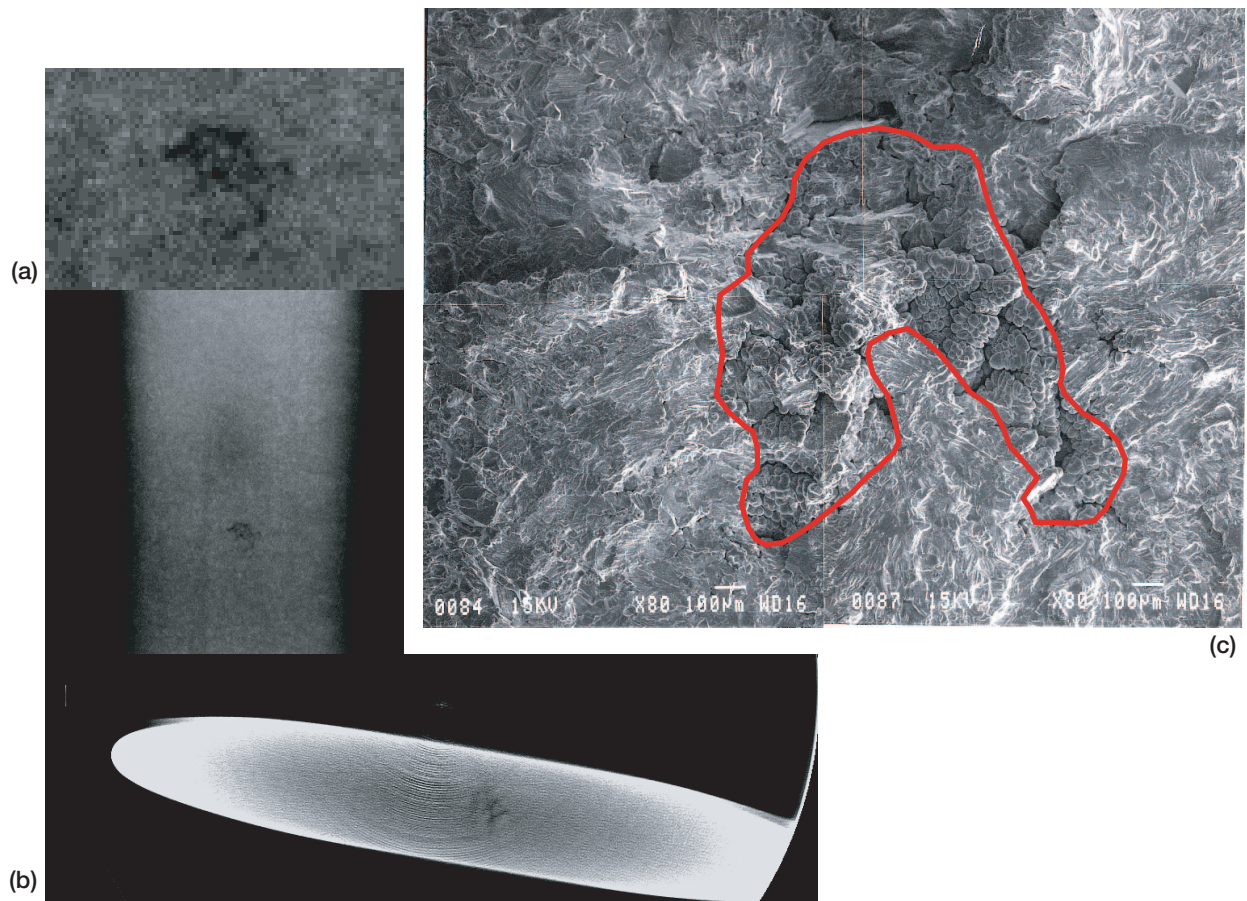


Figure 40.—Nondestructive evaluation identification of casting defect that initiated fatigue cracking.  
(a) Microfocus x-ray. (b) Computed tomography scan of cross section. (c) Scanning electron microscopy image of fracture surface (porosity outlined).

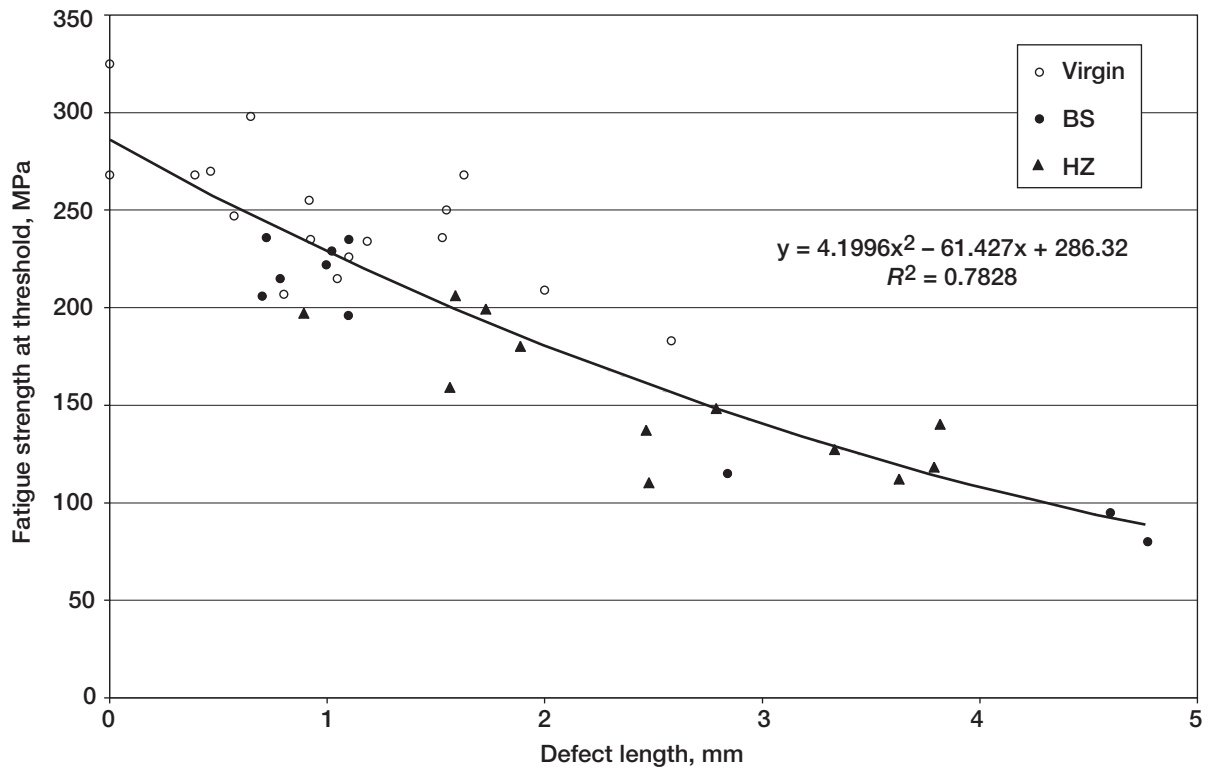


Figure 41.—Fatigue strength at threshold as function of defect length for cast-to-size Ti-48-2-2.



Figure 42.—Back-side crack encompassing most of specimen thickness for cast-to-size Ti-48-2-2.

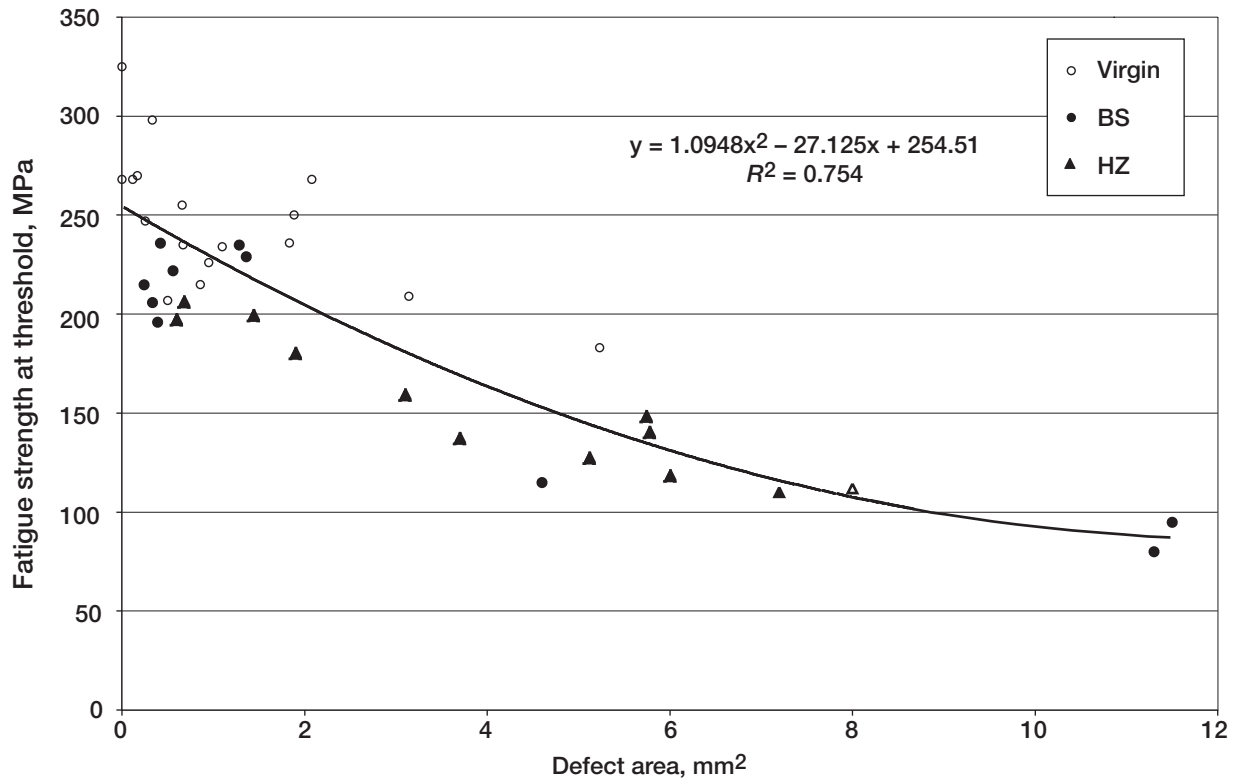


Figure 43.—Fatigue strength at threshold as function of defect area for cast-to-size Ti-48-2-2.



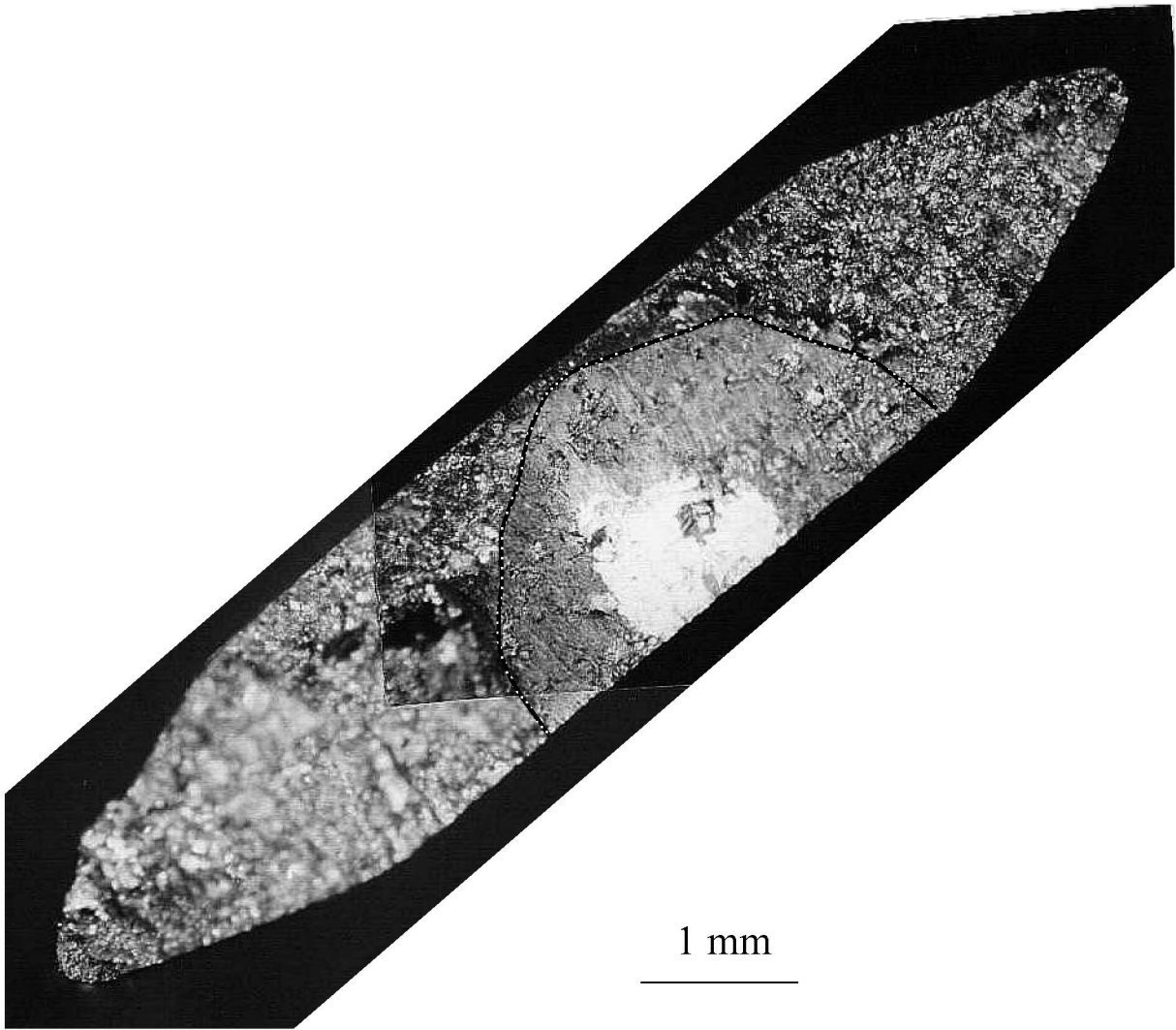


Figure 46.—Large interlamellar crack resulting in low fatigue strength for machined GEAE Ti-47-2-2.

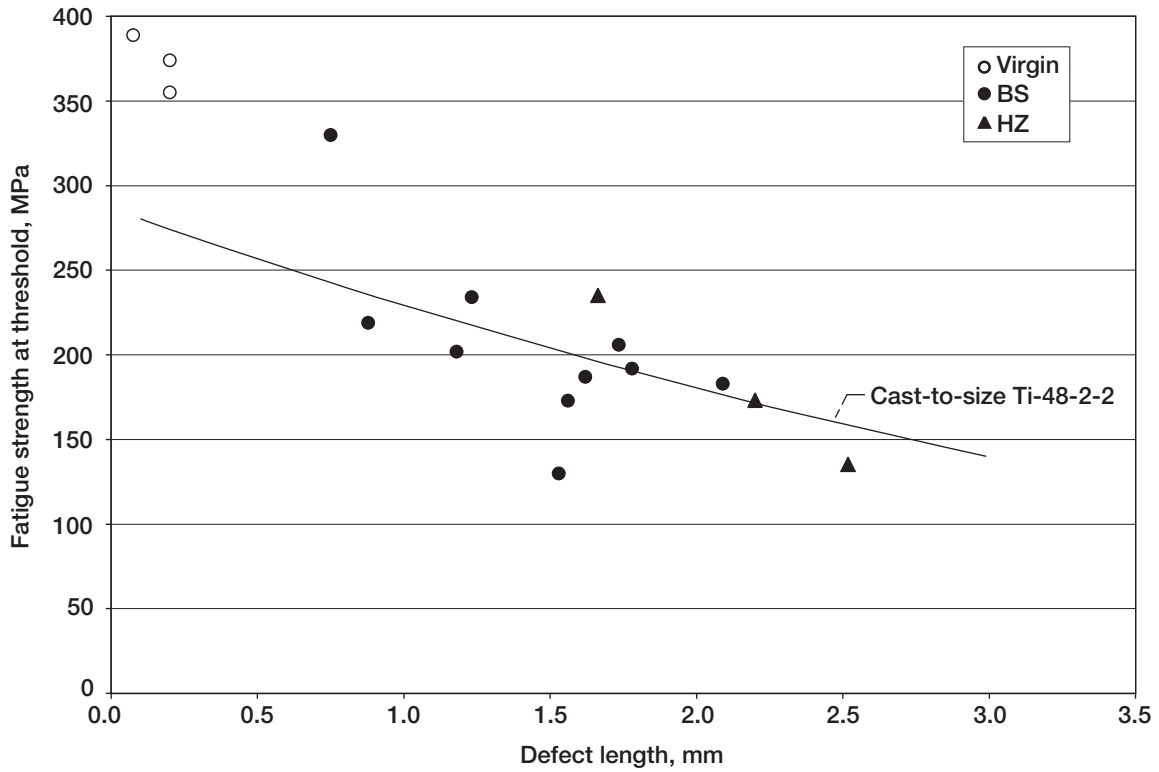


Figure 47.—Fatigue strength at threshold as function of defect length for CMU Ti-47-2-2.

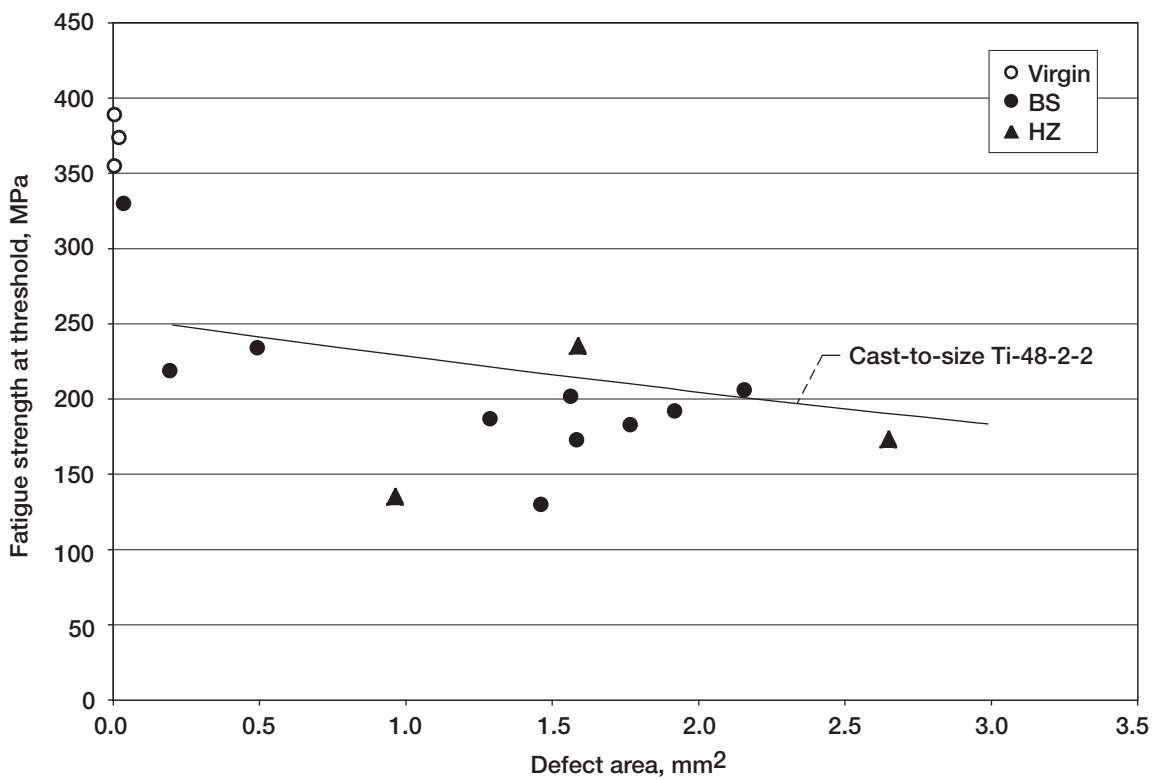


Figure 48.—Fatigue strength at threshold as function of defect area for CMU Ti-47-2-2.

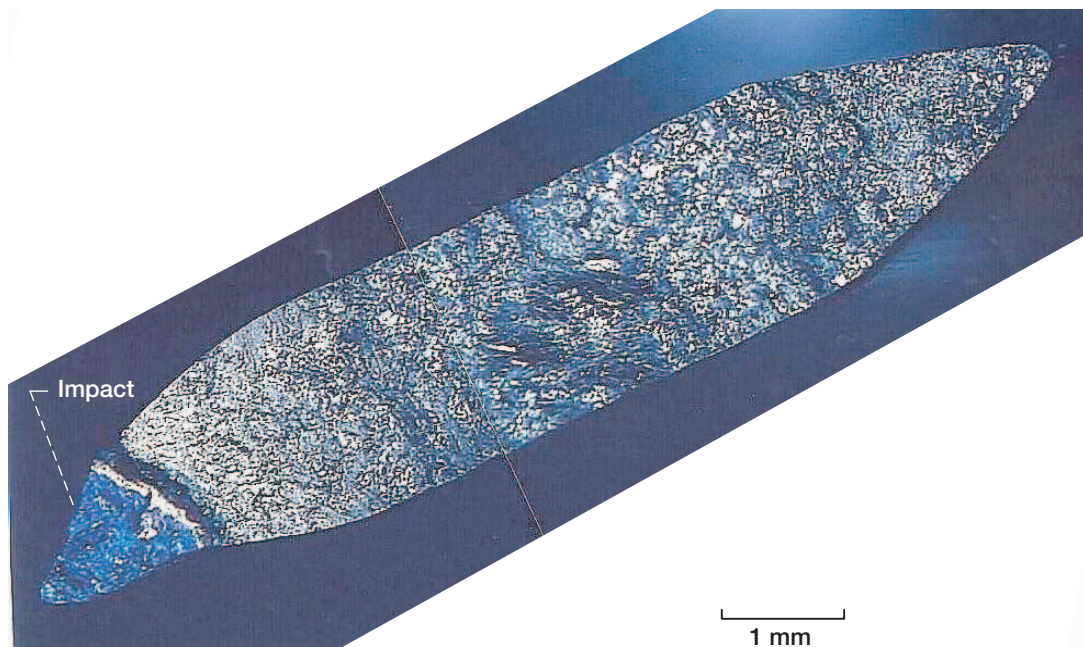


Figure 49.—Bent leading edge of CMU Ti-47-2-2 sample.

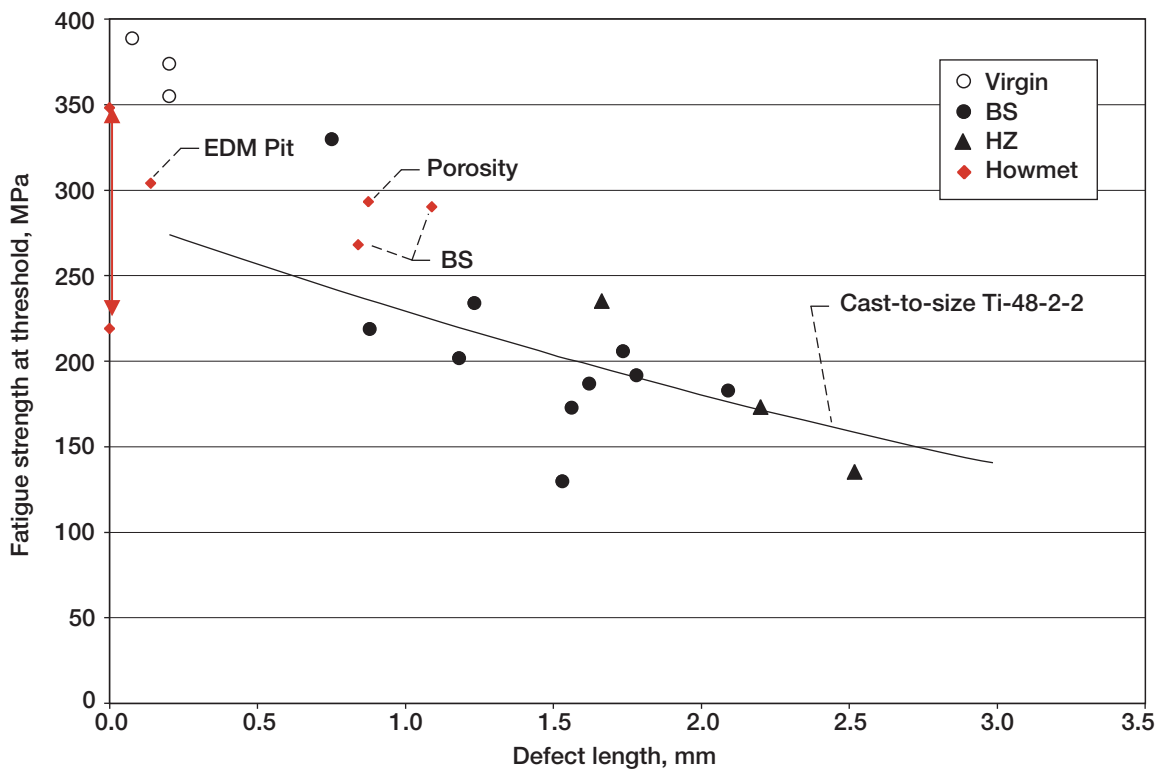


Figure 50.—Fatigue strength at threshold as function of defect length for CMU and Howmet Ti-47-2-2 low-aluminum alloys.

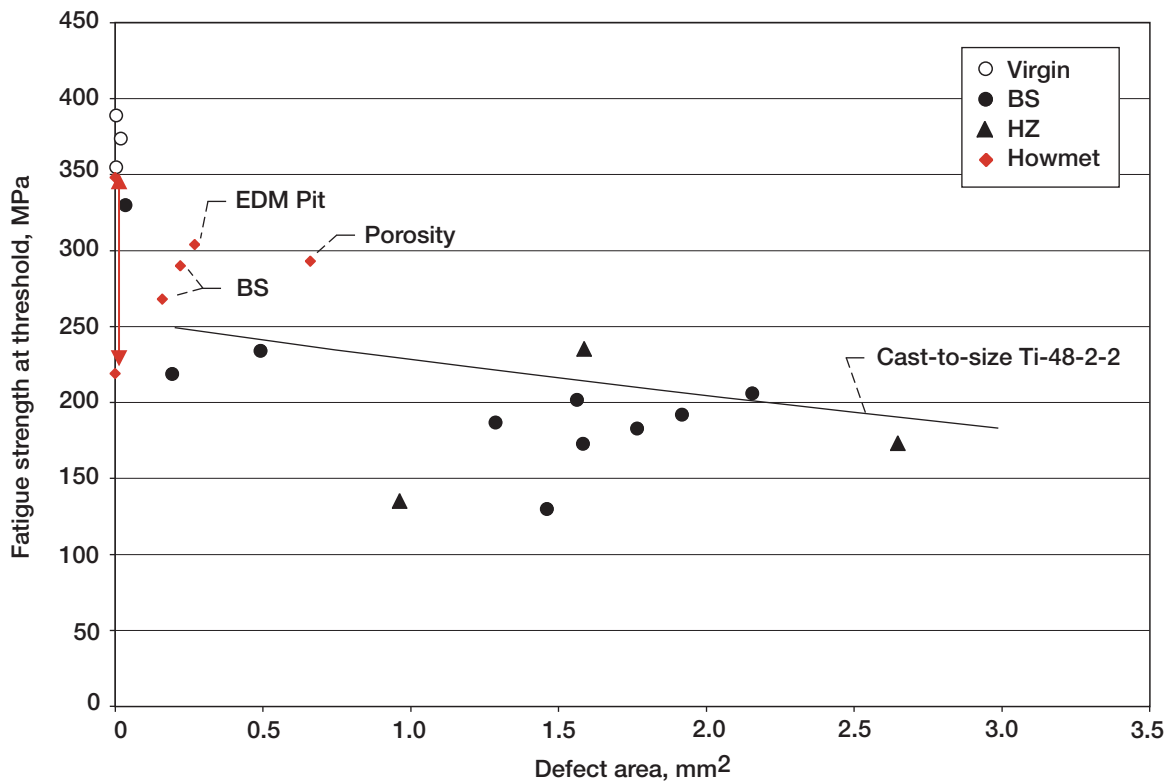


Figure 51.—Fatigue strength at threshold as function of defect area for CMU and Howmet Ti-47-2-2.

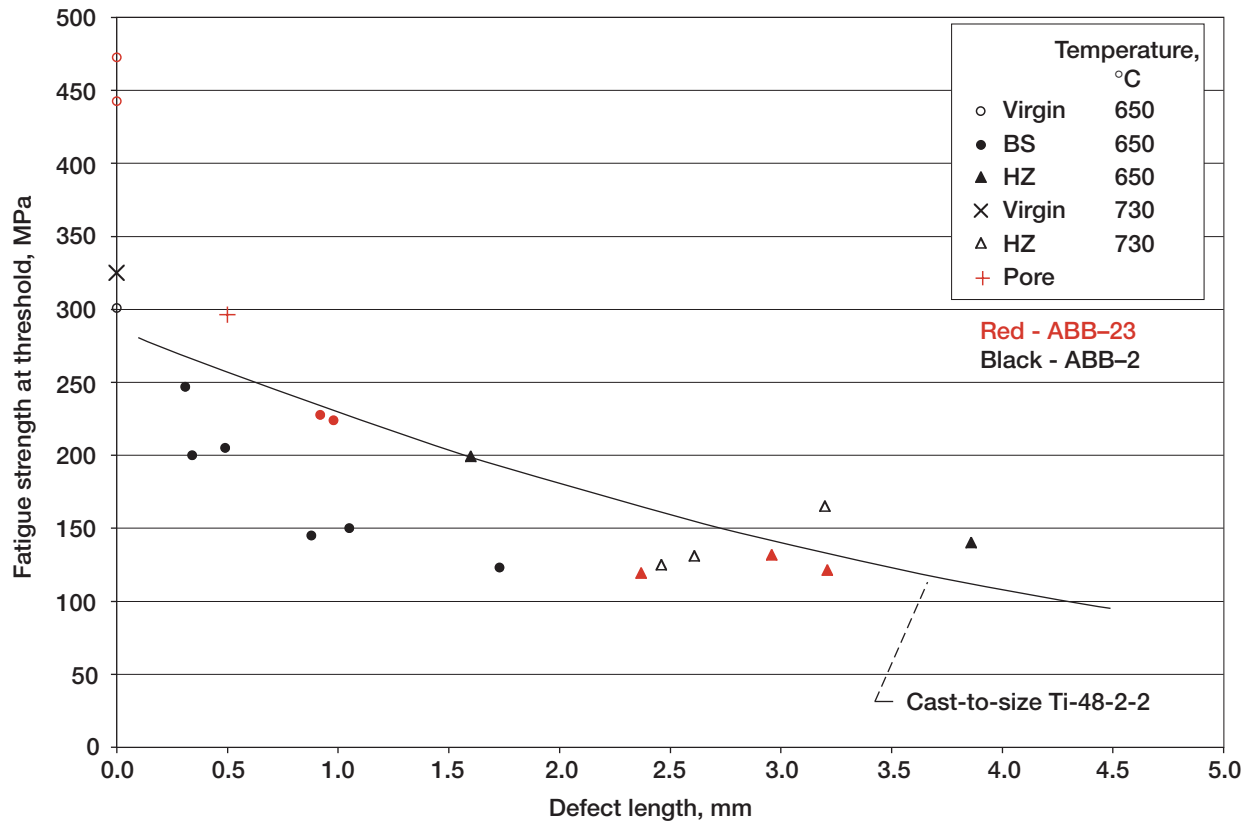


Figure 52.—Fatigue strength at threshold as function of defect length for cast-to-size ABB-2 and machined ABB-23.

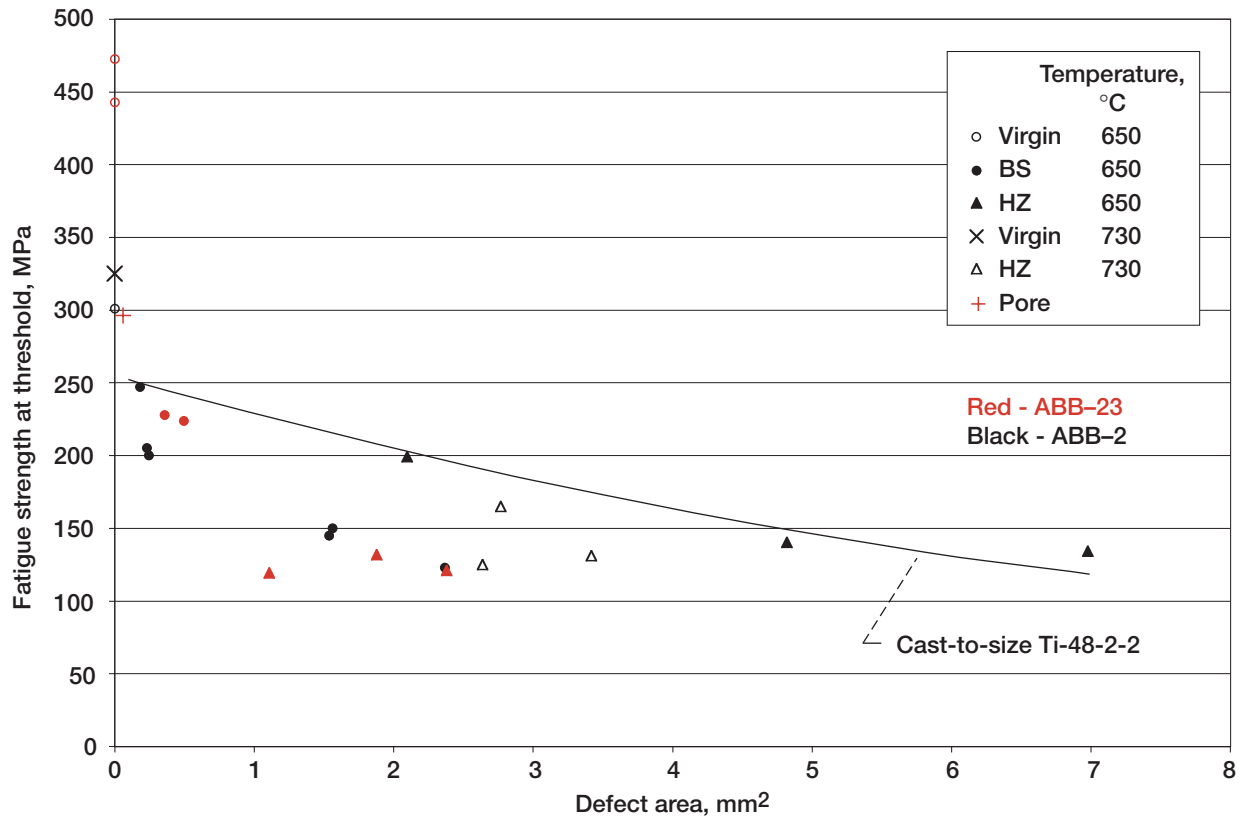


Figure 53.—Fatigue strength at threshold as function of defect area for cast-to-size ABB-2 and machined ABB-23.

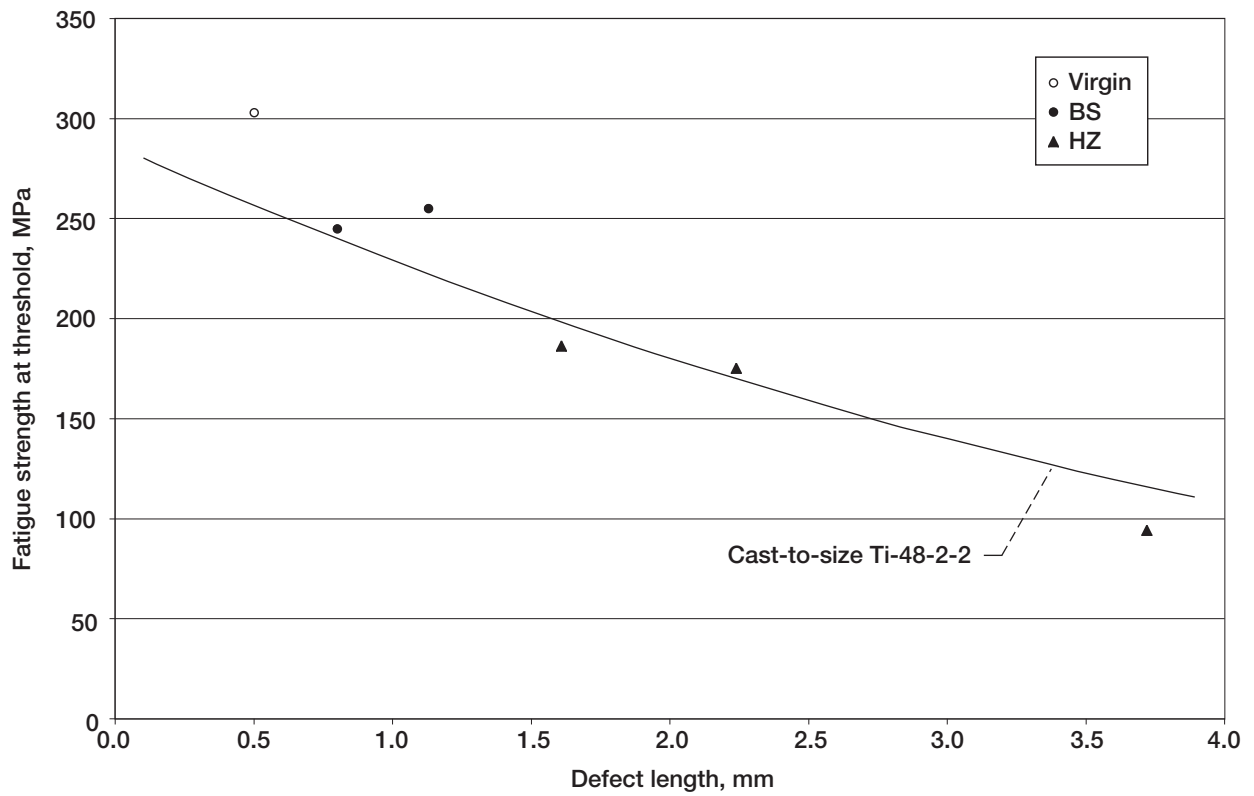


Figure 54.—Fatigue strength at threshold as function of defect length for machined NCG359E.

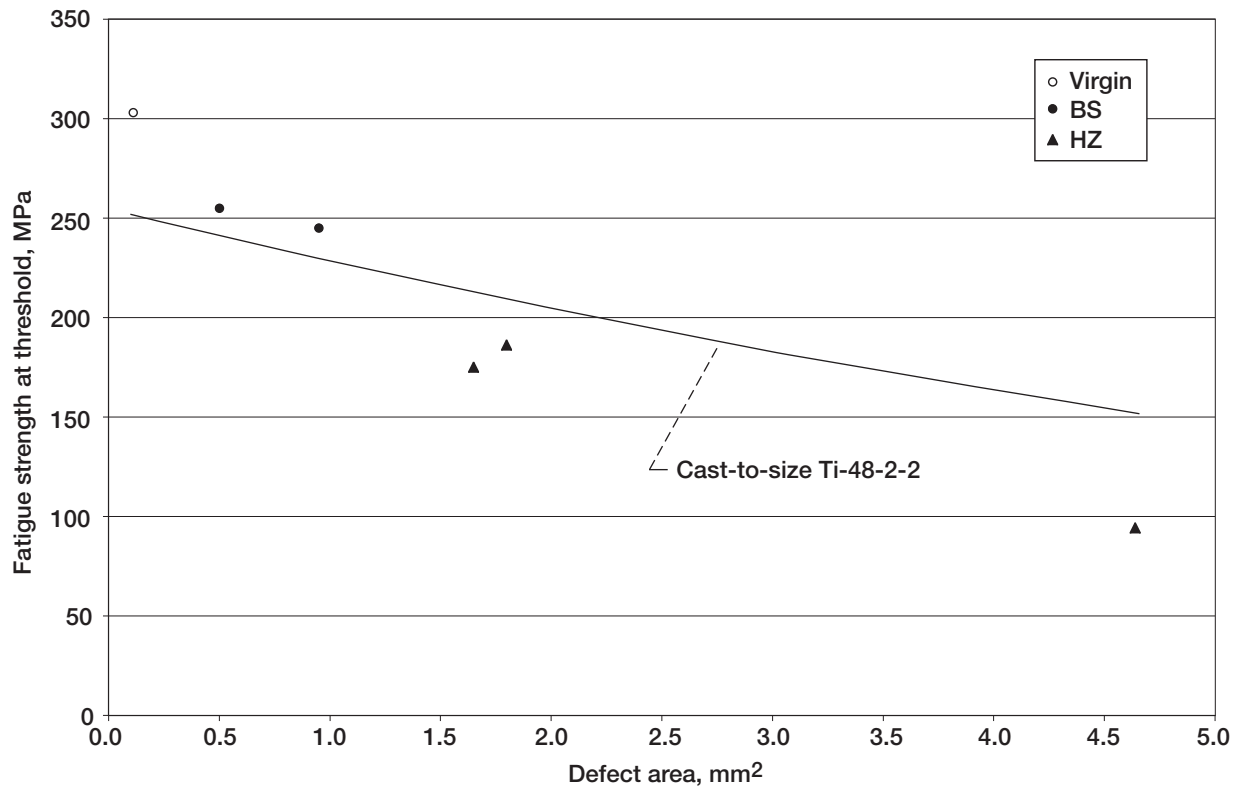


Figure 55.—Fatigue strength at threshold as function of defect area for machined NCG359E.

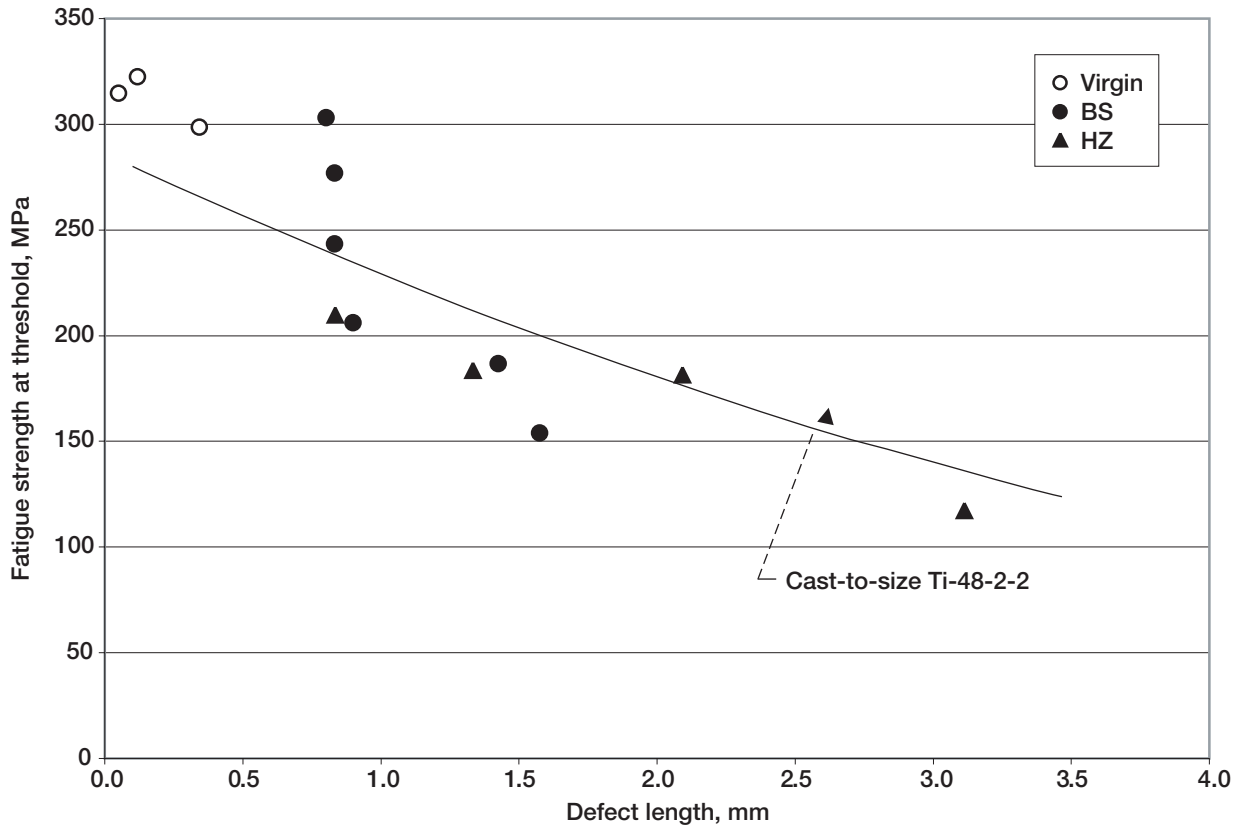


Figure 56.—Fatigue strength at threshold as function of defect length for machined 95A.

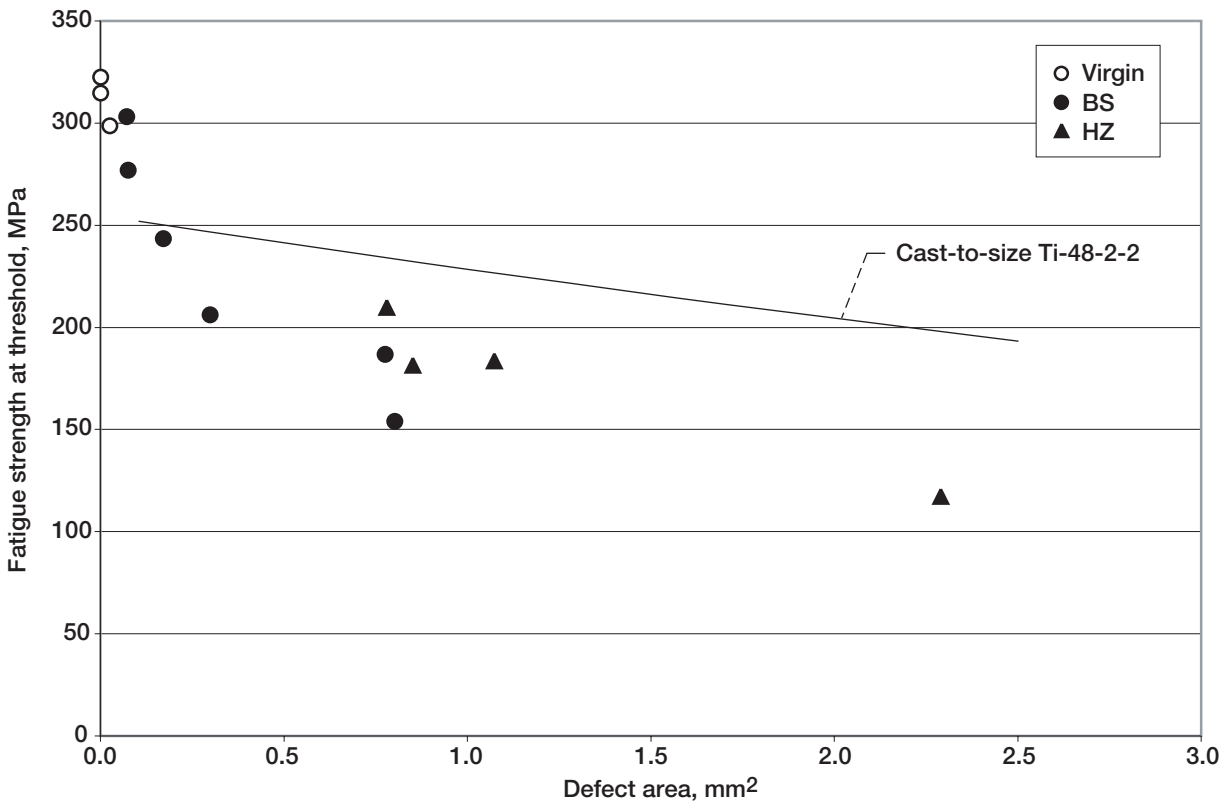


Figure 57.—Fatigue strength at threshold as function of defect area for machined 95A.

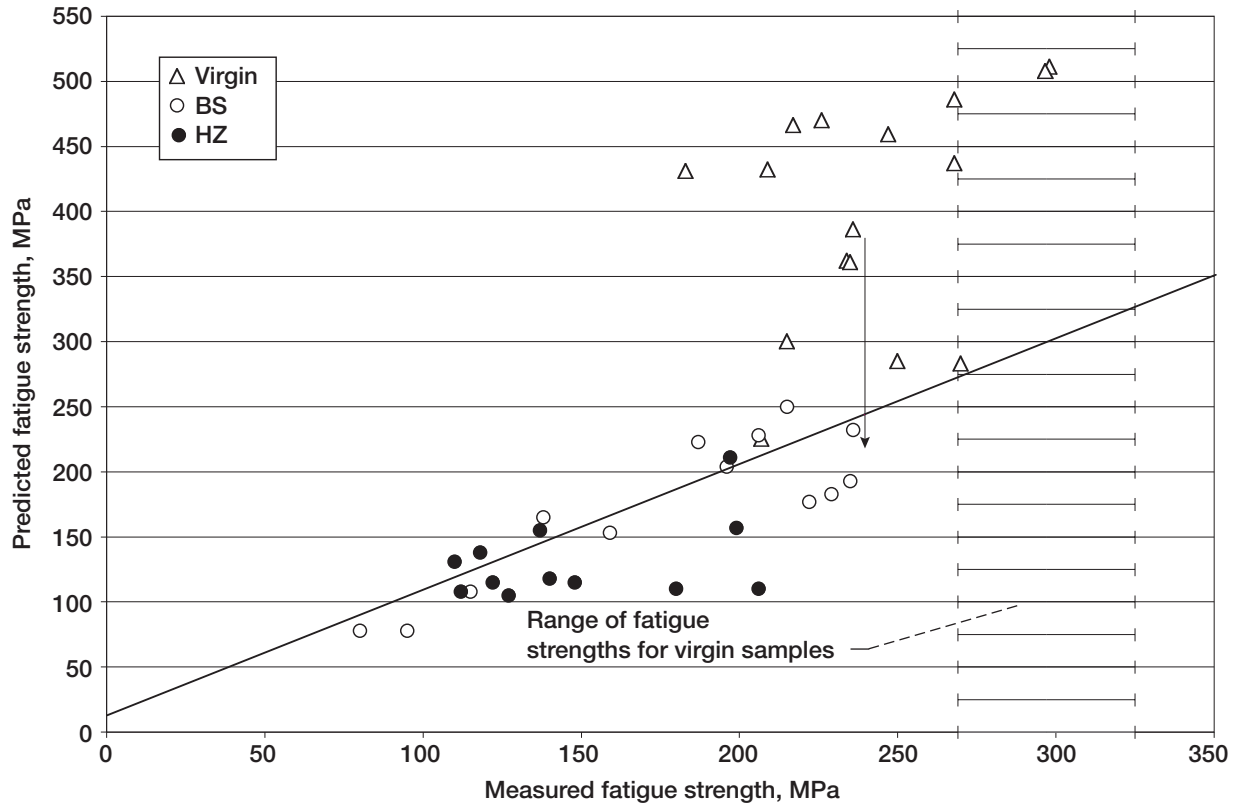


Figure 58.—Fatigue strengths predicted from equation (3) compared with measured fatigue strengths for cast-to-size Ti-48-2-2. Temperature was 650 °C; load ratio  $R_{\sigma}$ , 0.05; and estimated stress intensity  $K_{th}$ , 8.8  $\text{MPa}\sqrt{\text{m}}$ .

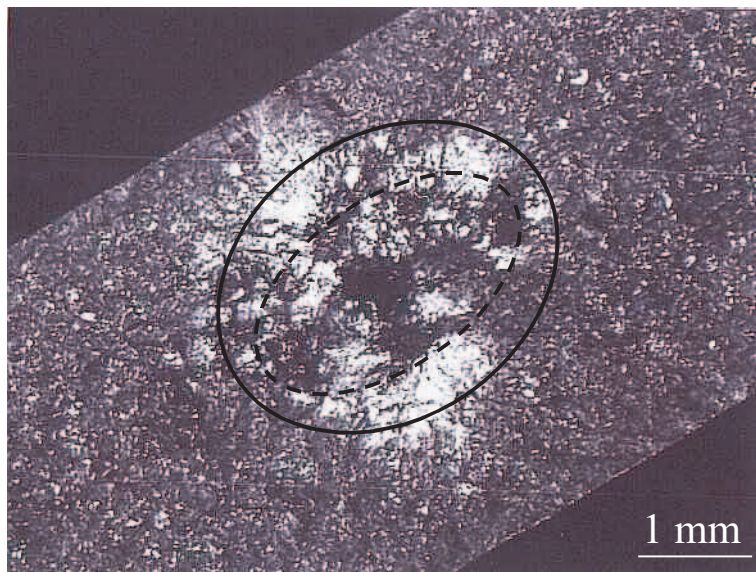


Figure 59.—Area of microshrinkage (dashed line) used in threshold analysis in figure 58. Solid line depicts corrected area indicated by arrow in figure 58.

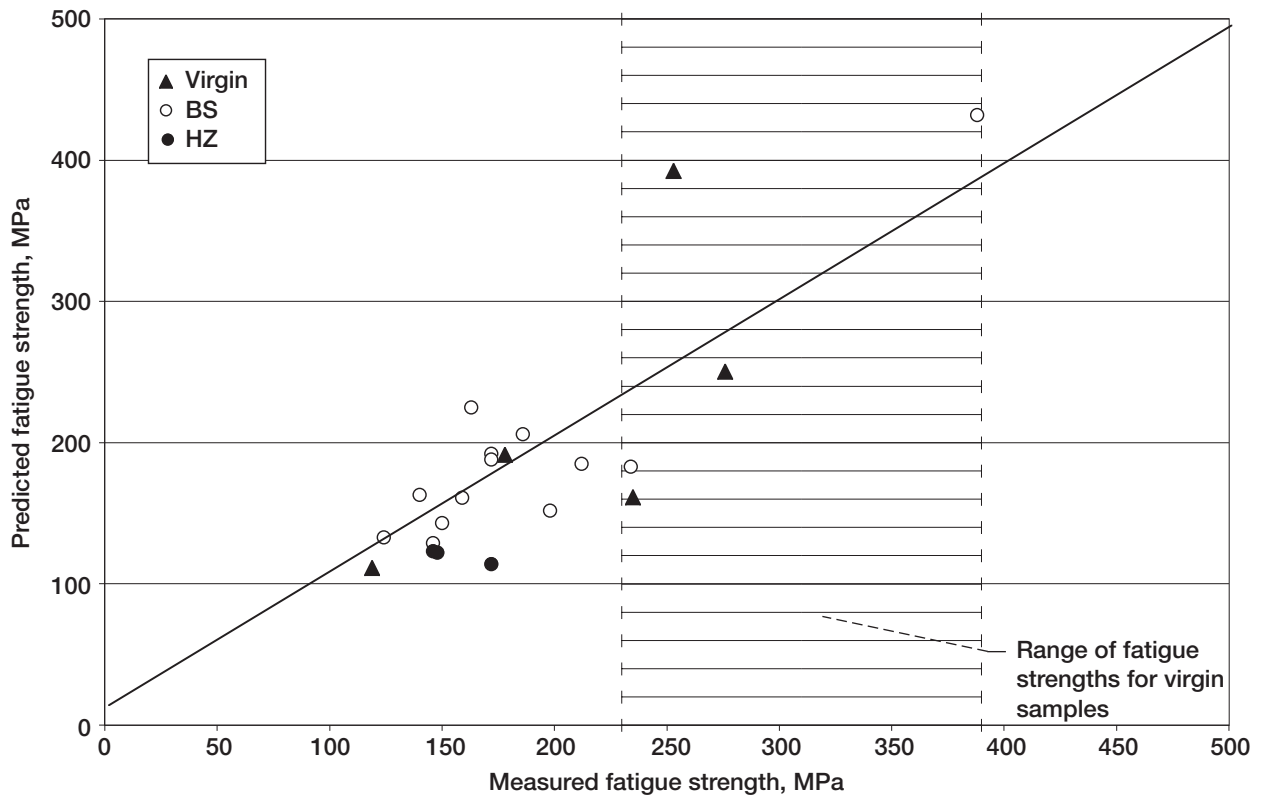


Figure 60.—Fatigue strengths predicted from equation (3) compared with measured fatigue strengths for machined GEAE Ti-47-2-2. Temperature was 650 °C; load ratio  $R_{\sigma}$ , 0.05; and estimated stress intensity  $K_{th}$ , 8.2 MPa $\sqrt{m}$ .

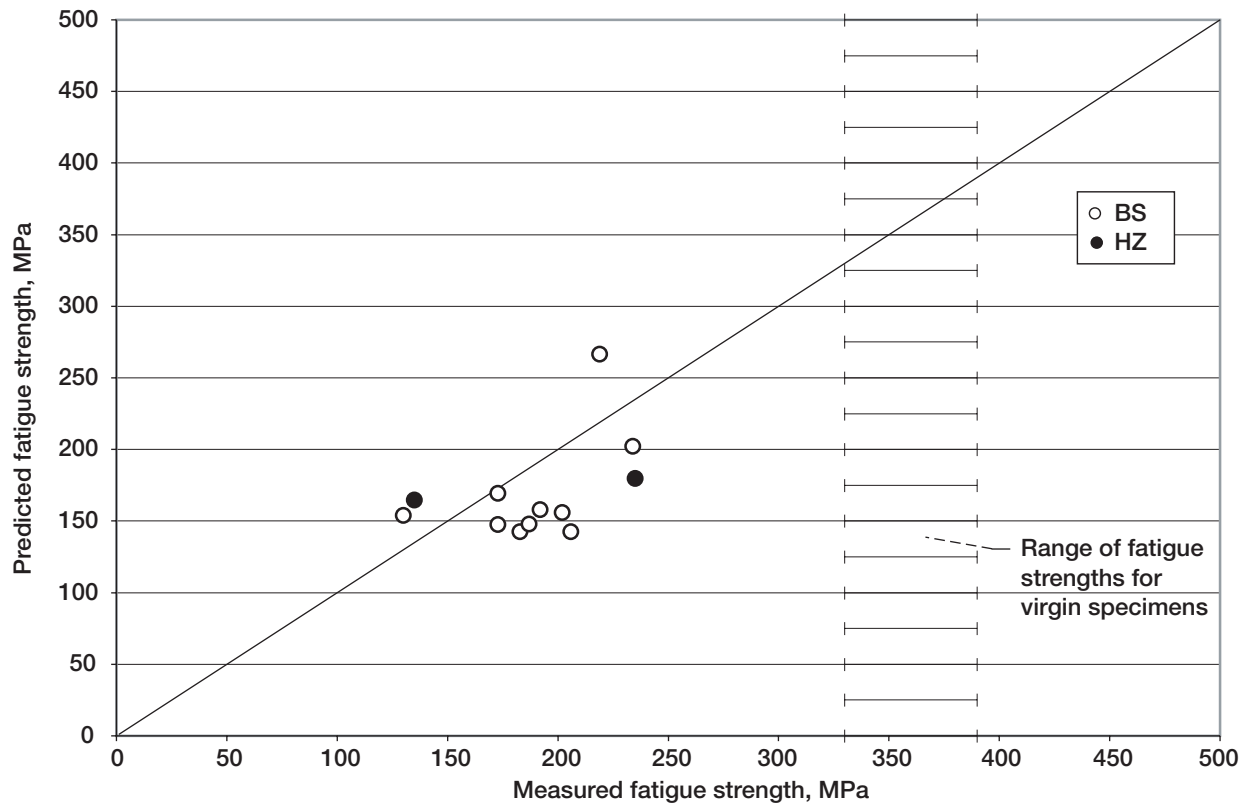


Figure 61.—Fatigue strengths predicted from equation (3) compared with measured fatigue strengths for CMU Ti-47-2-2. Temperature was 650 °C; load ratio  $R_\sigma$ , 0.05; and estimated stress intensity  $K_{th}$ , 12.1 MPa $\sqrt{m}$ .

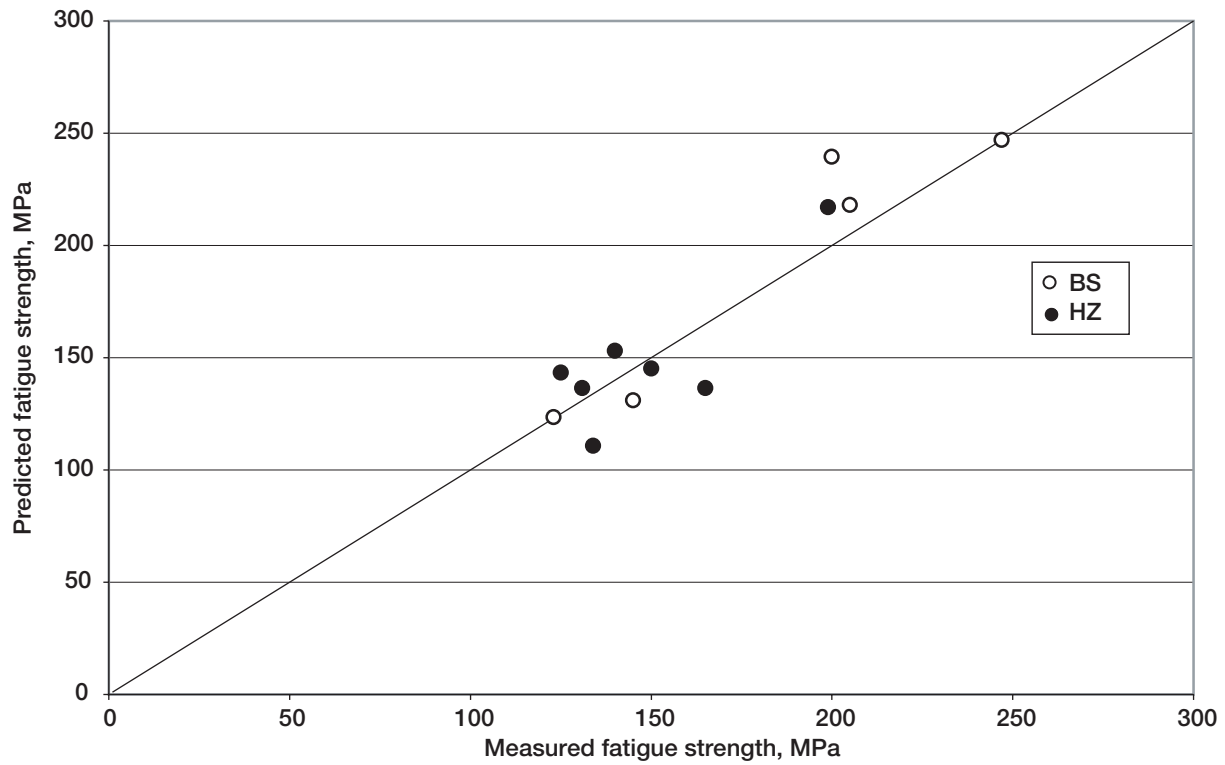


Figure 62.—Fatigue strengths predicted from equation (3) compared with measured fatigue strengths for cast-to-size ABB-2. Temperatures were 650 and 730 °C; load ratio  $R_{\sigma}$ , 0.05; and estimated stress intensity  $K_{th}$ ,  $9.9 \text{ MPa}\sqrt{\text{m}}$ .

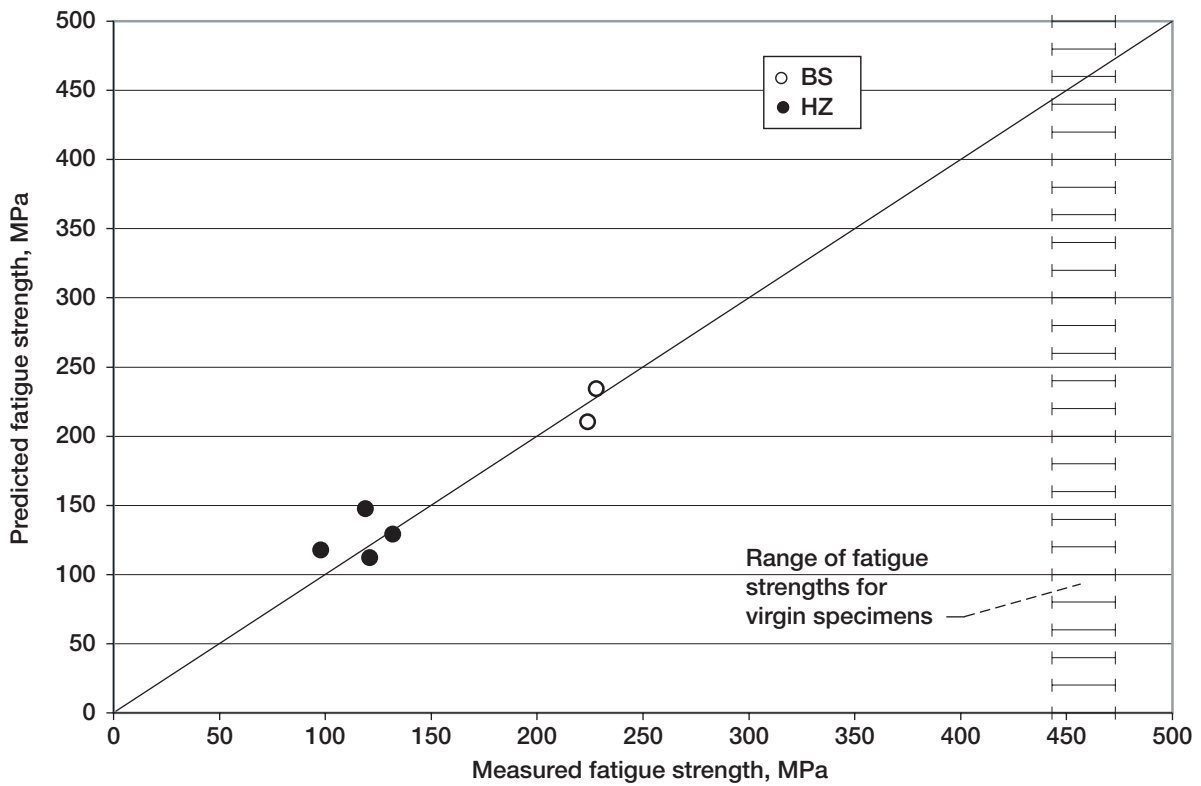


Figure 63.—Fatigue strengths predicted from equation (3) compared with measured fatigue strengths for machined ABB-23. Temperature was 650 °C; load ratio  $R_\sigma$ , 0.05; and estimated stress intensity  $K_{th}$ , 11 MPa $\sqrt{m}$ .

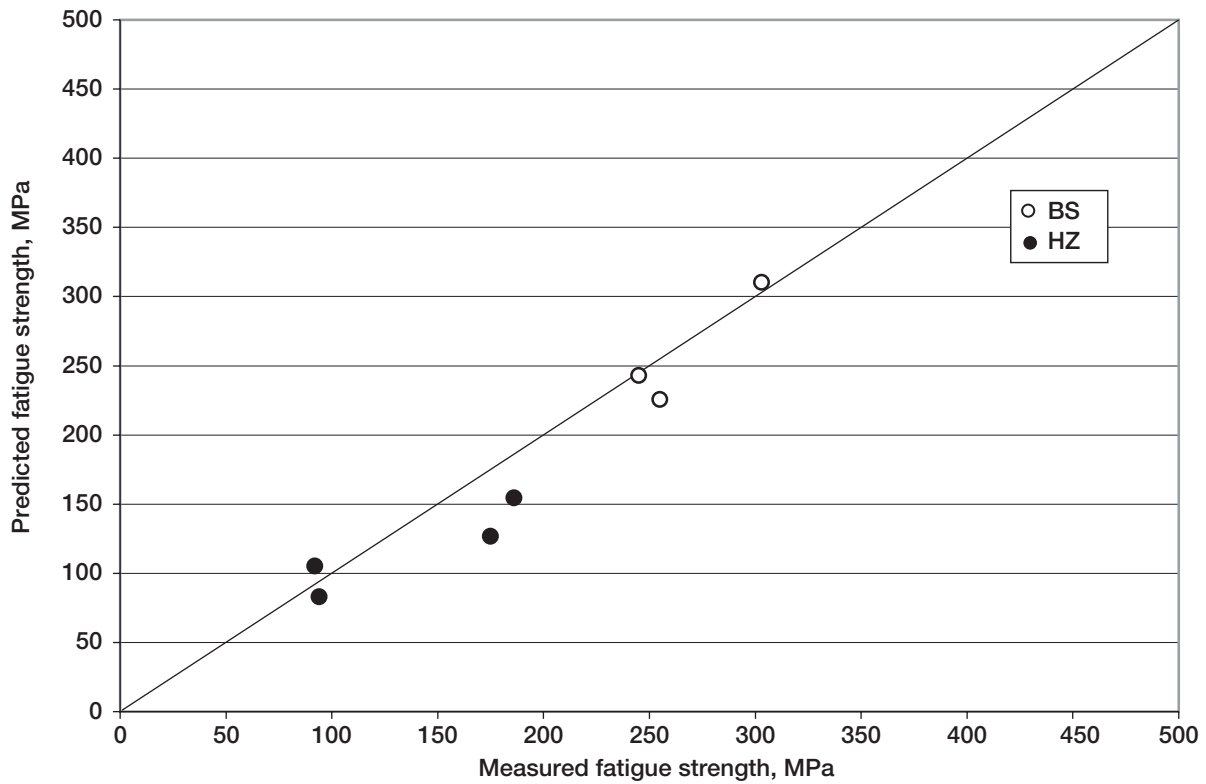


Figure 64.—Fatigue strengths predicted from equation (3) compared with measured fatigue strengths for machined NCG359E. Temperature was 650 °C; load ratio  $R_{\sigma}$ , 0.05; and estimated stress intensity  $K_{th}$ , 11  $\text{MPa}\sqrt{\text{m}}$ .

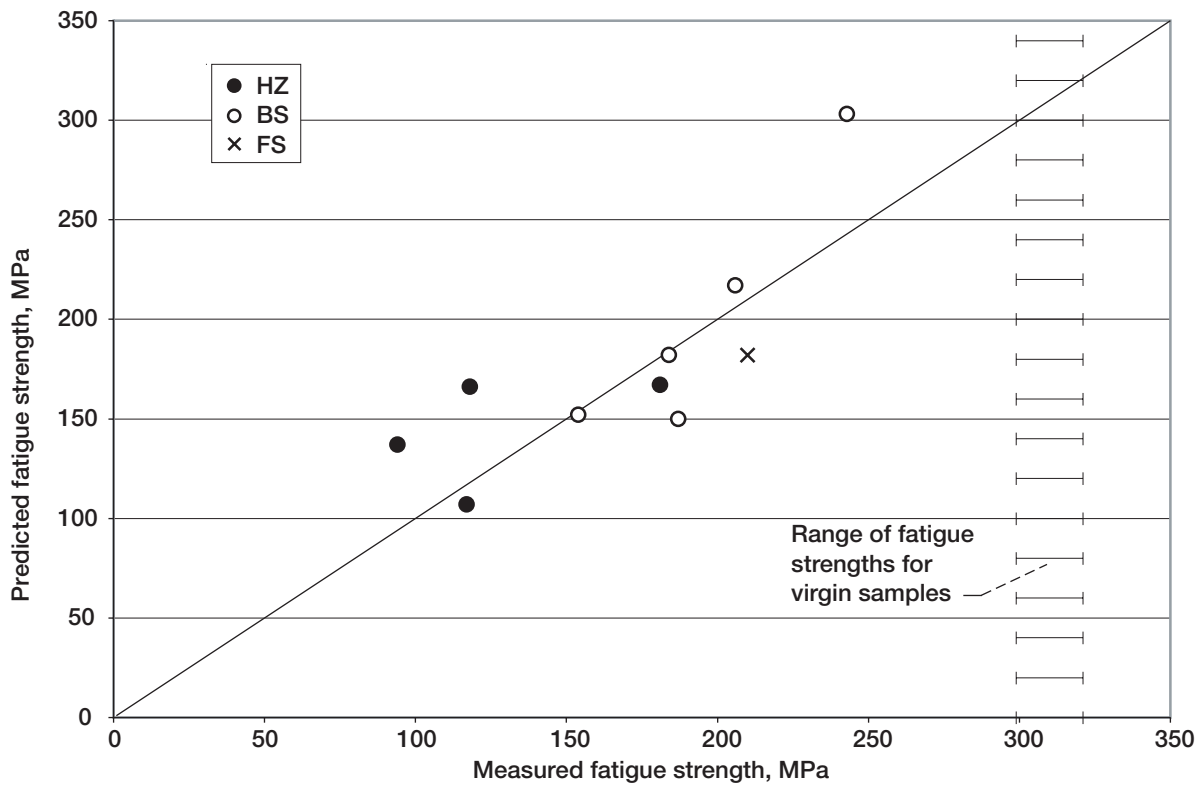


Figure 65.—Fatigue strengths predicted from equation (3) compared with measured fatigue strengths for machined 95A. Temperature was 650 °C; load ratio  $R_{\sigma}$ , 0.05; and estimated stress intensity  $K_{th}$ , 11  $\text{MPa}\sqrt{\text{m}}$ .

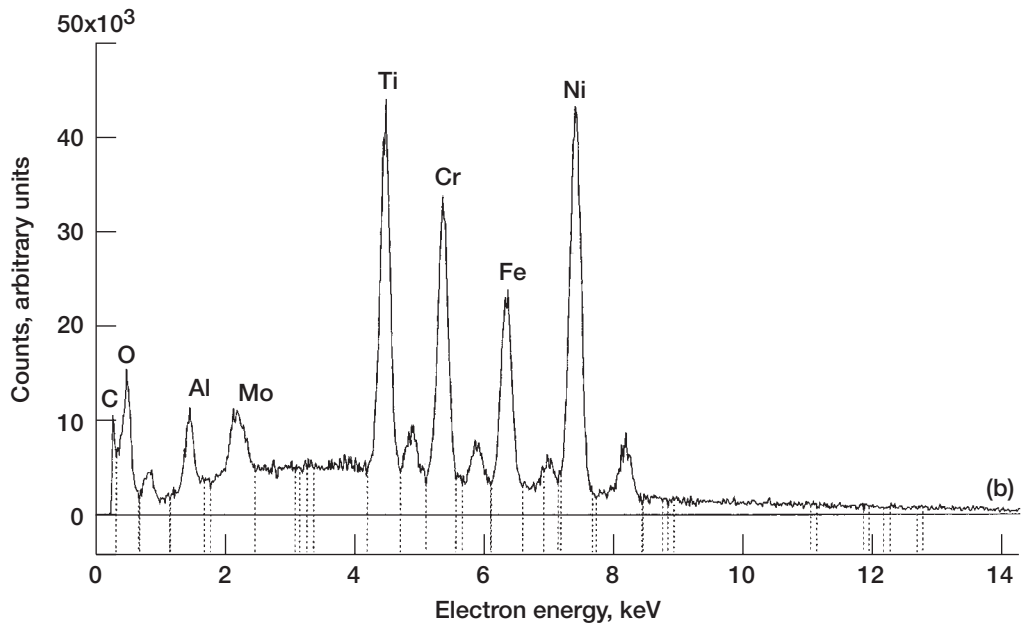
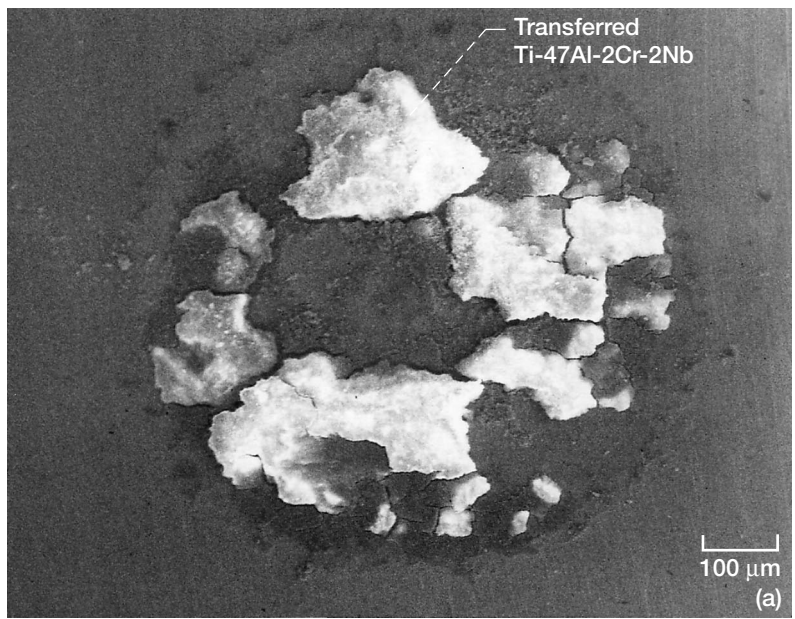


Figure 66.—Wear scar on IN718 pin fretted against Ti-47-2-2 flat. Fretting conditions: load, 1.5 N; frequency, 80 Hz; slip amplitude, 50 μm; total number of cycles, 1 million; environment, air; and temperature, 550 °C. (a) Scanning electron microscopy back-scattered electron image. (b) X-ray energy spectrum with energy dispersive spectroscopy.

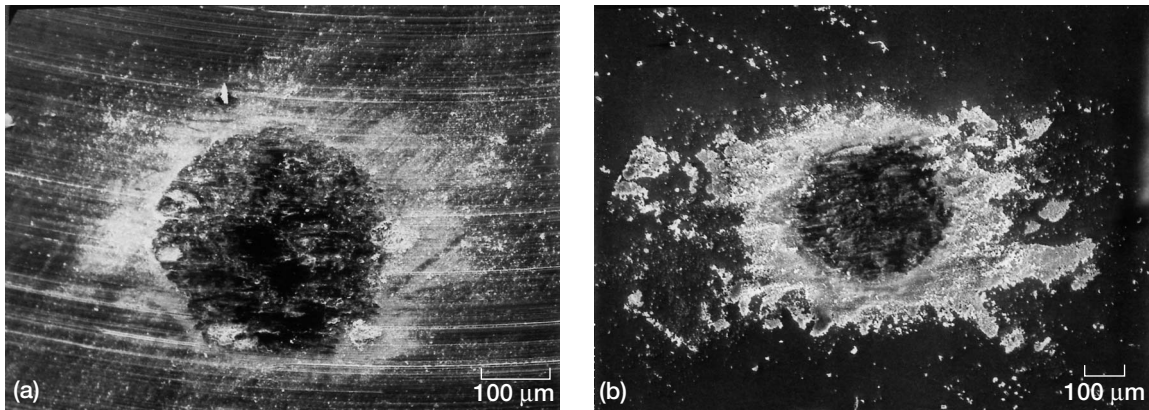


Figure 67.—Wear scars on (a) Ti-47-2-2 pin and (b) IN718 flat. Fretting conditions: load, 1 N; frequency, 80 Hz; slip amplitude, 50  $\mu\text{m}$ ; total number of cycles, 1 million; environment, air; and temperature, 550  $^{\circ}\text{C}$ .

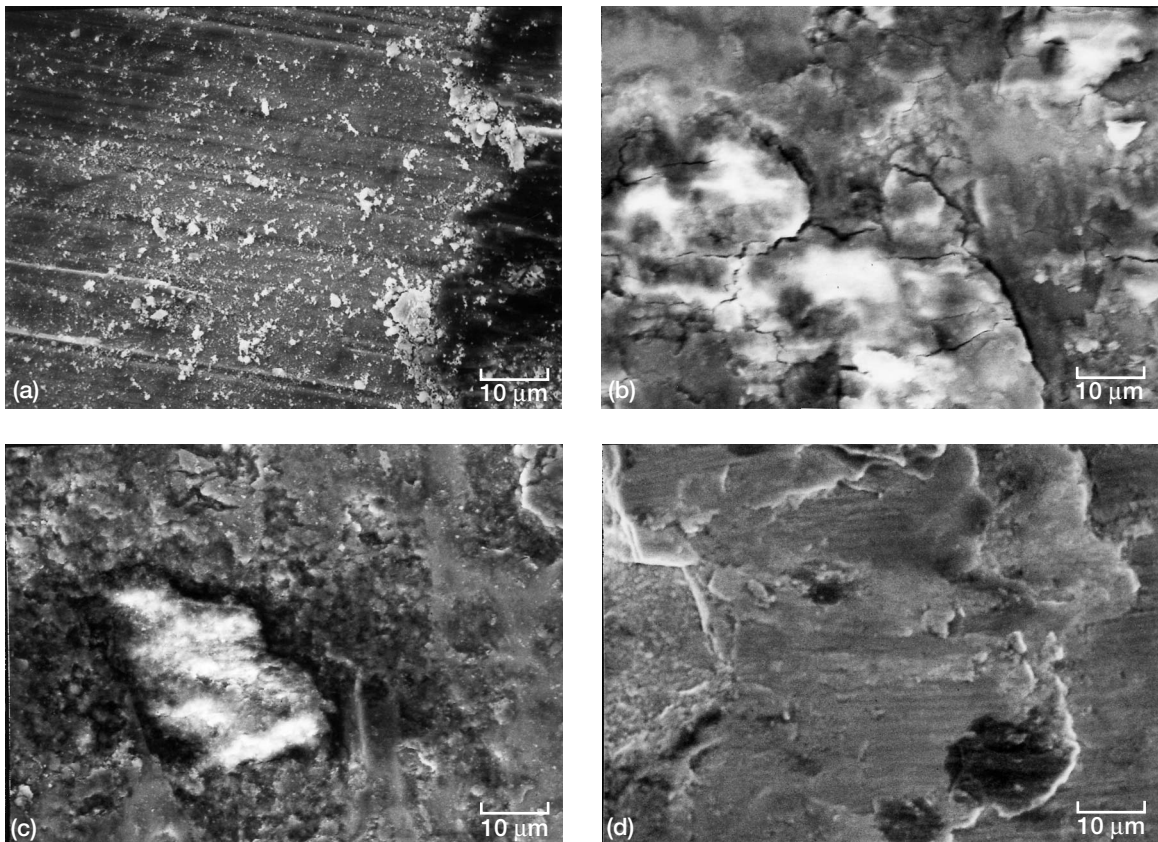


Figure 68.—Surface and subsurface damage in Ti-47-2-2 flat in contact with IN718 pin. Fretting conditions: environment, air; temperature, 550  $^{\circ}\text{C}$ ; load, 1 N; frequency, 80 Hz. (a) Scratches; slip amplitude, 50  $\mu\text{m}$ ; total number of cycles, 1 million. (b) Cracks in oxide layers; slip amplitude, 60  $\mu\text{m}$ ; total number of cycles, 10 million. (c) Cracks in oxide layers; slip amplitude, 50  $\mu\text{m}$ ; total number of cycles, 1 million. (d) Fracture pits and plastic deformation; slip amplitude, 70  $\mu\text{m}$ ; total number of cycles, 20 million.

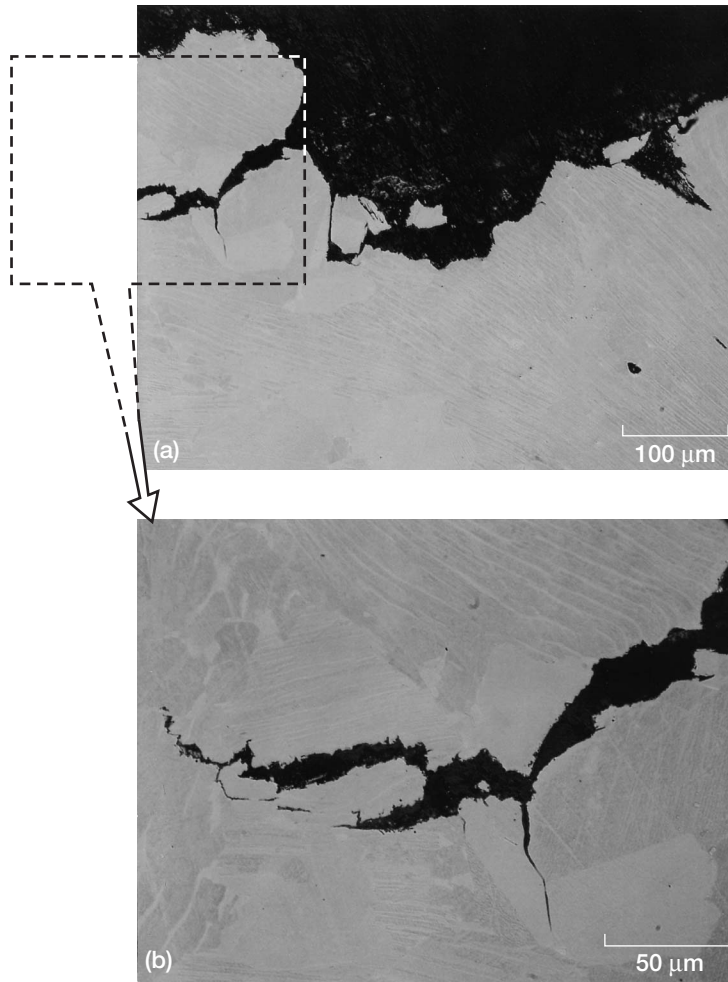


Figure 69.— Cross section of wear scar on Ti-47-2-2 flat in contact with IN718 pin. Fretting conditions: load, 30 N; frequency, 80 Hz; slip amplitude, 70  $\mu\text{m}$ ; total number of cycles, 20 million; environment, air; and temperature, 550  $^{\circ}\text{C}$ . (a) Overview. (b) Crack growth.

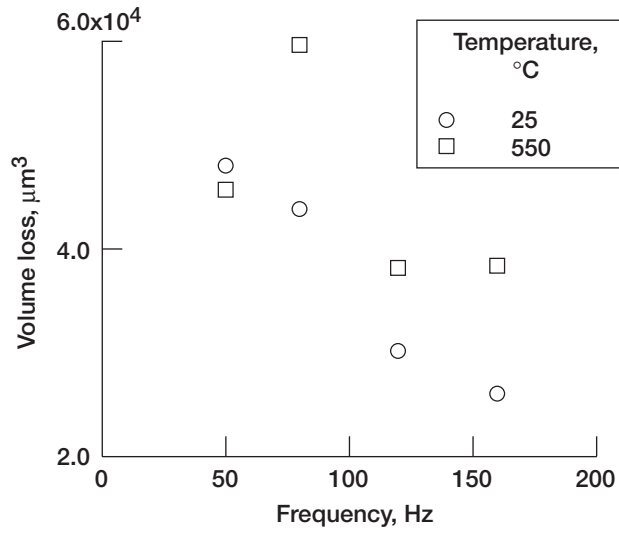


Figure 70.—Wear volume loss of Ti-47-2-2 flat in contact with IN718 pin in air as function of fretting frequency. Fretting conditions: load, 30 N; slip amplitude, 50  $\mu\text{m}$ ; total number of cycles, 1 million; environment, air; and temperatures, 25 and 550 °C.

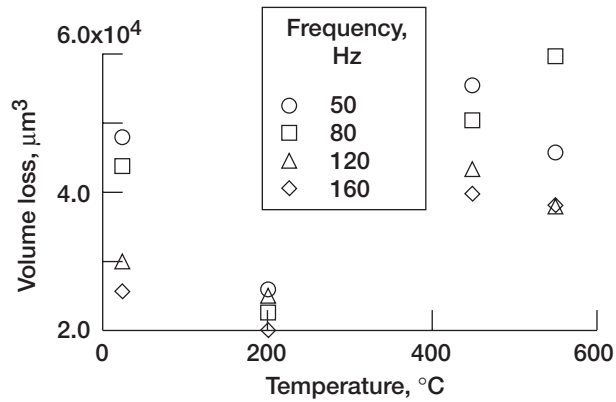


Figure 71.—Wear volume loss of Ti-47-2-2 flat in contact with IN718 pin in air as function of fretting temperature. Fretting conditions: load, 30 N; slip amplitude, 50  $\mu\text{m}$ ; total number of cycles, 1 million; and fretting frequencies, 50, 80, 120, and 160 Hz.

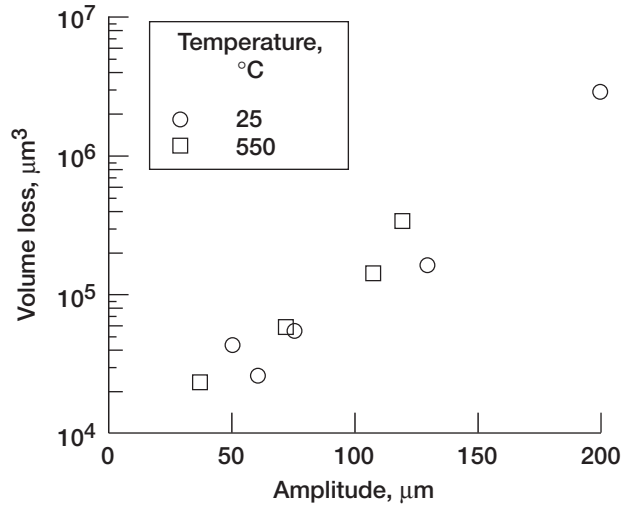


Figure 72.—Wear volume loss of Ti-47-2-2 flat in contact with IN718 pin in air as function of slip amplitude. Fretting conditions: load, 30 N; frequency, 50 Hz; total number of cycles, 1 million; and temperatures, 25 and 550  $^{\circ}\text{C}$ .

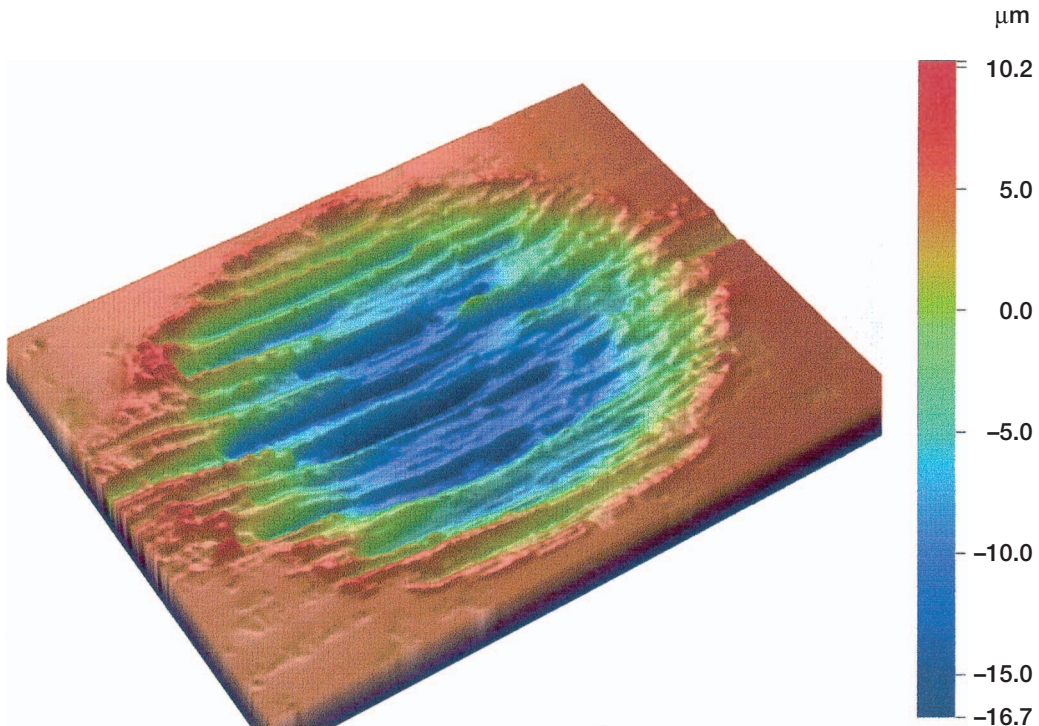


Figure 73.—Wear scar, showing scratches, on Ti-47-2-2 flat in contact with IN718 pin. Fretting conditions: load, 30 N; frequency, 50 Hz; slip amplitude, 200  $\mu\text{m}$ ; total number of cycles, 1 million; and temperature, 25  $^{\circ}\text{C}$ .

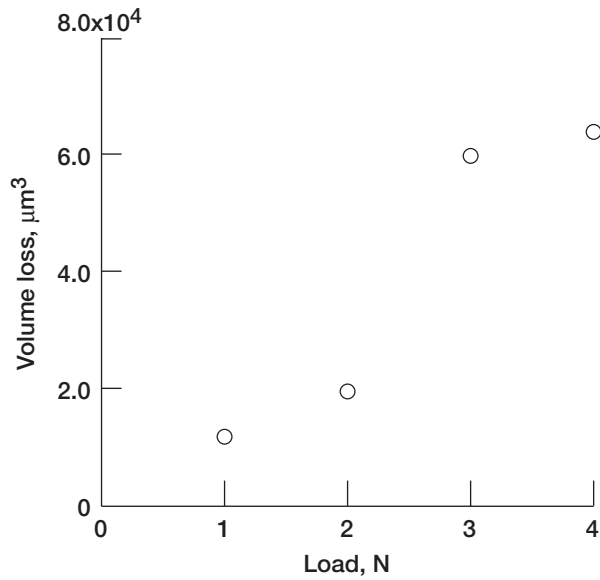


Figure 74.—Wear volume loss of Ti-47-2-2 flat in contact with IN718 pin as function of load. Fretting conditions: frequency, 80 Hz; slip amplitude, 50  $\mu\text{m}$ ; total number of cycles, 1 million; environment, air; and temperature, 550 °C.

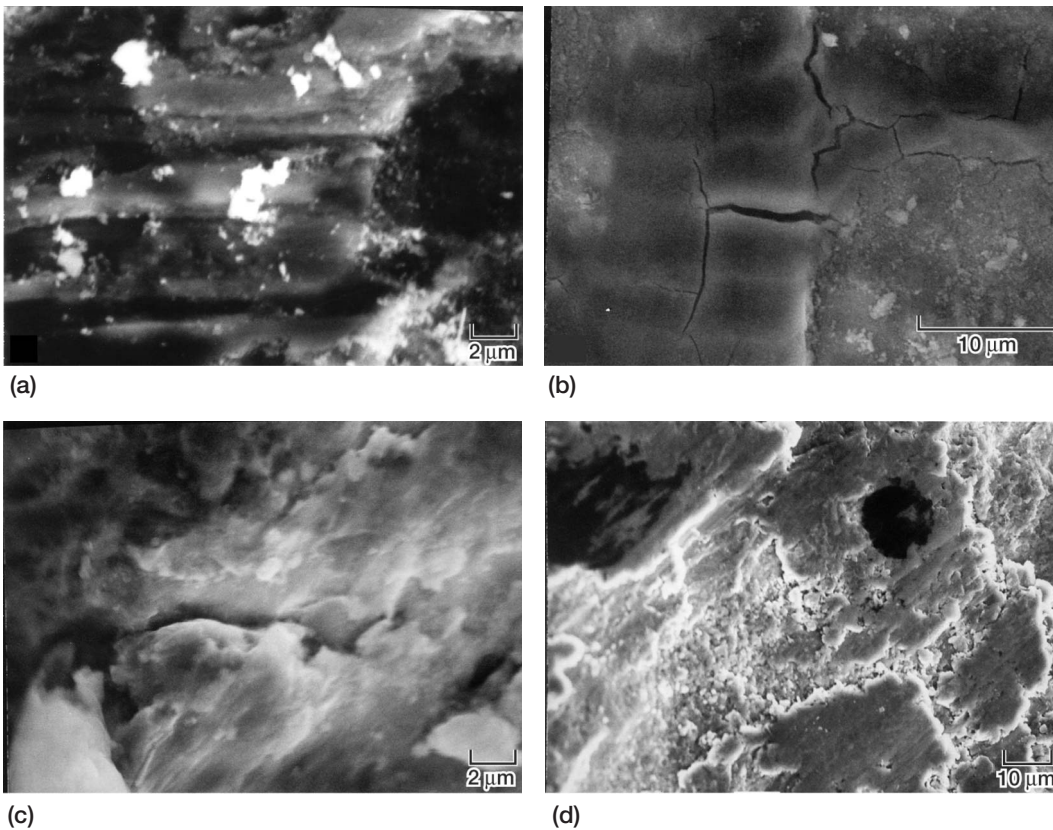


Figure 75.—Surface and subsurface damage in IN718 pin in contact with Ti-47-2-2 flat. Fretting conditions: load, 1 N; frequency, 80 Hz; slip amplitude, 50  $\mu\text{m}$ ; total number of cycles, 1 million; environment, air; and temperature, 550 °C. (a) Scratches. (b) and (c) Cracks in oxide layer.

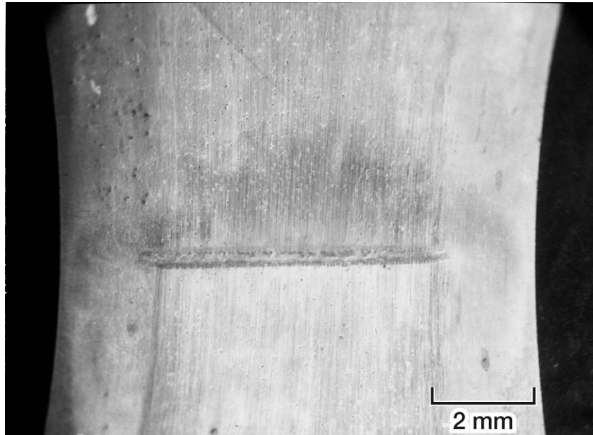


Figure 76.—Wear scar produced on Ti-47-2-2 fatigue specimen in contact with IN718 contact pad. Fretting conditions (table III(b), for fretting on back side): load, 1.5 to 3.0 N; frequency, 80 Hz; slip amplitude, 50  $\mu\text{m}$ ; total number of cycles, 40 million; environment, air; and temperature, 550  $^{\circ}\text{C}$ .



Figure 77.—Wear scar with wear debris produced on Ti-47-2-2 fatigue specimen in contact with IN718 contact pad. Fretting conditions (table III(b), for fretting on back side): load, 1.5 to 3.0 N; frequency, 80 Hz; slip amplitude, 50  $\mu\text{m}$ ; total number of cycles, 40 million; environment, air; and temperature, 550  $^{\circ}\text{C}$ .

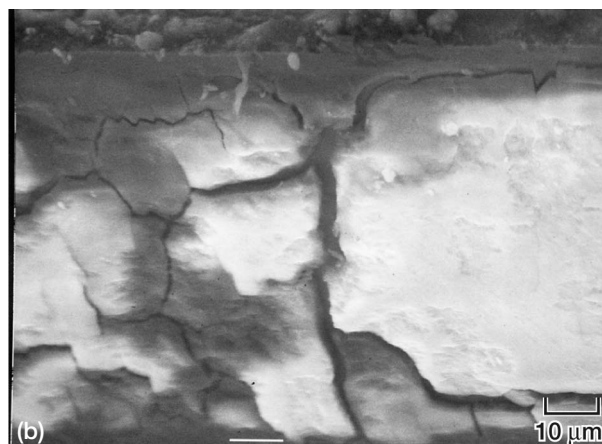


Figure 78.—Protective oxide layers produced on (a) Ti-47-2-2 fatigue specimen and (b) IN718 contact pad. Fretting conditions (table III(b), for fretting on back side): load, 1.5 to 3.0 N; frequency, 80 Hz; slip amplitude, 50  $\mu\text{m}$ ; total number of cycles, 40 million; environment, air; and temperature, 550  $^{\circ}\text{C}$ .

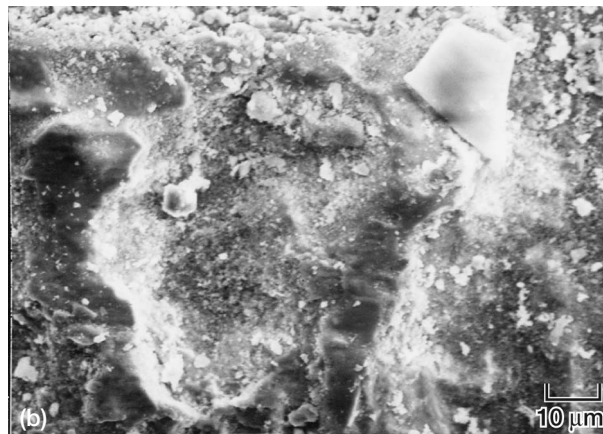


Figure 79.—Surface damage produced on (a) Ti-47-2-2 fatigue specimen and (b) IN718 contact pad. Fretting conditions (table III(b), for fretting on back side): load, 1.5 to 3.0 N; frequency, 80 Hz; slip amplitude, 50  $\mu\text{m}$ ; total number of cycles, 40 million; environment, air; and temperature, 550  $^{\circ}\text{C}$ .

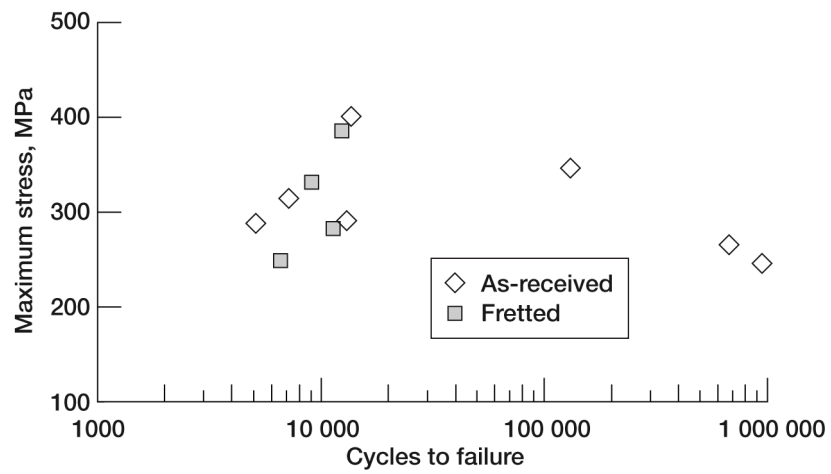


Figure 80.—Fatigue test results for both fretted and virgin, unfretted Ti-47-2-2 fatigue specimens.

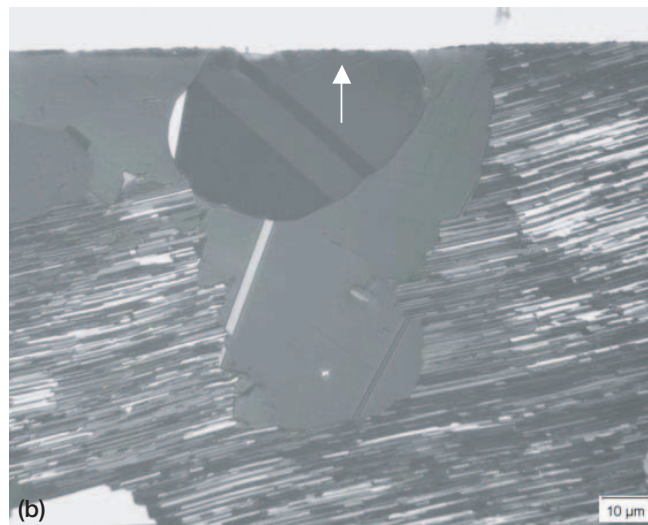
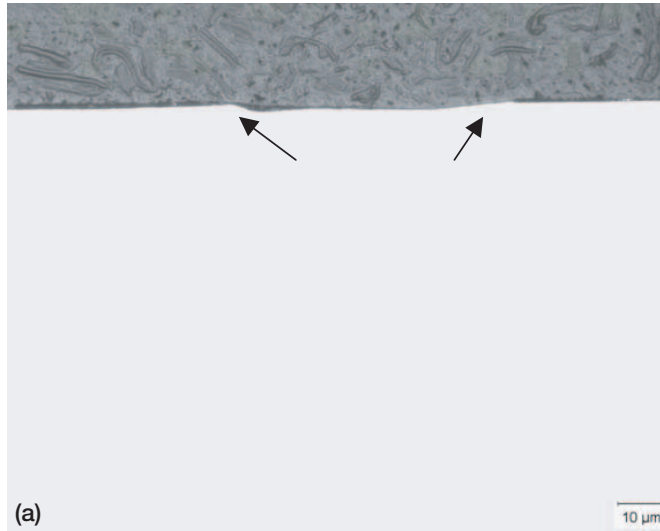


Figure 81.—Ti-47-2-2 fatigue sample 063-03-3. Arrows indicate fretted region. (a) Unetched. (b) Polarized. (c) Etched.

# REPORT DOCUMENTATION PAGE

*Form Approved*  
*OMB No. 0704-0188*

Public reporting burden for this collection of information is estimated to average 1 hour per response, including the time for reviewing instructions, searching existing data sources, gathering and maintaining the data needed, and completing and reviewing the collection of information. Send comments regarding this burden estimate or any other aspect of this collection of information, including suggestions for reducing this burden, to Washington Headquarters Services, Directorate for Information Operations and Reports, 1215 Jefferson Davis Highway, Suite 1204, Arlington, VA 22202-4302, and to the Office of Management and Budget, Paperwork Reduction Project (0704-0188), Washington, DC 20503.

<b>1. AGENCY USE ONLY</b> ( <i>Leave blank</i> )		<b>2. REPORT DATE</b> January 2004	<b>3. REPORT TYPE AND DATES COVERED</b> Technical Memorandum	
<b>4. TITLE AND SUBTITLE</b>  Durability Assessment of Gamma TiAl—Final Report			<b>5. FUNDING NUMBERS</b>  WBS-22-708-24-06	
<b>6. AUTHOR(S)</b>  Susan L. Draper, Bradley A. Lerch, J. Michael Pereira, Kazuhisa Miyoshi, Vinod K. Arya, and Wyman Zhuang				
<b>7. PERFORMING ORGANIZATION NAME(S) AND ADDRESS(ES)</b>  National Aeronautics and Space Administration John H. Glenn Research Center at Lewis Field Cleveland, Ohio 44135-3191			<b>8. PERFORMING ORGANIZATION REPORT NUMBER</b>  E-13659	
<b>9. SPONSORING/MONITORING AGENCY NAME(S) AND ADDRESS(ES)</b>  National Aeronautics and Space Administration Washington, DC 20546-0001			<b>10. SPONSORING/MONITORING AGENCY REPORT NUMBER</b>  NASA TM-2004-212303	
<b>11. SUPPLEMENTARY NOTES</b>  Susan L. Draper, Bradley A. Lerch, J. Michael Pereira, and Kazuhisa Miyoshi, NASA Glenn Research Center; Wyman Zhuang, Aeronautical and Maritime Research Laboratory, Melbourne, Victoria 3207, Australia; and Vinod K. Arya, University of Akron, Akron, Ohio 44325. Responsible person, Bradley A. Lerch, organization code 5920, 216-433-5522.				
<b>12a. DISTRIBUTION/AVAILABILITY STATEMENT</b>  Unclassified - Unlimited Subject Category: 26  Available electronically at <a href="http://gltrs.grc.nasa.gov">http://gltrs.grc.nasa.gov</a> This publication is available from the NASA Center for AeroSpace Information, 301-621-0390.			<b>12b. DISTRIBUTION CODE</b>	
<b>13. ABSTRACT</b> ( <i>Maximum 200 words</i> )  Gamma TiAl was evaluated as a candidate alloy for low-pressure turbine blades in aeroengines. The durability of g-TiAl was studied by examining the effects of impact or fretting on its fatigue strength. Cast-to-size Ti-48Al-2Cr-2Nb was studied in impact testing with different size projectiles at various impact energies as the reference alloy and subsequently fatigue tested. Impacting degraded the residual fatigue life. However, under the ballistic impact conditions studied, it was concluded that the impacts expected in an aeroengine would not result in catastrophic damage, nor would the damage be severe enough to result in a fatigue failure under the anticipated design loads. In addition, other gamma alloys were investigated including another cast-to-size alloy, several cast and machined specimens, and a forged alloy. Within this Ti-48-2-2 family of alloys aluminum content was also varied. The cracking patterns as a result of impacting were documented and correlated with impact variables. The cracking type and severity was reasonably predicted using finite element models. Mean stress affects were also studied on impact-damaged fatigue samples. The fatigue strength was accurately predicted based on the flaw size using a threshold-based, fracture mechanics approach. To study the effects of wear due to potential applications in a blade-disk dovetail arrangement, the machined Ti-47-2-2 alloy was fretted against In-718 using pin-on-disk experiments. Wear mechanisms were documented and compared to those of Ti-6Al-4V. A few fatigue samples were also fretted and subsequently fatigue tested. It was found that under the conditions studied, the fretting was not severe enough to affect the fatigue strength of g-TiAl.				
<b>14. SUBJECT TERMS</b>  Intermetallics; Titanium aluminides; Impact resistance; Fatigue tests; Life (durability); Fretting; Wear resistance; Tensile properties			<b>15. NUMBER OF PAGES</b> 138	
			<b>16. PRICE CODE</b>	
<b>17. SECURITY CLASSIFICATION OF REPORT</b> Unclassified	<b>18. SECURITY CLASSIFICATION OF THIS PAGE</b> Unclassified	<b>19. SECURITY CLASSIFICATION OF ABSTRACT</b> Unclassified	<b>20. LIMITATION OF ABSTRACT</b>	